**Dipartimento di Scienze Chimiche e Geologiche**
***Università degli studi di Modena e Reggio Emilia***

**Géo-Océan**
**Unité Mixte de Recherche 6538 CNRS - Ifremer - UBO - UBS**
***Université de Bretagne Occidentale***

# Melting a heterogeneous Earth's mantle under an extreme thermal gradient

**Léna Verhoest**

Supervisors:
Prof. Daniele Brunelli
Prof. Christophe Hémond

PhD. in
**Models and Methods for Material and Environmental Sciences**
Cycle XXXIV
PhD Course Coordinator: Prof. Alfonso Pedone

**Ecole doctorale des Sciences de la Mer et du Littoral**
PhD Course Coordinator: Prof. Catherine Meur Férec

A.A. 2018-2022

# *Acknowledgements*

# *Remerciements*

# *Ringraziamenti*

After these 4 years of hard work, a page is turned. All this would not have been possible alone, and now it is time to say thank you.

First, I would like to thank the jury members for agreeing to judge this work: Delphine Bosch, Jane Koornneef and Andrea Marzoli, I hope you will enjoy reading this PhD thesis. I also thank the reviewers, Jane Koornneef and Andrea Marzoli, for their very interesting comments and suggestions.

Thanks also to Catherine Chauvel and Andreas Stracke, members of my individual monitoring committee. Thanks a lot for all your advice and for coming to my PhD defence.

Many thanks to Daniele Brunelli and Christophe Hémond, my supervisors, who gave me the opportunity to work on this project. Thank you for your help, advice and support. There have been ups and downs, some tears, but much more laughs. These 4 years of PhD have been incredible, thanks again.

Thanks to the M3ES doctoral school for funding this PhD project. Thanks to the SML doctoral school, and more particularly to Elisabeth, Elodie and Aurélie for their help.

Molte grazie ad Anna Cipriani. Grazie per tutte le ore trascorse insieme a discutere, per il tuo aiuto, per la tua pazienza. Sei stata una parte indispensabile di questo lavoro.

Grazie a Fabio Lombardi, Federico Luglio e Tommaso Giovanardi. Vi ringrazio per il vostro aiuto, sia nella preparazione dei miei campioni che nell'elaborazione dei miei dati.

Merci à Marcia Maia, co-cheffe de mission de l’expédition SMARTIES avec Daniele Brunelli. Merci à vous de m’avoir fait participer à cette campagne océanographique, et par-dessus tout de m’avoir donné cette opportunité incroyable de plonger avec le Nautile. Ce fut une expérience extraordinaire.

Un grand merci à Philippe Nonnotte. Merci pour ton aide lors de mes galères de chimies et lors des analyses au TIMS. Merci pour ta gentillesse et ta patience, ça a toujours été un plaisir de discuter avec toi de sciences ou autre.

Thanks to all the people who have helped me in any way: Jean-Pierre Oldra, Sidonie Révillon, Jessica Langlade, Anna Trinquier, Daniela Manzini, Céline Liorzou, Bleuenn Gueguen, Marie-Laure Rouget, Margot Sauvadet, Stefan Lalonde, Maurizio Mazzucchelli, … Thanks also to all the people I met during the SMARTIES expedition, scientists or crew members, you helped to make this experience unforgettable.

Thanks to all my friends from both universities, PhD students, post-docs, etc. Thank you for all the good times, coffee breaks, lunches, aperitifs and other outings. A special thanks to Mohamad. We started together, my first friend in Modena (and an excellent English teacher), two foreigners in the middle of all these Italians. Thank you for everything.

Grazie alle ragazze della danza aerea. Queste poche ore alla settimana sono sempre una boccata d'aria fresca per me, un piccolo momento di evasione anche in tempi difficili.

Grazie alle mie coinquiline, Sofia, Maria-Paola, Marzia e Manuela. Gli ultimi due anni sono stati molto più belli con voi a casa.

Merci à tous les copains qui ont été présents, qui m'ont soutenu. Notamment, un grand merci aux filles du PIB et plus particulièrement à Aline et Noémie, mes deux plus grandes fans. Merci à Anne, Noémie et Brice de m'avoir hébergée à Paris ou Nantes au cours de mes nombreux allers-retours entre Brest et Modène.

Un énorme merci à Manon, co-bureau exceptionnelle. Merci pour ton aide, tes corrections et tous tes conseils. Merci pour ta bonne humeur et ta bêtise contagieuses, les vendredis spritz/pizza, ces soirées à danser toute la nuit. Merci d'être toi !!

Merci à ma famille. Merci pour votre soutien, même si ça n'a pas été toujours évident pour vous de comprendre en quoi consiste mon travail de thèse : « ouais, t'études les cailloux quoi », « mais pourquoi s'embêter à aller si loin chercher des cailloux, on en a plein devant la maison », et j'en passe.

Merci à mon père. Merci pour ton aide, ton soutien. Toujours le premier à faire des expériences scientifiques plus loufoques les unes que les autres, tu m'as donné goût aux sciences, et voilà où j'en suis.

Pour finir, merci à Matthieu, mon pilier tout au long de ces 4 années. Merci d'avoir supporté mon stress, mes plaintes, et ma folie. Ça y est, nous avons tous les 2 terminé cette aventure, et j'ai hâte d'en commencer de nouvelles avec toi.

## Contents

## Table of figures

## Abstract

Key words: mantle heterogeneity, cold spot, mid-ocean ridge, alkaline basalt, mantle geochemistry

The goal of this PhD thesis is to explore the lithological heterogeneity of the suboceanic mantle sourcing the Mid Ocean Ridge Basalts (MORB). Even though the heterogeneity of the mantle has been demonstrated to vary at short, kilometric scale, the composition of the basalts erupted at a single ridge axis segment usually appears relatively homogeneous. This apparent paradox is due to the relatively high degree of mantle partial melting that averages the different lithological contribution to the pooled melt, smoothing out the original variability. A way to separate the single lithological contributions is to explore the compositional variation of melts extracted from a composed mantle source that melts at different potential temperatures. Decreasing temperatures results in the preferential melting of low-solidus lithologies because of heat drained from the high-solidus components during melting. Sampling MORBs along lateral thermal gradients is therefore a promising way to collect separately the melt contributions from different lithologies.

Thermal gradients large enough to affect the melting region at the ridge axis scale can be generated by cooling edge effects where the ridge axis faces the transform fault. The cold-edge effect is usually restricted to a few km-wide region. Here I study the eastern intersection of the Romanche Transform Fault (RTF) with the Mid-Atlantic Ridge (MAR) axis in the Equatorial Atlantic Ocean. The RTF is the largest transform on Earth (950 km). It puts an old, cold and thick lithosphere (40 Ma) directly in contact with the tip of the axial segments of the MAR. This geometry results in a large lateral thermal gradient, reaching >50 km away from the transform and gives rise to peculiar tectonics and magmatism.

I studied a set of basaltic glasses, sampled along the MAR axis approaching the RTF during the PRIMAR expeditions and the SMARTIES 2019 oceanographic expedition, to which I took part. More than 180 samples have been studied for major and trace element compositions (EMPA and LA-ICP-MS) and Pb, Sr, Nd and Hf isotope ratios separated by chromatographic methods and measured by TIMS and HR-MC-ICP-MS.

These MORBs show an unusual high content of $K_2O$ and $Na_2O$, respectively up to 1.95 wt% and 4.45 wt%, plotting across the subalkaline/alkaline boundary. Overall, they vary from transitional- to highly enriched MORBs. Their compositions strictly depend on the local mantle temperature. In the colder section, both major and trace element compositions are very heterogeneous, while samples located from hotter sections have a homogeneous normal-MORB compositional patterns.

The isotopic variability in the region ($^{87}Sr/^{86}Sr$ from 0.702398 to 0.703919, $^{206}Pb/^{204}Pb$ from 18.49 to 19.7, εNd from 2.18 to 11.52, εHf from -2.88 to 23.73) covers almost the whole variability observed along the MAR, including axis portions showing ridge-hotspot interactions. Explaining the observed variability requires mixing various amounts of at least three different components in addition to the depleted MORB mantle. The first, an ultra-depleted melt signature, witnesses for the involvement of a mantle component recording a very ancient depletion event (Ga). The second, a HIMU-type signature linked to the recycling of a very old oceanic crust, and the third, derived from continental material, are evidence for deep ancient mantle processes.

A group of samples shows peculiar compositions, with marked Eu and Sr positive anomalies and homogeneous DMM-type isotopic signatures. These MORBs are proposed to result from partial melting of shallow mantle portions, previously impregnated in the plagioclase stability field, during the relocation of the spreading axis in oscillatory Core Complex tectonics.

## Riassunto

Parole chiave: eterogeneità del mantello, punto freddo, dorsale medio-oceanica, basalto alcalino, geochimica del mantello

Questa tesi esplora l'eterogeneità litologica del mantello suboceanico sorgente dei basalti eruttati lungo la Dorsale Medio-Oceanica (MORB). Sebbene l'eterogeneità del mantello vari a scala chilometrica, la composizione dei basalti eruttati all'asse della dorsale è in genere relativamente costante. Questo apparente paradosso deriva dall'alto grado di fusione parziale del mantello che media il contributo delle diverse litologie della sorgente al fuso aggregato riducendo la variabilità primaria. Un modo per distinguere il contributo delle singole litologie consite nell'esplorare la variazione composizionale dei fusi estratti da una sorgente composita che fonde a diverse temperature. La diminuzione della temperatura porta alla fusione preferenziale delle litologie a basso-solidus che fondendo per prime sottraggono calore alle componenti ad alto-solidus. Campionare i MORB in regioni ad alto gradiente termico appare quindi un modo promettente per separare il contributo delle diverse litologie.

Gradienti termici sufficientemente grandi da influenzare la regione di fusione alla scala dell'asse della dorsale sono generati dall'effetto di raffreddamento al bordo laddove l'asse della dorsale incontra la faglia trasforme. L'effetto di bordo freddo è solitamente limitato a una regione di pochi km. Nel mio lavoro ho studiato l'intersezione orientale della faglia transforme Romanche (RTF) con l'asse della Dorsale Medio-Atlantica (MAR) nell'Oceano Atlantico Equatoriale. La RTF è la più grande trasforme sulla Terra (950 km). Mette direttamente a contatto una litosfera vecchia, fredda e spessa (40 Ma) con la terminazione dei segmenti assiali della MAR. Questa geometria genera un forte gradiente termico laterale che si estende oltre i 50 km dalla intersezione e origina una peculiare tettonica e magmatismo.

Ho studiato una collezione di vetri basaltici, recuperati lungo l'asse MAR la spedizione oceanografica SMARTIES 2019, cui ho partecipato, e le precedenti spedizioni PRIMAR. Più di 180 campioni sono stati studiati per gli elementi maggiori e in traccia (EMPA e LA-ICP-MS) e rapporti isotopici di Pb, Sr, Nd e Hf separati tramite cromatografia e misurati con TIMS e HR-MC-ICP-MS.

Questi MORB mostrano un contenuto insolitamente elevato di $K_2O$ e $Na_2O$, rispettivamente fino all'1,95% in peso e al 4,45% in peso, superando il limite subalcalino/alcalino. Nel complesso, questi basalti variano da MORB transizionali a fortemente arricchiti. La loro composizione è strettamente correlata alla temperatura del mantello locale. Nella sezione più fredda, sia la composizione degli elementi maggiori sia quella degli elementi in traccia appare fortemente

eterogenea, mentre nelle sezioni più calde si osservano MORB normale composizionalmente omogenei.

La variabilità isotopica misurata ($^{87}Sr/^{86}Sr$: 0,702398 a 0,703919; $^{206}Pb/^{204}Pb$: 18,49 a 19,7; εNd: 2,18 a 11,52; εHf: -2,88 a 23,73) copre quasi completamente la variabilità della MAR, compresi i settori che mostrano interazioni dorsale-hotspot. Questa variabilità può essere spiegata da un mix di almeno tre diverse componenti oltre al mantello impoverito. La prima componente, ha una impronta di fuso ultra-impoverito, testimonia cioè un evento di fusione parziale molto antico (Ga). La seconda e la terza, rispettivamente con una impronta di tipo HIMU legata al riciclaggio di una crosta oceanica molto antica e una derivata da un materiale continentale, registrano processi processi antichi e profondi del mantello.

Un gruppo di campioni mostra composizioni particolari, con anomalie positive di Eu e Sr e rapporti isotopici omogenei simili a quelli del mantello impoverito. Questi MORBs derivano dalla fusione parziale del mantello poco profondo, precedentemente impregnato nel campo di stabilità del plagioclasio, durante lo spostamento dell'asse della dorsale all'interno di una superficie corrugata.

## Résumé

Mots clés: hétérogénéité du manteau, point froid, dorsale médio-océanique, basalte alcalin, géochimie du manteau.

Cette thèse explore l'hétérogénéité lithologique du manteau sub-océanique, source des basaltes de dorsales médio-océaniques (MORB). Bien que l'hétérogénéité du manteau varie à des échelles kilométriques, la composition des basaltes éruptés à l'axe de la dorsale est généralement relativement homogène. Ce paradoxe apparent est dû au degré élevé de fusion partielle du manteau, qui moyenne la contribution relative des différentes lithologies sources du magma, masquant leur signature chimique primaire. Une façon de distinguer les différentes lithologies contribuant à la composition des MORBs est d'explorer la variation de composition des magmas extraits à partir d'une source composite fondue à différentes températures. La diminution de la température entraîne la fusion préférentielle des lithologies à faible solidus grâce à la chaleur soustraite aux composants à solidus élevé. L'échantillonnage de MORBs dans des régions à fort gradient thermique permettrait donc de séparer la contribution des différentes lithologies.

L’intersection entre l’axe d’une dorsale et une faille transformante est une zone dite « froide », ce qui génère des gradients thermiques suffisamment importants pour influencer la zone de fusion partielle à l'axe de la dorsale. Cet effet de refroidissement est généralement limité à une région de quelques kilomètres. Ma thèse porte sur l'intersection orientale de la faille transformante Romanche (RTF) avec l'axe de la dorsale médio-Atlantique (MAR) dans l'océan Atlantique équatorial. La RTF est la plus grande faille transformante sur Terre (950 km). Elle met directement en contact une lithosphère ancienne, froide et épaisse (40 Ma) avec l’extrémité des segments axiaux de la MAR. Cette géométrie génère un fort gradient thermique latéral qui s'étend au-delà de 50 km de l'intersection, et donne lieu à une tectonique et un magmatisme particuliers.

J'ai étudié une collection de verres basaltiques, échantillonnés le long de l'axe de la MAR lors de l'expédition océanographique SMARTIES 2019, à laquelle j'ai participé, et des expéditions PRIMAR précédentes. Plus de 180 échantillons ont été analysés pour leur composition en éléments majeurs et en éléments en trace (EMPA et LA-ICP-MS) et leurs rapports isotopiques de Pb, Sr, Nd et Hf, séparés par chromatographie et mesurés par TIMS et HR-MC-ICP-MS.

Ces MORBs présentent une teneur inhabituellement élevée en $K_2O$ et $Na_2O$, jusqu'à 1,95 poids% et 4,45 poids% respectivement, dépassant la limite subalcaline/alcaline. Dans l'ensemble, ces basaltes ont une composition variant de MORB classiques à fortement enrichis. Leur composition est étroitement liée à la température locale du manteau. Dans la section axiale la plus

froide, les compositions en éléments majeurs et en trace des MORBs sont fortement hétérogènes, alors que dans les sections plus chaudes, des MORB classiques de composition homogène sont observés.

La variabilité isotopique mesurée ($^{87}Sr/^{86}Sr$: 0.702398 à 0.703919 ; $^{206}Pb/^{204}Pb$ : 18.49 à 19.7 ; εNd : 2.18 à 11.52 ; εHf : -2.88 à 23.73) couvre presque toute la variabilité observée le long de la MAR, y compris les zones axiales montrant des interactions avec des points chauds. Cette variabilité peut être expliquée par un mélange d'au moins trois composants différents en plus du manteau appauvri. Le premier, une signature ultra-appauvrie, témoigne d’un évènement de fusion partielle très ancien (Ga). Les deux autres composants, une signature de type HIMU liée au recyclage d'une croûte océanique très ancienne pour le second et une signature dérivée de matériel continental pour le troisième, mettent en évidence des processus mantelliques anciens et profonds.

Un groupe d'échantillons présente des compositions particulières, avec des anomalies positives marquées en Eu et Sr et des rapports isotopiques homogènes de type manteau appauvri. Ces MORBs résultent de la fusion partielle de manteau peu profond, précédemment imprégné dans le champ de stabilité du plagioclase, pendant le déplacement de l'axe de la dorsale au sein d’une surface corruguée.

# CHAPTER 1 Introduction

This thesis deals with the elemental and isotopic composition of basaltic glasses collected from the Ridge-Transform Intersection between the Romanche Transform Fault and the Eastern Mid Atlantic Ridge axis (Eastern Romanche Ridge Transform Intersection: ERRTI) in the equatorial Atlantic Ocean. This portion of the Mid-Atlantic ridge is part of a wider area characterized by a number of peculiarities:

(a) The MAR axis is displaced by a set of major, long-offset transforms, the longest being the Romanche (offset ~950 km);

(b) The axial, near-zero age topographic level is deeper than normal;

(c) Crustal thickness is anomalously low throughout the equatorial region, and mantle-derived peridotites are exposed over large areas;

(d) The chemistry of zero-age basalts and of mantle-derived peridotites both suggest that the degree of melting undergone by the upper mantle below the MAR is exceptionally low.

These features have been explained by the hypothesis that the upper mantle below the equatorial MAR is affected by a thermal minimum.

**The aim of this project is to take advantage of the anomalous regional thermal setting of the Romanche Transform fault to identify small scale heterogeneities distributed in the mantle source in a context devoid of hot-spot contamination.** Using geochemical tracers on lavas erupted at the ERRTI, I deciphered the different source contributions by sampling melts produced at different thermal conditions. The rationale can be summarized as follow: partial melting occurs at different thermal conditions between the segment centre and its tips. The segment centre, melts under the “normal” thermal conditions typical of a slow-spreading ridge. Conversely, axial regions toward the segment end, i.e., towards the transform, melt at decreasing mantle potential temperatures due to the extreme cold edge effect deriving by thermal diffusion to the old/cold plate facing the segment tip. Under these conditions, the low solidus lithologies will be preferentially sampled by partial melting.

## 1.1 **Thermal state of the mantle**

The terrestrial mantle extends to a depth of 2900 km and represents 83% of the Earth’s volume. It is commonly divided in two seismic regions: the upper mantle and the lower mantle, separated by the mantle transition zone (410 km to 660 km depth). In the upper part of the upper mantle, the temperature increases by 25–30°C/km. In the lower mantle, a lower thermal gradient occurs and the viscosity slightly decreases (Figure 1.1). In mid-plate oceanic regions and beneath continents where mantle flow lacks a strong upwelling component, this boundary represents the limit between the lithosphere (including the crust) and the asthenosphere (LAB, Lithosphere-Asthenosphere Boundary; Figure 1.1).

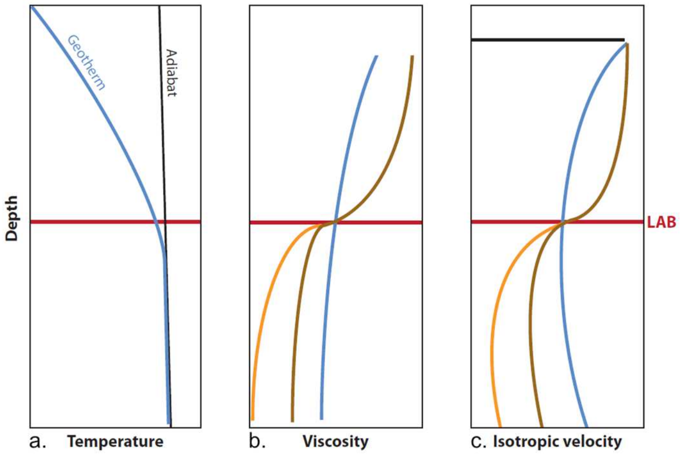

*Figure 1.1 - Schematic models of lithosphere-asthenosphere boundary (LAB) properties (from Fischer et al., 2010). (a) Upper mantle geotherm under "normal" conditions. (b) Evolution of the mantle viscosity with depth. Blue: at "normal geotherm". Brown: Geotherm for a compositional difference between lithosphere (dry) and the asthenosphere (hydrated). Orange: Same as brown with partial melting in the asthenosphere. (c) Evolution of the isotropic shear velocity with depth. Coloured lines are the same as (b). The black line schematically illustrates the velocity increase from the crust to the mantle.*

Under these conditions, the geotherm of the upper mantle never crosses the solidus, and melting is not allowed. Conversely, at Mid-Ocean Ridges (MOR), plate separation results in a drop of pressure, allowing the adiabatic rise of mantle material, which reaches the solidus and partially melts (Figure 1.2). Melting generally onsets at the average temperature of 1350°C at thermally "Normal" MORs. Depending on the spreading rate, mantle potential temperature can vary, with changes of about 150°C, from fast (more than 90 mm/y) to ultra-slow (less than 20 mm/y) spreading rates (Husson et al., 2015). Thus, magma supply changes significantly, from high volume of magma (i.e., East Pacific Rise, Scheirer and MacDonald, 1993) to nearly amagmatic system (i.e., Gakkel ridge, South-West Indian Ridge, and peri-Antarctic ridges, Michael et al., 2003, Sauter et al., 2004, West et al., 1994), respectively. Moreover, extreme thermal anomalies can occur at MOR. High positive mantle thermal anomalies are observed when MOR are located close to hot spots. This represents a significant portion (15-20%) of the ~ 60,000 km of MOR, i.e., Iceland, Azores, Ascension, Sierra Leone, Discovery and Shona hot spots along the Mid-Atlantic Ridge; Galapagos and Easter hot spots along the Pacific Ridge; Reunion, Saint Paul-Amsterdam, Crozet and Marion hot spots along the Indian Ridge. There, various amount of deep mantle material, source of the hot spots, raises beneath or close to the MOR axes (Schilling, 1991, Ito et al., 2003). These interactions give rise to high mantle thermal anomalies at the ridge axis, reaching +150/+225°C for ridge centred plumes (Ito and Lin, 1995) and increases of magma supply, due to higher degree of melting. These processes impact the geochemical fingerprint of the erupted lavas.

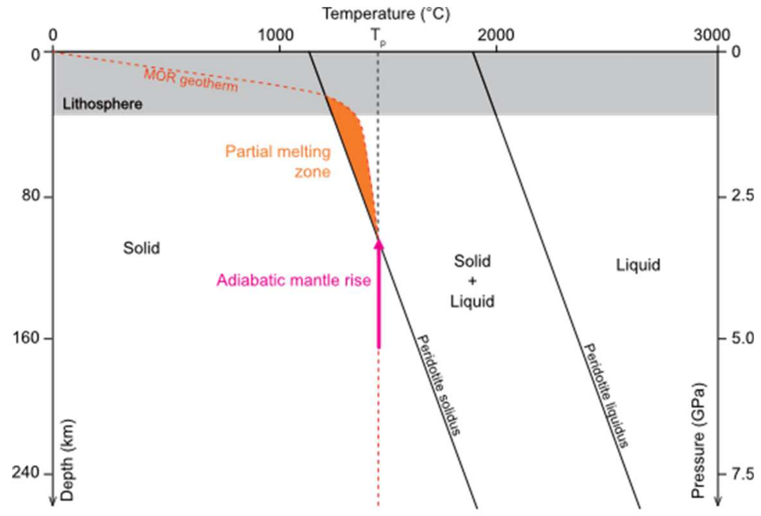

*Figure 1.2 - Oceanic geotherm at Mid-Ocean Ridge (modified after Paquet, 2016).*

On the contrary, certain portions of the oceanic crust are characterized by colder than normal mantle temperatures. These areas are seemingly characterized by the so-called cold spots. Cold spots can be generated by two factors: downwelling mantle asthenospheric flow beneath the ridge region, or when the MOR is crosscut by large-transform faults or closely spaced transform faults. In the first case, the shallow mantle is cooled because old/cold suboceanic asthenosphere is dragged to depth by the local downwelling direction of the deep asthenosphere (Marks et al., 1991; Bonatti et al., 1994). An example is the Antarctic-Australian Discordance, where asthenosphere downwelling may have induced a decrease of about 170°C of the mantle potential temperature (Marks et al., 1991). This component has been hypothesised also for the Romanche region by Bonatti et al. (1994) based on the chemical composition of abyssal peridotites. More recently this cold spot has been linked to the cooling effect of the Equatorial megatransform and the associated high age contrast between an old and cold oceanic lithosphere and the hot and young lithosphere of the zero-age ridge axis south of the Romanche transform (Ligi et al., 2002, and 2005). With age, the oceanic lithosphere progressively becomes thicker, denser, and colder. The encounter between this older lithosphere with a MOR axis results in a decrease of the upper mantle temperature beneath the ridge axis moving away from the RTI boundary (Ligi et al., 2005). Heat flow toward the old oceanic lithosphere results in a lateral thermal gradient (Fox and Gallo, 1984). Modelling of the thermal regime of the Romanche mega-transform shows that mantle potential temperature decreases of more than 200°C at the tip of the Ridge Transform Intersection, where mantle partial melting is completely suppressed (Bonatti et al., 2001; Ligi et al., 2005).

## 1.2 How temperature affects mantle melting

At normal conditions, about 10% to 15% of melting occurs beneath MORs, giving rise to an average 6 km thick oceanic crust (Forsyth, 1993). The erupted magma, called N-MORB (Normal-MOR Basalt) has average composition of 7.76 wt% MgO, 50.42 wt% $SiO_2$, 9.81 wt% FeO, 11.35 wt% CaO, 2.83 wt% $Na_2O$, 15.13 wt% $Al_2O_3$, 1.53 wt% $TiO_2$, 0.14 $K_2O$, 0.164 wt% $P_2O_5$ and 0.171 MnO (Gale et al., 2013). Due to the incompatible affinity of the Rare Earth Elements (REE), MORBs are enriched in REE compared to their depleted mantle source (Figure 1.3). N-MORB patterns are characterised by a slight depletion in Light-REE, with a $La/Sm_N$ of about 0.8 (Figure 1.3).

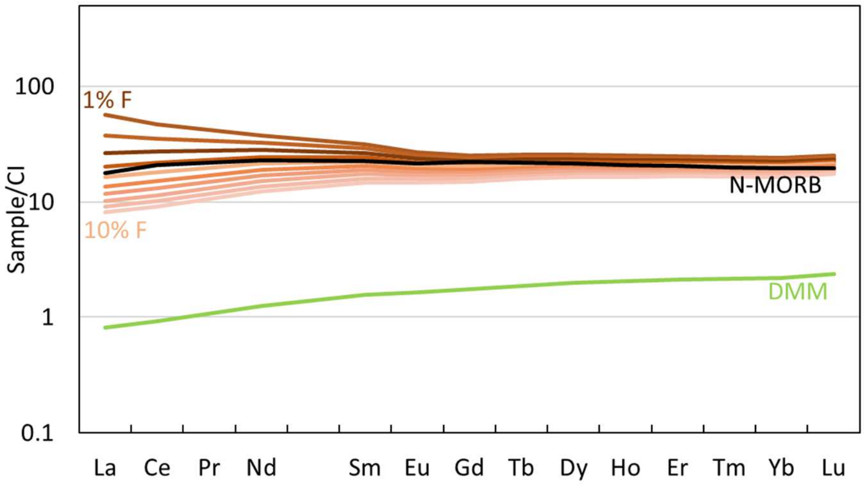

*Figure 1.3 - REE model showing the effect of the degree of partial melting on the melt composition. Fractional non-modal partial melting calculated from average DMM (green line) (Workman and Hart, 2005). Partition coefficient are from Brunelli et al. (2006), melt reaction and mineral modes from Hellebrand et al. (2002). Black line is N-MORB reference from Workman and Hart (2005). Data are normalised to CI chondrite from Barrat et al. (2012).*

An increase of mantle temperature will increase the extent of melting (Figure 1.4). The $SiO_2$, $Al_2O_3$, $Na_2O$ and $K_2O$ content of the extracted melt will progressively decrease, while the MgO, CaO and FeO content will increase (Figure 1.5). The REE will progressively be diluted, and the extracted melts will have more depleted MORB patterns, with lower $La/Sm_N$ ratios (Figure 1.3). The higher extent of melting results in a thicker oceanic crust (Figure 1.4).

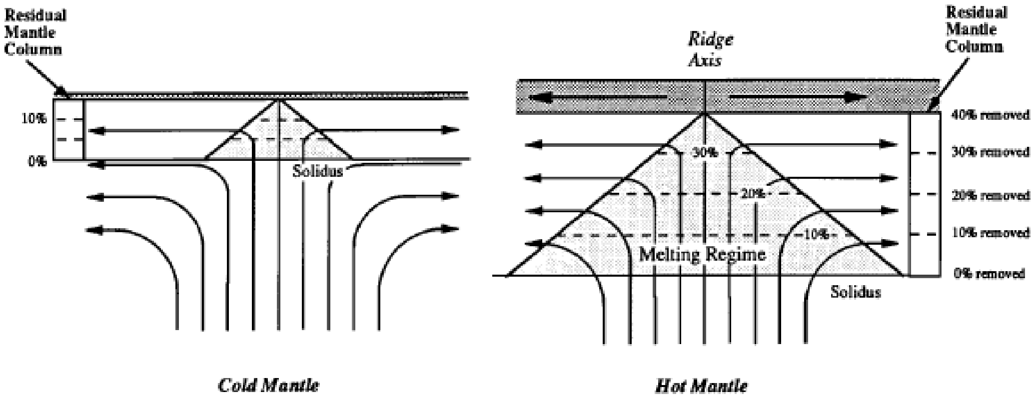

*Figure 1.4 - Evolution of the melting column and oceanic crust thickness within the change in mantle temperature (from Langmuir et al., 1992).*

On the contrary, at lower mantle potential temperature, partial melting starts shallower, resulting in an overall lower extent of melting. This result in a thinner oceanic crust (Figure 1.4), with higher $SiO_2$, $Al_2O_3$, $Na_2O$ and slightly higher $K_2O$ content and lower MgO, CaO and FeO content of the extracted melt (Figure 1.5). The most incompatible elements, being partitioned preferentially into the melt, will result in REE patterns enriched in LREE compared to HREE and in an increasing of the $La/Sm_N$ ratio up to more than 1.5 (Figure 1.3).

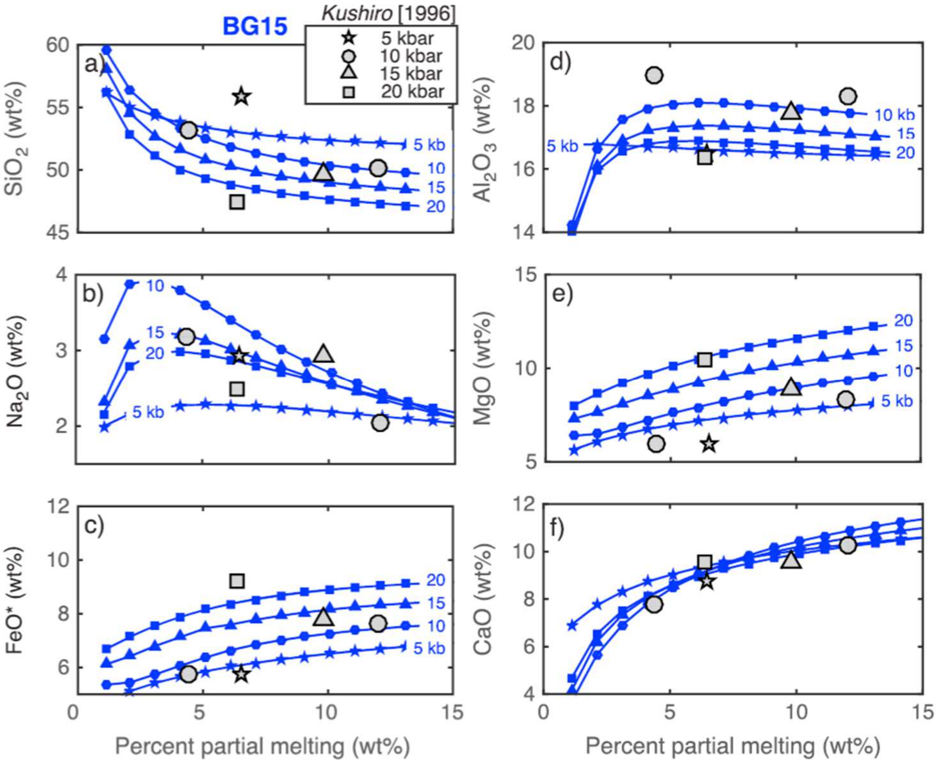

*Figure 1.5 - Modelled melt compositions (blue lines, BG15 model) compared to experimental compositions of melts from peridotitic source partial melting (figure from Behn and Grove, 2015).*

Due to the high influence of the extent of melting on the compositions of melts, geochemical proxies have been developed to estimate the degree of melting beneath MORs (Klein and Langmuir, 1987, Langmuir et al., 1992).

The $Na_2O$, being one of the incompatible elements, correlates inversely to the degree of melting. Generally, it is expressed as $Na_8$, i.e., $Na_2O$ normalized to 8 wt% MgO in order to correct for the effects of shallow crystal fractionation (Klein and Langmuir, 1987). In the case of a homogenous depleted mantle source, low $Na_8$ in MORBs suggests high extent of mantle melting, which results in higher crustal thickness (Klein and Langmuir, 1987; Behn and Grove, 2015) (Figure 1.6).

In a similar way, the ratio $CaO/Al_2O_3$ is frequently used to define the extent of melting of MORBs. $Al_2O_3$ is less incompatible than CaO (Figure 4) and the ratio of the two becomes higher by increasing the extent of melting (Figure 1.6).

In the global MOR data set, an overall positive correlation is observed between $CaO/Al_2O_3$ and spreading rate, which corresponds to the increase of extent of melting at higher spreading rate

(Figure 1.6). The negative correlation between the spreading rate and $Na_8$ is less evident (Figure 1.6). On the whole, the East Pacific Rise (EPR) undergoes higher extent of melting than the Indian or West Pacific MORs. However, at fast-spreading ridges, these proxies are quite homogeneous and correlate with the spreading rate, as for instance $CaO/Al_2O_3$ and $Na_8$ are respectively higher and lower for the S-EPR compared to the N-EPR. At slow-spreading ridges (~ 2 cm/yr), e.g., the Mid-Atlantic Ridge, the $Na_8$ dispersion is instead markedly higher (Figure 1.6).

Moreover, the major element composition of the melt is dependent on the source composition. Thus, the use of major elements to deduce the extent of melting has to be used with care, as it is based on the assumption of a homogenous peridotitic mantle (Klein and Langmuir, 1987, Salters and Hart, 1989, McKenzie and O'Nions, 1991) that is likely to be unrealistic.

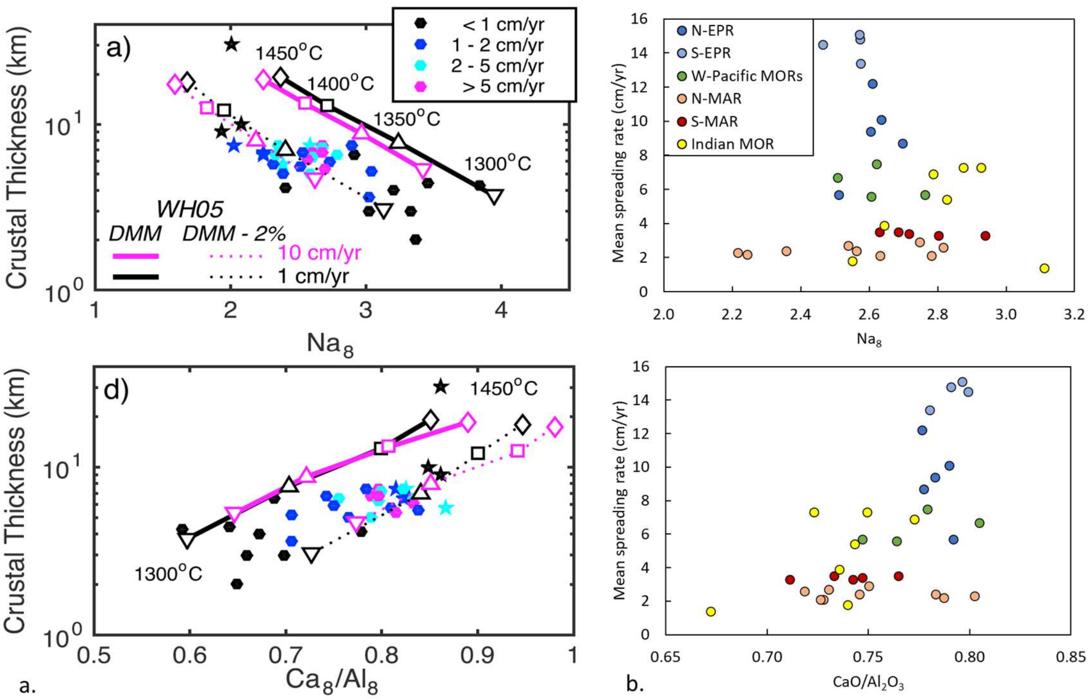

*Figure 1.6 - $Na_8$ and $CaO/Al_2O_3$ vs. crustal thickness and spreading rate. (a) Comparison between crustal thickness and experimental $Na_8$ and $CaO/Al_2O_3$ (from Behn and Grove, 2015). (b) Global MOR $Na_8$ and $CaO/Al_2O_3$ data vs. the mean spreading rate of the various segments (data from Rubin and Sinton, 2007). N-EPR and S-EPR are respectively North- and South-East Pacific Ridge. West Pacific MORs include Pacific-Antarctica ridge, Chile ridge, Gorda ridge, Juan de Fuca ridge and Galapagos ridge. MAR: Mid-Atlantic Ridge.*

## 1.3 How mantle fertility and heterogeneity affect partial melting

The study of MORB compositions and mantle xenoliths have shown that even in the absence of nearby hot spots, the upper mantle is chemically and isotopically heterogeneous (Tatsumoto et al., 1965, Hart, 1971, Schilling et al., 1994, Dosso et al., 1991). Geochemical and thermodynamic modelling have shown how these heterogeneities stem from a lithologically composite mantle (Hirschmann and Stolper, 1996; Phipps Morgan, 2001). Fertile lithologies (hereafter generalized as pyroxenites) have lower solidus temperatures than the surrounding mantle, affecting the melting conditions beneath MORs. Pyroxenite veins dispersed in a screen mantle peridotite will contribute to melt production relative to their abundance. Partial melts of pyroxenite will be extracted along a larger path in the source region than peridotite partial melts because the solidus of pyroxenite is lower than that of the peridotite and crosses the adiabat ~ 20 km deeper than the solidus of peridotite (Hirschman and Stolper, 1996). Moreover, melt productivity is expected to be greater in pyroxenite than in peridotite. Heat diffusion from the peridotite to the melting fertile material will increase the extent of melting of low solidus heterogeneities (Sleep, 1984, Phipps Morgan, 2001) resulting in thicker oceanic crust with possibly enriched compositions (Figure 1.7). If the fertile material is present in a large portion (~20%), it will delay the beginning of partial melting of the enclosing mantle, which will melt at shallower depth (Phipps Morgan, 2001). This results in a total lower extent of melting of the mantle, thus, a thinner oceanic crust (Brunelli et al., 2018).

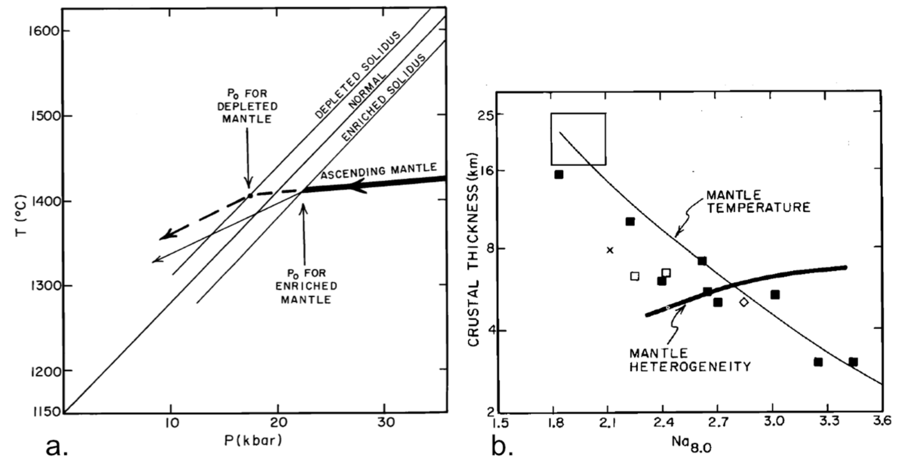

*Figure 1.7 - (a) Evolution of the solidus temperature within the fertility of the mantle (from Langmuir et al., 1992). (b) Change in correlation between Na8 and crustal thickness due to the change in mantle fertility (from Langmuir et al., 1992).*

This model has been confirmed by the study of parental mantle rocks and genetically associated MORBs across the 26 Ma long lithospheric section at the Vema fracture zone (Brunelli et al., 2018). There, the degrees of melting estimated from MORBs differ from those estimated from the peridotitic residues. While the basalts show a decrease in the extent of melting through time, their associated peridotitic mantle shows the opposite trend. The authors assume this decoupling as evidence for a multi-lithological source, composed by a depleted mantle screen veined by fertile lower-solidus material which undercools its host, decreasing the extent of melting of the latter. This result in low degree of melting of the screen peridotite, whereas the extracted melts inherit apparent higher degrees of melting from the fertile low-solidus material (Figure 1.8).

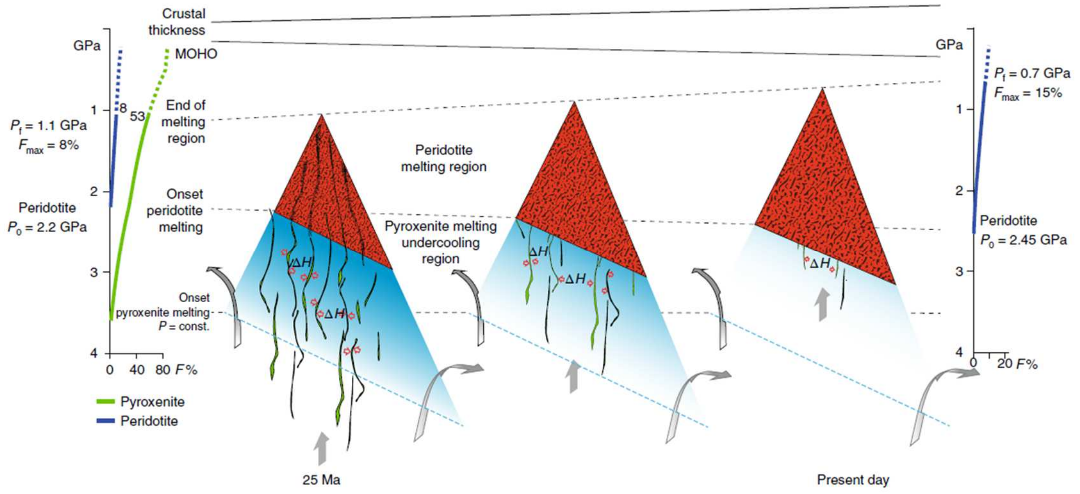

*Figure 1.8 - Evolution scheme of the partial melting column beneath the Vema lithospheric section (Brunelli et al., 2018). In the 25 Ma old lithospheric section, the degree of melting is reduced, preferentially melting the low-solidus lithology over its host peridotitic mantle. The heat released by the latter increases the extent of melting of the pyroxenite, delaying peridotite partial melting at shallower depth. At present day, larger extent of melting occur, allowing partial melting of the peridotite deeper.*

## 1.4 SMARTIES: towards a comprehensive understanding of the role of heterogeneities and mantle temperature in oceanic crust formation

Despite the lithological heterogeneity of the mantle source, MORBs generally have homogeneous compositions. This inconsistency can be explained by the small proportion of heterogeneities compared to the peridotitic mantle and the efficient mixing of melts below the axial ridge axis. Under “normal” thermal conditions at MOR, the signature of melts extracted from heterogeneities is diluted in the large amount of melt from the surrounding mantle, building the homogeneous 6 kms thick oceanic crust. The nature of the low-solidus lithologies and their composition are thus difficult to characterise.

A way to overcome this problem is to find a process that allows separating these heterogeneities. At cold thermal settings, the low solidus lithologies should be preferentially melted and sampled with respect to the mantle screen. It has been demonstrated that the thermal interplay regulated by heat exchange between low- and high-solidus lithologies (Phipps Morgan, 2001, Brunelli et al., 2018, see section 1.3) increases the effect of thermal separation of the different lithological contribution, thus enhancing the geochemical separation of the single contributions. Comparing the compositional fingerprints derived by melting this composite source at different temperatures should allow to obtain a precise definition of the source heterogeneity and the diversity of its components.

This approach was the main premise of the SMARTIES (*Smooth regions at the Mid-Atlantic Ridge Transform-Intersections under extreme thermal gradients*) oceanographic expedition, which took place in July and August 2019 in the Equatorial region of the Mid-Atlantic Ridge. There, a set of mega-transform faults crosscuts the Mid-Atlantic Ridge resulting in cold mantle thermal anomalies. The aim of the expedition was to study the peculiar tectonic and reduced alkaline magmatism due to the thermal minimum at the Eastern Romanche Ridge-Transform Intersection (ERRTI, see chapter 2).

## 1.5 Thesis outline

This thesis starts with the presentation of the geological context of the equatorial region of the MAR, and more specifically of the Romanche mega-transform fault (chapter 2). A detailed description of previous studies and new progress in the region is given, followed by a description of the various oceanographic expeditions that allowed the acquisition of data and samples.

Chapter 3 is dedicated to the description of the different analytical methods and protocols used to obtain the geochemical data.

Major and trace elements of the ERRTI MORBs are presented in chapter 4 and reveal a highly variable composition ranging from depleted to true alkaline basalts showing extreme alkali and incompatible element enrichment similar to those described at the hot spots. These data allowed to separate the effects of the various processes (fractional crystallization, partial melting and melt mixing) occurring at the ERRTI at the origin of the high variability observed in the chemical compositions. Fractional crystallization alone cannot explain the observed variability that requires an input of garnet-bearing lithologies in the MORB source. The presence of a strong lateral thermal regional gradient allows recognizing the temperature effects on mantle melting: a decrease in mantle temperature results in increased compositional variability and relative enrichment in incompatible elements while hotter ridge sections generate more homogeneous N-MORB composition.

Chapter 5 is a preliminary manuscript on the isotopic composition of the ERRTI basaltic glasses showing the presence of extreme mantle endmembers. The radiogenic isotope ratios of Pb, Sr, Hf and Nd allow defining and characterising the mantle components below the ERRTI. The Romanche ERTI isotope composition is extreme within ca. 100 km and shows spatial variability. At higher mantle temperature, in the middle of the ridge axis, the melts derived from each lithology are blended together to give N-MORB compositions, while at lower mantle temperature, close to the RTI, these melts are “unblended”.

A study of a specific group of samples showing peculiar trace element compositions is described in chapter 6. These sample show a positive europium and strontium anomalies along with high $SiO_2$ and $Al_2O_3$ and low $TiO_2$, CaO and FeO contents. These signatures originate from melting of a plagioclase impregnated peridotite due to local spatial readjustment (ridge migration) of the active ridge axis.

## References

Barrat, J.A., Zanda, B., Moynier, F., Bollinger, C., Liorzou, C., Bayon, G., 2012. *Geochemistry of CI chondrites: Major and trace elements, and Cu and Zn Isotopes.* Geochimica et Cosmochimica Acta 83, 79–92. doi:10.1016/j.gca.2011.12.011.

Behn, M.D., Grove, T.L., 2015. *Melting systematics in mid-ocean ridge basalts: Application of a plagioclase-spinel melting model to global variations in major element chemistry and crustal thickness.* J. Geophys. Res. Solid Earth 120 (7), 4863–4886. doi:10.1002/2015JB011885.

Bonatti, E., Brunelli, D., Fabretti, P., Ligi, M., Asunta, P.R., Seyler, M., 2001. *Steady-state creation of crust-free lithosphere at cold spots in mid-ocean ridges.* Geol 29 (11), 979. doi:10.1130/0091-7613(2001)029<0979:SSCOCF>2.0.CO;2.

Bonatti, E., Ligi, M., Gasperini, L., Peyve, A., Raznitsin, Y., Chen, Y.J., 1994. *Transform migration and vertical tectonics at the Romanche fracture zone, equatorial Atlantic.* Journal of Geophysical Research 99 (B11), 21,779-21,802.

Brunelli, D., Cipriani, A., Bonatti, E., 2018. *Thermal effects of pyroxenites on mantle melting below mid-ocean ridges.* Nature Geosci 11 (7), 520–525. doi:10.1038/s41561-018-0139-z.

Brunelli, D., Seyler, M., Cipriani, A., Ottolini, L., Bonatti, E., 2006. *Discontinuous Melt Extraction and Weak Refertilization of Mantle Peridotites at the Vema Lithospheric Section (Mid-Atlantic Ridge).* Journal of Petrology 47 (4), 745–771. doi:10.1093/petrology/egi092.

Dosso, L., Hanan, B.B., Bougault, H., Schilling, J.-G., Joron, J.-L., 1991. *Sr Nd Pb geochemical morphology between 10° and 17°N on the Mid-Atlantic Ridge: A new MORB isotope signature.* Earth and Planetary Science Letters 106 (1-4), 29–43. doi:10.1016/0012-821X(91)90061-L.

Fischer, K.M., Ford, H.A., Abt, D.L., Rychert, C.A., 2010. *The Lithosphere-Asthenosphere Boundary.* Annu. Rev. Earth Planet. Sci. 38 (1), 551–575. doi:10.1146/annurev-earth-040809-152438.

Forsyth, D.W., 1993. *Crustal thickness and the average depth and degree of melting in fractional melting models of passive flow beneath mid-ocean ridges.* J. Geophys. Res. 98 (B9), 16073. doi:10.1029/93JB01722.

Fox, P.J., Gallo, D.G., 1984. *A tectonic model for ridge-transform-ridge plate boundaries: Implications for the structure of oceanic lithosphere.* Tectonophysics 104 (3-4), 205–242. doi:10.1016/0040-1951(84)90124-0.

Gale, A., Dalton, C.A., Langmuir, C.H., Su, Y., Schilling, J.-G., 2013. *The mean composition of ocean ridge basalts.* Geochem. Geophys. Geosyst. 14 (3), 489–518. doi:10.1029/2012GC004334.

Hart, S.R., 1971. *K, Rb, Cs, Sr and Ba contents and Sr isotope ratios of ocean floor basalts.* Phil. Trans. R. Soc. Lond. A 268 (1192), 573–587. doi:10.1098/rsta.1971.0013.

Hellebrand, E., Snow, J.E., Hoppe, P., Hofman, A.W., 2002. *Garnet-field Melting and Late-stage Refertilization in 'Residual' Abyssal Peridotites from the Central Indian Ridge.* Journal of Petrology 43 (12), 2305–2338. doi:10.1093/petrology/43.12.2305.

Hirschmann, M.M., Stolper, E.M., 1996. *A Possible Role For Garnet Pyroxenite in the origin of the garnet signature in MORB* 124, 185–208.

Husson, L., Yamato, P., Bézos, A., 2015. *Ultraslow, slow, or fast spreading ridges: Arm wrestling between mantle convection and far-field tectonics.* Earth and Planetary Science Letters 429, 205–215. doi:10.1016/j.epsl.2015.07.052.

Ito, G., Lin, J., Graham, D., 2003. *Observational and theoretical studies of the dynamics of mantle plume-mid-ocean ridge interaction.* Rev. Geophys. 41 (4). doi:10.1029/2002RG000117.

Ito, G.: Lin, J., 1995. *Oceanic spreading center– hotspot interactions: Constraints from along-isochron bathymetric and gravity anomalies.* Geology 23 (7), 657–660.

Klein, E.M., Langmuir, C.H., 1987. *Global Correlations of Ocean Ridge Basalt Chemistry with Axial Depth and Crustal Thickness.* American Geophysical Union.

Langmuir, C. H., Klein, E.M., Plank, T., 1992. *Petrological systematics of mid-ocean ridge basalts: Constraints on melt generation beneath ocean ridges.* American Geophysical Union.

Ligi, M., Bonatti, E., Cipriani, A., Ottolini, L., 2005. *Water-rich basalts at mid-ocean-ridge cold spots.* Nature 434 (7029), 66–69. doi:10.1038/nature03264.

Ligi, M., Bonatti, E., Gasperini, L., Poliakov, A.N.B., 2002. *Oceanic broad multifault transform plate boundaries.* Geology 30 (1), 11–14. doi:10.1130/0091-7613(2002)030<0011:OBMTPB>2.0.CO;2.

McKenie, D., O'Nions, R.K., 1991. *Partial Melt Distributions from Inversion of Rare Earth Element Concentrations.* J Petrology 32 (5), 1021–1091. doi:10.1093/petrology/32.5.1021.

Marks, K.M., Sandwell, D.T., Vogt, P.R., Hall S. A., 1991. *Mantle downwelling beneath the Australian-Antarctic discordance zone: evidence from geoid height versus topography.* Earth and Planetary Science Letters 103, 325–338.

Michael, P.J., Langmuir, C.H., Dick, H.J.B., Snow, J.E., Goldstein, S.L., Graham, D.W., Lehnert, K., Kurras, G., Jokat, W., Mühe, R., Edmonds, H.N., 2003. *Magmatic and amagmatic seafloor generation at the ultraslow-spreading Gakkel ridge, Arctic Ocean.* Nature 423 (6943), 956–961. doi:10.1038/nature01704.

Paquet, M., 2016. *Pétrogenèse des MORB en contexte de dorsale ultralente : exemple de la dorsale Sud-Ouest Indienne entre 61°-67°E*, 289 pp.

Phipps Morgan, J., 2001. *Thermodynamics of pressure release melting of a veined plum pudding mantle.* Geochem. Geophys. Geosyst. 2.

Rubin, K.H., Sinton, J.M., 2007. *Inferences on mid-ocean ridge thermal and magmatic structure from MORB compositions.* Earth and Planetary Science Letters 260 (1-2), 257–276. doi:10.1016/j.epsl.2007.05.035.

Salters, V.J.M., Hart, S.R., 1989. *The hafnium paradox and the role of garnet in the source of mid-ocean ridge basalts.* Nature 342, 420–422.

Sauter, D., Mendel, V., Rommevaux-Jestin, C., Parson, L.M., Fujimoto, H., Mével, C., Cannat, M., Tamaki, K., 2004. *Focused magmatism versus amagmatic spreading along the ultra-slow spreading Southwest Indian Ridge: Evidence from TOBI side scan sonar imagery.* Geochem. Geophys. Geosyst. 5 (10). doi:10.1029/2004GC000738.

Scheirer, D.S., MacDonald, K.C., 1993. *Variation in cross-sectional area of the axial ridge along the East Pacific Rise: Evidence for the magmatic budget of a fast spreading center.* J. Geophys. Res. Solid Earth 98 (B5), 7871–7885. doi:10.1029/93JB00015.

Schilling, J.-G., 1991. *Fluxes and excess temperatures of mantle plumes inferred from their interaction with migrating mid-ocean ridges.* Nature 352 (6334), 397–403. doi:10.1038/352397a0.

Schilling, J.-G., Hanan, B.B., McCully, B., Kingsley, R.H., Fontignie, D., 1994. *Influence of the Sierra Leone mantle plume on the equatorial Mid-Atlantic Ridge: A Nd-Sr-Pb isotopic study.* J. Geophys. Res. 99 (B6), 12005–12028. doi:10.1029/94JB00337.

Sleep, N.H., 1984. *Tapping of magmas from ubiquitous mantle heterogeneities: An alternative to mantle plumes?* J. Geophys. Res. 89 (B12), 10029–10041. doi:10.1029/JB089iB12p10029.

Tatsumoto, M., Hedge, C.E., Engel, A.E., 1965. *Potassium, Rubidium, Strontium, Thorium, Uranium, and the Ratio of Strontium-87 to Strontium-86 in Oceanic Tholeiitic Basalt.* Science (New York, N.Y.) 150 (3698), 886–888. doi:10.1126/science.150.3698.886.

West, B.P., Sempéré, J.-C., Pyle, D.G., Phipps Morgan, J., Christie, D.M., 1994. *Evidence for variable upper mantle temperature and crustal thickness in and near the Australian-Antarctic Discordance.* Earth and Planetary Science Letters 128 (3-4), 135–153. doi:10.1016/0012-821X(94)90141-4.

Workman, R.K., Hart, S.R., 2005. *Major and trace element composition of the depleted MORB mantle (DMM).* Earth and Planetary Science Letters 231, 53-72. doi:10.1016/j.epsl.2004.12.005.

# CHAPTER 2 Geological and geochemical background

## 2.1 The equatorial Mid-Atlantic Ridge

The equatorial region of the Mid-Atlantic Ridge (MAR) has been suggested to represent a cold spot, i.e., a region where mantle potential temperature is lower than MOR average (Bonatti et al., 1993, Schilling et al., 1995, Bonatti et al., 2001, Ligi et al., 2005). The origin of this anomaly has been suggested to lay in a peculiar mantle flow pattern, inheriting the thermal setting of the opening of the MAR (Bonatti et al., 1993). However, more recent interpretations point to the extreme cold-edge effect of the set of East-West mega-transform faults offsetting the Equatorial MAR: from north to south Saint Paul, Romanche and the Chain transform faults (Figure 2.1). Their large age contrast bring in contact an old, thick and cold lithosphere with the tip of the ridge axis. This results in a cooling of the lithosphere beneath the ridge axis, giving rise to low magma budget and peculiar tectonics (Bonatti et al., 1996, Ligi et al., 2002 and 2005).

The Saint Paul Transform Fault (SPTF) is composed by four, en-echelon, transform faults, cutting the MAR in three spreading centres and cumulating a total offset of 580 km (Hekinian et al., 2000). At the regional scale, the degree of melting is very low (Schilling et al., 1995, Le Voyer et al., 2015). Mantle rocks are largely exposed, and the northern fault is characterized by the presence of a regional-sized transpressional sigmoid culminating at the St. Peter and Paul Archipelago (Motoki et al., 2014, Maia et al., 2016) exposing highly deformed mantle rocks (Barão et al., 2020, Campos et al., 2021).

The Romanche Transform Fault (RTF) is the longest transform on Earth. It offsets the MAR by 950 km (Heezen et al., 1964) resulting in an age contrast of about 40 Ma between the old lithosphere and the ridge axis. The present study focus on this transform fault and a complete description is given in section 2.2.

The Chain Transform Fault (CTF) offsets the MAR by 300 km (Heezen et al., 1964).

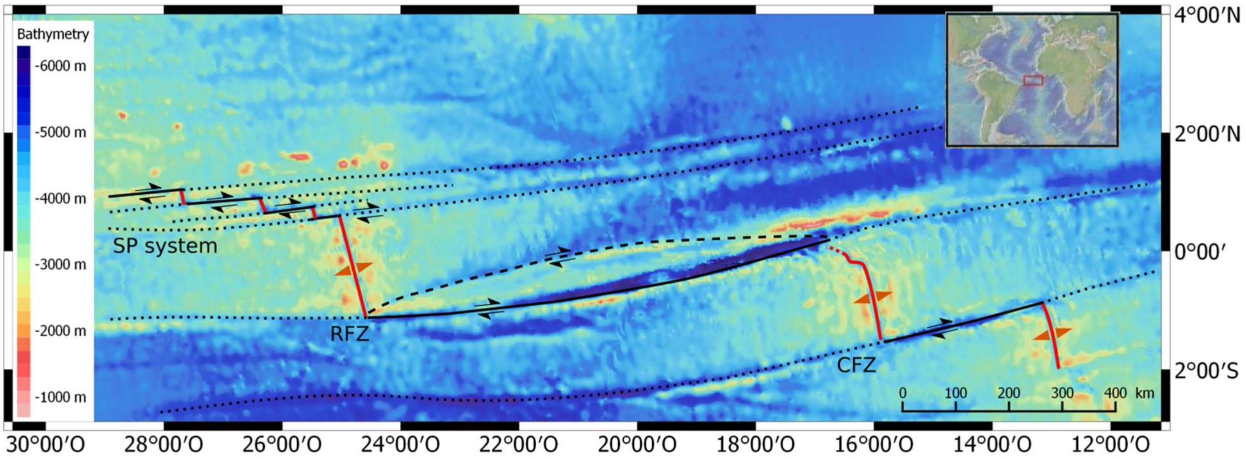

*Figure 2.1 - Bathymetric map of the equatorial region of the MAR. The continuous red and black lines represent the MAR ridge axis and the transform faults respectively. Thin dashed lines represent the fracture zones. SP: Saint Paul; RFZ: Romanche Fracture Zone; CFZ: Chain Fracture Zone.*

Studies of the compositions of peridotites and MORBs from the equatorial MAR revealed that the degree of melting undergone by the subridge mantle is lower than average (Schilling et al., 1995, Bonatti et al., 1993). The abundant expositions of mantle rocks, attests for an incomplete magmatic coverage during spreading thus confirming the regional decrease of mantle partial melting. Recovered residual peridotites are mainly lherzolite with minor harzburgite. Characteristic of this area is the presence of abundant fertile, plagioclase-bearing peridotites, resulting from melt-impregnation at shallow depth (Bonatti et al., 1993, 2001, Brunelli and Seyler, 2010, Seyler and Bonatti, 1997, Tartarotti et al., 2002).

Based on the isotope signature of the MORBs, Schilling et al. (1994) have separated the equatorial MAR in two areas: The North Equatorial Zone (NEZ), from 5°N to 0°, and the South Equatorial Zone (SEZ), from 1°S to 7°S. In the NEZ, the samples have enriched isotope signatures, high Pb and Sr and low Nd isotopes ratios, especially in the northern part of the SPTF (Figure 2.2). Moreover, basalts enriched in $La/Sm_N$ with high alkaline content have been observed there (Hekinian et al., 2000, Schilling et al., 1994 and 1995) (Figure 2.2). The authors named this signature the 1.7°N anomaly (Figure 2.2) and proposed an influence of the Sierra Leone hotspot, located further North-East, to account for it. This enriched signature is not observed continuously in the SEZ. The ridge axis that intersects the RTF at its eastern boundary appears instead as a transitional region. Even if this axis is clearly not influenced by the Sierra Leone hotspot, some scattered compositions similar to those observed North of the SPTF have been reported particularly concentrated in the eastern Romanche Ridge-Transform Intersection (Bonatti et al., 2001, Kelley et al., 2013, Le Voyer et al., 2015, Ligi et al., 2005, Schilling et al., 1994, see section 2.2 for details).

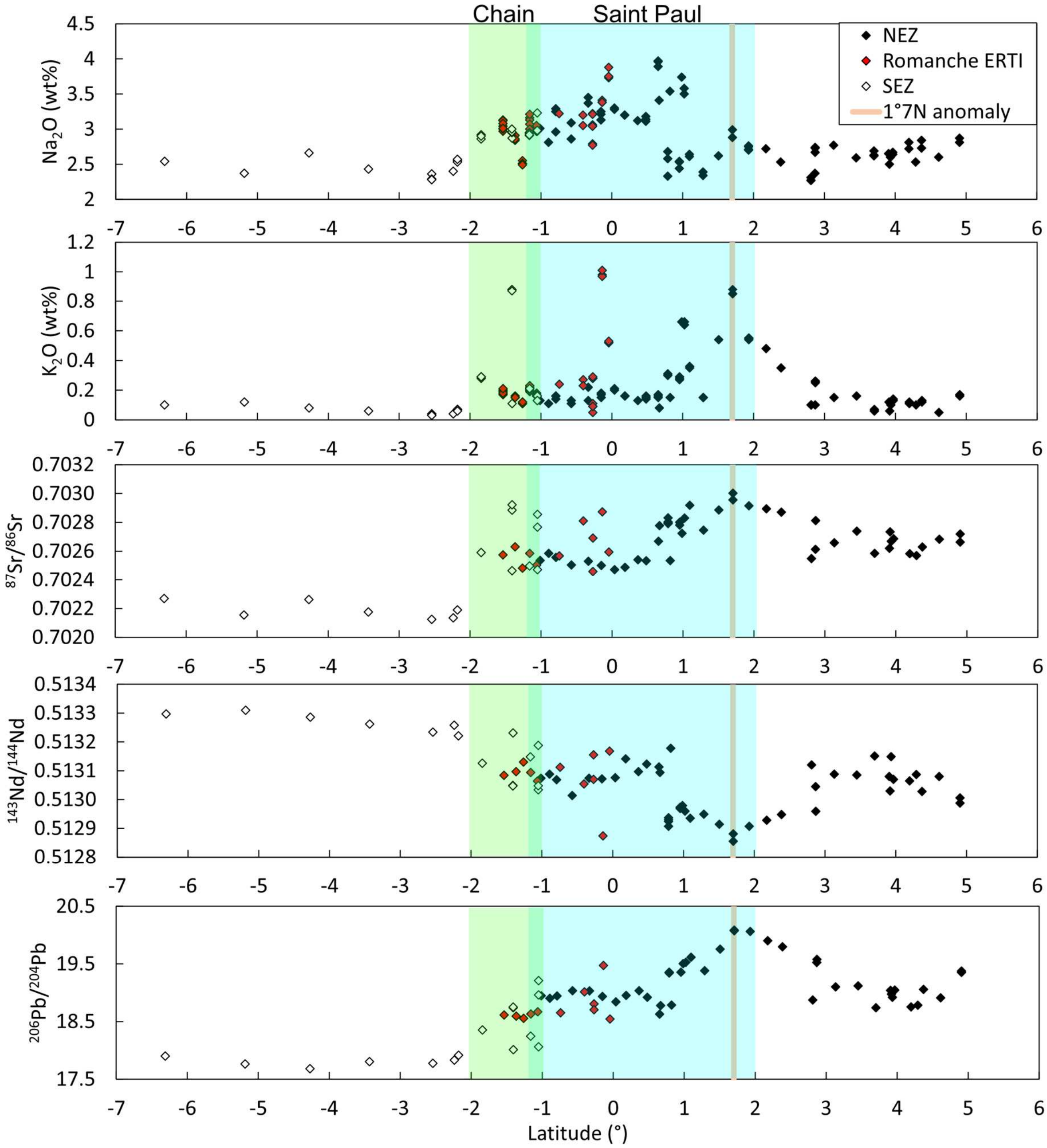

*Figure 2.2 - $K_2O$ and $Na_2O$ content of MORBs from the equatorial MAR (Schilling et al., 1995) and their Sr-Pb-Nd isotope ratios (data from Schilling et al., 1994). NEZ: North Equatorial Zone from 5°N to 0°, SEZ: South Equatorial Zone from 1°S to 7°S. ERTI: Eastern Ridge-Transform Intersection.*

## 2.2 The Romanche mega-transform fault and the Eastern Ridge-Transform Intersection

### Tectonics

The trace of Romanche Fracture Zone marks the equatorial Atlantic from near the continental in the Gulf of Guinea to a branch of the North Brazilian Ridge (Haxby, 1987). It has been supposed to be inherited from the opening of the Atlantic Ocean starting as a continent-continent transform (Haxby, 1987).

The Romanche transform fault is oriented East-West. It is composed by a deep valley (~ 5000 m deep, Searle et al., 1994) enclosed in a lensoidal, highly deformed region > 900 km long and > 100 km wide (Ligi et al., 2002). Important topographic anomalies characterize the region both as depressions and reliefs: the Vema Deep, in the eastern part of the RTF, reaches 7856 m b.s.l., while a shallow transverse ridge, capped by a fossil atoll is located directly North of the Vema Deep (Figure 2.3, Bonatti and Chermak., 1981, Bonatti et al., 1996, Heezen et al., 1964, Ligi et al., 2002).

Where the RTF intersects the eastern MAR, the ridge axis is not well defined, appearing to deviate toward the west. This tectonic setting has been first interpreted as the result of a ridge jump toward the East, the ancient ridge axis being still visible one hundred km to the West (Bonatti et al., 1994, Figure 2.3). However, the result of the recent bathymetric acquisition, made during the SMARTIES 2019 expedition (see section 2.4 for details), revealed that the westward deviation of the ridge termination is not linked to ridge jumps. The obliquity of the system appears to derive from the peculiar tectonics of the RTI where a large core complex accommodates the extension because of an extremely low magma supply. This tectonic feature is described in detail in chapter 6.

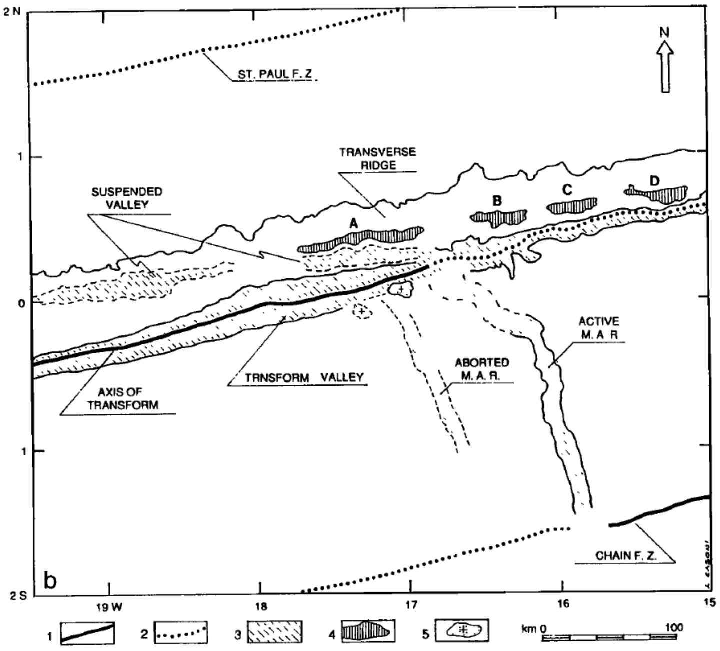

*Figure 2.3 - Schematic representation of the eastern boundary of the RTF from Bonatti et al. (1994). A, B, C and D represent the shallower regions. Sedimentary carbonated rocks and coral reef fossil samples have been found in the A, B and C peaks, evidence for the presence of a drowned atoll active ~ 10-13 Ma ago.*

This complex geometry has first been proposed to result from transform migration (Bonatti et al., 1994) (Figure 2.4), interpreting the northern boundary as a transform being first in activity. The activity should have stopped after 8-10 Ma and the deformation migrated toward the South, activating a new transform, and leaving a paleo transform to the North (Bonatti et al., 1994). Consequently, the sliver of lithosphere located between the two transforms was transferred from the South American plate to the African plate. The direction of the deformation in this area changed, making the determination of rocks age located between the two faults very difficult. Because of that, rocks of the area could be older than expected. This transform migration results in alternating transpressional and transtensional events, giving rise to the presence of very deep and very shallow areas close to each other (Figure 2.4).

This extreme model of transform migration has been reconsidered by Ligi et al. (2002). Indeed, the seismicity mostly located along the southern transform agrees with a present-day deformation there, but some earthquakes have also been observed along the northern transform. These authors proposed that the strike-slip deformation occur simultaneously along the two transform boundaries, the southern one predominating at the present day. The presence of the two transforms may be the result of the thermal setting generated by the enhanced cold-edge effect due to the mega-transform (see section 2.3 for details) (Fox and Gallo, 1984). Thus, a thick and cold lithosphere, resulting from high age contrast > 30 Ma, will gives rise to complex multi transform faults (Ligi et al., 2002) (Figure 2.4).

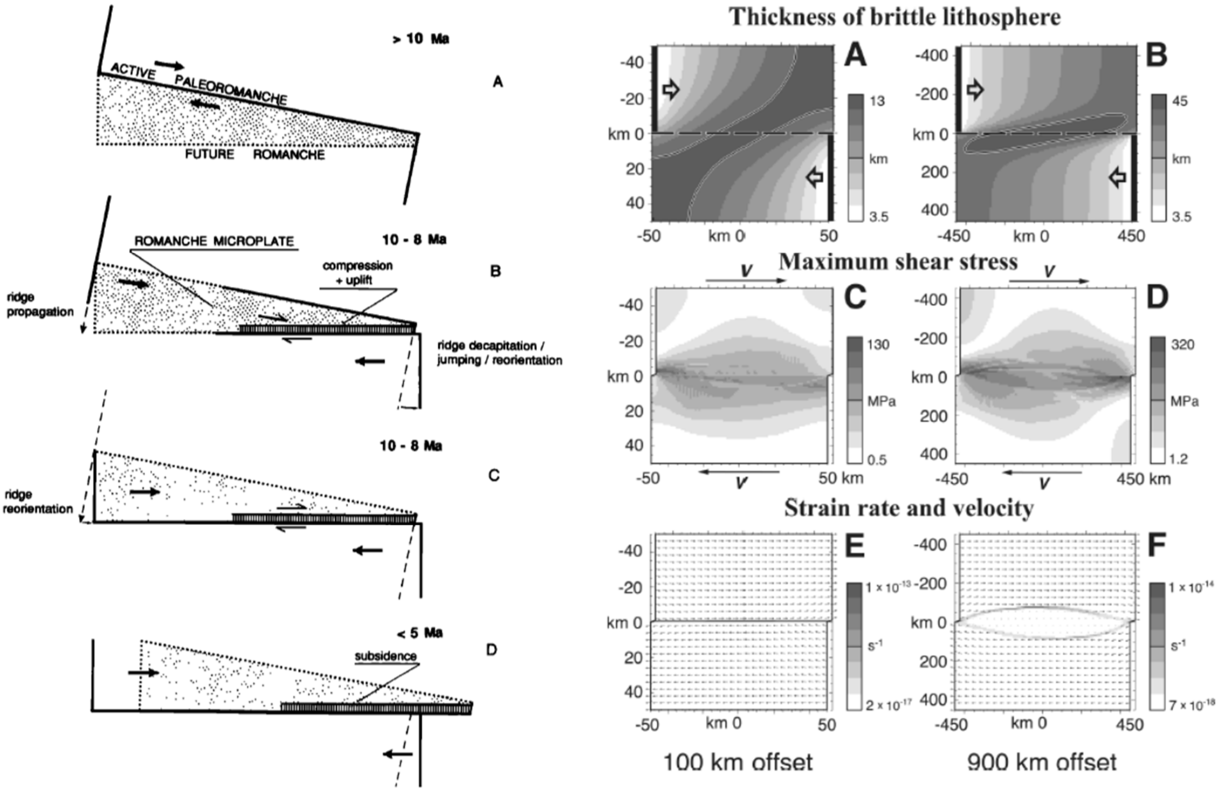

*Figure 2.4 - Two models for the RTF lens-shaped deformation. On the left transform migration after Bonatti et al. (1994). A. The northern RTF segment was active before 10 Ma. B and C. Migration and reorientation of the transform with the creation of a highly deformed region between the two transforms involving compression and uplift together with the ridge-jump toward the East. D. Present Day (< 5 Ma) geometry. On the right, two right lateral slow-slip deformations modelled at two different offset, 100 km and 900 km, after Ligi et al. (2002). A and B. Thickness of the lithosphere. Dashed line represents area with > 10 km for A and > 40 km for B lithosphere thickness. C and D. Maximum stress shear field for these deformations. E and F. The arrows represent the velocity, and the grey shaded the strain rate for the two deformation models.*

### Petrology and geochemistry

A complete oceanic lithosphere section has been described at the northern flank of the RTF, while on the Southern flank the magmatic crust is essentially absent in a ~ 20 km wide region where only few gabbroic rocks have been recovered (Bonatti et al., 2001). This region seems to be present for a great part of the transform life, suggesting a near steady-state setting of the thermal regime (Bonatti et al., 2001).

Study of mantle-derived rocks all along the RTF allows to recognize two compositional groups (Seyler and Bonatti, 1997). A first group (Gr1) is characterised by fertile spinel lherzolite and harzburgites (Bonatti et al., 1992, 1993, Seyler and Bonatti, 1997, Tartarotti et al., 2002). This group represents residues from various but very low degree of melting (4%-10%, Seyler and Bonatti, 1997) from a MORB-type mantle. A second group (Gr2) is characterised by the presence of plagioclase and high clinopyroxene content and have high Cr# and $TiO_2$ content. They have been interpreted as resulting from shallow depth (plagioclase-field) impregnation of mantle residua by a basaltic melt partially retained in the source (Seyler and Bonatti, 1997, Tartarotti et al., 2002). This interpretation is consistent with the cold thermal state proposed in the region, preventing the low amount of magma produced to aggregate and reach the surface, being instead partially retained at the base of the lithosphere (Seyler and Bonatti, 1997, Tartarotti et al., 2002). While Gr1 peridotites have been observed all along the RTF and on both, north and south, flanks, Gr2 peridotites are essentially described on the southern flank and closer to the Eastern Romanche Ridge Transform Intersection (ERRTI, Bonatti et al., 2001). There, it has been shown that the magmatic crust progressively disappears, from the centre of the ridge axis northward to the transform, to be replaced by mantle rocks (Bonatti et al., 2001). The presence of an amagmatic region has thus been supposed close to the transform. Small-scale heterogeneities have been described studying MORB compositions in this region. In addition to N-MORB compositions, a number of alkali-rich basalts have been reported having $Na_2O$ up to 3.9 wt% and $K_2O$ up to 1.01 wt% (Figure 2.2), and enriched LREE ($La/Sm_N > 2.5$) (Schilling et al., 1995, Melson et al., 1967, Sushchevskaya et al., 2002, Le Voyer et al., 2015). Moreover, these samples have a very high content in $H_2O$, reaching 1.18 wt% (Figure 2.5), and in volatile, up to 348 ppm in F and 246 ppm in Cl (Ligi et al., 2005, Le Voyer et al., 2015).

The isotopic signatures of the ERRTI MORB are generally intermediate between NEZ and SEZ signatures ($^{206}Pb/^{204}Pb$ from 18.54 to 19.01, $^{87}Sr/^{86}Sr$ from 0.702483 to 0.702811, $^{143}Nd/^{144}Nd$ from 0.513054 to 0.513168, Schilling et al., 1994), but few samples have values close to the 1°7N anomaly, reaching 19.5, 0.702874 and 0.512874 respectively for $^{206}Pb/^{204}Pb$, $^{87}Sr/^{86}Sr$ and $^{143}Nd/^{144}Nd$ (Schilling et al., 1995, Sushchevskaya et al., 2002) (Figure 2.2). Few hypotheses have been proposed to explain this signature, pointing to the presence of a heterogeneous mantle experiencing very low degree of partial melting (see section 2.3 for details) (Schilling et al., 1994, 1995, Sushchevskaya et al., 2002, Le Voyer et al., 2015). Schilling and co-workers, 1994, suggested heterogeneities resulting from a combined effect of a hotspot together with subcontinental mantle lithosphere delamination. The authors suggest a far-effect from the St Helena hotspot or Ascension hotspots, however, there is no morphotectonic evidence for their influence on this part of the MAR. The involvement of subcontinental lithosphere metasomatized during the opening of the Atlantic Ocean have been also proposed by Sushchevskaya et al. (2002). Another proposed hypothesis suggests the redistribution of a delaminated plume residue underplating the continental lithosphere by secondary convection processes (Schilling et al., 1994). These peculiar compositions have been found also in some older basalts located in the centre of the RTF (Sushchevskaya et al., 2002).

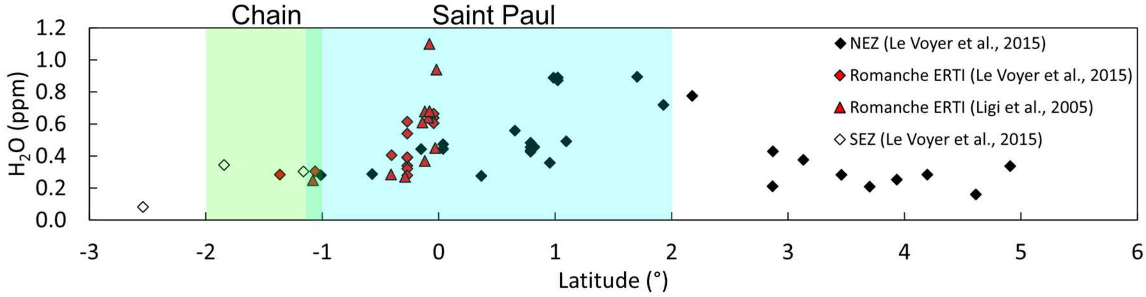

*Figure 2.5 - Profile of the $H_2O$ content in MORBs across the Equatorial MAR.*

## 2.3 The thermal state of the Eastern Ridge-Transform Intersection

The lack of magmatic crust together with the presence of impregnated peridotites suggests the presence of a thermal minimum at the ERRTI. At slow spreading rate, numerical modelling shows that significant changes, especially on the crustal thickness, can be observed for a small change in the mantle temperature (Su et al., 1994). Calculations of the degree of melting and geochemical study of MORB and peridotites mineral relics show a decrease of the degree of melting, reaching less than 5%, together with the decrease of the crustal thickness approaching the transform (Schilling et al., 1995, Bonatti et al., 2001, Ligi et al., 2005).

Large transform offsets may strongly affect the structure of the oceanic crust and its composition because of cooling the mantle beneath the ridge tips (Phipps Morgan and Forsyth, 1988). This cooling effect has been modelled for the ERRTI by Ligi et al., 2002, 2005. They show that approaching the transform fault along the ridge axis, the lithosphere thickness increases, and the melting region becomes smaller and asymmetric until melting is no longer observed in a region 30-40 km large from the transform. These authors suggest that the generation of melt closer to the transform fault is only possible by addition of water in the mantle. Indeed, addition of water deepens the onset of melting by about 20 km, reaching the garnet stability field and lowers the onset melting temperature. This agrees with the high $H_2O$ content of MORBs sampled close to the transform and the higher garnet signature, i.e., higher $Sm/Yb_N$ (Ligi et al., 2005).

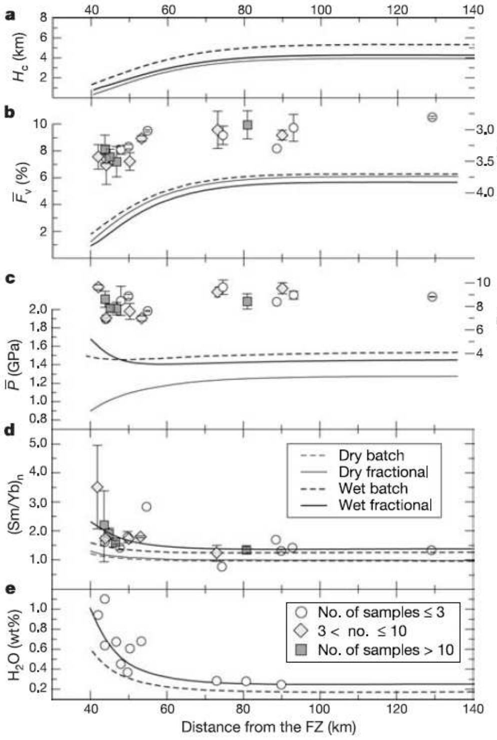

*Figure 2.6 - Comparison of the MORB geochemistry (symbols) $Na_8$, $Fe_8$, $Sm/Yb_N$ (chondrite normalised $Sm/Yb_N$ and $H_2O$ with the calculated parameters (lines): a. Hc crustal thickness, b. Average degree of melting, c. Average pressure of melting, d. Predicted $Sm/Yb_N$, e. Predicted $H_2O$ content. Figure from Ligi et al. (2005).*

Recent unpublished results of the micro seismicity beneath the ERRTI collected during the SMARTIES cruise, show evidence for a thick and cold lithosphere, around 25 km thick at the ridge axis. This thickening is not only visible in the first km away from the fracture zone, as supposed by previous models, but is visible for more than 60 km along the ridge axis (Yu Z., personal communication). This imply a colder lithosphere, i.e., higher cooling effect, than previously expected.

The observed decrease of the crustal thickness, thick and cold lithosphere, and impregnated peridotites and MORB compositions together with the calculated decreasing of the degree of melting, are all indicators that a cold thermal regime affects the ERRTI. Indeed, the real interrelation between lower mantle potential temperature and enhanced top-down lithospheric cooling is not yet defined.

## 2.4 Sampling

A high quantity of samples has been recovered during several expeditions made along the RTF (Figure 2.7). Only few basaltic glasses from the AII20 and PRIMAR 92/93/96 expeditions have been studied. A new sampling occurred during the SMARTIES 2019 expedition on which the present PhD project is based along with the integration of some previous recoveries.

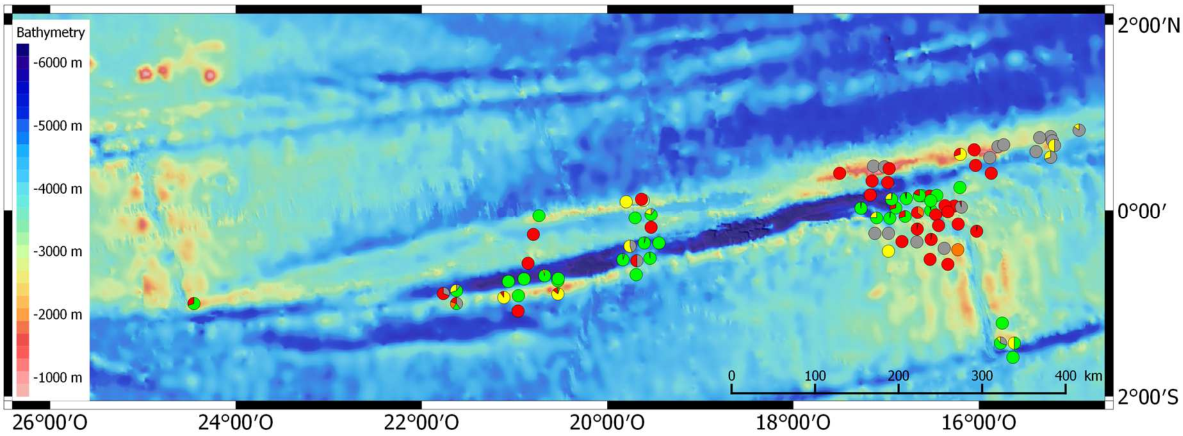

*Figure 2.7 - Location of the dredge sites and their lithological composition along the Romanche transform fault recovered during the previous expeditions: AII20, PRIMAR 92, PRIMAR 93 and PRIMAR 96. Green: peridotite; yellow: gabbro; red: basalt; grey: others.*

The AII20 expedition took place in 1966 on the R/V Atlantis II. Samples from this expedition have been kindly made available to D. Brunelli by H. Dick, Woods Hole Oceanographic Institution, MA-USA. Samples from two dredges are studied here, AII20-11 and AII20-21, located at the centre of the RTF on the northern wall.

The PRIMAR project, a joint program between Russian Academy of Sciences and the Italian CNR (National Research Council) for the geological study of the equatorial Atlantic, has supported several expeditions:

- PRIMAR 92, November 1991-January 1992, R/VAkademik Nikolaj Strakhov
- PRIMAR 93, April-May 1993, R/V Strakhov
- PRIMAR 96, 1996, R/V Gelendzhik

These expeditions allowed multibeam bathymetry, gravimetric and magnetometric surveys, multichannel high-resolution seismic reflection, and dredged rock sampling (Gasperini et al., 1997, Bonatti et al., 1991, 1994). The samples studied here are from the ERRTI at both East and West of the topographic ridge axis.

The SMARTIES (*Smooth regions at the Mid-Atlantic Ridge Transform-Intersections under extreme thermal gradients*) oceanographic expedition took place in summer 2019 (July and August) at the ERRTI. I took part to this expedition together with 23 scientists (researchers, doctoral students, and trainees) from the laboratories of the Université de Bretagne Occidentale of Brest (France), the Universities of Modena (Italy), of Toulouse (France), the Institut de Physique du Globe de Paris (Paris, France), the Universities of Bergen (Norway) and of Querétaro (Mexico).

Bathymetry, gravimetry and magnetic data were acquired during this expedition along with the deployment of 19 Ocean bottom seismometers (OBS). The study of seismicity on the bottom, combined with geophysical data will help to better constrain the location of the ridge axis, the deformation system in the region of the intersection, and the base of the lithosphere. These data will allow a better understanding of the tectonics and magmatism of the area.

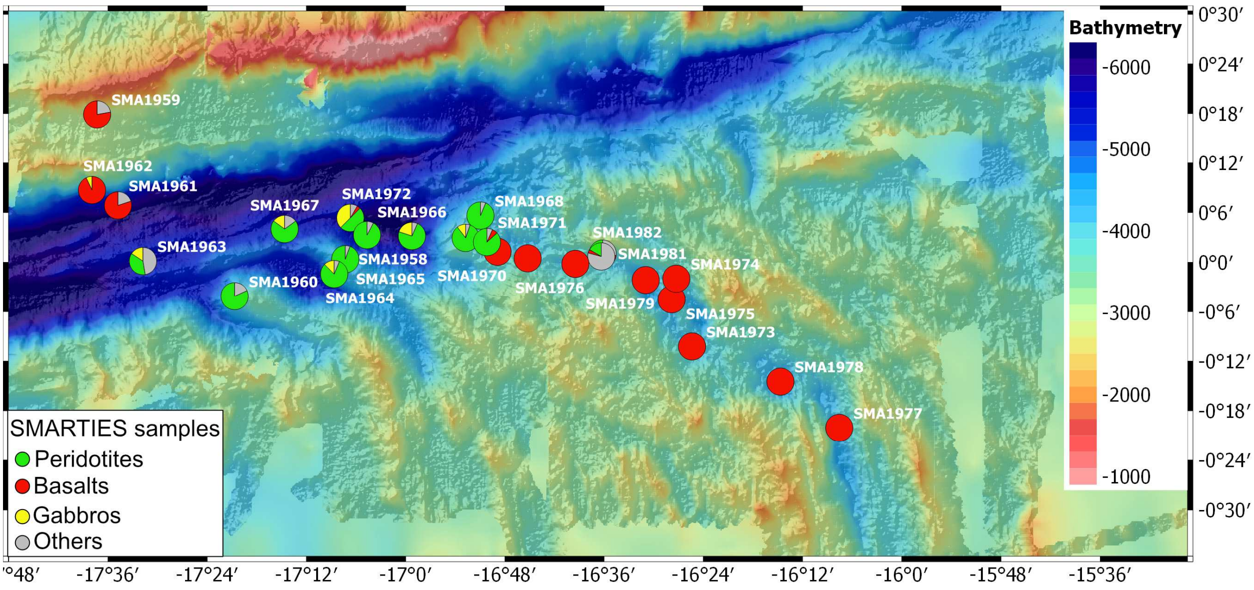

*Figure 2.8 - Bathymetric data from the SMARTIES oceanographic expedition and location of the Nautile dives. Others: sediments, breccia, shells.*

The Nautile submersible was used to carry out 25 dives down to 6000 metres (Figure 2.8). These dives allowed direct observation of the bottom and the acquisition of numerous pictures and videos. More than 400 samples have been collected.

The various dives reveal a highly deformed region culminating in a neo-volcanic zone. At the centre of the ridge axis, highly magmatic domains with big pillow lavas are present (Figure 2.9). Depending on the degree of the slope and viscosity, basalts take various shape: rounded pillows lava, elongated, basaltic crust, small volcanic edifice (Figures 2.9 and 2.10). Contrary to what has been previously described in the literature, magmatism is present near the transform fault, although localised and in very small volumes. There, magmatism is accompanied by many tectonic structures: faults (Figure 2.9) and large zones made of exhumed and deformed mantle rocks (Figure 2.9) resulting in a succession of oceanic core complexes.

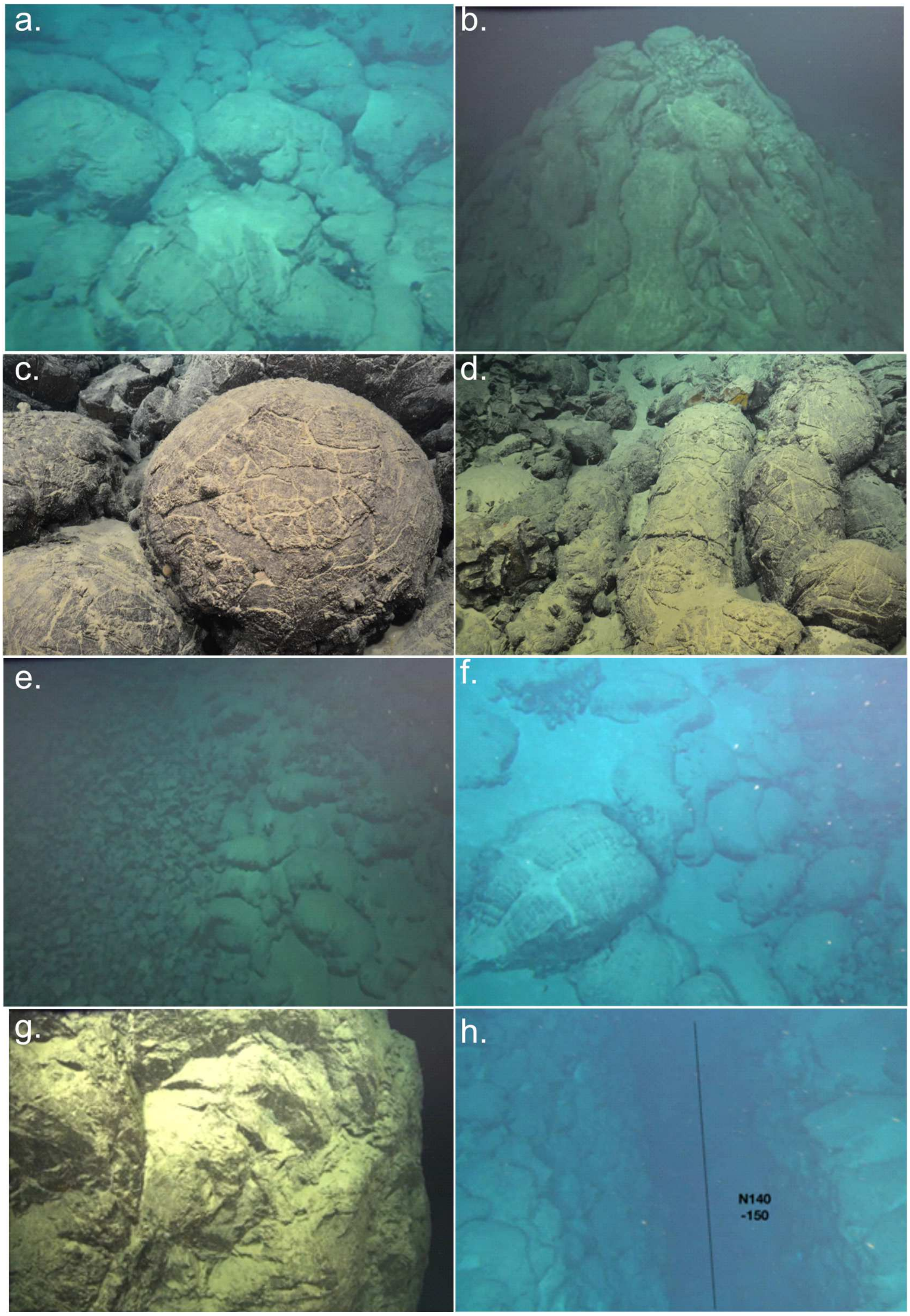

*Figure 2.9 - Various outcrops observed at the ERRTI. (a) Magmatic ridge at the centre of the ridge axis with fresh pillows lavas covered by a thin layer of sediments (SMA1977). (b) Small volcanic edifice with tubular pillows (SMA1979). (c) and (d) Various shape of fresh lavas observed during the dive SMA1975: (c) rounded pillow, (d) tubular pillows. (e) Debris flow in contact with pillows (SMA1979). (f) Localised magmatic domains close to the transform fault (SMA1970). (g) Massive outcrop of exhumed mantle rocks (SMA1969). (h) Fault with broken pillows (SMA1976).*

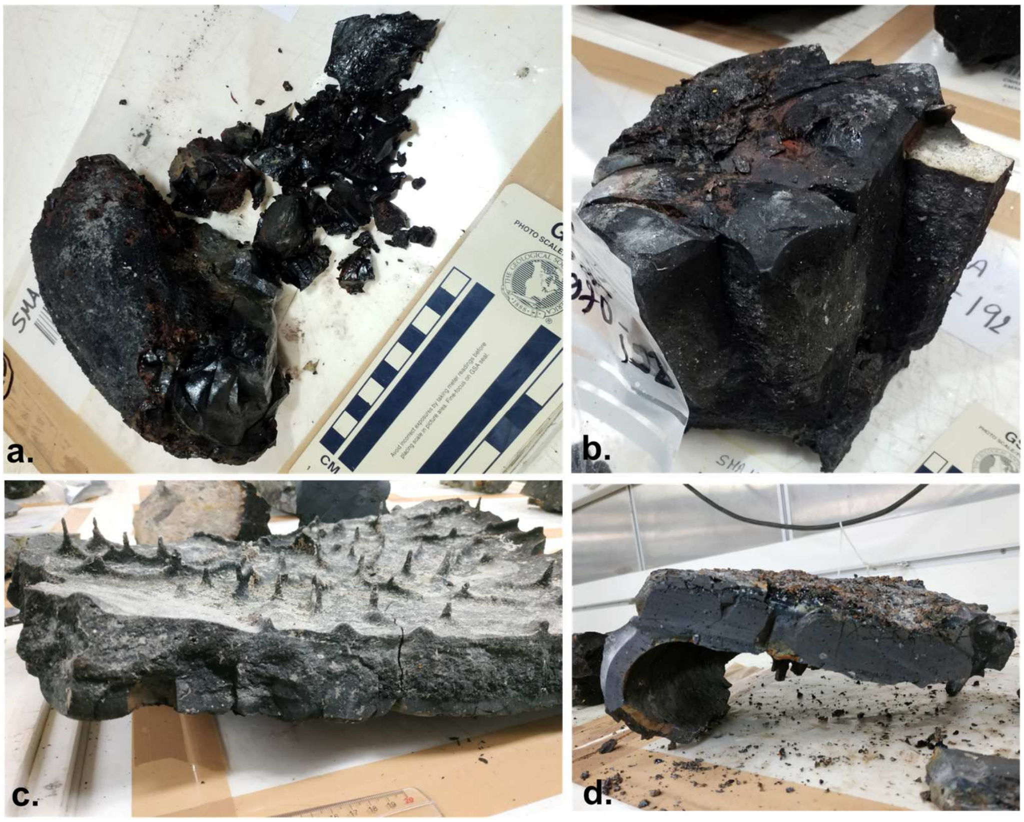

*Figure 2.10 - Various basaltic samples recovered during SMARTIES 2019 expedition (a) Tubular pillow entirely made of glass (SMA1975-304). (b) Pillow sector (SMA1970-192). (c) Crust of basaltic lava tube with drips (SMA1970-195). (d). Crust of lava tube (SMA1977-342).*

A total of 433 samples were collected, mostly basalts and peridotites (Figure 2.11). Of the basaltic samples, 137 have a glass rim (Figure 2.10). Their composition in major and trace elements and isotope ratios of strontium, neodymium, lead and hafnium have been analysed in this work.

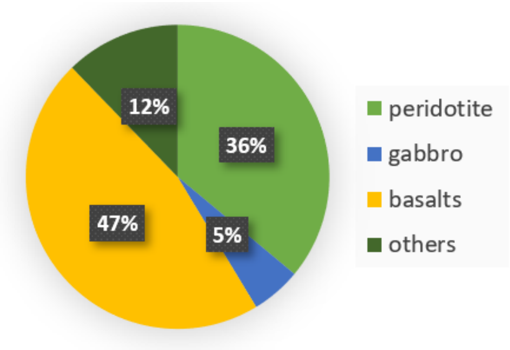

*Figure 2.11 - Percentage of lithologies sampled during the SMARTIES 2019 expedition. Others: sediments, breccia, shells, etc.*

## References

Barão, L.M., Trzaskos, B., Angulo, R.J., Souza, M.C. de, 2020. *Deformation and structural evolution of mantle peridotites during exhumation on transform faults: A forced transition from ductile to brittle regime.* Journal of Structural Geology 133, 103981. doi:10.1016/j.jsg.2020.103981.

Bonatti, E., Brunelli, D., Fabretti, P., Ligi, M., Asunta, P.R., Seyler, M., 2001. *Steady-state creation of crust-free lithosphere at cold spots in mid-ocean ridges.* Geology 29 (11), 979. doi:10.1130/0091-7613(2001)029<0979:SSCOCF>2.0.CO;2.

Bonatti, E., Chermak, A., 1981. *Formerly emerging crustal blocks in the equatorial atlantic.* Tectonophysics 72, 165–180.

Bonatti, E., Ligi, M., Carrara, G., Gasperini, L., Turko, N., Perfiliev, S., Peyve, A., Sciuto, P.F., 1996. *Diffuse impact of the Mid-Atlantic Ridge with the Romanche transform: an ultracold ridge-transform intersection.* J. Geophys. Res. 101 (B4), 8043–8054. doi:10.1029/95JB02249.

Bonatti, E., Ligi, M., Gasperini, L., Peyve, A., Raznitsin, Y., Chen, Y.J., 1994. *Transform migration and vertical tectonics at the Romanche fracture zone, equatorial Atlantic.* Journal of Geophysical Research 99 (B11), 21779–21802. doi:10.1029/94JB01178.

Bonatti, E., Peyve, A., Kepezhinskas, P., Kurentsova, N., Seyler, M., Skolotnev, S., Udintsev, G., 1992. *Upper mantle heterogeneity below the Mid-Atlantic Ridge, 0°-15°N.* Journal of Geophysical Research 97 (B4), 4461–4476.

Bonatti, E., Raznitzin, Y., Bortoluzzi, G., Budillon, F., Alteriis, G. de, Gasperini, L., Gasperini, M., Giacquinto, G., Ligi, M., Lodolo, E., Mazarovich, A., Peyve, A., Sacchi, M., Skolotnev, S., Trofimov, V., Turko, N., Zacharov, M., Auzende, J.-M., Mamaloukas-Frangoulis, V., Searle, R.C., 1991. *Geological studies of the eastern part of the Romanche transform (equatorial Atlantic): a first report.* Giornale di Geologia 53/2, 31–48.

Bonatti, E., Seyler, M., Sushchevskaya, N.M., 1993. *A cold suboceanic mantle belt at the Earth's equator.* Science 261 (5119), 315–320. doi:10.1126/science.261.5119.315.

Brunelli, D., Seyler, M., 2010. *Asthenospheric percolation of alkaline melts beneath the St. Paul region (Central Atlantic Ocean).* Earth and Planetary Science Letters 289 (3-4), 393–405. doi:10.1016/j.epsl.2009.11.028.

Campos, T.F., Sichel, S.E., Maia, M., Brunelli, D., Motoki, K.F., Magini, C., Barão, L.M., Vargas, T., Szatmari, P., Fonseca, E., Melo, G. de, 2021. *The singular St. Peter and St. Paul Archipelago, equatorial Atlantic, Brazil*, in: Santos, A.C.d., Hackspacher, P.C. (Eds.), Meso-Cenozoic Brazilian Offshore Magmatism. Academic Press, pp. 121–165.

Fox, P.J., Gallo, D.G., 1984. *A tectonic model for ridge-transform-ridge plate boundaries: Implications for the structure of oceanic lithosphere.* Tectonophysics 104 (3-4), 205–242. doi:10.1016/0040-1951(84)90124-0.

Gasperini, L., Bonatti, E., Brunelli, D., Carrara, G., Cipriani, A., Fabretti, P., Gilod, D., Ligi, M., Peyve, A., Skolotnev, S., Susini, S., Tartarotti, P., Turko, N., 1997. *New data on the geology of the Romanche FZ, equatorial Atlantic: PRIMAR-96 cruise report.* Giornale di Geologia 59/1-2, 3–18.

Haxby W. F., 1987. *Gravity field of the world's oceans (map).*

Heezen, B.C., Bunce, E.T., Hersey, J.B., Tharp, M., 1964. *Chain and romanche fracture zones.* Deep Sea Research and Oceanographic Abstracts 11 (1), 11–33. doi:10.1016/0011-7471(64)91079-4.

Hekinian, R., Juteau, T., Gracia, E., Sichel, S., Udintsev, G., Apprioual, R., Ligi, M., 2000. *Submersible observations of Equatorial Atlantic mantle: The St. Paul Fracture Zone region.* Marine Geophysical Research, 2000, 529–560.

Kelley, K.A., Kingsley, R.H., Schilling, J.G., 2013. *Composition of plume-influenced mid-ocean ridge lavas and glasses from the Mid-Atlantic Ridge, East Pacific Rise, Galápagos Spreading Center, and Gulf of Aden.* Geochemistry Geophysics Geosystems 14 (1). doi:10.1029/2012GC004415.

Le Voyer, M., Cottrell, E., Kelley, K.A., Brounce, M., Hauri, E.H., 2015. *The effect of primary versus secondary processes on the volatile content of MORB glasses: An example from the equatorial Mid-Atlantic Ridge (5°N-3°S).* J. Geophys. Res. Solid Earth 120 (1), 125–144. doi:10.1002/2014JB011160.

Ligi, M., Bonatti, E., Cipriani, A., Ottolini, L., 2005. *Water-rich basalts at mid-ocean-ridge cold spots.* Nature 434 (7029), 66–69. doi:10.1038/nature03264.

Ligi, M., Bonatti, E., Gasperini, L., Poliakov, A.N., 2002. *Oceanic broad multifault transform plate boundaries.* Geol 30 (1), 11. doi:10.1130/0091-7613(2002)030<0011:OBMTPB>2.0.CO;2.

Maia, M., Sichel, S., Briais, A., Brunelli, D., Ligi, M., Ferreira, N., Campos, T., Mougel, B., Brehme, I., Hémond, C., Motoki, A., Moura, D., Scalabrin, C., Pessanha, I., Alves, E., Ayres, A., Oliveira, P. 2016. *Extreme mantle uplift and exhumation along a transpressive transform fault.* Nature Geosci, 619–623. doi:10.1038/ngeo2759.

Melson, W.G., Jarosewich, E., Cifelli, R., Thompson, G., 1967. *Alkali Olivine Basalt dredged near St. Paul's Rocks, Mid-Atlantic Ridge.* Nature 215 (5099), 381–382. doi:10.1038/215381a0.

Motoki, K.F., Motoki, A., Sichel, S.E.2014. *Gravimetric structure for the abyssal mantle massif of Saint Peter and Saint Paul peridotite ridge, Equatorial Atlantic Ocean, and its relation to active uplift.* An. Acad. Bras. Ciênc., 571–588. doi:10.1590/0001-37652014117712.

Phipps Morgan, J., Forsyth, D.W., 1988. *Three-dimensional flow and temperature perturbations due to a transform offset: Effects on oceanic crustal and upper mantle structure.* Journal of Geophysical Research, 1988, 2955–2966.

Schilling, J.G., Hanan, B.B., McCully, B., Kingsley, R.H., Fontignie D., 1994. *Influence of the Sierra Leone mantle plume on the equatorial Mid-Atlantic Ridge: A Nd-Sr-Pb isotopic study.* Journal of Geophysical Research 99 (B6), 12005–12028.

Schilling, J.-G., Ruppel, C., Davis, A.N., McCully, B., Tighe, R.H., Lin, J., 1995. *Thermal structure of the mantle beneath the equatorial Mid-Atlantic Ridge: Inferences from the spatial variation of dredged basalt glass compositions.* Journal of Geophysical Research 100 (B7), 10057–10076.

Searle, R.C., Thomas, M.V., Jones, J.W., 1994. *Morphology and tectonics of the Romanche Transform and its environs.* Marine Geophysical Research 16, 427–453.

Seyler, M., Bonatti, E., 1997. *Regional-scale melt-rock interaction in lherzolitic mantle in the Romanche Fracture Zone (Atlantic Ocean).* Earth and Planetary Science Letters 146, 273–287.

Su, W., Mutter, C.Z., Mutter, J.C., Buck, W.R., 1994. *Some theoretical predictions on the relationships among spreading rate, mantle temperature, and crustal thickness.* J. Geophys. Res. 99 (B2), 3215–3227. doi:10.1029/93JB02965.

Sushchevskaya, N.M., Bonatti, E., Peive, A.A., Kamenetskii, V.S., Belyatskii, B.V., Tsekhonya, T.I., Kononkova, N.N., 2002. *Heterogeneity of Rift Magmatism in the Equatorial Province of the Mid-Atlantic Ridge (15° N to 3° S).* Geochimistry International 40 (1), 26–50.

Tartarotti, P., Susini, S., Nimis, P., Ottolini, L., 2002. *Melt migration in the upper mantle along the Romanche Fracture Zone (Equatorial Atlantic).* Lithos 63 (3-4), 125–149. doi:10.1016/S0024-4937(02)00116-0.

# CHAPTER 3 Methodology

## 3.1 Major and trace elements

We have studied basaltic glasses to avoid possible compositional changes due to crystal accumulation. Thus, glasses do not represent the bulk lava compositions but the last melts after fractional crystallization. Compared to bulk rocks, glasses are also preserved from any observable alteration.

### 3.1.1 Samples preparation

Glass samples were crushed with an agate mortar and reduced to smaller chips. At least two chips of glass from each sample were handpicked under a binocular microscope and washed with deionised water in an ultrasonic bath. Clean glass chips were embedded in resin (in a 5:1 resin:hardener ratio) to make rounded mounts of one inch in diameter. Each mount was then polished using alumina powder of three different granulometric sizes: the first, coarser-grained, is used to remove the excess of resin and to expose the glass at the top of the mount; the second step with a smaller size of grains is transitional before final polishing with a very fine powder to perfectly polish the surface (Figure 3.1). These mounts are necessary to analyse the samples using the Electron Probe Micro Analysis (EPMA) and Laser Ablation Inductively Coupled Mass Spectrometry (LA-ICP-MS) respectively for major element and trace element analyses.

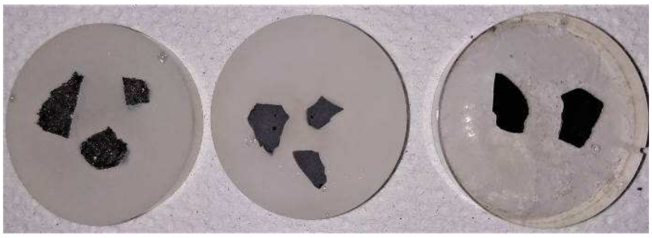

*Figure 3.1 - Mounts showing the three different polishing steps.*

### 3.1.2 Major element analysis with an EPMA

The major element composition of all the SMARTIES samples were analysed by Electron Probe Micro Analysis (EPMA) using the “Microsonde Ouest”, with a microprobe Cameca SX 100 (a regional facility operated by the Université de Bretagne Occidentale through the Institut Universitaire Européen de la Mer, IFREMER, INSA Rennes, Université de Rennes1 and Université de Nantes). This method allows in situ analysis of the major elements.

The instrument consists of a column, surrounded by five spectrometers, at the top of which a W filament is heated in a vacuum and emits electrons, which are accelerated. These electrons form a light beam, which, under the effect of a magnetic field, is concentrated towards the sample. The beam strikes the surface of the sample at an impact point chosen by the operator. This will disrupt the electron pattern of the atoms in the sample. The atoms are then excited by electron loss. Then, the atoms emit X-rays with a specific wavelength for each element. The spectrometers make it possible to characterise the X-rays produced, and thus determine the nature and proportion of the chemical elements contained in the sample.

Prior to start the analysis, each sample is carbon coated to allow electrical conductivity. The sample is then loaded into the chamber that is pumped out to obtain a high vacuum. On each sample, four spots of 5 µm diameter have been analysed (Figure 3.2). These analyses are then averaged to obtain the sample composition. Standard deviation for each sample is given in chapter 4 (supplementary).

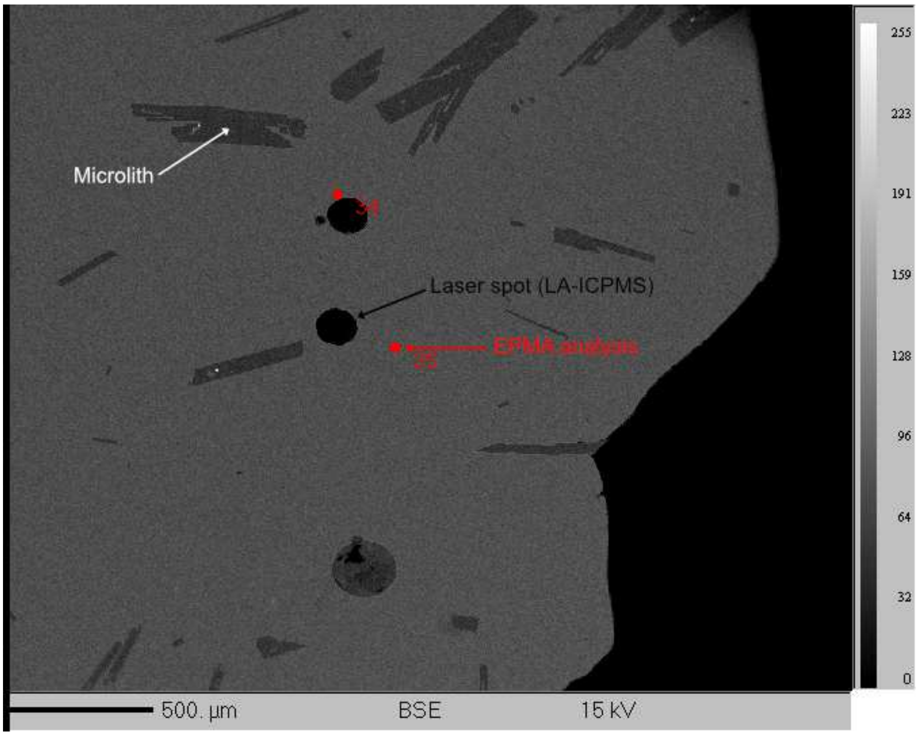

*Figure 3.2 - Back-scattered electron imaging of a plagioclase-bearing basaltic glass during the EPMA analyses. Red dots are the location of the analysed spots.*

### 3.1.3 Trace element analysis with a LA-ICP-MS

The trace element abundances of the samples have been determined by Laser Ablation Inductively Coupled Mass Spectrometry (LA-ICP-MS). A first batch of samples has been analysed at Centro Interdipartimentale Grandi Strumenti (CIGS, Modena) using an ICPMS X Series II coupled with a laser ablation X 213. A second batch of the samples was analysed at Pôle Spectrométrie Océan (PSO, Plouzané) using a High Resolution Inductively Coupled Plasma Mass-spectrometer (HR-ICP-MS Element XR) coupled with a laser ablation system 193 nm Compex Pro 102 Coherent. Two samples (SMA1976-317 and SMA1979-367) have been analysed using both instrument in order to check the reproducibility of the analysis and equivalent results have been obtained. Data and duplicates are given in chapter 4 (supplementary material, Table S4.2).

For the analysis, the sample is placed in a sealed cell where the laser ablates the sample, producing ions that are transported to the ICP-MS by a permanent flow of Helium. The coupling of a microscope and a camera to this device allows precise adjustment of the ablation zone and live monitoring of the quality of the ablation.

All measurements were performed in low resolution. To avoid variations in plasma conditions during the measurement, an internal standard with a known and constant concentration in the sample is used (in this case Ca determined by EPMA).

The standard reference materials NIST612 and NIST614 have been analysed to calculate the concentration of each element in the samples. The natural reference sample BHVO2 has been also regularly measured.

The analysis sequence was carried out as follows: NIST614 - NIST612 - NIST614 - 3 x sample #1 – 3 x sample #2. Dwell times on each isotope during one run was 30 ms per amu. One run consists of 50 replicates per analysis.

After the analysis, the measured intensities of each element for both standards and samples are corrected from the background noise, i.e., the average blank signal measured before each analysis. This signal is then normalised to the measured intensity of the Ca internal standard for each sample. The corrected signal of the 50 replicates is averaged for each element, and the standard deviation and 2$\sigma$ sigma error are then calculated.

The references values used of the NIST612, NIST614 and BHVO2 are preferred values from GeoRem database (Jochum et al., 2005). These standard concentrations are also normalised to the Ca concentration (ppm). The Ca normalised measured intensity plotted vs. the Ca normalised composition of the standard forms a calibration curve (Figure 3.3). By projection on this calibration curve, the concentration of the element is calculated as followed:

$$C_i = \frac{I^i_{mes} \times Ca_{EPMA}}{y^i} \qquad [3.1]$$

in which

$C_i$ is the final calculated concentration of element $i$,
$I^i_{mes}$ is the measured, Ca normalised, intensity of the element $i$,
$Ca_{EPMA}$ is the concentration in ppm of Ca previously measured in the sample by EPMA,
$y^i$ is the slope of the calibration curve of the element $i$.

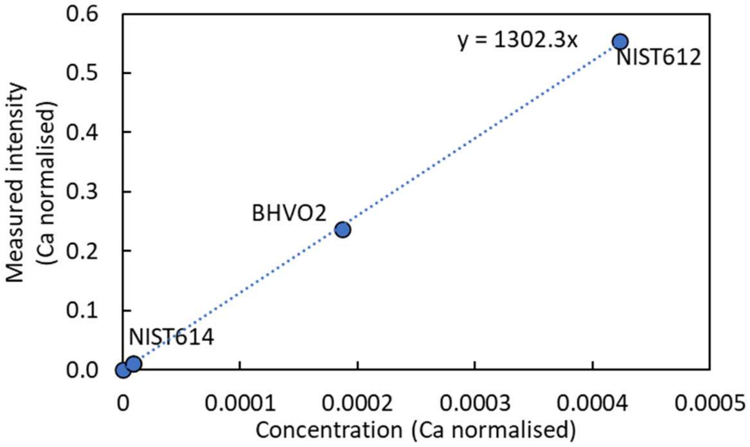

*Figure 3.3 - Example of the standards' calibration curve for La. The dashed line is the regression line.*

These calculations are made for each of the 3 analyses on each sample. Average value and standard deviation are then calculated.

To check the data corrections, Mg, Ti, Mn and Fe have been measured by the LA-ICP-MS and compared to the one measured with the EPMA.

## 3.2 Chemical protocols and analysis of Pb, Sr, Hf and Nd isotopes

### 3.2.1 Samples preparation

*Leaching*

After picking, around 100-200 mg of clean glasses for each sample were leached. This step allows to clean the samples from possible seawater contamination. First, 7.5N $HNO_3$ was added to each beaker. Then, after removing the acid, the samples were rinsed 4 times with MilliQ water. The beakers were put in an ultrasonic bath for 20 min during the acid step and first rinse step.

*Dissolution*

The samples were dissolved in an acid mixture of clean concentrated $HNO_3$ + HF. Both acids were double distilled to reduce the contamination. The samples were left on a hotplate at 90°C for a few days and regularly placed in an ultrasonic bath for about 30 min. After complete dissolution, the solution is evaporated.

### 3.2.2 Chromatographic separation protocols

After dissolution two distinct chemical separation have been performed (detailed protocols are given in figures 3.4 and 3.5). The first was done at the Laboratory Géo-Océan (GO, Plouzané, France, Figure 3.4) on a first set of samples from older expeditions to complete the existing database. Concentrated HF was added to the dried fraction of each dissolved sample and left on a hotplate at 90°C for a few days. This solution was sonicated and centrifuged and the supernatants were evaporated for Hf separation. The formed fluoride residue was dissolved with 6N HCl Clean Acid and well sonicated to break the fluoride salts for Pb, Sr and Nd separation (Blichert-Toft et al., 1997).

The 6N HCl solutions were evaporated and concentrated HBr was added on each beaker. After evaporation, 0.5N HBr was added, and samples were centrifuged. They were then loaded on micro-columns containing some anionic resin AG1-X8 (200-400 mesh). First, REE and Sr were eluted with 0.5N HBr and then Pb was collected using 6N HCl. The Pb fractions were evaporated and redissolved with 0.5N HBr and the samples were loaded on the same columns with 0.5N HBr. Pb was eluted with 6N HCl and these final fractions were evaporated. This 2nd passage on the columns allowed to purify the Pb (protocol after Manhes et al., 1978 modified by Janin, 2010).

After evaporation, the REE and Sr fraction were redissolved twice using concentrated $HNO_3$. There were then centrifuged and were loaded with 2.5N HCl on columns containing 5mL of anionic resin AG50W X8 (200-400 mesh) (White and Patchett, 1984). Rb, Ca and K were removed with 2.5N HCl and Sr were collected using a bigger volume of the same acid. On the same columns, Ba was removed and REE were collected with 4N $HNO_3$. Both Sr and REE fractions were evaporated.

The solution containing REE was evaporated and re-dissolved first with 4N HCl and then 0.2N HCl. The samples were loaded on columns containing LN-spec resin (LaNthanides Specification) (Richard et al., 1976). Ce and La were eluted using 0.2N HCl and Nd was collected with 0.25N HCl.

Fractions with Hf were dissolved with 0.5N HCl + 0.5N HF and left on a hotplate for few hours. After evaporation, they were redissolved using the same mix. These solutions were loaded on a 1st set of columns containing an anionic resin AG1-X8 (100-200 mesh). This step allowed to remove all the elements except Hf, Ti and Zr which were collected with 6N HCl. $HClO_4$ was added and the solutions were evaporated at 180°C to remove 0.5N HF from the samples. This step was repeated 3 times. A mix of 2.5N HCl + $H_2O_{2(trace)}$ was added and the samples were centrifuged. This step allowed to oxidize the Ti, which becomes $Ti(H_2O_2)_X$. That enabled to separate the Ti and the Hf. The supernatants were loaded on a 2nd set of columns containing a cationic resin AG50W-X8 (200-400 mesh). Ti was thus removed. Hf was then recovered using 2.5N HCl + 0.3N HF and these solutions were evaporated (protocol after Blichert-Toft et al., 1997)

Another protocol has been used, for the entire set of SMARTIES samples, with the idea to develop the combined Pb-Sr chemistry (Deniel and Pin, 2001) at Dipartimento di Scienze Chimiche e Geologiche (DSCG, Modena). Following the Pb-Sr chemistry, the Hf and Nd chromatographic separation were done at GO (Plouzané).

After the sample dissolution step, 8N $HNO_3$ was added to each beaker and evaporated to remove any trace of HF. The protocol starts with a combined Pb-Sr separation (after Denial and Pin, 2001), followed by a chemistry to separate Hf from REE (Chauvel et al., 2011). Clean up of Hf and Nd was then performed in the same way than for the first batch of samples from older cruises (Blichert-Toft et al., 1997, Richard et al., 1976).

Samples in solution in 2N $HNO_3$ were loaded on 150 µL Sr-spec resin. All the elements, except Ba, Sr and Pb, were eluted with 2N $HNO_3$. Ba was then eluted with 7N $HNO_3$ and 2N $HNO_3$. To finish, the Sr was collected with MilliQ followed by Pb elution with 6N HCl.

2N HCl + HF was added to the dry fraction with Hf and REE. This solution was loaded on 2 mL AG50W-X8 (200-400mesh) resin. The Hf, Zr and Ti were collected directly and dried. Then 3.5N HCl are added to collect Sr that in this case was already separated. The REEs were then eluted with 6N HCl.

The Hf and Nd purification have then been done in the same way as previously described (Blichert-Toft et al., 1997, Richard et al., 1976).

To finish the solutions have been evaporated.

The chemical blanks are given in table 3.1.

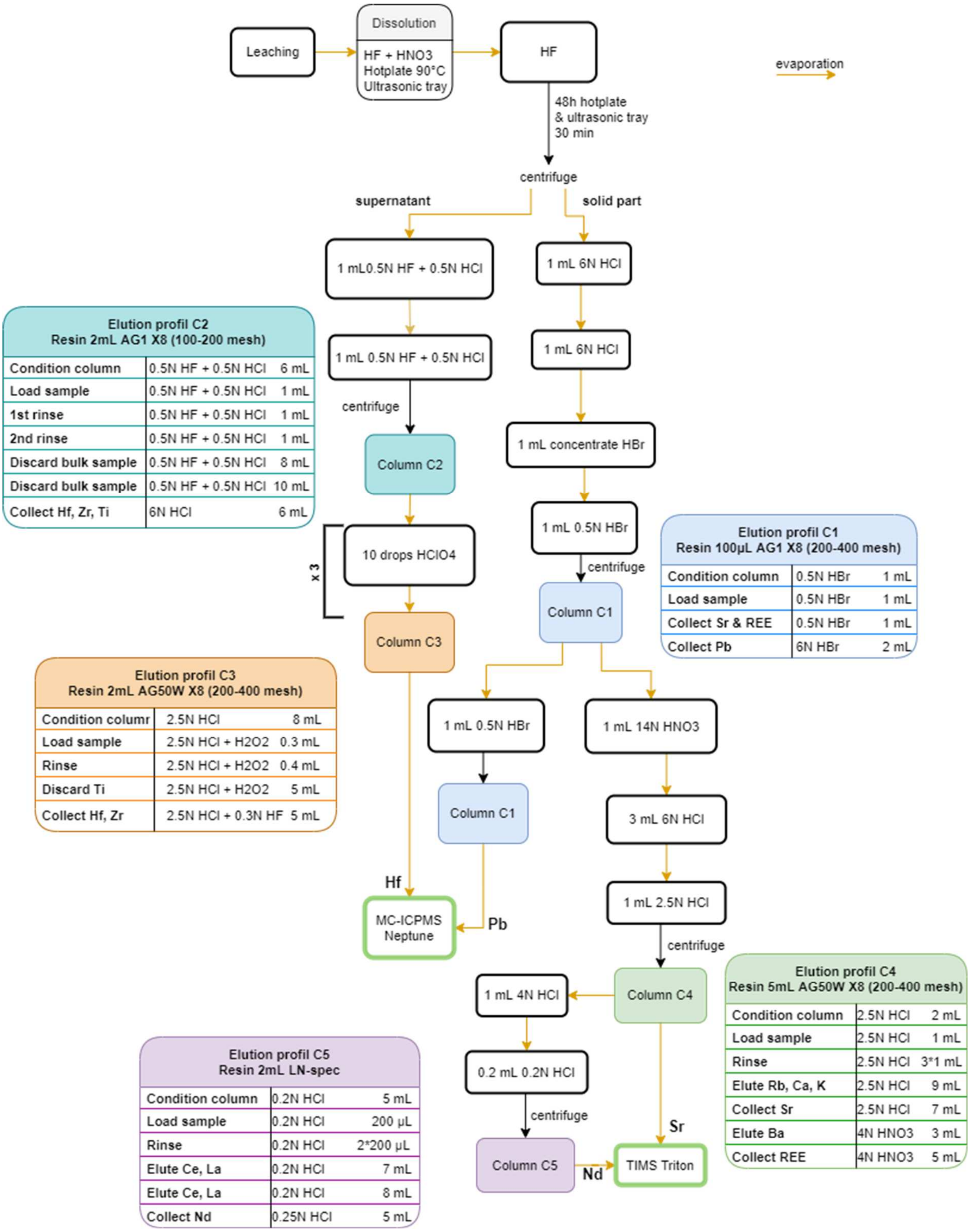

**Elution profil C2**
**Resin 2mL AG1 X8 (100-200 mesh)**

| | | |
|---|---|---|
| Condition column | 0.5N HF + 0.5N HCl | 6 mL |
| Load sample | 0.5N HF + 0.5N HCl | 1 mL |
| 1st rinse | 0.5N HF + 0.5N HCl | 1 mL |
| 2nd rinse | 0.5N HF + 0.5N HCl | 1 mL |
| Discard bulk sample | 0.5N HF + 0.5N HCl | 8 mL |
| Discard bulk sample | 0.5N HF + 0.5N HCl | 10 mL |
| Collect Hf, Zr, Ti | 6N HCl | 6 mL |

**Elution profil C3**
**Resin 2mL AG50W X8 (200-400 mesh)**

| | | |
|---|---|---|
| Condition columr | 2.5N HCl | 8 mL |
| Load sample | 2.5N HCl + H2O2 | 0.3 mL |
| Rinse | 2.5N HCl + H2O2 | 0.4 mL |
| Discard Ti | 2.5N HCl + H2O2 | 5 mL |
| Collect Hf, Zr | 2.5N HCl + 0.3N HF | 5 mL |

**Elution profil C1**
**Resin 100µL AG1 X8 (200-400 mesh)**

| | | |
|---|---|---|
| Condition column | 0.5N HBr | 1 mL |
| Load sample | 0.5N HBr | 1 mL |
| Collect Sr & REE | 0.5N HBr | 1 mL |
| Collect Pb | 6N HBr | 2 mL |

**Elution profil C4**
**Resin 5mL AG50W X8 (200-400 mesh)**

| | | |
|---|---|---|
| Condition column | 2.5N HCl | 2 mL |
| Load sample | 2.5N HCl | 1 mL |
| Rinse | 2.5N HCl | 3*1 mL |
| Elute Rb, Ca, K | 2.5N HCl | 9 mL |
| Collect Sr | 2.5N HCl | 7 mL |
| Elute Ba | 4N HNO3 | 3 mL |
| Collect REE | 4N HNO3 | 5 mL |

**Elution profil C5**
**Resin 2mL LN-spec**

| | | |
|---|---|---|
| Condition column | 0.2N HCl | 5 mL |
| Load sample | 0.2N HCl | 200 µL |
| Rinse | 0.2N HCl | 2*200 µL |
| Elute Ce, La | 0.2N HCl | 7 mL |
| Elute Ce, La | 0.2N HCl | 8 mL |
| Collect Nd | 0.25N HCl | 5 mL |

*Figure 3.4 – Workflow and chemical protocols used for the separation of Hf, Pb, Sr and Nd at Géo-Océan (Plouzané, France) integrating procedures from Richard et al. (1976), Manhès et al. (1978), White and Patchett (1984) and Blichert-Toft et al. (1997).*

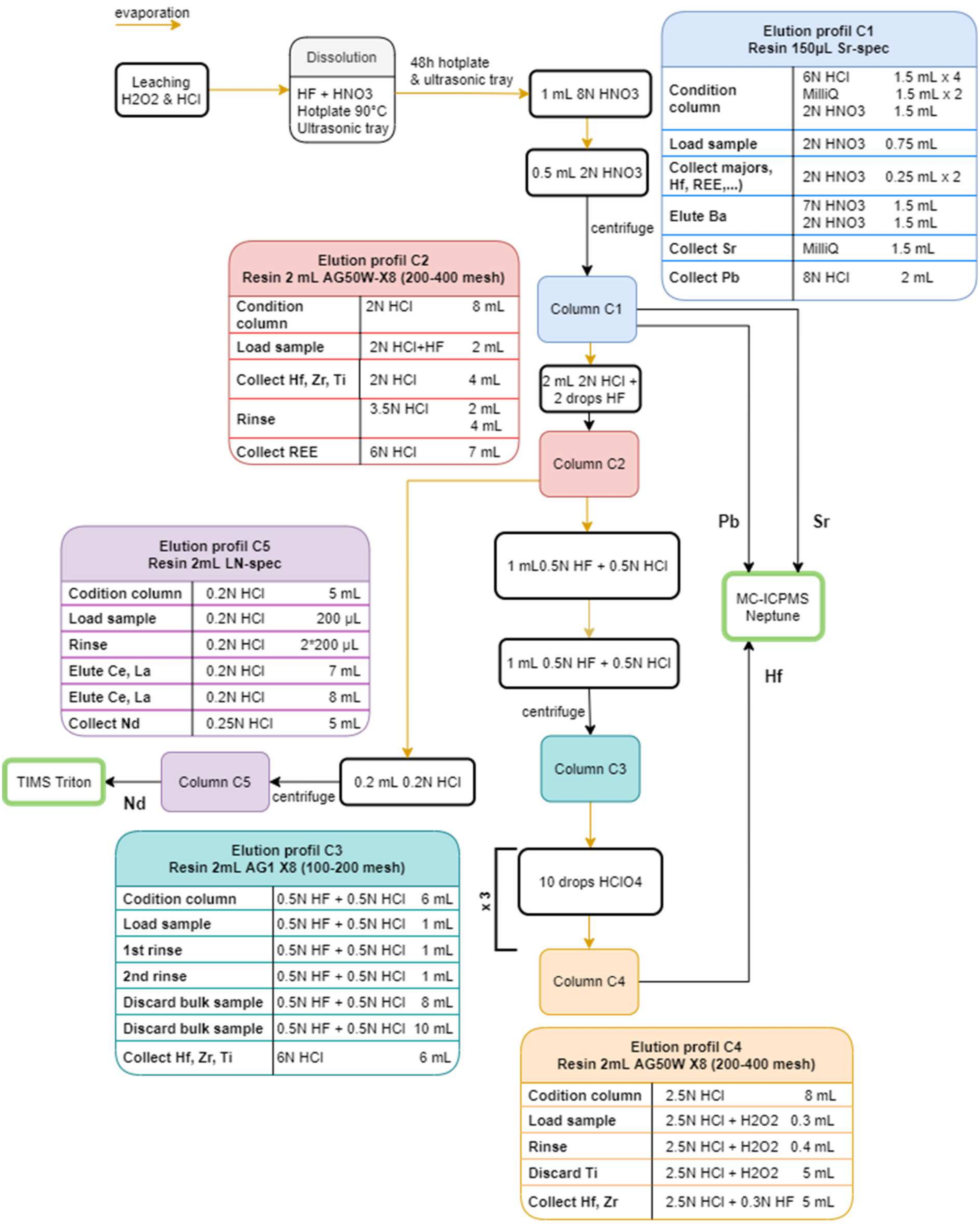

Elution profil C1
Resin 150µL Sr-spec

| | | |
|---|---|---|
| Condition column | 6N HCl<br>MilliQ<br>2N HNO3 | 1.5 mL x 4<br>1.5 mL x 2<br>1.5 mL |
| Load sample | 2N HNO3 | 0.75 mL |
| Collect majors, Hf, REE,...) | 2N HNO3 | 0.25 mL x 2 |
| Elute Ba | 7N HNO3<br>2N HNO3 | 1.5 mL<br>1.5 mL |
| Collect Sr | MilliQ | 1.5 mL |
| Collect Pb | 8N HCl | 2 mL |

Elution profil C2
Resin 2 mL AG50W-X8 (200-400 mesh)

| | | |
|---|---|---|
| Condition column | 2N HCl | 8 mL |
| Load sample | 2N HCl+HF | 2 mL |
| Collect Hf, Zr, Ti | 2N HCl | 4 mL |
| Rinse | 3.5N HCl | 2 mL<br>4 mL |
| Collect REE | 6N HCl | 7 mL |

Elution profil C5
Resin 2mL LN-spec

| | | |
|---|---|---|
| Codition column | 0.2N HCl | 5 mL |
| Load sample | 0.2N HCl | 200 µL |
| Rinse | 0.2N HCl | 2*200 µL |
| Elute Ce, La | 0.2N HCl | 7 mL |
| Elute Ce, La | 0.2N HCl | 8 mL |
| Collect Nd | 0.25N HCl | 5 mL |

Elution profil C3
Resin 2mL AG1 X8 (100-200 mesh)

| | | |
|---|---|---|
| Codition column | 0.5N HF + 0.5N HCl | 6 mL |
| Load sample | 0.5N HF + 0.5N HCl | 1 mL |
| 1st rinse | 0.5N HF + 0.5N HCl | 1 mL |
| 2nd rinse | 0.5N HF + 0.5N HCl | 1 mL |
| Discard bulk sample | 0.5N HF + 0.5N HCl | 8 mL |
| Discard bulk sample | 0.5N HF + 0.5N HCl | 10 mL |
| Collect Hf, Zr, Ti | 6N HCl | 6 mL |

Elution profil C4
Resin 2mL AG50W X8 (200-400 mesh)

| | | |
|---|---|---|
| Codition column | 2.5N HCl | 8 mL |
| Load sample | 2.5N HCl + H2O2 | 0.3 mL |
| Rinse | 2.5N HCl + H2O2 | 0.4 mL |
| Discard Ti | 2.5N HCl + H2O2 | 5 mL |
| Collect Hf, Zr | 2.5N HCl + 0.3N HF | 5 mL |

*Figure 3.5 – Workflow and chemical protocol used for the combined Pb-Sr separation according to Deniel and Pin( 2001) at Dipartimento di Scienze Chimiche e Geologiche (Modena, Italy) and Hf-Nd separation integrating procedures from Richard et al. (1976), Blichert-Toft et al., (1997) and Chauvel et al. (2011) realised at Géo-Océan (Plouzané, France).*

| | Nd (pg) | Sr (pg) | Hf (pg) | Pb (pg) |
|---|---|---|---|---|
| B1 | 87 | 75 | 27 | 328 |
| B2 | 794 | 363 | 24 | 261 |
| B3 | >10pg | 505 | 14 | 240 |
| B4 | 66 | 576 | 21 | 573 |
| B5 | 42 | 412 | 26 | 691 |
| B6 | 27 | 826 | 29 | 906 |
| B7 | 29 | 339 | 33 | 175 |
| B8 | 32 | 191 | 26 | 384 |

*Table 3.1- Chemical blanks values.*

### 3.2.3 Chemistry tests and elution curves

Given that the combined Pb-Sr chemistry with Sr-spec resin (Deniel and Pin, 2001) at DSCG (Modena) and the Hf-REE separation using AG50W-X8 (200-400mesh) resin (Chauvel et al., 2011) at GO (Plouzané) were never used in these laboratories, elution profiles were collected to calibrate both chemical protocols.

To separate Hf-Zr-Ti from REE, a chemical protocol, developed by Chauvel et al. (2011), was tested at GO (C2 Figure 3.5). A multi elemental solution (2 ppm) has been mixed to test the procedure. This solution is then evaporated, re-dissolved in 2N HCl + $HF_{trace}$ and loaded on the columns. During the protocol, the acid is added in small volumes of 0.5 mL, each 0.5 mL step is recovered. The 0.5 mL fractions are then evaporated, and $HNO_3$+HF is added for analysis by HR-ICPMS (ThermoFisher Scientific Element XR). An elution curve of this method is reported in figure 3.6.

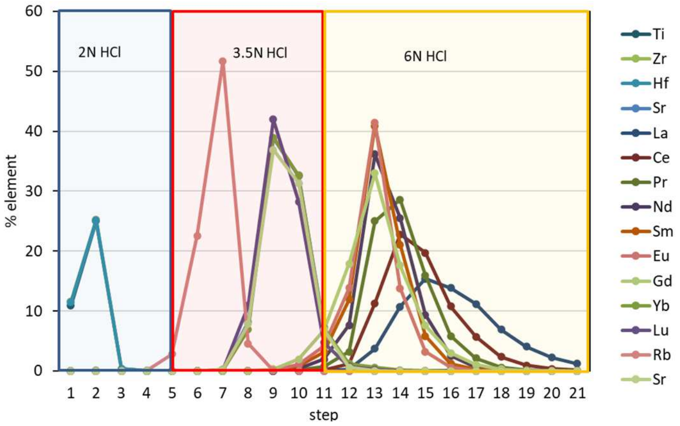

*Figure 3.6 - Elution curve for the calibration of the C5 column (Figure 3.5, Chauvel et al., 2011). Each step corresponds to the addition of 0.5 mL of acid added to the columns.*

The Pb-Sr separation protocol has been tested in the same way as the new Hf-Nd protocol. First the columns have been produced using a thermally shrinkable Teflon tube. Pieces of the tube are cut and heated with a welding torch using a Teflon or metal mould. With heat, the tube shrinks around the mould to form the column. A frit made of porous Teflon material is cut out and added to the tip of each column. The columns thus made are rinsed with MilliQ water and cleaned several times in various acid baths for few days (1N HBr, 7N $HNO_3$, 6N HCl). The columns are then stored in HBr.

To make a first check of the efficiency of the columns, a first protocol has been tested using a mixed Sr and Pb solution (respectively 1.5 mL of a 23 ppb Sr solution and 1 mL of a 310 ppb Pb solution). Again, 1N HBr is added in small volume of 0.5 mL, each 0.5 mL step is recovered, and each fraction is dried and analysed in $HNO_3$ by ICP-MS. An elution curve of this chemistry is given in figure 3.7a.

A second test has been made using a multi-elemental 33 ppb solution, the aim is to check the efficiency of the separation with all the other elements (Hf, REE, Ba, etc). The elution curve is given in figure 3.7b.

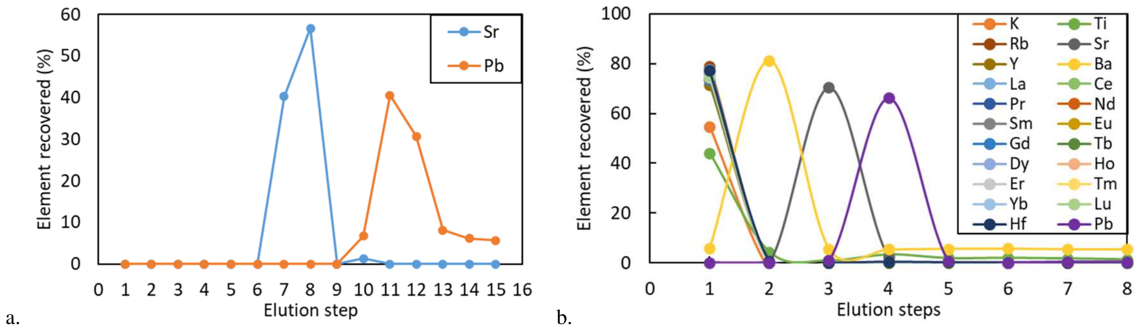

*Figure 3.7 - Elution curve for the calibration of the C1 column (see Figure 3.5 for details, Deniel and Pin, 2001). (a) First test made with the Pb-Sr solution (Sr 23 ppb Pb 310 ppb). Each step corresponds to the addition of 0.5 mL of acid added to the columns. (b) Second test made with the multi elements solution (33 ppb solution). Elements recovered during steps 1, 2 and 3 are respectively: Hf-Zr-Ti-REE-major elements (2x0.5 mL and 4x0.15 mL 2N $HNO_3$), Ba (1.5 mL 7N $HNO_3$ and 0.3 mL 2N $HNO_3$) and Sr (1.5 mL MilliQ). The other steps correspond to the addition of 0.5mL 6N HCl to recover the Pb fraction.*

### 3.3 Isotope ratios analysis

All isotope ratios have been analysed using a magnetic sector mass spectrometer. Pb and Sr isotope ratios have been analysed with a High Resolution Inductively Coupled Mass Spectrometer Thermo Fisher Scientific Neptune (HR ICP-MS) at the Centro Interdipartimentale Grandi Strumenti (CIGS, Modena). The Hf isotope ratios have been measured with a HR ICP-MS Thermo Fisher Scientific Neptune at the Pôle de Spectrométrie Océan (PSO, Plouzané) and the Nd with a Thermal Ionisation Mass Spectrometer (TIMS) Thermo Fisher Scientific Triton T1 at PSO too.

The first set of samples for Sr was analysed at PSO (Plouzané) by TIMS (Thermo Fisher Scientific Triton T1). The $^{87}Sr/^{86}Sr$ ratios of few samples have been measured also by HR ICP-MS at CIGS (Modena) for comparison and were all reproducible. All the data are given in chapter 5 (supplementary).

In a mass spectrometer, the ions are deviated in a magnetic sector. This deviation is given by the relation:

$$R = \frac{1}{B} \times \sqrt{\frac{m \times U}{q}} \qquad [3.2]$$

in which

R is the radius of curvature,
B is the value of the magnetic field,
m is the mass of the ion,
U is the electric field voltage,

q is the charge of the ion.

This allows to separate different isotopes of the same element, the heavier ion with the highest kinetic energy being less deviated by the magnetic field. This technique does not allow to separate isotopes from different elements with the same mass, as $^{87}Rb$ and $^{87}Sr$, which will be recovered in the same collector, changing the original $^{87}Sr/^{86}Sr$ ratios. The chromatographic separation of each element before the analysis and/or interferences corrections after the analysis are thus very important.

### 3.3.1 Analysis of Pb, Sr and Hf isotopes with HR ICP-MS

For the HR ICP-MS analysis, the sample is introduced in liquid phase into the instrument. All the dried fractions from the chemistry are thus put into solution, 4% $HNO_3$ for Pb and Sr and 2% $HNO_3$ + 0.05% $HF_{trace}$ for Hf. Solutions are diluted to 50 ppb and introduced in the mass spectrometer by Apex (desolvation nebulizer) for Pb and Sr isotopes analyses. Solutions are diluted to 150-200 ppb for Hf analysis and nebulized with a spray chamber. A thallium spike is added to the Pb solutions to correct the instrumental mass fractionation as the Pb does not have an unradiogenic natural isotope ratio. Mass fractionation of Tl isotopes is then considered as identical to that of Pb.

For the Sr and Pb isotopes, 100 ratios have been measured for each analysis. The standard solutions NBS987 (20 ppb) and NIST981 (40 ppb) are analysed every 3 samples for the calibration of the Sr and Pb isotopes respectively. The standards values measured and the reference values are given in figure 3.8. The average values are 0.710246, 16.926, 15.481 and 36.668 for NBS987 $^{87}Sr/^{86}Sr$ and NIST981 $^{206}Pb/^{204}Pb$, $^{207}Pb/^{204}Pb$ and $^{208}Pb/^{204}Pb$ respectively.

For the Hf isotopes, 50 ratios have been measured for each sample and the standard solution used for the calibration is AMES (150 ppb). The most common standard solution JMC475 (150 ppb) has also been regularly analysed. The standards values measured and the reference values are given in figure 3.9. The average values measured are 0.282161 and 0.282160 for $^{176}Hf/^{177}Hf$ of AMES and JMC475 respectively.

The values obtained after the analyses must undergo several corrections in order to obtain the true values of the sample. First, the blank values are subtracted from the values measured for each sample.

It is then necessary to calculate the mass bias f produced by the velocity variations between ions of different masses:

$$f = \frac{ln\left[\left(\frac{x^i}{x^j}\right)_{measured} \Big/ \left(\frac{x^i}{x^j}\right)_{real}\right]}{ln\left[\frac{M_{X_i}}{M_{X_j}}\right]} \qquad [3.3]$$

where $\frac{X_i}{X_j}$ the wanted isotope ratios and M the mass of each isotope.

To determine f, a naturally stable isotope ratio with a known value is measured. Its value is integrated into the equation (3.3). Once f has been calculated, it is used in the equation to determine the unknown ratio of $\frac{X_i}{X_j}$ from the measured value. The approximation is made that the instrumental fractionation between $X_i$ and $X_j$ is the identical to the one between the isotopes of the stable natural ratio. To correct the $^{176}$Hf/$^{177}$Hf, the instrumental bias is corrected using the naturally stable ratio $^{179}$Hf/$^{177}$Hf, and for $^{87}$Sr/$^{86}$Sr with $^{88}$Sr/$^{86}$Sr (references values used are 0.7325 for $^{179}$Hf/$^{177}$Hf and 8.716584 for $^{88}$Sr/$^{86}$Sr). In the case of the Pb isotope ratios, there is no naturally stable ratio. The correction of the fractionation is therefore made by using an element with a similar mass, a spike of thallium, which is added to the Pb solution prior to the measurement. The $^{205}$Tl/$^{203}$Tl isotopic composition of the spike (reference value used is 2.38714) allows the calculation of f to be applied to the $^{206}$Pb/$^{204}$Pb, $^{207}$Pb/$^{204}$Pb and $^{208}$Pb/$^{204}$Pb ratios.

Some elements naturally have isotopes of similar mass to the element measured. It is for example the case for $^{176}$Lu, $^{176}$Yb and $^{176}$Hf, for $^{204}$Hg and $^{204}$Pb, for $^{86}$Kr and $^{86}$Sr and for $^{87}$Rb and $^{87}$Sr. The chemical purification is supposed to overcome these interferences. However, these elements can be present in trace and the ratios have to be corrected.

For Pb, the presence of Hg is checked by measuring the $^{202}$Hg isotope. The ratio $^{202}$Hg/$^{204}$Hg being stable in nature, it is possible to calculate the contribution of Hg on the measurement of the mass 204 and thus to subtract it to obtain the value of $^{204}$Pb:

$$^{204}Pb = {}^{204}Tot - {}^{202}Hg \times \left(\frac{^{204}Hg}{^{202}Hf}\right)_{natural} \qquad [3.4]$$

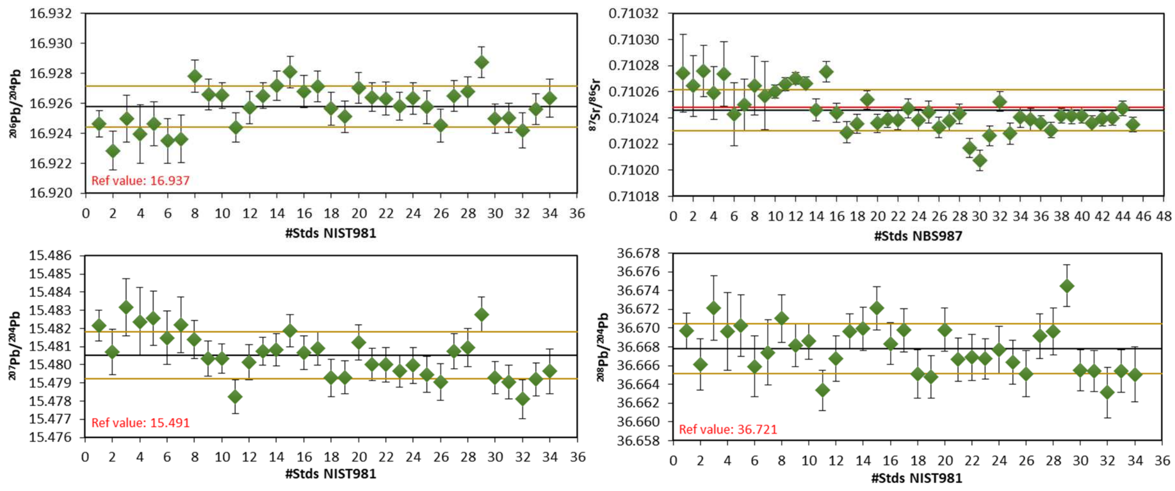

*Figure 3.8 - Values measured with the HR-ICP-MS for the NBS981 and NBS987 standards. The 2σ error (2 standard error SE) is drawn for each value. The black line is the average measured*

*standard value. The yellow lines represent the standard deviation (SD). The red line is the given reference value for the standard. Data are given in supplementary material tables S3.1 and S3.2.*

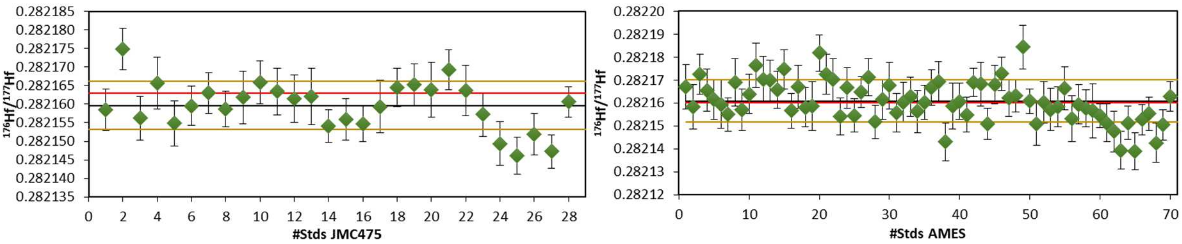

*Figure 3.9 - Values measured with the HR-ICP-MS for the JMC475 and AMES standards. The 2σ error (2SE) is drawn for each value. The black line is the average measured standard value. The yellow lines represent the standard deviation (SD). The red line is the given reference value for the standard. Data are given in supplementary material table S3.3.*

### 3.3.2 Analysis of Nd and Sr isotopes with TIMS

After preparing and degassing the Re filament (99.95% purity), the Nd residue, previously dissolved in few µL of 1N HCl, is loaded on a Re filament. Around 500 ng of Nd were loaded on the filament for the analysis. The deposit was then evaporated and oxidized. The filament with the loaded sample allows the sample to evaporate, a second filament is then put in front of the evaporation one, allowing the ionisation of the Nd.

For the Sr, a single W filament (99.95% purity) is used. Before deposition of the Sr, a TaO activator is loaded, this step allows to facilitate the ionisation of Sr. The Sr is then loaded on the filament, dried, and oxidized. The W filament allows both evaporation and ionisation of the sample.

The emission of the different isotopes is not obtained in a homogeneous way during the ionisation, the light isotopes being emitted first. It is thus required to correct for mass fractionation. The measured ratio is corrected by relating it to the ratios of stable chondritic isotopes: for Sr, $^{88}$Sr/$^{86}$Sr = 8.3752 and for Nd, $^{146}$Nd/$^{144}$Nd = 0.7219.

The standards La Jolla and NBS987 are analysed, respectively for Nd and Sr, at the beginning and at the end of each session to check the stability of the instrument. JNdi standard has also been regularly analysed for Nd. The analysed standard values and reference values are given in figure

3.10. The average values are 0.511843, 0.512099 and 0.710257 respectively for La Jolla, JNdi and NBS987.

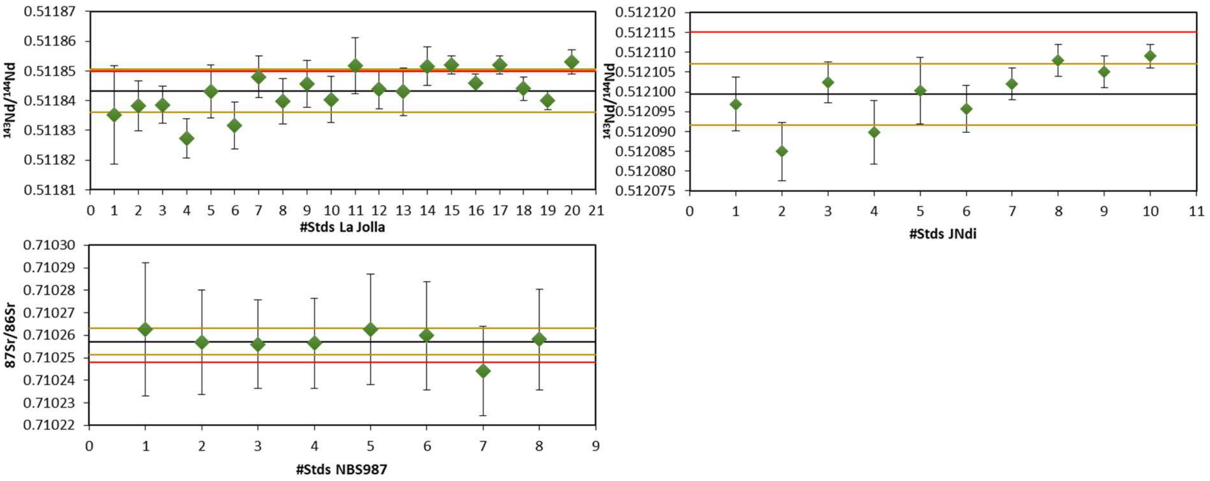

*Figure 3.10 - Values measured with the TIMS for the La Jolla, JNdi and NBS987 standards. The 2σ error (2SE) is drawn for each value. The black line is the average measured standard value. The yellow lines represent the standard deviation (SD). The red line is the given reference value for the standard. Data are given in supplementary material table S3.4 and S3.2.*

## References

Blichert-Toft, J., Chauvel, C., Albarède, F., 1997. *Separation of Hf and Lu for high-precision isotope analysis of rock samples by magnetic sector-multiple collector ICP-MS.* Contrib Mineral Petrol 127 (3), 248–260. doi:10.1007/s004100050278.

Chauvel, C., Bureau, S., Poggi, C., 2011. *Comprehensive Chemical and Isotopic Analyses of Basalt and Sediment Reference Materials.* Geostandards and Geoanalytical Research 35 (1), 125–143. doi:10.1111/j.1751-908X.2010.00086.x.

Deniel, C., Pin, C., 2001. *Single-stage method for the simultaneous isolation of lead and strontium from silicate samples for isotopic measurements.* Analytica Chimica Acta 426 (1), 95–103. doi:10.1016/S0003-2670(00)01185-5.

Janin, M., 2010. *Le plateau d'Amsterdam-St Paul : Caractérisation du point chaud éponyme et évolution de son interaction avec la dorsale Sud-est indienne*.

Jochum, K.P., Nohl, U., Herwig, K., Lammel, E., Stoll, B., Hofmann, A.W., 2005. *GeoReM: A New Geochemical Database for Reference Materials and Isotopic Standards.* Geostand Geoanalyt Res 29 (3), 333–338. doi:10.1111/j.1751-908X.2005.tb00904.x.

Manhes, G., Minster, J.F., Allègre, C.J., 1978. *Comparative uranium-thorium-lead and rubidium-strontium study of the Saint Sèverin amphoterite: consequences for early solar system chronology.* Earth and Planetary Science Letters 39 (1), 14–24. doi:10.1016/0012-821X(78)90137-1.

Richard, P., Shimizu, N., Allègre, C.J., 1976. *143Nd/146Nd, a natural tracer: an application to oceanic basalts.* Earth and Planetary Science Letters 31 (2), 269–278. doi:10.1016/0012-821X(76)90219-3.

White, W.M., Patchett, J., 1984. *Hf Nd Sr isotopes and incompatible element abundances in island arcs: implications for magma origins and crust-mantle evolution.* Earth and Planetary Science Letters 67 (2), 167–185. doi:10.1016/0012-821X(84)90112-2.

## Supplementary material

*Table S3.1 - NIST981 isotope ratios measured with HR-ICP-MS (2σ represents the error 2SE).*

| $^{206}$Pb/$^{204}$Pb | 2σ | $^{207}$Pb/$^{204}$Pb | 2σ | $^{208}$Pb/$^{204}$Pb | 2σ |
|---|---|---|---|---|---|
| 16.925 | 0.001 | 15.482 | 0.001 | 36.670 | 0.002 |
| 16.923 | 0.001 | 15.481 | 0.001 | 36.666 | 0.003 |
| 16.925 | 0.002 | 15.483 | 0.002 | 36.672 | 0.003 |
| 16.924 | 0.002 | 15.482 | 0.002 | 36.670 | 0.004 |
| 16.925 | 0.001 | 15.483 | 0.002 | 36.670 | 0.003 |
| 16.923 | 0.002 | 15.481 | 0.001 | 36.666 | 0.003 |
| 16.924 | 0.002 | 15.482 | 0.002 | 36.667 | 0.004 |
| 16.928 | 0.001 | 15.481 | 0.001 | 36.671 | 0.003 |
| 16.927 | 0.001 | 15.480 | 0.001 | 36.668 | 0.002 |
| 16.927 | 0.001 | 15.480 | 0.001 | 36.669 | 0.002 |
| 16.924 | 0.001 | 15.478 | 0.001 | 36.663 | 0.002 |
| 16.926 | 0.001 | 15.480 | 0.001 | 36.667 | 0.002 |
| 16.927 | 0.001 | 15.481 | 0.001 | 36.670 | 0.002 |
| 16.927 | 0.001 | 15.481 | 0.001 | 36.670 | 0.002 |
| 16.928 | 0.001 | 15.482 | 0.001 | 36.672 | 0.002 |
| 16.927 | 0.001 | 15.481 | 0.001 | 36.668 | 0.002 |
| 16.927 | 0.001 | 15.481 | 0.001 | 36.670 | 0.002 |
| 16.926 | 0.001 | 15.479 | 0.001 | 36.665 | 0.003 |
| 16.925 | 0.001 | 15.479 | 0.001 | 36.665 | 0.002 |
| 16.927 | 0.001 | 15.481 | 0.001 | 36.670 | 0.002 |
| 16.926 | 0.001 | 15.480 | 0.001 | 36.667 | 0.002 |
| 16.926 | 0.001 | 15.480 | 0.001 | 36.667 | 0.002 |
| 16.926 | 0.001 | 15.480 | 0.001 | 36.667 | 0.002 |
| 16.926 | 0.001 | 15.480 | 0.001 | 36.668 | 0.002 |
| 16.926 | 0.001 | 15.479 | 0.001 | 36.666 | 0.002 |
| 16.925 | 0.001 | 15.479 | 0.001 | 36.665 | 0.002 |
| 16.927 | 0.001 | 15.481 | 0.001 | 36.669 | 0.002 |
| 16.927 | 0.001 | 15.481 | 0.001 | 36.670 | 0.002 |
| 16.929 | 0.001 | 15.483 | 0.001 | 36.674 | 0.002 |
| 16.925 | 0.001 | 15.479 | 0.001 | 36.666 | 0.002 |
| 16.925 | 0.001 | 15.479 | 0.001 | 36.665 | 0.002 |
| 16.924 | 0.001 | 15.478 | 0.001 | 36.663 | 0.003 |
| 16.926 | 0.001 | 15.479 | 0.001 | 36.665 | 0.002 |
| 16.926 | 0.001 | 15.480 | 0.001 | 36.665 | 0.003 |

*Table S3.2 - NBS987 isotope ratios measured with both HR-ICP-MS and TIMS.*

| | $^{87}Sr/^{86}Sr$ | 2σ | $^{87}Sr/^{86}Sr$ | 2σ |
|---|---|---|---|---|
| **HR-ICP-MS** | 0.710274 | 0.000030 | 0.710238 | 0.000008 |
| | 0.710264 | 0.000023 | 0.710245 | 0.000008 |
| | 0.710276 | 0.000020 | 0.710233 | 0.000008 |
| | 0.710259 | 0.000020 | 0.710238 | 0.000008 |
| | 0.710274 | 0.000025 | 0.710243 | 0.000008 |
| | 0.710243 | 0.000024 | 0.710217 | 0.000007 |
| | 0.710250 | 0.000020 | 0.710208 | 0.000008 |
| | 0.710265 | 0.000022 | 0.710226 | 0.000008 |
| | 0.710257 | 0.000026 | 0.710253 | 0.000008 |
| | 0.710260 | 0.000005 | 0.710228 | 0.000008 |
| | 0.710266 | 0.000005 | 0.710240 | 0.000008 |
| | 0.710270 | 0.000004 | 0.710239 | 0.000008 |
| | 0.710266 | 0.000005 | 0.710236 | 0.000005 |
| | 0.710246 | 0.000008 | 0.710231 | 0.000006 |
| | 0.710276 | 0.000008 | 0.710242 | 0.000005 |
| | 0.710244 | 0.000007 | 0.710242 | 0.000006 |
| | 0.710229 | 0.000008 | 0.710242 | 0.000006 |
| | 0.710236 | 0.000007 | 0.710236 | 0.000006 |
| | 0.710254 | 0.000007 | 0.710240 | 0.000006 |
| | 0.710236 | 0.000007 | 0.710240 | 0.000006 |
| | 0.710239 | 0.000006 | 0.710247 | 0.000006 |
| | 0.710239 | 0.000007 | 0.710235 | 0.000005 |
| | 0.710247 | 0.000007 | | |

| | $^{87}Sr/^{86}Sr$ | 2σ |
|---|---|---|
| **TIMS** | 0.710263 | 0.000004 |
| | 0.710257 | 0.000004 |
| | 0.710256 | 0.000004 |
| | 0.710256 | 0.000005 |
| | 0.710263 | 0.000004 |
| | 0.710260 | 0.000005 |
| | 0.710244 | 0.000004 |
| | 0.710258 | 0.000006 |

*Table S3.3 - AMES and JMC475 isotope ratios measured with HR-ICP-MS.*

| AMES 150ppb | | | |
|---|---|---|---|
| $^{176}Hf/^{177}Hf$ | 2σ | $^{176}Hf/^{177}Hf$ | 2σ |
| 0.282167 | 0.000010 | 0.282167 | 0.000008 |
| 0.282158 | 0.000010 | 0.282169 | 0.000009 |
| 0.282173 | 0.000009 | 0.282143 | 0.000008 |
| 0.282165 | 0.000009 | 0.282159 | 0.000010 |
| 0.282162 | 0.000009 | 0.282161 | 0.000008 |
| 0.282159 | 0.000010 | 0.282155 | 0.000008 |
| 0.282155 | 0.000007 | 0.282169 | 0.000006 |
| 0.282169 | 0.000010 | 0.282168 | 0.000009 |
| 0.282157 | 0.000009 | 0.282151 | 0.000007 |
| 0.282164 | 0.000009 | 0.282168 | 0.000008 |
| 0.282176 | 0.000010 | 0.282173 | 0.000007 |
| 0.282170 | 0.000010 | 0.282162 | 0.000008 |
| 0.282170 | 0.000009 | 0.282163 | 0.000007 |
| 0.282166 | 0.000008 | 0.282184 | 0.000010 |
| 0.282175 | 0.000009 | 0.282161 | 0.000005 |
| 0.282157 | 0.000008 | 0.282151 | 0.000009 |
| 0.282167 | 0.000009 | 0.282160 | 0.000009 |
| 0.282158 | 0.000009 | 0.282157 | 0.000009 |
| 0.282159 | 0.000011 | 0.282158 | 0.000009 |
| 0.282182 | 0.000008 | 0.282166 | 0.000009 |
| 0.282173 | 0.000009 | 0.282153 | 0.000010 |
| 0.282170 | 0.000009 | 0.282159 | 0.000008 |
| 0.282154 | 0.000008 | 0.282158 | 0.000008 |
| 0.282167 | 0.000009 | 0.282157 | 0.000012 |
| 0.282155 | 0.000007 | 0.282154 | 0.000005 |
| 0.282165 | 0.000007 | 0.282151 | 0.000008 |
| 0.282171 | 0.000008 | 0.282148 | 0.000009 |
| 0.282152 | 0.000007 | 0.282139 | 0.000008 |
| 0.282161 | 0.000009 | 0.282151 | 0.000007 |
| 0.282168 | 0.000010 | 0.282139 | 0.000008 |
| 0.282156 | 0.000008 | 0.282153 | 0.000007 |
| 0.282160 | 0.000008 | 0.282155 | 0.000007 |
| 0.282163 | 0.000009 | 0.282143 | 0.000009 |
| 0.282156 | 0.000009 | 0.282150 | 0.000007 |
| 0.282160 | 0.000007 | 0.282163 | 0.000006 |

| JMC475 150ppb | |
|---|---|
| $^{176}Hf/^{177}Hf$ | 2σ |
| 0.282159 | 0.000006 |
| 0.282175 | 0.000006 |
| 0.282156 | 0.000006 |
| 0.282166 | 0.000007 |
| 0.282155 | 0.000006 |
| 0.282160 | 0.000005 |
| 0.282163 | 0.000005 |
| 0.282159 | 0.000005 |
| 0.282162 | 0.000007 |
| 0.282166 | 0.000006 |
| 0.282163 | 0.000006 |
| 0.282162 | 0.000006 |
| 0.282162 | 0.000008 |
| 0.282154 | 0.000004 |
| 0.282156 | 0.000006 |
| 0.282155 | 0.000005 |
| 0.282159 | 0.000007 |
| 0.282164 | 0.000005 |
| 0.282165 | 0.000006 |
| 0.282164 | 0.000007 |
| 0.282169 | 0.000005 |
| 0.282164 | 0.000007 |
| 0.282157 | 0.000006 |
| 0.282149 | 0.000006 |
| 0.282146 | 0.000005 |
| 0.282152 | 0.000006 |
| 0.282147 | 0.000005 |
| 0.282161 | 0.000004 |

*Table S3.4 - La Jolla and JNdi isotope ratios measured with TIMS.*

| **La Jolla** | |
|---|---|
| **$^{143}$Nd/$^{144}$Nd** | **2σ** |
| 0.511835 | 0.000017 |
| 0.511838 | 0.000008 |
| 0.511839 | 0.000006 |
| 0.511827 | 0.000007 |
| 0.511843 | 0.000009 |
| 0.511832 | 0.000008 |
| 0.511848 | 0.000007 |
| 0.511840 | 0.000008 |
| 0.511846 | 0.000008 |
| 0.511840 | 0.000008 |
| 0.511852 | 0.000009 |
| 0.511844 | 0.000007 |
| 0.511843 | 0.000008 |
| 0.511852 | 0.000006 |
| 0.511852 | 0.000003 |
| 0.511846 | 0.000003 |
| 0.511852 | 0.000003 |
| 0.511844 | 0.000004 |
| 0.511840 | 0.000003 |
| 0.511853 | 0.000004 |

| **JNdi** | |
|---|---|
| **$^{143}$Nd/$^{144}$Nd** | **2σ** |
| 0.512097 | 0.000007 |
| 0.512085 | 0.000007 |
| 0.512102 | 0.000005 |
| 0.512090 | 0.000008 |
| 0.512100 | 0.000008 |
| 0.512096 | 0.000006 |
| 0.512102 | 0.000004 |
| 0.512108 | 0.000004 |
| 0.512105 | 0.000004 |
| 0.512109 | 0.000003 |

# CHAPTER 4 Petrological constraints to mantle source and crustal processes for the ERRTI MORBs

## Abstract

MORBs are mixtures of various components dispersed in the upper mantle by secular stirring of primitive, residual and recycled components. Their compositional variability is generally low due to the extreme homogenization deriving from mixing and pooling melts from a large melting region, with the effect of smoothing out the source variability.

Here we study a group of MORBs sampled at the Eastern Romanche Ridge Transform Intersection (ERRTI), a region affected by a strong cold-edge effect (Bonatti et al., 2001; Ligi et al., 2005). Major and trace elements systematics reveal a highly variable composition ranging from depleted to true alkaline basalts showing extreme alkali and incompatible element enrichment similar to those described at the hot spots. A significant fraction of MORBs present significant $K_2O$ enrichment, an element usually negligible in the MORB systematics. On this base we recognize three major compositional groups: N-MORBs, E-MORBs and K-rich MORBs. Fractional crystallization alone cannot explain the observed variability that requires an input of garnet-bearing lithologies in the MORB source. The low ambient temperature resulting in very low melting degrees, allows separating the contribution of garnet-bearing pyroxenites to the final mixture. The presence of a strong lateral thermal regional gradient allows recognizing the temperature effects on mantle melting: a decrease in mantle temperature results in increased compositional variability and relative enrichment in incompatible elements while hotter ridge sections generate more homogeneous N-MORB composition.

## Introduction

The equatorial portion of the Mid Atlantic Ridge (MAR) is characterized by a number of peculiarities: (a) The MAR axis is displaced for over 2000 km by a set of major, long-offset transforms, the longest being the Romanche (offset ~950 km) and the St. Paul (offset ~450 km) (Figure 4.1); (b) The axial, near-zero age topographic level is deeper than normal; (c) Crustal thickness is anomalously low throughout the equatorial region, and mantle peridotites are exposed in large areas; (d) The chemistry of zero-age basalts and of mantle peridotites both suggest that the degree of melting undergone by the upper mantle below the MAR is exceptionally low (Schilling et al., 1995; Bonatti et al, 2001, Ligi et al., 2005). These features have been explained by the hypothesis that the upper mantle below the equatorial MAR is affected by a thermal minimum (Bonatti et al., 1993; Schilling et al., 1995, Ligi et al., 2005).

Here we describe a number of basaltic glass samples recovered by dredges and submersible dives from the equatorial MAR along the Eastern Romanche Ridge Transform Intersection (ERRTI) (Figure 4.2). These basalts have compositions significantly different from “classical” MORB, that could be explained by the peculiar thermal/tectonic setting of the region.

This paper presents the major and trace element compositions of the ERRTI MORBs. By identifying different processes (fractional crystallization, partial melting and melt mixing), the compositional variability of the ERRTI basalts is explained by the presence of various lithologies.

## Geological setting

The Romanche Transform Fault (RTF) offsets the MAR by 950 km (Heezen et al., 1964) resulting in an age contrast of about 40 Ma between the old lithosphere and the ridge axis (Figure 4.1). It is composed of a deep valley (~ 5000 m deep; Searle et al., 1994) enclosed in a lensoidal, highly deformed region of more than 900 km long and 100 km wide (Ligi et al., 2002).

Abundant expositions of mantle rocks attest of an incomplete magmatic coverage during spreading (Bonatti et al., 2001). The lack of magmatic crust and the compositions of peridotites and MORBs suggest the presence of a thermal minimum at the ERRTI (Schilling et al., 1995;

Bonatti et al., 1993, Ligi et al., 2005) (Figure 4.2). The study of MORB compositions in this region highlighted small-scale mantle heterogeneities: in addition to N-MORB compositions, a number of LREE enriched, alkali-rich basalts have been reported (Melson et al., 1967; Schilling et al., 1995; Sushchevskaya et al., 2002; Le Voyer et al., 2015). These compositions are associated to very high content in $H_2O$ (Ligi et al., 2005; Le Voyer et al., 2015).

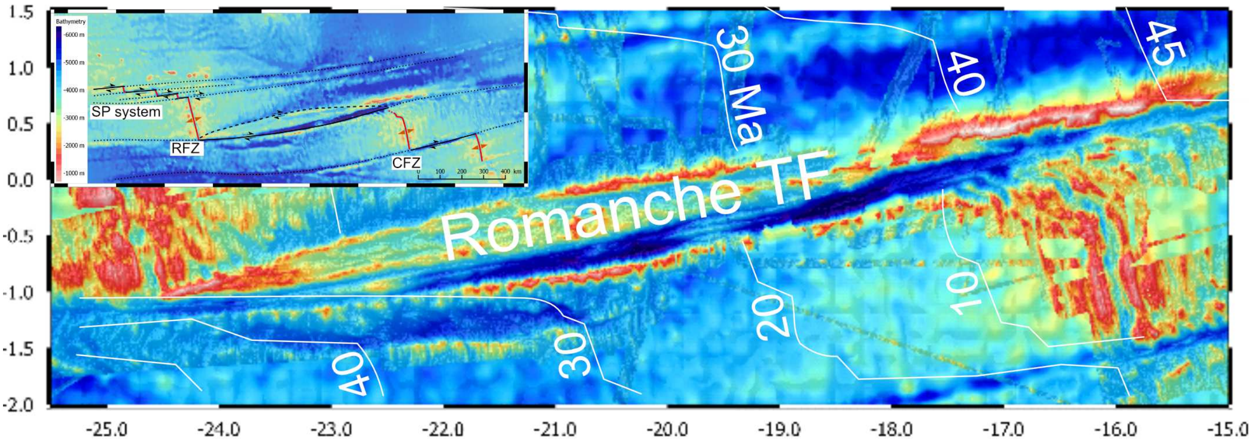

*Figure 4.1 - Bathymetric map of the Romanche Transform Fault. The white lines indicate the age of the oceanic lithosphere (from Yu et al., 2021). SP system: Saint Paul system; RFZ: Romanche Fracture Zone; CFZ: Chain Fracture Zone.*

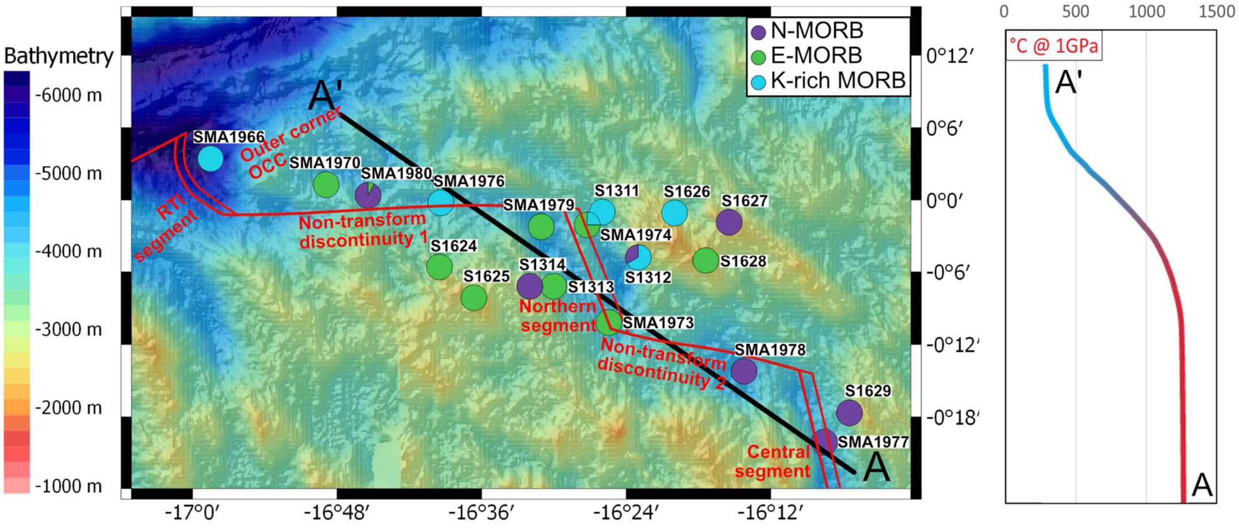

*Figure 4.2 - Sampling sites considered in this chapter. SP: Saint Paul; RFZ: Romanche Fracture Zone; CFZ: Chain Fracture Zone. The thermal profile shows the thermal gradient along the A-A' section. Temperature is calculated according to Ligi et al. (2005) at the pressure of 1 GPa.*

## Methods

Glass samples were crushed by hand using an agate mortar and pestle, cleaned ultrasonically in ultrapure water and handpicked to remove any altered chips. Unaltered grains were embedded in epoxy resin, polished and carbon coated for electron probe analyses. Basaltic glass chips were analyzed for major elements by means of the Electron Probe Micro Analysis (EPMA) Cameca SX 100 (operated by Université de Bretagne Occidentale, IFREMER, Institut Universitaire Européen de la Mer, INSA Rennes, Université de Rennes1 and Université de Nantes), using a 5 mμ diameter beam.

Trace elements have been analysed by Laser Ablation Inductively Coupled Mass Spectrometry (LA-ICP-MS) using an ICPMS X Series II coupled with a laser ablation X 213 at Centro Interdipartimentale Grandi Strumenti (CIGS, Modena), and a High Resolution Inductively Coupled Plasma Mass-spectrometer (HR-ICP-MS Element XR) coupled with a laser ablation system 193 nm Compex Pro 102 Coherent at the Pôle de Spectrométrie Océan (PSO, a Université de Brest, CNRS, Ifremer and IRD facility). Dwell times on each isotope during one run was 30 ms per amu. One run consists of 50 replicates per analysis. The standard reference materials NIST612 and NIST614 have been analyzed following the sequence of analysis: NIST614 - NIST612 - NIST614 - 3 x sample #1 – 3 x sample #2. The natural reference sample BHVO2 has been regularly measured. A number of samples have been analysed using both instrument in order to check the reproducibility of the analysis.

## Results

### Major elements

The major element compositions of the basaltic glasses are presented in supplementary material and figures 4.3, 4.4, 4.5 and 4.6.

In the following figures, samples are colour coded following a group definition that will be discussed in the trace element section (see section 4.2). Measured compositions are very heterogeneous (Figure 4.3). Samples with N-MORB composition are mainly sampled in the central segment and show small compositional variability comparable to the average MAR MORB field (MgO 7.2 – 7.9 wt%; $SiO_2$ 50 – 52 wt%; $Al_2O_3$ 14.8 – 15.7 wt%; FeO 8.7 – 9.7 wt%; CaO 10.5 – 11.7 wt%; $Na_2O$ 2.8 – 3.2 wt%; $K_2O$ 0.16 – 0.25 wt%). By converse all the other samples in the region have extremely variable composition (Figure 4.3). Their $SiO_2$ content varies from 44.4 wt%, which is very low compared to the global Atlantic MORB, to 54.6 wt%. The samples generally have lower CaO (< 10.5 wt%) and FeO (< 9 wt%) for high $Al_2O_3$ (> 16 wt%) compared to the Atlantic MORB field (Figure 4.3). This compositional character has been already reported for a large group of rocks sampled along the Southwest Indian Ridge (Meyzen et al., 2003, Standish et al., 2008). The maximum MgO content measured in all the samples is significantly lower than the maximum observed in the global MAR MORB, respectively 8.95 wt% and > 10 wt%.

ERRTI samples show in general higher $Na_2O$ with respect to the MAR field, reaching very high $Na_2O$ (up to 4.45 wt%, Figures 4.3, 4.4) and contextually showing a significant $K_2O$ enrichment higher than the MAR normal range (up to 1.95 wt%, Figures 4.3, 4.4). Because of their lower content in MgO and FeO and higher alkalinity, most of the ERRTI samples do not plot within the field of the Atlantic MORBs in the AFM diagram (Figure 4.5) (Alkalies-FeO-MgO) but appear shifted along the calc-alkaline trend (Figure 4.5a). This behaviour is partly consistent with that of the samples from the southern MAR that present a Fe-enrichment trend slightly displaced toward higher alkali contents with respect to the northern MAR ones (Figure 4.5a).

By definition, tholeiitic samples should follow a Fe-enrichment trend due to the absence of crystallization of Fe-Ti oxides at early stage of magma differentiation (trend TB, Tholeiitic Basalt, to FB, Ferro-Basalt in the AFM diagram), later followed by an alkali enrichment/Fe depletion trend (from TAB, Tholeiitic Andesitic Basalt, to TR, Tholeiitic Rhyolite, in the AFM diagram). Usually, the Fe-enrichment trend is not observed in calc-alkaline samples, which only experienced the alkaline enrichment. This alkaline enrichment is unusual for MORB, and particularly high in rocks sampled close to the ERRTI reaching up to 5.8 wt% in $Na_2O+K_2O$. These enrichments bring these samples beyond the McDonald-Katsura line, i.e., the boundary between the alkaline and tholeiitic basalts, into the alkaline field, in the Total-Alkali Silica (TAS) plot (Figure 4.5b, MacDonald and Katsura, 1964).

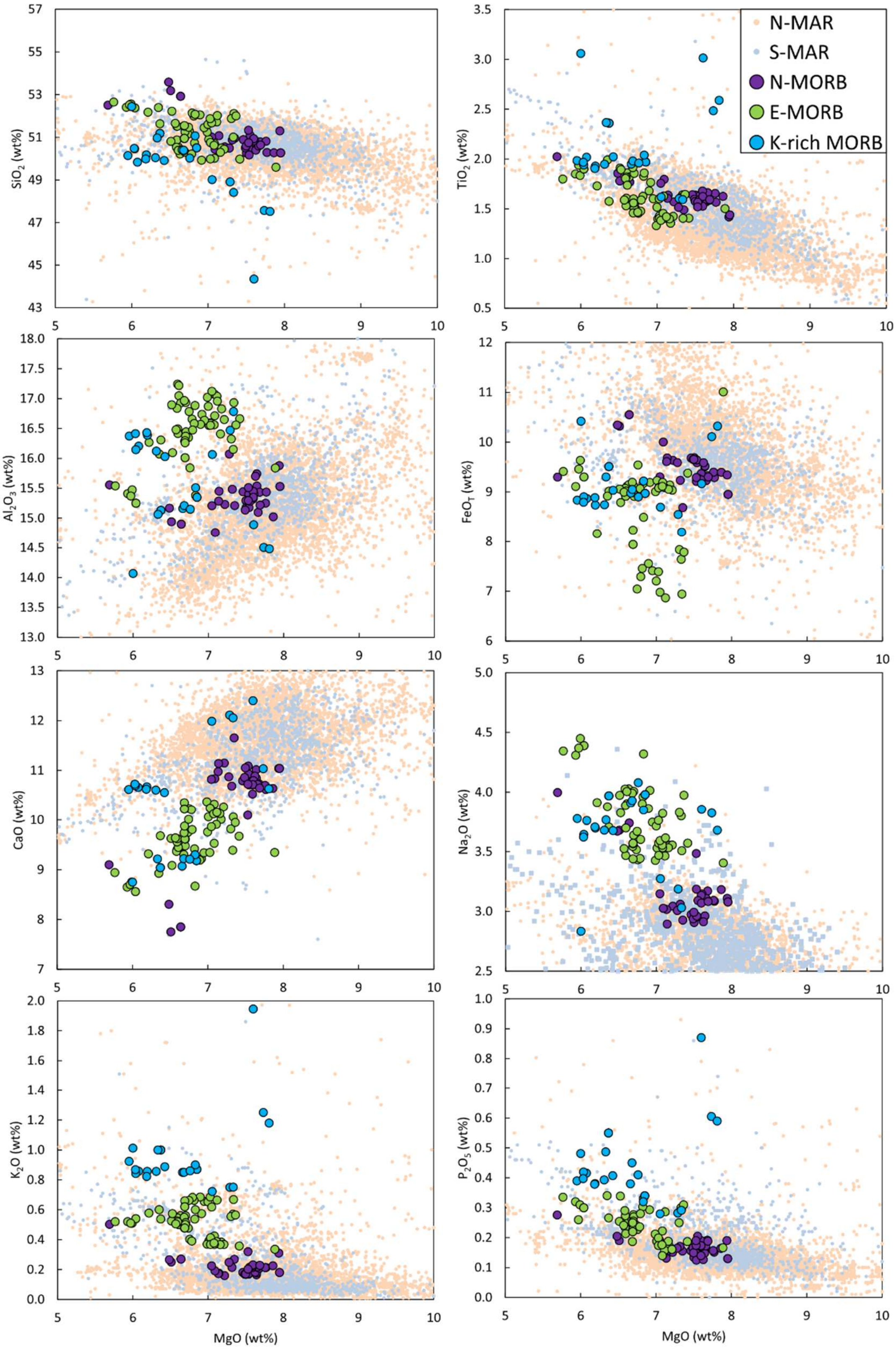

*Figure 4.3 - Major element composition vs. MgO compared to the Atlantic MORBs. North MAR (small solid orange circles) and South MAR (small solid blue circles) data are from PetDB database. Samples are grouped as a function of their REE signature, La/Sm$_{PM}$ ratio and K$_2$O content (see section 4.2 for details). FeO$_T$ of the MAR database has been calculated according to Gale et al. (2013).*

The most alkaline samples are Si-depleted and have among the highest content in $K_2O$ of the whole MAR (Figures 4.3, 4.4b). Overall, these $SiO_2$-depleted $K_2O$-rich samples show a high variability in $Al_2O_3$, from 14.1 wt% to 16.8 wt%, and CaO, from 8.8 wt% to 12.4 wt%, and have higher $P_2O_5$ and $TiO_2$, respectively up to 0.87 wt% and 3.06 wt%, compared to the other samples in the region (Figure 4.3). It is worth noting that the total alkali content forms a broad negative trend with silica (Figure 4.5b). This same trend is clearly visible in the $K_2O$-$SiO_2$ distribution (Figure 4.4b).

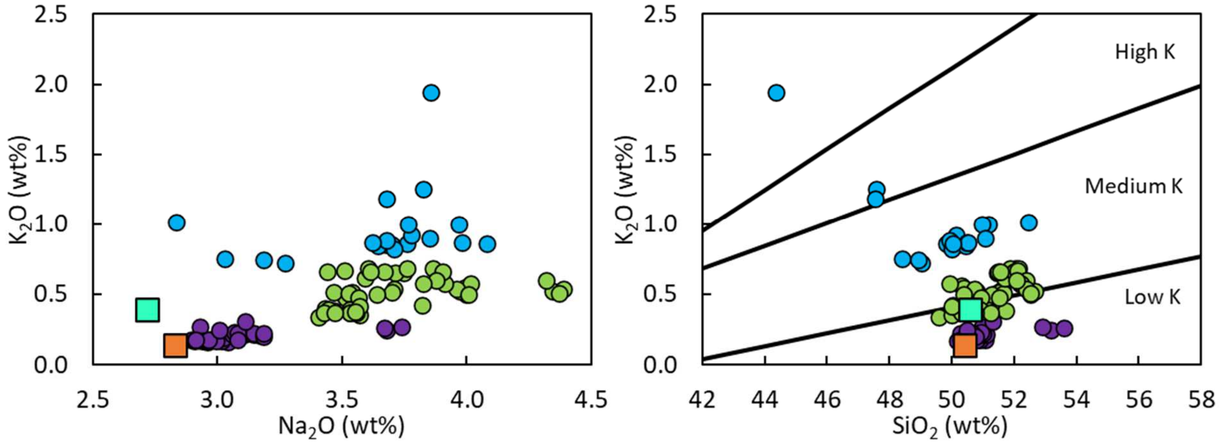

*Figure 4.4 - (a) $K_2O$ vs $Na_2O$ contents in ERRTI basalts. (b) $K_2O$ vs $SiO_2$ content in ERRTI basalts. Compositional fields are from Middlemost (1975). Orange and green squares are N-MORB and E-MORB references respectively (Gale et al., 2013). Symbols are the same as in the previous figure.*

The $Na_2O$+$K_2O$ content of some samples is among the highest along the MAR, reaching the contents observed in the hotspot influenced MAR stretches (Gale et al., 2013). Most of the high $Na_2O$+$K_2O$ samples are nepheline-normative (see normative compositions in supplementary table S4.3), matching the alkaline basalt definition of Irvine and Baragar (1971) based on the clinopyroxene-olivine-nepheline-quartz tetrahedron (Figure 4.6). Consistently, the presence of high alkali contents, together with nepheline normative compositions, allow to classify the samples as true alkaline basalts similar to those sampled in hotspot environments (Irvine and Baragar, 1971, MacDonald and Katsura, 1964, Gale et al., 2013). All K-rich samples ($K_2O$>0.7, blue dots) and some E-MORBs (green dots) with "normal" $K_2O$ contents are alkaline. Given the peculiar trace element composition of the K-rich samples (see section 4.2), we separate them as a coherent compositional group in the discussion.

While a general continuity in the enrichment trends can be observed in the overall distribution of the major element contents (Figure 4.3), it clearly appears that samples form distinct clusters particularly in the distribution of the alkalies (Figures 4.4b, 4.5b). However, while $Na_2O$ increases more continuously (Figures 4.3, 4.4a), $K_2O$ tends to define clear clusters (Figure 4.3, 4.4b). This compositional character is paired by the distribution of the trace elements, as described in section 4.2, and allows identifying different compositional groups that illustrate source variability, melt mixing and/or fractionation process.

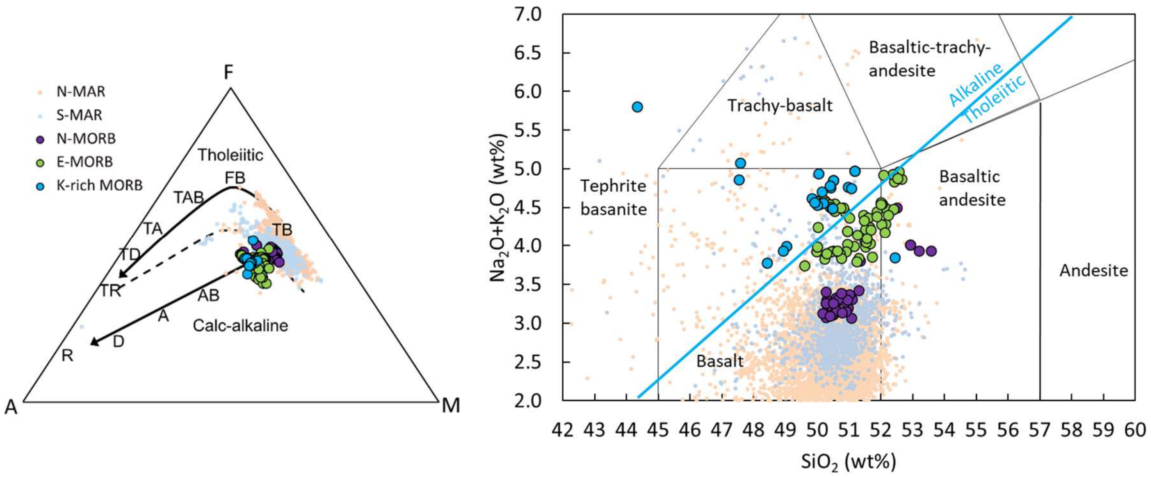

*Figure 4.5 – (a) AFM diagram (Alkali-FeO-MgO, Irvine and Baragar, 1971). Abbreviations stand for: TB: Tholeiitic Basalt, FB: Ferro-Basalt, TAB: Tholeiitic Andesitic Basalt, TA: Tholeiitic Andesite, TD: Tholeiitic Diorite, TR: Tholeiitic Rhyolite, AB: Andesitic Basalt, A: Andesite, D: Diorite, R: Rhyolite. The dashed line represents the limit between tholeiitic and calc-alkaline (Irvine and Baragar, 1971). (b) Total Alkali-Silica diagram (Irvine and Baragar, 1971). The alkaline-tholeiitic boundary is after MacDonald-Katsura (1964).*

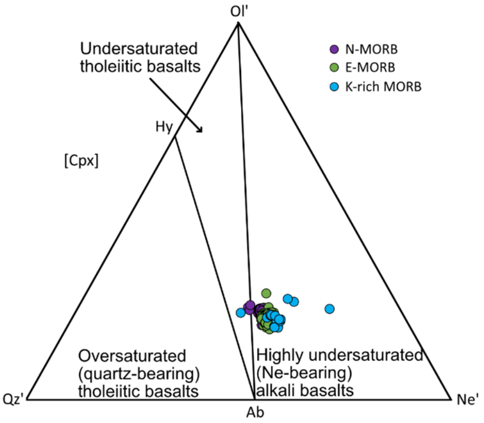

*Figure 4.6 - Ternary olivine–nepheline–quartz plot projected from the clinopyroxene pole of the basalt tetrahedron (after the projection scheme of Irvine & Baragar, 1971; Ol' = Ol + 0.75Hy; Ne' = Ne + 0.6Ab; Qz' = Qz + 0.4Ab + 0.25Hy). Normative values are reported in supplementary table S4.3.*

In summary, MORBs sampled at the ERRTI have a remarkably high variability in their major element contents (Figure 4.3). While a group of samples have N-MORB compositions, others have particularly high alkaline contents, $Na_2O$ and $K_2O$, reaching values comparable to MAR axis hotspot influenced samples (Figures 4.3, 4.4, 4.5). These alkali-rich basalts are all nepheline normative, and thus are true alkaline basalts as observed in hotspot environments (Figures 4.4a, 4.6). A group of these MORBs is exceptionally rich in $K_2O$ and poor in $SiO_2$ content, giving a characteristic compositional signature (Figures 4.3, 4.4b). The enriched $K_2O$ samples appear to form a separated cluster in the general Na-K trend reported in Figure 4.4a. Consistently, they form in the K-Si plot a discontinuous group ranging from the Medium to High and Very High K compositional groups (Figure 4.4b). These samples are here considered as a single coherent group, defined K-rich MORBs. Their trace element contents, shown in the next section, will confirm their unicity.

Overall, MORBs from the ERRTI have higher contents in $Al_2O_3$, $Na_2O$ and $K_2O$ and lower content in FeO and CaO than MORBs all along the MAR (Figure 4.3). These peculiar compositions have also been described in the SWIR (Meyzen et al., 2003, Standish et al., 2008) and will be discussed later.

## Trace elements

The trace element compositions of the ERRTI glasses are presented in supplementary material and figures 4.7, 4.8 and 4.9.

Trace elements are affected by partial melting depending on their bulk partition coefficient D (quantifying the affinity of an element to go preferentially in the liquid or to remain in the solid phase during partial melting). For a multiphase source, this affinity can be approximated by the partition coefficient D as:

$$D = \sum {K_D}_i^{min/l} x_{min} \qquad [4.1]$$

in which $K_{Di} = \frac{C^i_{mineral}}{C^i_{liquid}}$ with $C^i_{mineral}$ and $C^i_{liquid}$ the concentrations of the element $i$ respectively in the mineral phase $i$ and in the liquid, and $x_{min}$ the mode of the mineral in the source.

MORBs are generally enriched in incompatible elements compared to their mantle source, because the elements with D<1 preferentially partition to the liquid phase over the residual solid, (Hofmann et al. 1988). N-MORBs are relatively depleted in highly incompatible elements compared to moderately incompatible elements, such as the large-ion lithophile elements (LILE) and high-field strength elements (HFSE), E-MORBs are characterised by an enrichment of the highly incompatible elements (Figure 4.7) (Engel et al., 1965, Melson et al., 1976, Hofmann, 1988, Sun and McDonough, 1989, Hofmann, 2003, Arevalo and McDonough, 2010). A N-MORBs common feature is their canonical trace element ratios, such as Ce/Pb, Nb/Ta, Nb/U, Th/U, Zr/Hf or Ba/Rb, which remain relatively constant during partial melting and therefore represent the ratio values of the source. This is due to the very close bulk D of both elements of a ratio, which are removed from the source in about equal amount early after few per-cents of partial melting (Hofmann et al., 1986, Hofmann, 1988, Jochum et al., 1983, 1986, 1991, Salters and Stracke, 2004, Workman and Hart, 2005). This results in typical N-MORB trace element anomalies in the extended trace element patterns normalised to the primitive mantle (hereafter marked with the subscript PM), such as slightly positive $Ta_{PM}$ anomalies compared to $Nb_{PM}$ or negative $Pb_{PM}$ anomalies compared to $Ce_{PM}$ (Figure 4.7), which are inherited from their depleted-mantle source.

As observed in the major element compositions, the ERRTI MORBs are overall very heterogeneous in their trace element distribution, varying from N-MORB to very enriched signatures in the extended trace element patterns (Figure 4.7). While nearly all samples have $Cs_{PM}$

to $Ta_{PM}$ higher than N-MORB, the other elements are more variable (Figure 4.7a). Similarly to N- and E-MORB defined by Gale et al. (2013), all samples have negative $Cs_{PM}$, $U_{PM}$, $Th_{PM}$ and $Pb_{PM}$ anomalies and a positive $Ta_{PM}$ anomaly, all varying from slight to strong anomalies (Figure 4.7a).

The negative $Sr_{PM}$ anomaly usually observed in MORB is not present in all the samples and on the contrary, some samples have a strong positive Sr anomaly with Sr/Sr* ($Sr/Sr^{*} = \frac{Sr}{\sqrt{Pr \times Nd}}$) up to 1.3 (Figure 4.7a).

Overall, the Rare Earth Element (REE) patterns vary from depleted to flat Light-REE (LREE) to steep patterns with highly enriched LREE, with $La/Sm_{PM}$ up to 3.6 (Figure 4.7b, 4.8). It is worth noting that the REE patterns are hereafter normalized to the CI chondritic composition of Barrat et al. (2012) and marked with the subscript N. Part of the samples have a steep slope between Middle-REEs and Heavy-REEs (HREE) compared to both N- and E-MORB references. MREE and HREE are highly variable in the ERRTI samples with, for example, $Lu_N$ (normalised to CI chondrite) varying from 9.3 to 37.3.

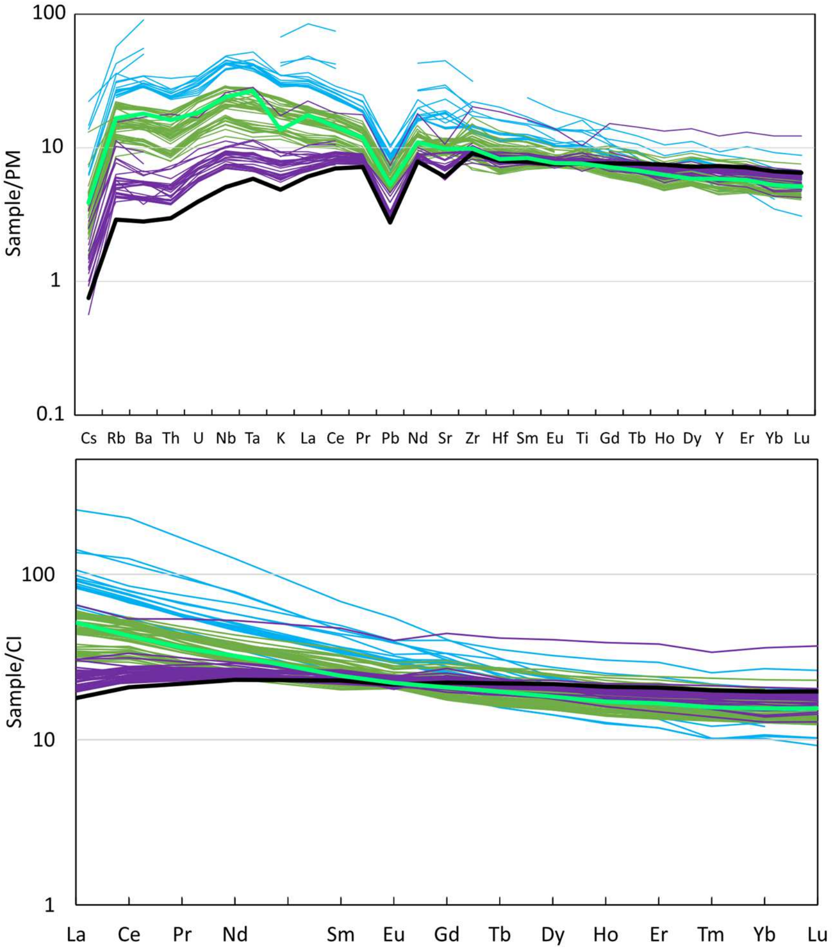

*Figure 4.7 - (a) Extended trace element patterns normalised to Primitive Mantle (PM, Sun and McDonough, 1989) and (b) REE normalised to CI chondrite (Barrat et al., 2012) of glasses from the ERRTI. Black and light green lines represent respectively N-MORB and E-MORB after Gale et al. (2013). Purple: N-MORB; green: E-MORB; blue: K-rich MORB. Incomplete patterns are from the first set of samples recovered by dredges and analysed at Lamont Doherty Earth Observatory (Cipriani, A.).*

As observed for the alkali distribution, trace element patterns reveal the presence of different compositional groups. Three compositional groups have been defined based on REE patterns, $La/Sm_{PM}$ (Primitive Mantle normalised ratio) and $K_2O$ content (Figures 4.4b, 4.7, 4.8). First **N-MORB** and **E-MORB** have been defined after Gale et al. (2013), E-MORB having $La/Sm_{PM}$ ratio higher than 1.5. Samples with marked positive $La_N$, $Eu_N$ and $Sr_{PM}$ anomalies are excluded from these groups. One sample has a flat REE pattern, as its $La/Sm_{PM}$ is lower than 1.5 and is consequently plotted together with the N-MORB group.

The group of samples with very high $K_2O$ contents (> 0.7 wt%) has a unique major and trace element composition, with strong enrichment in LREE (Figures 4.4, 4.5, 4.7 and 4.8), and is here defined as **"K-rich MORB" group**. The average REE pattern has a steeper slope with respect to the E-MORBs and appears not in continuity with the E-MORB LREE enrichment.

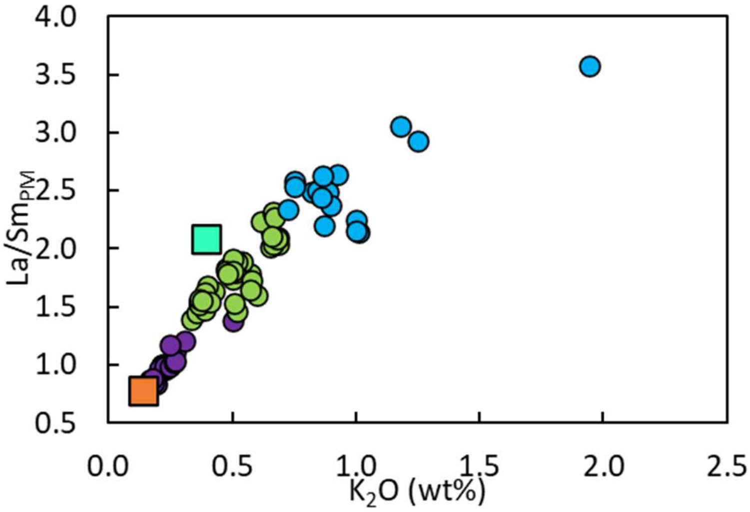

*Figure 4.8 - La/Sm$_{PM}$ normalised to Primitive Mantle (Sun and McDonough, 1989) vs $K_2O$ diagram. Three groups have been defined based on their La/Sm$_{PM}$ and $K_2O$ content: 1. Normal-MORB (N-MORB, violet solid circle): compositionally homogeneous N-MORB. 2. Enriched MORB (E-MORB, solid green circle) with La/Sm$_{PM}$ > 1.5 as defined by Gales et al (2013). 3. K-rich MORB, they have high $K_2O$ content > 0.7 wt% and very enriched LREE. Orange and green squares are N-MORB and E-MORB references respectively (Gale et al., 2013).*

The extended trace element patterns of the N-MORB group almost fully follow the N-MORB reference pattern (Figure 4.7a), one particularity being the slight enrichment in Cs$_{PM}$ to Ta$_{PM}$ elements toward signatures transitional between N- and E-MORBs. Similarly, the E-MORB group is coherent with the reference signature, with just few samples having positive Sr$_{PM}$ or Nb$_{PM}$ anomalies (Figure 4.7a). The K-rich MORBs are very enriched in all trace elements and plot beyond the E-MORB compositional boundary. While some samples are parallel to the E-MORB reference, others have a steeper slope (Figure 4.7a).

The variability observed at the scale of the entire studied region is also visible at local scale, within a single dive/dredge (Figure 4.9). While the samples from the dives SMA1977 and SMA1978, located along the central segment (Figure 4.2), have homogeneous N-MORB REE patterns, other locations have samples with heterogeneous REEs. Thus, within the same dive there are two populations of LREE enriched patterns (SMA1973, SMA1970, SMA1974). On the contrary, LREE enriched samples from the dive SMA1979 have homogeneous LREE and a high variability in HREE. One dredge, S1312, has samples with highly heterogeneous REE patterns varying from steep LREE enriched pattern to flat REE enriched pattern.

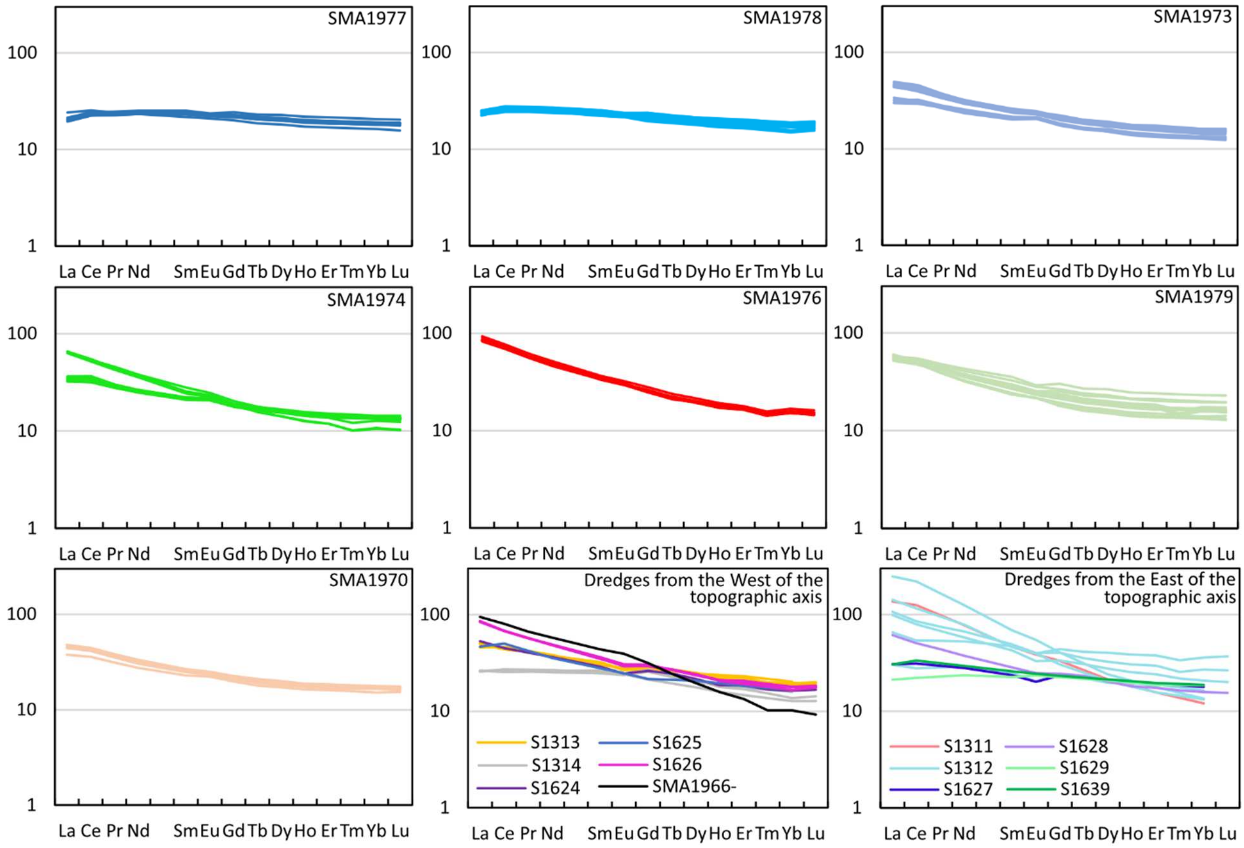

*Figure 4.9 – REE patterns normalised to CI chondrite of Barrat et al. (2012) of the glasses from the ERRTI grouped by dives/dredges from South to North along the ridge axis.*

## Discussion

### Evaluating the compositional effects of fractional crystallization at the ERRTI

Fractional crystallization assumes the instantaneous separation of a solid (crystal) fraction from a parental melt during cooling. This implies crystals in equilibrium only with the last drop of generated melt, effectively changing the composition of the melt as crystals form. The composition of the melt evolves following lines whose slope changes according to the fractionated mineral phases. These lines are defined as Liquid Line of Descent (LLD). The variation in the major element composition along a LLD assumes a single parental magma evolving during fractional crystallization. However, fractional crystallization is sensitive to a large number of parameters. Those with the strongest impact are the starting melt composition, which can be influenced by melt mixing or melt-rock reaction, pressure and oxidation state.

We check the effects of fractional crystallization on the ERRTI basaltic glasses compositional variability calculating LLDs with the Petrolog3 software (Danyushevsky and Plechov, 2011). Various initial melt compositions have been tested with varying pressure at constant oxidation state. Romanche basalts have been recognized to bear an important enrichment in water (Ligi et al., 2005, Le Voyer et al., 2015). Water content has a strong impact on the fractional crystallization hence LLDs with addition of water have also been calculated. All the parameters used for LLD models are summarized in supplementary table S4.4.

We first tested LLDs calculated from the primary N-MORB composition of Presnall and Hoover (1987) that is a “normal” primary melt representative of partial melting of a depleted mantle source and derived from the average composition of MORBs. We calculated the liquid-olivine (L-Ol), liquid-olivine-plagioclase (L-Ol-Pl) and liquid-olivine-plagioclase-clinopyroxene (L-Ol-Pl-Cpx) isobaric LLDs at 0.2 GPa (Figure 4.10 and supplementary figure S4.1, red line). The mineral-melt fractional crystallization model used for olivine, plagioclase and clinopyroxene is from Danyushevsky (2001). The original Petrolog3 parameters have been preserved for the initial oxidation state (calculated along a QFM buffer after Borisov and Shapkin, 1990), density (calculated after Lange and Carmichael, 1987), and viscosity (calculated after Bottinga and Weill, 1971).

The LLD of this primitive melt does not cover the variability observed in the ERRTI samples. In general, it has lower $SiO_2$, $Al_2O_3$ and much lower $Na_2O$ and $K_2O$ content than the majority of the samples (Figure 4.10 and supplementary figure S4.1). In the FeO-MgO diagram, the calculated LLD has much higher FeO for a given MgO content. This fractional crystallization model cannot even fit the N-MORB samples (Figure 4.10 and supplementary figure S4.1), the latter having higher $Al_2O_3$ and $Na_2O$ content and lower FeO for a given MgO.

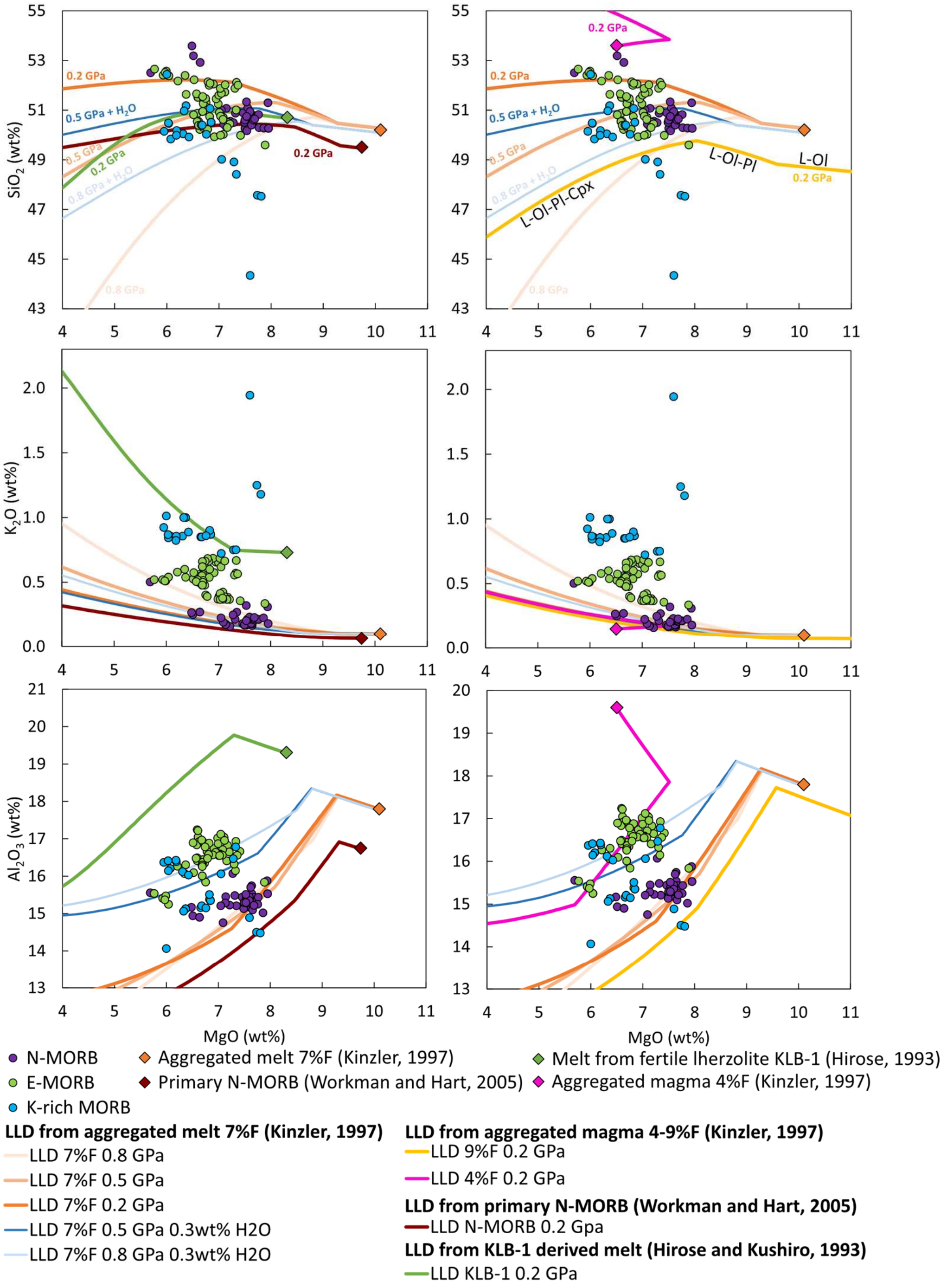

*Figure 4.10 - L-Ol, L-Ol-Pl, L-Ol-Pl-Cpx liquid lines of descent calculated with Petrolog3 using Danyushevsky (2001) model for the calculation of Ol, Pl and Cpx fractionation (see text for details). The first model (left) compares calculated LLDs from various primary liquid: primary N-MORB (Presnall and Hoover (1987) (red line), aggregated melt from a fertile spinel lherzolite (orange and blue lines) (Kinzler, 1997) and a fertile spinel lherzolite (KLB-1) derived melt (Hirose and Kushiro, 1993). The second model (right) compare calculated LLDs from melt derived from the same source but at various degree of melting: near-fractional aggregate melts at average 4% F (pink line), 7% F (orange and blue lines) and 9% F (yellow line) of a fertile spinel-peridotite (Kinzler, 1997). Other major element diagrams are shown in supplementary figure S4.1.*

We further calculated LLDs from primary melts representative of partial melting of a fertile mantle source with mineral mode of 53% olivine, 27% orthopyroxene, 17% clinopyroxene, 3% spinel (Kinzler, 1997). We first tested the melt produced by an average extent of melting (F) of 7%, 1.15 GPa of pressure and temperature varying from 1340°C to 1064°C (experimental data from Kinzler, 1997). From this primary melt, LLDs have been calculated isobarically at three different pressures: 0.2 GPa, 0.5 GPa and 0.8 GPa (Figure 4.10 and supplementary figure S4.1, orange lines). Hydrous LLDs (blue lines in Figure 4.10 and supplementary figure S4.1) have been calculated at 0.5 GPa and 0.8 GPa with addition of 0.3 wt% $H_2O$ (average $H_2O$ content observed in this group, Ligi et al., 2005). These LLDs, at various pressure values and especially with the addition of water, cover most of the variability observed for $SiO_2$, $TiO_2$, CaO and $Al_2O_3$ but are not able to reproduce the low CaO and high $Na_2O$ scatter and in particular the very high $K_2O$ and very low $SiO_2$ and FeO samples (Figure 4.10 and supplementary figure S4.1). However, they reasonably fit the N-MORB group, except for $Na_2O$, which is overestimated (Figure 4.10 and supplementary figure S4.1).

We further tested two primitive melts derived by higher and lower degrees of melting (F= 9% and F=4%, Kinzler, 1997) of the same fertile peridotitic source (Kinzler, 1997). For the 9% F melt, the average pressure of melting is 1.5 GPa and the temperature varies from 1420°C to 1070°C. For the 4% F melt, the average P is 0.8 GPa and T varies from 1221°C to 1056°C (experimental data from Kinzler, 1997). The only LLDs displayed here have been calculated at 0.2 GPa for each primary melt with the same parameters as previously described (Figures 4.10 and supplementary figure S4.1). For the 9% F melt, the calculated LLD are lower for $SiO_2$, $Na_2O$ and $Al_2O_3$ and higher for $TiO_2$, CaO and FeO than the previously calculated LLDs (Figures 4.10 and supplementary figure S4.1) whereas the opposite is true for the 4% F melt. LLDs from various degrees of melting from this source followed by fractional crystallization of Ol-Pl-Cpx bracket the dispersion in the ERRTI major element compositions, except for the high $K_2O$, very low $SiO_2$ and high $TiO_2$ contents.

Overall, primitive melts resulting by variable degrees of melting of a fertile mantle source fit and bracket the observed variability for the N-MORB group (7%-9% F, Figure 4.10 and supplementary figure S4.1) and the E-MORB group (4%-7% F, Figure 4.10 and supplementary figure S4.1), except for the high $K_2O$ E-MORB group.

We finally tested a second fertile melt derived from partial melting of a fertile spinel lherzolite KLB-1 at 1.5 GPa and 1300°C (Hirose and Kushiro, 1993). The mineral abundance of the source is 58% olivine, 25% orthopyroxene, 15% clinopyroxene and 2% spinel. L-Ol, L-Ol-Pl, L-Ol-Pl-Cpx LLDs have been calculated isobarically at 0.2 GPa, using the same parameters as previously described (Figures 4.10 and supplementary figure S4.1, green line).

This calculated LLD plots very close to the ERRTI samples for $SiO_2$ and $TiO_2$. However, the calculated $K_2O$ is higher and the FeO is lower than most of the samples and fits only a few K-rich samples in the $K_2O$-MgO plot and a few samples with the lowest FeO content. For a given MgO the $Na_2O$ and $Al_2O_3$ are higher and CaO lower in the calculated LLD than in the ERRTI samples.

Compared to the N-MORB group, samples from the E-MORB group generally have lower $TiO_2$, FeO, CaO and higher $Al_2O_3$, $Na_2O$, $K_2O$ and $P_2O_5$ for a given MgO. These compositions could be obtained from various degrees of fertility, or various amount of mixing between depleted peridotite-derived melts and fertile lherzolite-derived melts (KLB-1), followed by Ol-Pl-Cpx fractional crystallisation (Figure 4.10 and supplementary figure S4.1).

Regardless the parameters used in the calculations, LLDs from one single primary liquid do not cover the variability observed in the ERRTI basaltic glasses (Figure 4.10 and supplementary figure S4.1), especially for samples with high $K_2O$, $Na_2O$ and $Al_2O_3$ and low $SiO_2$ content. This implies that the range of major element compositions observed in the ERRTI basaltic glasses are not related to fractional crystallization from one primary melt alone, but that other processes have to be considered to explain their variability. Nevertheless, the N-MORB major elements seem to follow fractional crystallization trends from a fertile mantle-derived primary magma at various degrees of melting (Figure 4.10 and supplementary figure S4.1).

### Evaluating the compositional effects of partial melting and mixing processes at the ERRTI

We test now whether partial melting processes and mixing between melts of various compositions can explain the compositional variability of the ERRTI basaltic glasses. Major and trace element compositions are very sensitive to partial melting. For example, partial melting of a Cpx-bearing source, as lherzolite, increases the $CaO/Al_2O_3$ ratio compared to a cpx-free source while decreasing the $Ti_2O$ content (Klein and Langmuir, 1987, Langmuir et al., 1992) resulting in a broad negative correlation in the $ti_8$ ($TiO_2$ oxide corrected to MgO 8%, see Figure 4.11 caption for details) vs. $CaO/Al_2O_3$ diagram (Figure 4.11) for MORBs from the MAR. Only the N-MORB group of the ERRTI basaltic glasses fits the negative trend. Thus, a lherzolitic mantle experiencing variable degrees of partial melting is a reasonable source for the N-MORB group of the ERRTI basaltic glasses.

This hypothesis can be tested modelling the trace element contents. Simple fractional non-modal melting calculations have been performed using the equation (Shaw, 1970, Zou, 1998):

$$\overline{C_L} = \frac{C_0}{F} \times \left[1 - \left(1 - \frac{FP}{D_0}\right)^{\frac{1}{P}}\right] \qquad [4.2]$$

in which

$\overline{C_L}$ is the concentration of a trace element in the extracted melt,

$C_0$ is the concentration of a trace element in the source before melting,

F is the fraction of extracted melt relative to the initial amount of source before melting,

P is the proportion in which the mineral contributes to the melt as $P = \sum Kd^{i/l}p^i$, with $p_i$ the melting mode of the phase *i*,

$D_0$ is the initial bulk solid/liquid distribution coefficient of the source as $D_0 = \sum Kd^{i/l}x_{0,i}$, with $x_{0,i}$ the initial mode of the phase *i* in the source.

The melt reactions used for a peridotitic source are from Hellebrand et al. (2002), partition coefficients from Brunelli et al. (2006), with F (in %) varying from 1 to 10. From the calculated melts, fractional crystallization effects have been calculated using the equation:

$$C_l = C_0 \times f^{D_0 - 1} \qquad [4.3]$$

in which

$C_l$ is the concentration of a trace element in the melt after fractional crystallization,

$C_0$ is the concentration of a trace element in the primary liquid before,

$f$ is the fraction of melt remaining after fractional crystallization.

We note here that these models are used to explain the slope and enrichment of REE. Absolute REE contents, degree of melting and proportion of melts are just indicative as they are relative to the source mode used in the calculations. All the parameters used for trace element models are summarized in supplementary table S4.5.

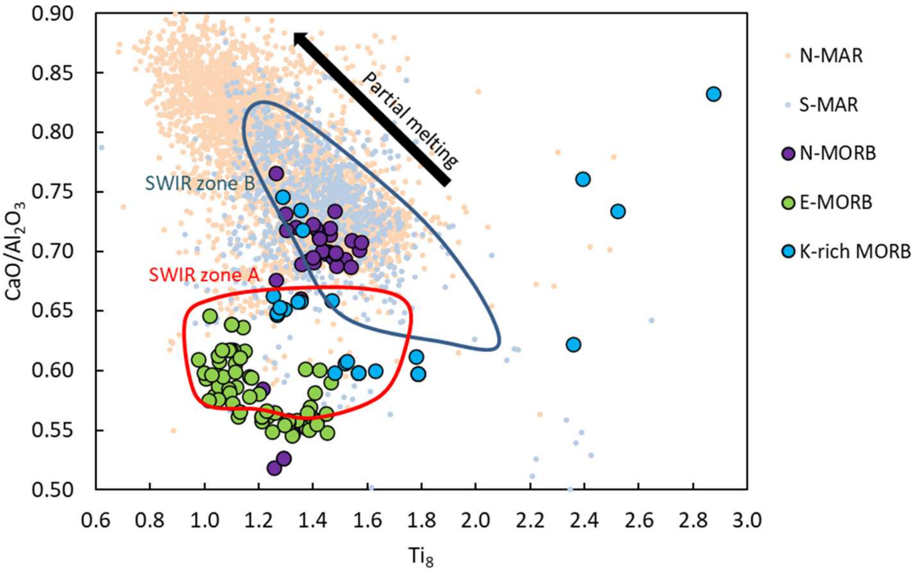

*Figure 4.11 - Ti$_8$ vs CaO/Al$_2$O$_3$ diagram. Southwest Indian Ridge (SWIR) fields are from Meyzen et al. (2003). Ti$_8$, the TiO$_2$ oxide corrected to MgO 8%, have been calculated after Langmuir et al. (1992) as* $Ti_8 = TiO_2 + 0.351 \times (MgO - 8)$.

We used two different depleted MORB mantle (DMM) compositions: the depleted-DMM and the enriched-DMM of Workman and Hart (2005). The mineral abundances used to model the D-DMM partial melting are from Workman and Hart. (2005) with 57% olivine, 28% orthopyroxene, 13% clinopyroxene and 2% spinel. The mineral abundances for the E-DMM are the same as the fertile peridotitic source from Kinzler (1997) with 53% olivine, 27% orthopyroxene, 17% clinopyroxene and 3% spinel. We plot in figure 4.12 only the calculated melts that fit the N-MORB ERRTI.

For the D-DMM source, an aggregated melt derived from 4% total partial melting, 2% F in the garnet stability field and 2% F in the spinel stability field, can reproduce the shape observed in the N-MORB group REE pattern (Figure 4.12, red pattern). This melt, corrected from 25% to 40% fractional crystallization, produces REE patterns that cover the range of variability observed in the N-MORB ERRTI samples (Figure 4.12, pink patterns).

Similarly, for the E-DMM, 9% partial melting can reproduce the shape of the N-MORB patterns (Figure 4.12, brown pattern). Here, partial melting have been calculated at 2% F in the garnet stability field and 7% F in the spinel stability field. This melt, corrected from 20% to 35% fractional crystallization, produces REE patterns that cover the range of variability observed in the N-MORB ERRTI samples (Figure 4.12, pink patterns).

The one sample with a flat strongly enriched REE pattern can either be explained by higher degree of fractional crystallization from the same D-DMM or E-DMM primary liquid, or by involvement of another source.

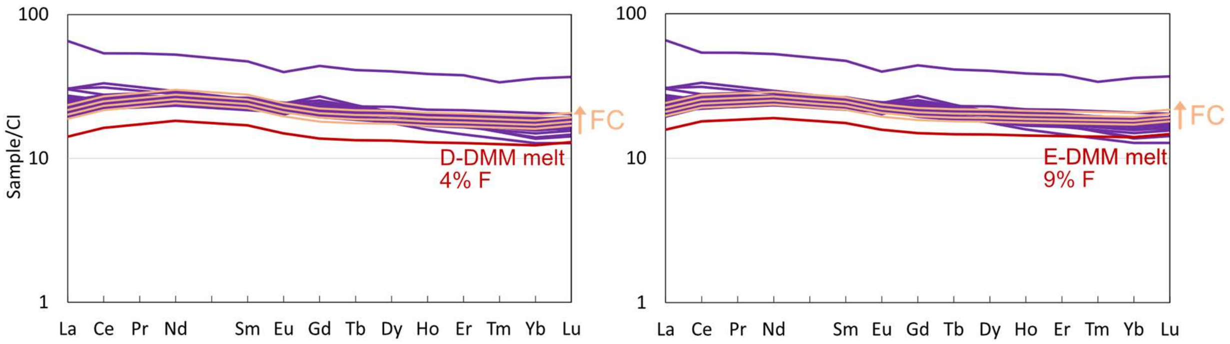

*Figure 4.12 – Rare Earth elements abundances normalized to CI Chondrite of ERRTI N-MORB basaltic glasses and calculated melts after partial melting of D-DMM and E-DMM sources of Workman and Hart (2005). CI chondrite is from Barrat et al. (2012). (a) Aggregated melt derived from fractional non-modal melting from D-DMM melted at 4% F, 2% in the garnet stability field and 2% in the spinel stability field (red line). From this melt, fractional crystallization patterns have been calculated (pink lines) from 25% to 40% fractional crystallization at a step interval of 5%. (b) Aggregated melt derived from fractional non-modal melting from E-DMM melted at 9% F, 2% in the garnet stability field and 7% in the spinel stability field (red line). From this melt, fractional crystallization patterns have been calculated (pink lines) from 20% to 35% fractional crystallization at a step interval of 5%.*

To explain the trace element enrichment of the E-MORB ERRTI basaltic glasses we need to model different sources. E-MORB signatures have been ascribed to various processes: (1) very low degree of melting of a peridotitic mantle, (2) a two-stage metasomatic enrichment (Donnelly et al., 2004), (3) melting of recycled oceanic material (Hofmann and White, 1982, Hémond et al., 2006, McKenzie et al., 2004).

As shown when discussing the LLDs, various low degree of melting of a peridotitic source, cover the major element variability of the E-MORBs, except for those with high $K_2O$ content. We therefore model the D-DMM and E-DMM sources (Workman and Hart, 2005) using low degrees of partial melting followed by low-pressure fractionation correction. Even at very low degree, partial melting of the D-DMM cannot reproduce the enrichment observed in the E-MORB ERRTI group (Figure 4.13, red line).

For the E-DMM source, a total 3% F (2% F in the garnet stability field and 1% F in the spinel stability field) can reproduce the shape of the E-MORB (Figure 4.13, red line). This melt, corrected for 20% to 35% fractional crystallization, produces REE patterns that cover part of the range of variability observed in the E-MORB ERRTI samples (Figure 4.13, orange lines), except for few elements (Eu, La).

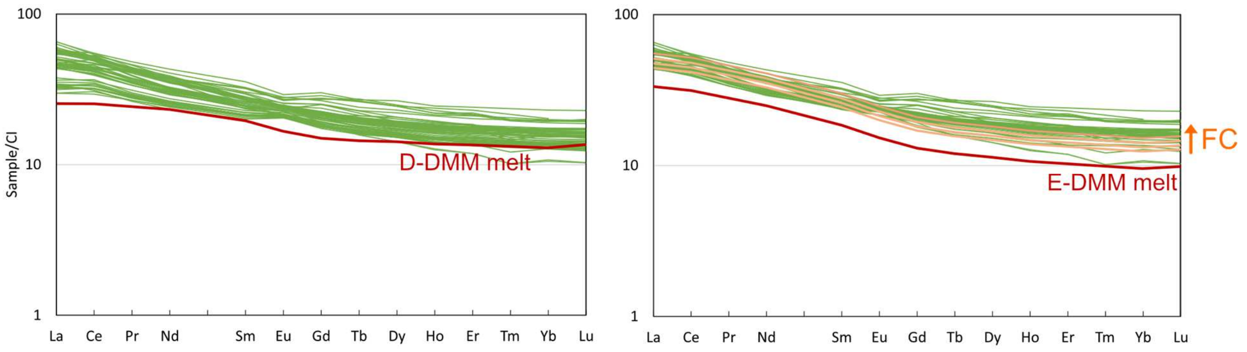

*Figure 4.13 – Fractional non-modal melting modelling followed by fractional crystallisation from partial melting of D-DMM and E-DMM. Melting reaction are from Hellebrand et al. (2002), partition coefficients are from Brunelli et al. (2006). (a) E-MORBS compared to partial melting modelling from D-DMM, mineral mode are from Hellebrand et al. (2002). The red line represents aggregated melt from fractional non-modal melting calculation at 2% F, with 1% F in the garnet stability field and 1% F in the spinel stability field. (b) E-MORBs with the highest LREE enrichment compared to calculated aggregated melt derived from fractional non-modal melting calculation from the E-DMM (red line) at 3% F, 2% in the garnet stability field and 1% in the spinel stability field. Mineral mode are from Kinzler (1997). From this melt, fractional crystallization patterns have been calculated (orange lines) from 25% to 40% fractional crystallization at a step interval of 5%.*

The possible involvement of recycled oceanic material to produce ERRTI E-MORBs is tested by calculating major and trace elements compositions derived by simple binary mixing between melts from partial melting of depleted mantle material and enriched lithologies (Figures 4.14 and 4.15). Given that the depleted peridotitic source from Kinzler (1997) at 7% average melting was the one producing the closest melts to the ERRTI depleted samples in terms of major elements (Figure 4.10), we decided to use it as reference source for this model.

For the enriched lithology, we use a melt from partial melting of M5-40 Si-undersaturated pyroxenite, garnet websterite, at 2.5 GPa and 1375 °C (Lambart et al., 2013). Our primary liquid, corrected for low-pressure fractionation, is produced by mixing 25% of melt derived from the pyroxenitic source with 75% of the melt derived from the depleted-peridotite source (Kinzler, 1997). LLDs have been calculated at 0.2 GPa, 0.8 GPa and addition of 0.5 wt% $H_2O$ at 0.8 GPa (Figure 4.14 and supplementary figure S4.2). The $SiO_2$, $Na_2O$ and $K_2O$ variability of the ERRTI E-MORB samples is bracketed by the LLDs calculated from this mixed source and the LLDs from the melt derived from the depleted peridotite. However, for a given MgO the LLDs are too high in FeO and CaO, and too low in $Al_2O_3$ compared to the E-MORB samples.

Mixing with a melt from the silica-enriched pyroxenite (G2K, Pertermann et al., 2003) has also been tested, but does not cover the variability observed in the E-MORB ERRTI group (Figure 4.14 and supplementary figure S4.2).

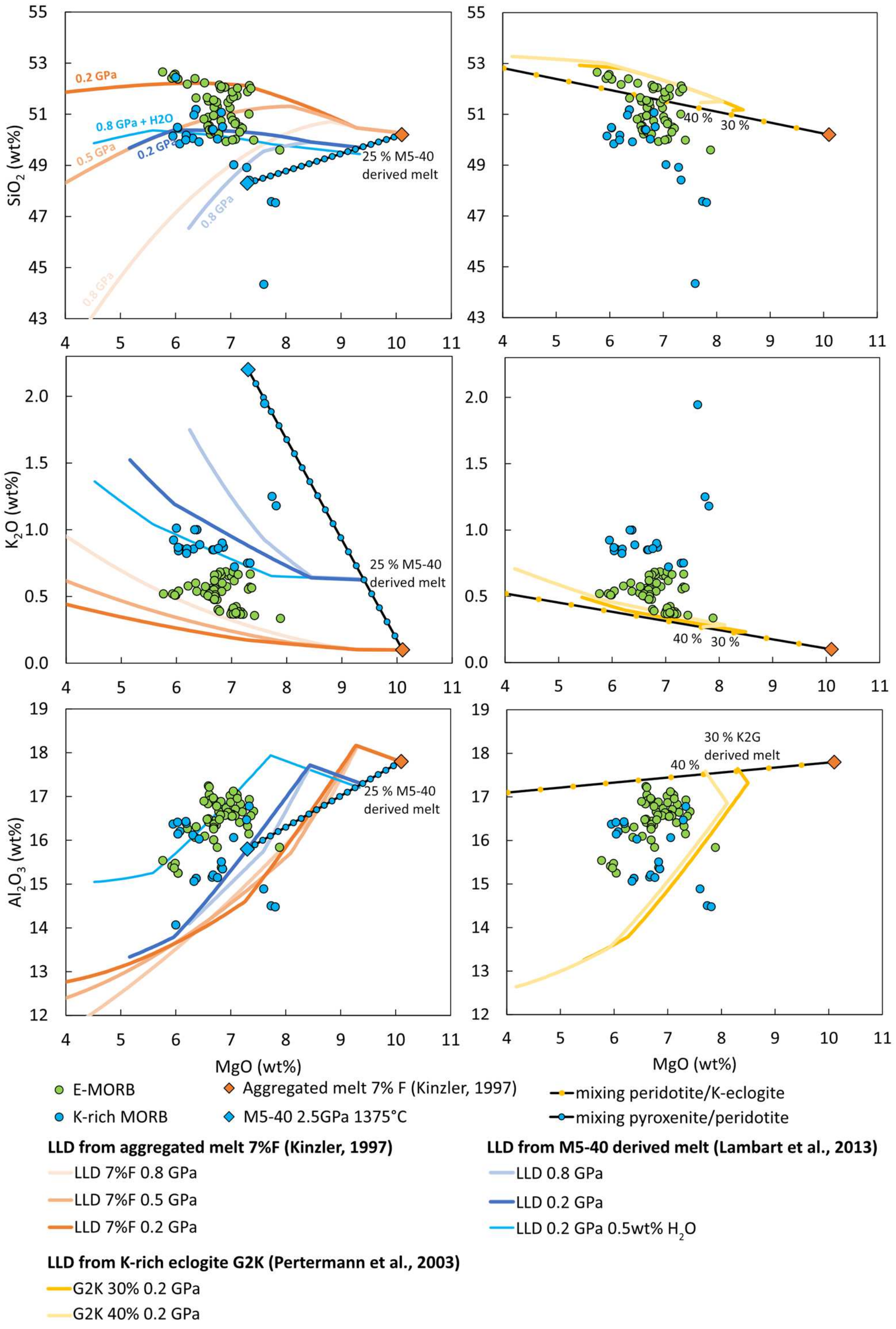

*Figure 4.14 – Calculated L-Ol, L-Ol-Pl, L-Ol-Pl-Cpx liquid lines of descent from mixing between aggregated melt at average melting of 7% of a depleted peridotite (data source from Kinzler, 1997) with various sources: Left: Experimental melt from partial melting of M5-40 Si-undersaturated pyroxenite at 2.5 GPa 1375 °C (Lambart et al., 2013). Right: Experimental melt from partial melting of K-rich eclogite (G2K) at 2 GPa and 1325°C (Pertermann et al., 2003). Other major element diagrams are shown in supplementary figure S4.2.*

Regardless of the different sources, $Al_2O_3$ is generally lower and FeO higher in the calculated LLDs than in the E-MORBs ERRTI glasses for a given MgO (Figures 4.10, 4.14). A possible explanation is linked to the presence of water, which delays plagioclase saturation (Figure 4.14 and supplementary figure S4.2), and thus results in higher $Al_2O_3$ and lower FeO content in E-MORBs (Michael and Chase, 1987). This process could explain the shift toward lower FeO in the AFM diagram (Figure 4.5a). A variable amount of water in the primary melts can thus also be at the origin of the very low $CaO/Al_2O_3$ ratio observed for the E-MORB ERRTI group (Figure 4.11). Another explanation for this compositional fingerprint is related to melt-rock reaction, which increases the $Al_2O_3$ and MgO content of the melt while decreasing CaO and $SiO_2$ (Lissenberg and Dick, 2008).

To model the trace element composition, we use the altered MORB composition of Staudigel et al., (1996) as recycled oceanic material (Figure 4.15). Mineral modes are from the GV10 pyroxenite (Borghini et al., 2016) with 61% clinopyroxene, 18% garnet and 21% orthopyroxene in the garnet facies. The melt reaction is from Borghini et al. (2017).

The calculated pyroxenite-derived aggregated melts have been mixed with calculated aggregated melt from the D-DMM (Workman and Hart, 2005) (Figure 4.15). The D-DMM has been partially melted at 2% F, 1% F in the garnet stability field and 1% F in the spinel stability field. The pyroxenitic source has been partially melted at 7% F in the garnet stability field.

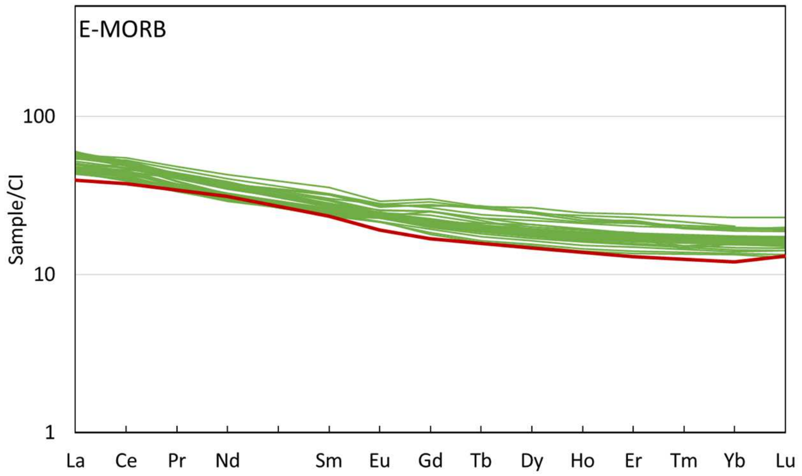

*Figure 4.15 – Mixing between fractional non modal aggregated melt from D-DMM (Workman and Hart, 2005) and pyroxenitic source (altered MORB data from Staudigel et al., 1996) to model the REE patterns observed in the E-MORB group. E-MORBs samples with the higher LREE enrichment. The red line represents 80% aggregated melt from 2% F of the D-DMM (1%F in the*

*garnet stability field and 1% F in the spinel stability field) mixed with 20% aggregated melt from 7% melting of the pyroxenitic source in the garnet stability field.*

K-rich MORBs have already been described along MOR, especially at ultra-slow spreading ridges as the South-West Indian Ridge (SWIR; Standish et al., 2008) and the Gakkel ridge/Lena Trough (Nauret et al., 2011). This signature has been interpreted as evidence of a pyroxenitic lithology in the SWIR mantle source (Standish et al., 2008) or derived from a lithospheric mantle source bearing a K-rich mineral, as amphibole, phlogopite or phengite, at the Lena Trough and Gakkel ridge (Nauret et al., 2011, Richter et al., 2020). Both hypotheses are tested hereafter.

The K-rich ERRTI MORB group has very high Sm/Yb for low Lu/Hf, respectively up to 3.9 and 0.05, compared to the other samples (Figure 4.16). These ratios together with the strong depletion observed in HREE compared to MREE (Figure 4.7) suggest the presence of garnet as a residual phase in the mantle source (Salters and Hart, 1989, Hirschmann and Stolper, 1996, Chauvel and Blichert-Toft, 2001).

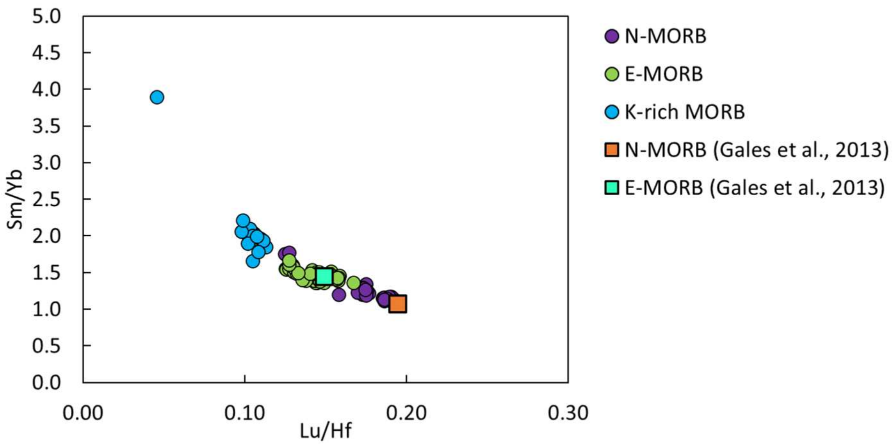

*Figure 4.16 – Correlation between Sm/Yb and Lu/Hf. The K-rich MORBs have very high Sm/Yb for very low Lu/Hf, evidence for a strong garnet signature.*

The very low silica content in few samples from the K-rich group suggests the involvement of silica-undersaturated pyroxenite. This is supported by their distribution in the Fo-CaTs-$SiO_2$ diagram (Figure 4.17). This diagram does not allow discriminating whether the samples derive from melting of a N-MORB mantle or a silica-enriched pyroxenite, because the two areas are superimposed. However, it allows distinguishing within silica-undersaturated pyroxenite melt signatures. While most of the ERRTI samples are grouped close to the N-MORB area, three outliers from the K-rich group plot in, or toward, the silica-depleted region. Lambart et al. (2013) have shown that the separation between silica-enriched (SE) pyroxenite and silica-depleted (SD) pyroxenite is observable only at high pressure (> 2 GPa), because at this pressure the thermal divide, represented by CaTs-En line, is effective. Thus, this would suggest involvement, in the source of the K-rich ERRTI MORB, of SD pyroxenite partially melted at pressure higher than 2 GPa.

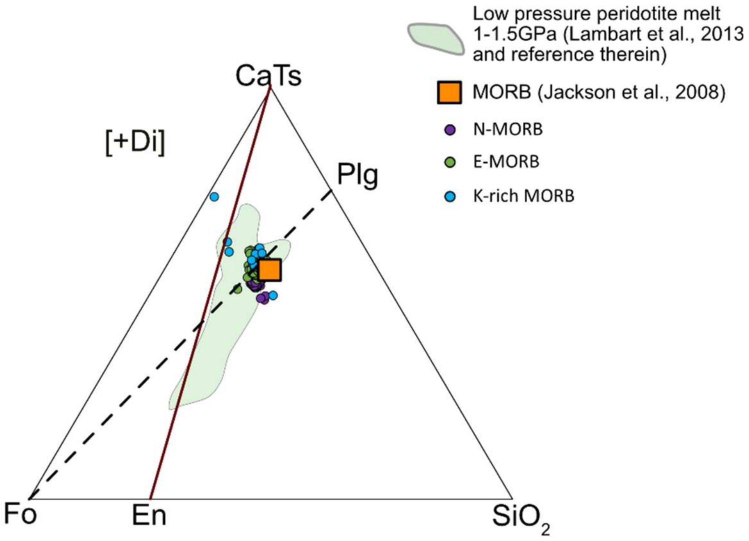

*Figure 4.17 - Fo-CaTs-$SiO_2$ diagram calculated after O'Hara (1972). Pyroxenite melts are from Lambart et al. (2013); MORB area is from Jackson and Dasgupta (2008).*

We first note that LLDs starting from a melt derived from mixing between an experimental melt from partial melting of M5-40 SD pyroxenite (Lambart et al., 2013) and a depleted peridotitic source (Kinzler, 1997), previously calculated to cover the E-MORB ERRTI group (Figure 4.14 and supplementary figure S4.2), account for the chemical variability of a few K-rich samples, especially with addition of water. However, they do not fit the lower $SiO_2$, $Na_2O$ and higher $TiO_2$, CaO compositions (Figure 4.14 and supplementary figure S4.2). In addition, the high $CaO/Al_2O_3$ ratios observed for few samples in the K-rich group could suggest the involvement of garnet-clinopyroxenite whether by melt mixing or melt-rock interaction (Kamenetsky et al., 1998). Thus, we use the experimental melt from partial melting of 77SL-582 SD high-Mg garnet-clinopyroxenite mantle nodule at 2.5 GPa and 1430 °C (Keshav et al., 2004) and calculate LLDs at 0.2 GPa, 0.5 GPa and 0.8 GPa and with addition of 1 wt% $H_2O$ at 0.8 GPa (average $H_2O$ content measured in this group, Ligi et al., 2005) (Figure 4.18 and supplementary figure S4.3). Mixing this melt with the depleted peridotitic source (Kinzler, 1997) derived melt can account for most of the variability observed in this group for all the major elements, except for the high $Na_2O$ glasses.

To fit the extremely enriched LREE patterns of some K-rich ERRTI samples, we used a subducted oceanic crust garnet pyroxenite (Donnelly et al., 2004) (Figure 4.19) more enriched in trace elements compared to the altered MORBs (Figure 4.15). The melting reaction and mineral mode are the same as those of the pyroxenite source (Borghini et al., 2016, 2017). Partition coefficient are from Pertermann et al. (2002, 2004).

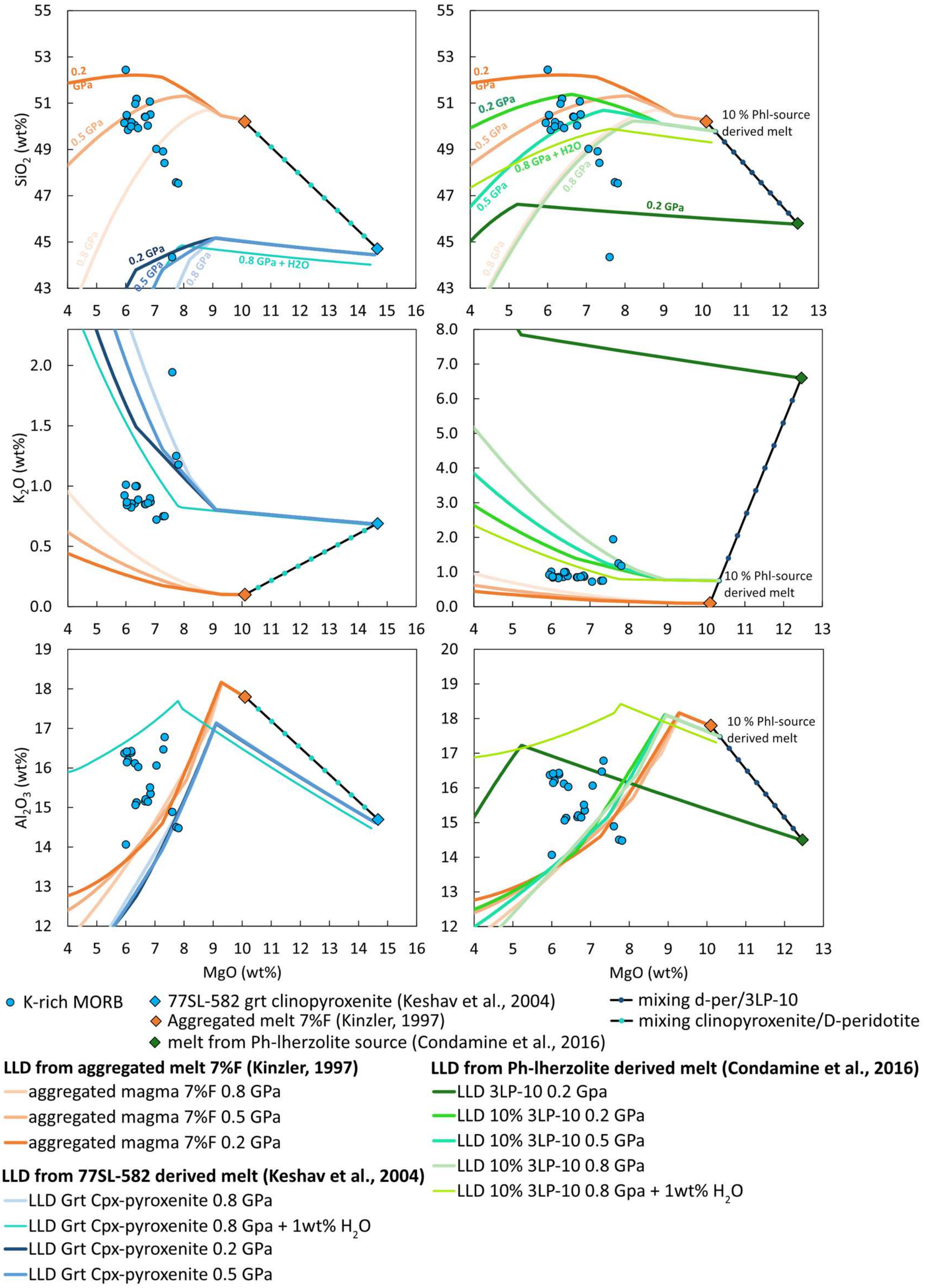

*Figure 4.18 - Calculated L-Ol, L-Ol-Pl, L-Ol-Pl-Cpx LLD from mixing between aggregated melt at average melting of 7% of a depleted peridotite (data source from Kinzler, 1997) with various source: Left: Experimental melt from partial melting of M5-40 Si-undersaturated pyroxenite at 2.5 GPa 1375 °C (Lambart et al., 2013). Right: Experimental melt from partial melting of garnet clinopyroxenite 77SL-582 at 2.5 GPa and 1430°C (Keshav et al., 2004). (c) Experimental melt from partial melting of phlogopite-bearing lherzolite partially melted at 1250°C (Condamine et al., 2016). Other major element diagrams are shown in supplementary figure S4.3.*

The most LREE-enriched samples can be reproduced by mixing melts derived from very low degree of partial melting of an enriched pyroxenite (2% F in the garnet stability field) mixed with melts derived from very low degree of partial melting of D-DMM across the garnet to spinel transition (2% F, 1% F in the garnet stability field and 1% F in the spinel stability field) (Figure 4.19). However, the steepest measured patterns have lower HREE and higher LREE that cannot be reproduced by this model.

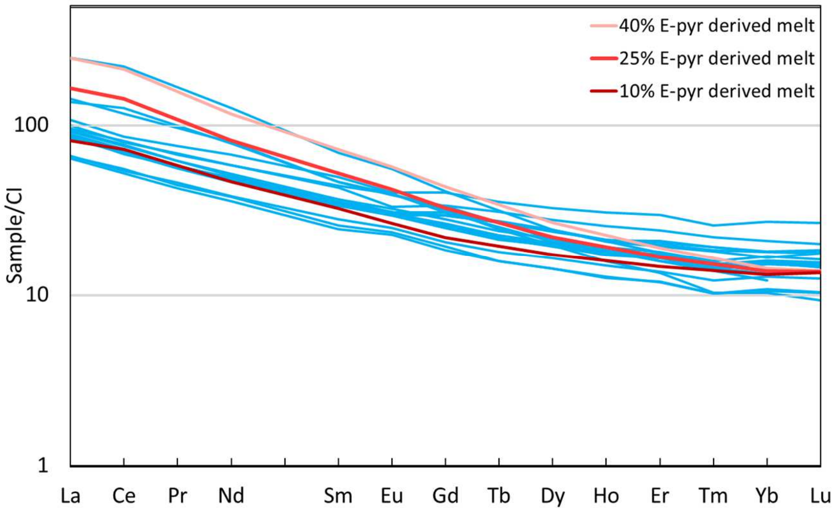

*Figure 4.19 – REE non-modal fractional partial melting calculations from enriched pyroxenite source (subducted oceanic crust garnet pyroxenite data from Donnelly et al., 2004) compared to the K-rich MORBs. Red lines are calculated fractional non modal aggregated melt from the enriched pyroxenite melted at 2% F in the garnet stability field mixed at variable degree with aggregated melt from the D-DMM melted at 2% F, 1% F in the garnet stability field and 1% F in the spinel stability field.*

The K-rich MORB group has generally a low CaO and FeO and high $K_2O$ and $Na_2O$ content. This signature can result from partial melting of amphibole or phlogopite and clinopyroxene (Frey and Green, 1974; Condamine et al., 2016). Thus, we tested a phlogopite-bearing lherzolite partially melted at 1250°C (Condamine et al., 2016) mixed to the depleted-peridotite melt (Kinzler, 1997). LLDs have then be calculated from the phlogopite lherzolite at 0.2 GPa and from a mixing of 10% phlogopite lherzolite melt and 90% depleted peridotitic melt at 0.2 GPa, 0.5 GPa, 0.8 GPa and 0.8 Gpa with addition of 1 wt% $H_2O$ (Figure 4.18 and supplementary figure S4.3). These LLDs bracket well the majority of the K-rich MORBs, except for the very low $SiO_2$, high CaO sample. However, addition of water appears necessary.

In the same way, fractional non-modal aggregated melts have been calculated from a phlogopite-bearing lherzolite source (Grégoire et al., 2002). The mineral abundance is from Grégoire et al. (2002), melting reaction in the spinel stability field from Condamine et al. (2014) and the partition coefficients are from Condamine et al. (2022). To reproduce the patterns of the K-rich MORBs, 60%-80% aggregated melt from D-DMM melted at about 2% F, 1% F in the garnet stability field and 1% F in the spinel stability field, has been mixed with an aggregated melt from 4% F in the spinel stability field of the phlogopite-bearing lherzolite (Figure 4.20).

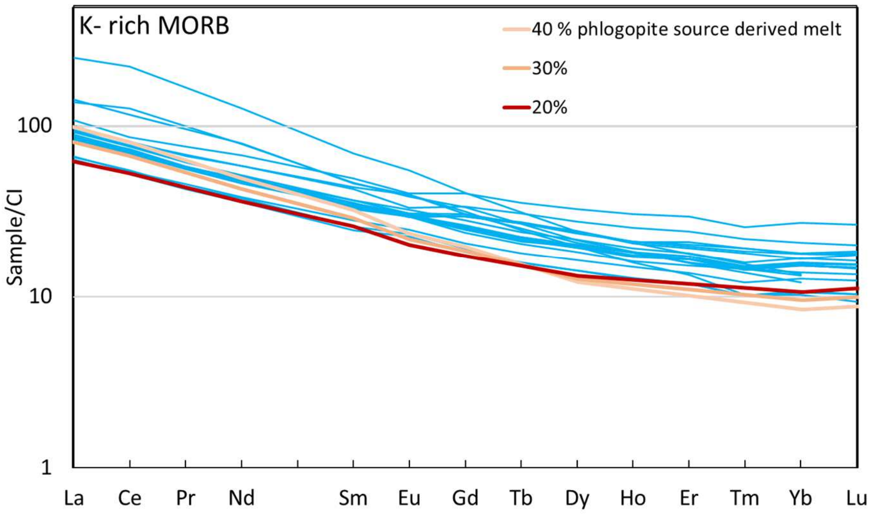

*Figure 4.20 - REE non-modal fractional partial melting calculations from mixing between phlogopite-bearing lherzolite (Grégoire et al., 2002) and D-DMM (Workman and Hart, 2005) compared to the K-rich MORBs. The red lines represent aggregated melt from 2% F of the D-DMM (1%F in the garnet stability field and 1% F in the spinel stability field) mixed with aggregated melt from 4% F of the phlogopite-bearing lherzolite in the spinel stability field.*

At Lena Trough and Gakkel Ridge, the K-rich basalts have been proposed to result from phlogopite-bearing source possibly deriving by integration of delaminated Sub-Continental Lithospheric Mantle (SCLM) in the source (Goldstein et al., 2008, Nauret et al., 2011) or from phlogopite- and/or phengite-bearing peridotite originated from metasomatism in a subduction environment (Richter et al., 2020). Each scenario seems plausible, but while phengite is stable in subduction environment (Schmidt et al., 2004), it is not under MOR conditions (Figure 4.21).

Two processes can explain to presence of phlogopite at MOR: (1) a primary phlogopite-bearing lithology within the upwelling mantle; (2) crystallization of secondary phlogopite due to metasomatism of the mantle by a K-rich lithology. To test the stability of phlogopite at the ERRTI condition, we plot the local oceanic geotherms along with the phlogopite stability field (Condamine et al., 2016, and references therein) (Figure 4.21). Local geotherms have been calculated based on the thin plate 3D flow model of Ligi et al. (2011) at variable distance from the ERRTI along the ridge axis, i.e., 10, 20, 30 km and at the centre of the ridge segment (not influenced by the cold edge effect).

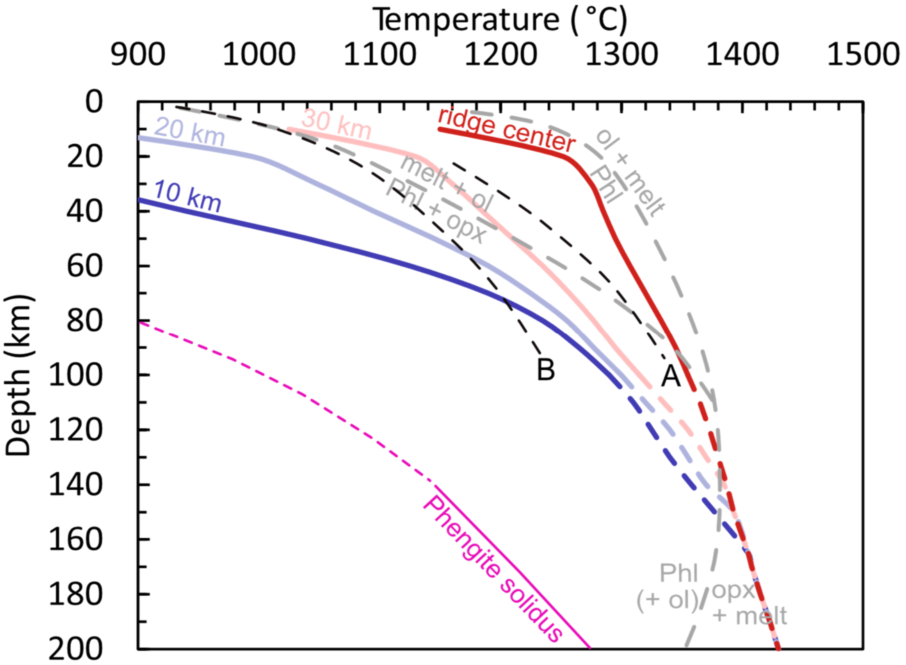

*Figure 4.21 - Phlogopite stability fields compared to oceanic geotherms. Thin dashed lines represents the phlogopite breakdown after Condamine et al. (2016) and references therein: grey lines are the maximum stability of pure phlogopite; black lines are the breakdown curve of natural (A) F-bearing phlogopite and (B) F-free phlogopite in a peridotitic assemblage. Red and blue lines represent geotherms at different distance from the ERRTI after Ligi et al. (2011) model. After 100 km depth, the ERRTI geotherms have been extrapolated to reach the oceanic geotherm. Fluid absent phengite solidus after Schmidt et al. (2004).*

At low pressure, phlogopite (+opx) appears stable in a 30 km region away from the fracture zone. Phl breakdown (grey and black dashed curves in figure 4.21) occurs at variable distance depending on the assumed stability model (Condamine et al., 2016, A and B in figure 4.21). At depth, however, all geotherms converge to the normal mantle temperature because of the limitation of the cold edge effect to the lithospheric thickness. This makes phlogopite always unstable at high depth along a normal oceanic geotherm (Figure 4.21), and hence proving wrong assumption (1).

However, the oceanic geotherm plots at the limit of the phlogopite stability field making possible crystallization of phlogopite due to sub-ridge metasomatism (Figure 4.21). In fact, K-bearing pyroxenites melting at depth may crystallize secondary Phl-bearing pyroxenite following the Opx+melt→Phl+Ol reaction (Yoder and Kushiro, 1969, Trønnes, 2002) (Figure 4.21) in a process similar to the formation of the secondary pyroxenites postulated by Sobolev et al. (2005) for the Hawaii mantle plume.

To summarise, the compositional dispersion in the ERRTI samples cannot be explained only by various degrees of fractional crystallization (Figures 4.10) and degrees of melting (Figure 4.10) from a single primary source, but it is due to the contribution of different lithologies. The figure 4.22 summarizes the main trace element partial melting models calculated here. Thus, the N-MORBs can originate from various degree of melting from a fertile peridotitic source (Figure 4.10,4.22). The same source, at lower degree of melting, could explain most of the compositions observed in the E-MORBs. However, it does not fit the $K_2O$ content of some samples from this group, and it needs extremely low degree of melting to reproduce the REE patterns (Figures 4.10, 4.13).

A more likely source for the E-MORBs would be oceanic recycled material, altered MORBs, partially molten together with the surrounding mantle (Figures 4.14, 4.15, 4.21). This source can also reproduce the sample composition with the lowest LREE enrichment from the K-rich group (Figures 4.14, 4.21) but not those with the highest LREE enrichment (Figure 4.22).

The extremely LREE enriched samples patterns can be reproduced by either a more enriched pyroxenitic source (Figure 4.19), and/or by involvement of phlogopite in the source (Figure 4.20). However, to reach the most LREE enriched pattern, the enriched pyroxenite source has to partially melt in the garnet stability field (Figure 4.19).

These models evidence the presence of a composite mantle at ERRTI, with peridotitic-type and pyroxenitic-type lithologies. Thus, all the E-MORBs and K-rich MORBs studied here possibly result from mixing of variable amounts of melts derived by these two lithologies, at least. In order to reproduce the E-MORBs and K-rich MORBs compositions, partial melting degree of the pyroxenite component is required to be higher than that of the peridotitic component. This observation is in line with model prediction of partial melting of composite peridotite/pyroxenite mantle suggesting partial melting of the low-solidus lithology (pyroxenite) being enhanced by heat diffusion from the high solidus host (peridotite), (Sleep, 1984, Hirschmann and Stolper, 1996, Phipps Morgan, 2001, Brunelli et al., 2018).

Conversely, mixing relationships require small amounts of pyroxenite-derived melts to be mixed with large amounts of peridotite-derived melts in order to fit the observed compositions (< 35% of melt from the pyroxenite). This points to pyroxenite representing a minor component dispersed into the peridotitic source.

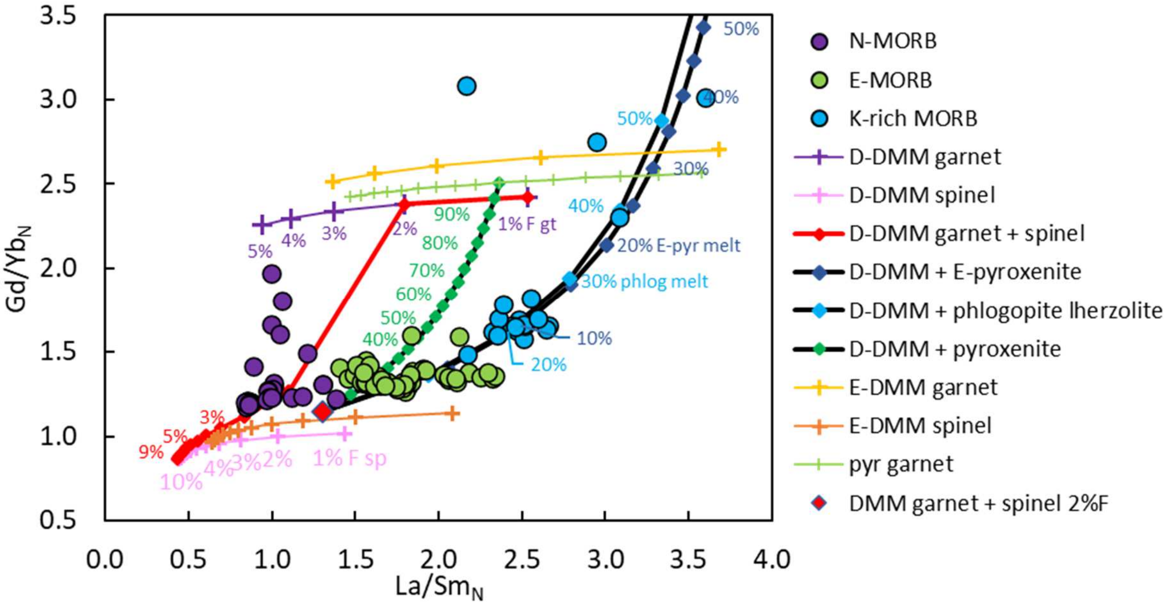

*Figure 4.22 – Comparison of the different trace element melting models calculated. Purple and pink lines are respectively aggregated melt calculated from fractional non-modal melting of D-DMM (Workman and Hart 2005) in the garnet and the spinel stability field, respectively. The red line represents an aggregated melt from partial melting in the garnet stability field (3% F) and spinel stability field. Orange and yellow lines are respectively melting of E-DMM (Workman and Hart, 2005) in the garnet and the spinel stability field. The thin green line represents aggregated fractional melting in the garnet stability field from the pyroxenite (altered MORB source from Staudigel et al., 1996). The thick black line with green diamonds represents mixing between aggregated melt derived from D-DMM fractional non-modal melting and aggregated melt derived from pyroxenite fractional non-modal melting (altered MORB source from Staudigel et al., 1996). The thin dark blue line represents aggregated fractional melting from enriched pyroxenite (subducted oceanic crust garnet pyroxenite source from Donnelly et al., 2004) in the garnets stability field. The thick black line with blue diamond symbols represents mixing between D-DMM derived aggregated fractional melting and enriched pyroxenite-derived aggregated fractional melting (subducted oceanic crust garnet pyroxenite source from Donnelly et al., 2004). The thick black line with light blue diamond symbols represents mixing between aggregated melt from 2%*

*F of D-DMM and phlogopite bearing lherzolite derived aggregated melt (source data from Grégoire et al., 2002).*

## Evaluating the compositional effects of changes in mantle potential temperature at the ERRTI

To evaluate a potential link between the variability of melt compositions and the evolution of the mantle temperature at the ERRTI, we use the distance to the transform fault as a proxy of the mantle potential temperature and check for chemical changes. While all the previously identified MORB groups are present only closer to the transform fault, i.e., at colder mantle potential temperature, the N-MORB are the only compositions observed furthest away from the RTI in the well-developed ridge axis (Figures 4.2, 4.23). The major element composition varies from homogeneous compositions of about 3 wt% $Na_2O$, 0.2 wt% $K_2O$, 11 wt% CaO and 50 wt% $SiO_2$ in the central segment of the ridge axis, to highly heterogeneous compositions, from 2.68 wt% to 4.39 wt% $Na_2O$, 0.09 wt% to 1.95 wt% $K_2O$, 7.75 wt% to 12.4 wt% CaO and 44.35 wt% to 53.59 wt% $SiO_2$, at less than 50 km from the transform fault.

The trace element variability shows the same variability patterns from south to north, with homogeneous N-MORB REE signatures in the southern part, and highly heterogeneous REE signatures from N-MORB to highly enriched LREE closer to the transform fault (Figure 4.24).

Thus, after the major and trace element models, the samples with the lower degree of melting of the peridotite, i.e., higher $K_2O$, are the ones located where the mantle is possibly colder because closer to the transform fault. This decrease of the degree of melting is linked to an increase of the garnet signature and higher involvement of the pyroxenite. This suggests an efficient temperature control on the melting process involving lithologies with different solidus temperature. At the centre of the axis, where the mantle temperature is higher, all source lithologies are extensively melted, melts are pooled together, well mixed and erupted as homogeneous N-MORB material. In contrast, when the mantle temperature decreases, the low-solidus lithologies are preferentially molten, melt mixing does not take place and single melt components are kept separated with the preservation of chemical heterogeneities shown by a greater variability in their final composition.

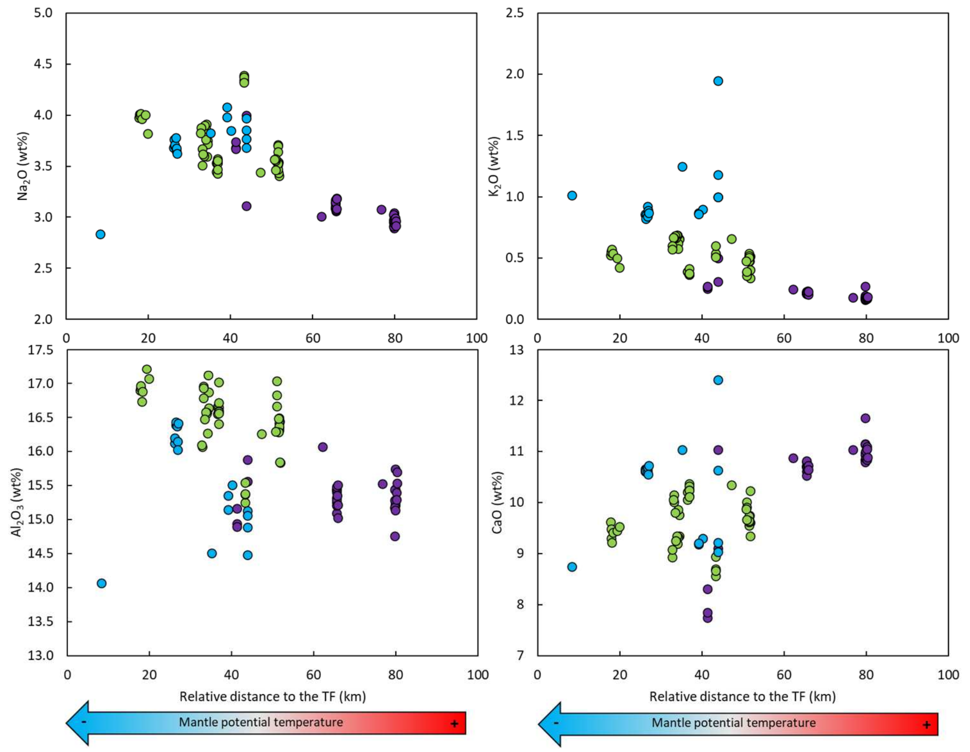

*Figure 4.23 - Major elements vs relative distance to the fracture zone, proxy of the mantle temperature.*

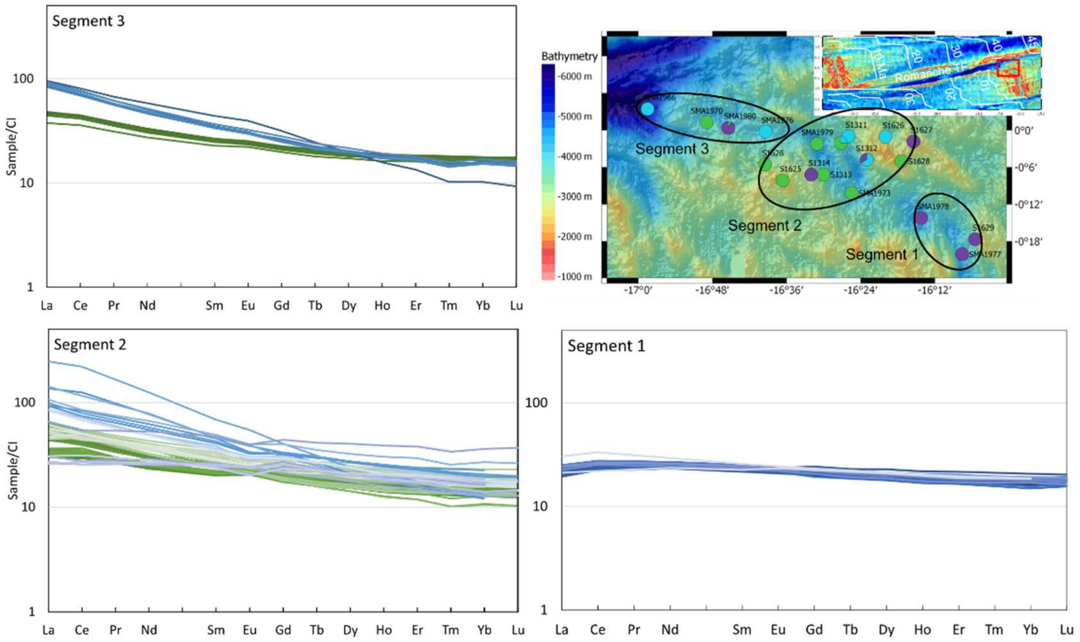

*Figure 4.24 – REE patterns grouped by location.*

## Conclusions

The extreme cold-edge effect of the set of the East-West mega-transform faults offsetting the Equatorial MAR reaches its maximum at the Eastern Romanche Ridge Transform Intersection (ERRTI).

Major and trace element compositions of MORBs recovered at the ERRTI present a high variability, with in particular, the presence of true alkaline samples, with high $Na_2O$ and $K_2O$ content and nepheline normative compositions.

Overall, the ERRTI MORBs have higher $Al_2O_3$, $Na_2O$ and $K_2O$ contents and lower CaO and FeO than Mid Atlantic Ridge MORBs. Both major and trace elements allow to separate the samples into three groups: N-MORB, E-MORB and K-rich MORBs. The latter group of samples has very high $K_2O$ content and extremely enriched incompatible element patterns.

Fractional crystallization following olivine, plagioclase and clinopyroxene LLDs shows that primary melts deriving from a depleted peridotitic mantle cannot account for the observed variability, especially for the high $K_2O$, $Na_2O$ and $Al_2O_3$ and very low $SiO_2$ of some samples. Only the N-MORB group compositions could result from fractional crystallization of a fertile peridotitic mantle partially melted at various degrees of melting.

Conversely, an enriched pyroxenitic material is necessary to reproduce the high LREE content and most of the major element compositions of the E- and most of the K-rich MORBs.

The very high K content of few samples from the K-rich group can be explained by the involvement of phlogopite in their source.

Composite mantle has thus been highlighted at ERRTI, with a peridotitic mantle in which very small scale fertile pyroxenitic lithologies are present.

The compositional variability observed in the MORB ERRTI is directly linked to the evolution of the mantle potential temperature, function of the distance from the fracture zone. While a very high variability and extreme enrichments in incompatible elements are present close to the transform fault, where the mantle potential temperature is colder, at higher mantle potential temperatures, only homogeneous N-MORBs compositions are present. At the ridge axis tips, in conditions of low mantle potential temperature, fertile mantle lithologies are preferentially sampled by partial melting and present a lower degree of homogenisation. An increase of the mantle temperature extends the melting to more refractory components, i.e, to the depleted mantle hosting the enriched components. This dilutes the small amount of melt from the most fertile lithology in the large amount of melt from the surrounding mantle, progressively erasing the fertile lithology signature.

## References

Arevalo, R., McDonough, W.F., 2010. *Chemical variations and regional diversity observed in MORB.* Chemical Geology 271 (1-2), 70–85. doi:10.1016/j.chemgeo.2009.12.013.

Barrat, J.A., Zanda, B., Moynier, F., Bollinger, C., Liorzou, C., Bayon, G., 2012. *Geochemistry of CI chondrites: Major and trace elements, and Cu and Zn Isotopes.* Geochimica et Cosmochimica Acta 83, 79–92. doi:10.1016/j.gca.2011.12.011.

Bonatti, E., Brunelli, D., Fabretti, P., Ligi, M., Asunta Portaro, R., Seyler, M., 2001. *Steady-state creation of crust-free lithosphere at cold spots in mid-ocean ridges.* Geol 29 (11), 979. doi:10.1130/0091-7613(2001)029<0979:SSCOCF>2.0.CO;2.

Bonatti, E., Seyler, M., Sushevskaya, N., 1993. *A Cold Suboceanic Mantle Belt at the Eart''s Equator.* Science (New York, N.Y.) 261 (5119), 315–320. doi:10.1126/science.261.5119.315.

Borghini, G., Fumagalli, P., Rampone, E., 2017. *Partial melting of secondary pyroxenite at 1 and 1.5 GPa, and its role in upwelling heterogeneous mantle.* Contrib Mineral Petrol 172 (8). doi:10.1007/s00410-017-1387-4.

Borghini, G., Rampone, E., Zanetti, A., Class, C., Cipriani, A., Hofmann, A.W., Goldstein, S.L., 2016. *Pyroxenite Layers in the Northern Apennines' Upper Mantle (Italy)—Generation by Pyroxenite Melting and Melt Infiltration.* J Petrology 57 (4), 625–653. doi:10.1093/petrology/egv074.

Borisov, A.A., Shapkin, A.I., 1990. *New empirical equation rating Fe3+/Fe2+ in magmas to their composition, oxygen fugacity, and temperature.* Geochemistry International 27 (1), 111–116.

Bottinga, Y., Weill, D.F., 1971. *The viscosity of magmatic silicate liquids: A model for calculation* NASA-CR-126381. https://ntrs.nasa.gov/citations/19720015655.

Brunelli, D., Cipriani, A., Bonatti, E., 2018. Thermal effects of pyroxenites on mantle melting below mid-ocean ridges. Nature Geosci 11 (7), 520–525. doi:10.1038/s41561-018-0139-z.

Brunelli, D., Seyler, M., Cipriani, A., Ottolini, L., Bonatti, E., 2006. *Discontinuous Melt Extraction and Weak Refertilization of Mantle Peridotites at the Vema Lithospheric Section (Mid-Atlantic Ridge).* Journal of Petrology 47 (4), 745–771. doi:10.1093/petrology/egi092.

Carmichael, I.S.E., 1991. *The redox states of basic and silicic magmas: a reflection of their source regions?* Contr. Mineral. and Petrol. 106 (2), 129–141. doi:10.1007/BF00306429.

Chauvel, C., Blichert-Toft, J., 2001. *A hafnium isotope and trace element perspective on melting of the depleted mantle.* Earth and Planetary Science Letters 190 (3-4), 137–151. doi:10.1016/S0012-821X(01)00379-X.

Condamine, P., Couzinié, S., Fabbrizio, A., Devidal, J.-L., Médard, E., 2022. *Trace element partitioning during incipient melting of phlogopite-peridotite in the spinel and garnet stability fields.* Geochimica et Cosmochimica Acta 327, 53–78. doi:10.1016/j.gca.2022.04.011.

Condamine, P., Médard, E., 2014. *Experimental melting of phlogopite-bearing mantle at 1 GPa: Implications for potassic magmatism.* Earth and Planetary Science Letters 397, 80–92. doi:10.1016/j.epsl.2014.04.027.

Condamine, P., Médard, E., Devidal, J.-L., 2016. *Experimental melting of phlogopite-peridotite in the garnet stability field.* Contrib Mineral Petrol 171 (11). doi:10.1007/s00410-016-1306-0.

Cottrell, E., Kelley, K.A., 2011. *The oxidation state of Fe in MORB glasses and the oxygen fugacity of the upper mantle.* Earth and Planetary Science Letters 305 (3-4), 270–282. doi:10.1016/j.epsl.2011.03.014.

Danyushevsky, L.V., Plechov, P., 2011. *Petrolog3: Integrated software for modeling crystallization processes.* Geochem. Geophys. Geosyst. 12 (7). doi:10.1029/2011GC003516.

Danyushevsky, L.V., 2001. *The effect of small amounts of H2O on crystallisation of mid-ocean ridge and backarc basin magmas.* Journal of Volcanology and Geothermal Research 110 (3-4), 265–280. doi:10.1016/S0377-0273(01)00213-X.

Donnelly, K.E., Goldstein, S.L., Langmuir, C.H., Spiegelman, M., 2004. *Origin of enriched ocean ridge basalts and implications for mantle dynamics.* Earth and Planetary Science Letters 226 (3-4), 347–366. doi:10.1016/j.epsl.2004.07.019.

Engel, A.E.J., Engel, C.G., Havens, R.G., 1965. *Chemical Characteristics of Oceanic Basalts and the Upper Mantle.* GSA Bulletin 76 (7), 719. doi:10.1130/0016-7606(1965)76[719:CCOOBA]2.0.CO;2.

Frey, F.A., Green, D.H., 1974. *The mineralogy, geochemistry and origin of Iherzolite inclusions in Victorian basanites.* Geochimica et Cosmochimica Acta 38 (7), 1023–1059. doi:10.1016/0016-7037(74)90003-9.

Gale, A., Dalton, C.A., Langmuir, C.H., Su, Y., Schilling, J.-G., 2013. *The mean composition of ocean ridge basalts.* Geochem. Geophys. Geosyst. 14 (3), 489–518. doi:10.1029/2012GC004334.

Grégoire, M., Bell, D., Le Roex, A., 2002. *Trace element geochemistry of phlogopite-rich mafic mantle xenoliths: their classification and their relationship to phlogopite-bearing peridotites and kimberlites revisited.* Contrib Mineral Petrol 142 (5), 603–625. doi:10.1007/s00410-001-0315-8.

Goldstein, S.L., Soffer, G., Langmuir, C.H., Lehnert, K.A., Graham, D.W., Michael, P.J., 2008. Origin of a 'Southern Hemisphere' geochemical signature in the Arctic upper mantle. Nature 453 (7191), 89–93. doi:10.1038/nature06919.

Heezen, B., Bunce, E., Hersey, J., Tharp, M., 1964. *Chain and romanche fracture zones.* Deep Sea Research and Oceanographic Abstracts 11 (1), 11–33. doi:10.1016/0011-7471(64)91079-4.

Hellebrand, E., Snow, J.E., Hoppe, P., Hofmann, A.W., 2002. *Garnet-field Melting and Late-stage Refertilization in''Residua'' Abyssal Peridotites from the Central Indian Ridge.* Journal of Petrology 43 (12), 2305–2338. doi:10.1093/petrology/43.12.2305.

Hémond, C., Hofmann, A.W., Vlastélic, I., Nauret, F., 2006. *Origin of MORB enrichment and relative trace element compatibilities along the Mid-Atlantic Ridge between 10° and 24°N.* Geochem. Geophys. Geosyst. 7 (12). doi:10.1029/2006GC001317.

Hirose, K., Kushiro, I., 1993. *Partial melting of dry peridotites at high pressures: Determination of compositions of melts segregated from peridotite using aggregates of diamond.* Earth and Planetary Science Letters 114 (4), 477–489. doi:10.1016/0012-821X(93)90077-M.

Hirschmann, M.M., Stolper, E.M., 1996. *A possible role for garnet pyroxenite in the origin of the "garnet signature" in MORB.* Contr. Mineral. and Petrol. 124 (2), 185–208. doi:10.1007/s004100050184.

Hofmann, A.W., 1988. *Chemical differentiation of the Earth: the relationship between mantle, continental crust, and oceanic crust.* Earth and Planetary Science Letters 90 (3), 297–314. doi:10.1016/0012-821X(88)90132-X.

Hofmann, A.W., 2003. *Sampling Mantle Heterogeneity through Oceanic Basalts: Isotopes and Trace Elements.* Treatise on Geochemistry 2, 1–44. doi:10.1016/B0-08-043751-6/02123-X.

Hofmann, A.W., Jochum, K.P., Seufert, M., White, W.M., 1986. *Nb and Pb in oceanic basalts: new constraints on mantle evolution.* Earth and Planetary Science Letters 79, 33–45.

Hofmann, A.W., White, W.M., 1982. *Mantle plumes from ancient oceanic crust.* Earth and Planetary Science Letters 57 (2), 421–436.

Irvine, T.N., Baragar, W.R.A., 1971. *A Guide to the Chemical Classification of the Common Volcanic Rocks.* Canadian Journal of Earth Sciences 8 (5), 523–548. doi:10.1139/e71-055.

Jackson, M.G., Dasgupta, R., 2008. *Compositions of HIMU, EM1, and EM2 from global trends between radiogenic isotopes and major elements in ocean island basalts.* Earth and Planetary Science Letters 276 (1-2), 175–186. doi:10.1016/j.epsl.2008.09.023.

Jochum, K.P., Arndt, N.T., Hofmann, A.W., 1991. *Nb-Th-La in komatiites and basalts: constraints on komatiite petrogenesis and mantle evolution.* Earth and Planetary Science Letters 107 (2), 272–289.

Jochum, K.P., Hofmann, A.W., Ito, E., Seufert, H.M., White, W.M., 1983. *K, U and Th in mid-ocean ridge basalt glasses and heat production, K/U and K/Rb in the mantle.* Nature 306.

Jochum, K., Seufert, H., Spettel, B., Palme, H., 1986. *The solar-system abundances of Nb, Ta, and Y, and the relative abundances of refractory lithophile elements in differentiated planetary* *bodies.* Geochimica et Cosmochimica Acta 50 (6), 1173–1183. doi:10.1016/0016-7037(86)90400-X.

Kamenetsky, V.S., Eggins, S.M., Crawford, A.J., Green, D.H., Gasparon, M., Falloon, T.J., 1998. *Calcic melt inclusions in primitive olivine at 43°N MAR: evidence for melt–rock reaction/melting involving clinopyroxene-rich lithologies during MORB generation.* Earth and Planetary Science Letters 160 (1-2), 115–132. doi:10.1016/S0012-821X(98)00090-9.

Keshav, S., Gudfinnsson, G.H., Sen, G., Fei, Y., 2004. *High-pressure melting experiments on garnet clinopyroxenite and the alkalic to tholeiitic transition in ocean-island basalts.* Earth and Planetary Science Letters 223 (3-4), 365–379. doi:10.1016/j.epsl.2004.04.029.

Kinzler, R.J., 1997. *Melting of mantle peridotite at pressures approaching the spinel to garnet transition: Application to mid-ocean ridge basalt petrogenesis.* J. Geophys. Res. 102 (B1), 853–874. doi:10.1029/96JB00988.

Klein, E.M., Langmuir, C.H., 1987. *Global correlations of ocean ridge basalt chemistry with axial depth and crustal thickness.* J. Geophys. Res. 92 (B8), 8089. doi:10.1029/JB092iB08p08089.

Lambart, S., Laporte, D., Schiano, P., 2013. *Markers of the pyroxenite contribution in the major-element compositions of oceanic basalts: Review of the experimental constraints.* Lithos 160-161, 14–36. doi:10.1016/j.lithos.2012.11.018.

Lange, R.A., Carmichael, I.S., 1987. *Densities of Na2O-K2O-CaO-MgO-FeO-Fe2O3-Al2O3-TiO2-SiO2 liquids: New measurements and derived partial molar properties.* Geochimica et Cosmochimica Acta 51 (11), 2931–2946. doi:10.1016/0016-7037(87)90368-1.

Langmuir, C.H., Klein, E.M., Plank, T., 1992. *Petrological systematics of mid-ocean ridge basalts: Constraints on melt generation beneath ocean ridges.* Mantle Flow and Melt Generation at Mid-Ocean Ridges 71.

Le Voyer, M., Cottrell, E., Kelley, K.A., Brounce, M., Hauri, E.H., 2015. *The effect of primary versus secondary processes on the volatile content of MORB glasses: An example from the equatorial Mid-Atlantic Ridge (5°N–3°S).* J. Geophys. Res. Solid Earth 120 (1), 125–144. doi:10.1002/2014JB011160.

Ligi, M., Bonatti, E., Cipriani, A., Ottolini, L., 2005. *Water-rich basalts at mid-ocean-ridge cold spots.* Nature 434 (7029), 66–69. doi:10.1038/nature03264.

Ligi, M., Bonatti, E., Gasperini, L., Poliakov, A.N., 2002. *Oceanic broad multifault transform plate boundaries.* Geol 30 (1), 11. doi:10.1130/0091-7613(2002)030<0011:OBMTPB>2.0.CO;2.

Lissenberg, C.J., Dick, H.J.B., 2008. *Melt–rock reaction in the lower oceanic crust and its implications for the genesis of mid-ocean ridge basalt.* Earth and Planetary Science Letters 271 (1-4), 311–325. doi:10.1016/j.epsl.2008.04.023.

MacDonald, G.A., Katsura, T., 1964. *Chemical Composition of Hawaiian Lavas1.* J Petrology 5 (1), 82–133. doi:10.1093/petrology/5.1.82.

McKenzie, D., Stracke, A., Blichert-Toft, J., Albarède, F., Grönvold, K., O'Nions, R.K., 2004. *Source enrichment processes responsible for isotopic anomalies in oceanic island basalts.* Geochimica et Cosmochimica Acta 68 (12), 2699–2724. doi:10.1016/j.gca.2003.10.029.

Melson, W.G., Jarosewich, E., Bowen, V.T., Thompson, G., 1967. *St. Peter and st. Paul rocks: a high-temperature, mantle-derived intrusion.* Science (New York, N.Y.) 155 (3769), 1532–1535. doi:10.1126/science.155.3769.1532.

Melson, W.G., Vallier, T.L., Wright, T.L., Byerly, G., Nelen, J., 1976. *Chemical diversity of abyssal volcanic glass erupted along sea-floor spreading centers.* The Geophysics of the Pacific Ocean Basin and Its Margin 19. doi:10.1029/GM019p0351.

Meyzen, C.M., Toplis, M.J., Humler, E., Ludden, J.N., Mével, C., 2003. *A discontinuity in mantle composition beneath the southwest Indian ridge.* Nature 421 (6924), 731–733. doi:10.1038/nature01424.

Michael, P.J., Chase, R.L., 1987. *The influence of primary magma composition, H2O and pressure on mid-ocean ridge basalt differentiation.* Contr. Mineral. and Petrol. 96 (2), 245–263. doi:10.1007/BF00375237.

Middlemost, E.A., 1975. *The basalt clan.* Earth-Science Reviews 11 (4), 337–364. doi:10.1016/0012-8252(75)90039-2.

Nauret, F., Snow, J.E., Hellebrand, E., Weis, D., 2011. *Geochemical Composition of K-rich Lavas from the Lena Trough (Arctic Ocean).* Journal of Petrology 52 (6), 1185–1206. doi:10.1093/petrology/egr024.

O''Hara, M.S., 1972. *Data reduction and projection scheme for complex compositions.* Nat. Environment Res. Counc. Publ. 6 (103-126).

Pertermann, M., Hirschmann, M.M., Hametner, K., Günther, D., Schmidt, M.W., 2004. Experimental determination of trace element partitioning between garnet and silica-rich liquid during anhydrous partial melting of MORB-like eclogite. Geochem. Geophys. Geosyst. 5 (5), n/a-n/a. doi:10.1029/2003GC000638.

Pertermann, M., Hirschmann, M. M., 2003. *Anhydrous Partial Melting Experiments on MORB-like Eclogite: Phase Relations, Phase Compositions and Mineral-Melt Partitioning of Major Elements at 2-3 GPa.* Journal of Petrology 44 (12), 2173–2201. doi:10.1093/petrology/egg074.

Pertermann, M., Hirschmann, M.M., 2002. Trace-element partitioning between vacancy-rich eclogitic clinopyroxene and silicate melt. American Mineralogist 87 (10), 1365–1376. doi:10.2138/am-2002-1012.

Presnall, D.C., Hoover, J.D., 1987. *High pressure phase equilibrium constraints on the origin of mid-ocean ridge basalts.* Geochem. Soc. Spec. Publ., Magmatic Processes : Physicochemical Principles 1, 75–89.

Phipps Morgan, J., 2001. Thermodynamics of pressure release melting of a veined plum pudding mantle. Geochem. Geophys. Geosyst. 2 (4). doi:10.1029/2000GC000049.

Richter, M., Nebel, O., Maas, R., Mather, B., Nebel-Jacobsen, Y., Capitanio, F.A., Dick, H.J.B., Cawood, P.A., 2020. An Early Cretaceous subduction-modified mantle underneath the ultraslow spreading Gakkel Ridge, Arctic Ocean. Science advances 6 (44). doi:10.1126/sciadv.abb4340.

Salters, V.J.M., Hart, S.R., 1989. *The hafnium paradox and the role of garnet in the source of mid-ocean-ridge basalts.* Nature 342 (6248), 420–422. doi:10.1038/342420a0.

Salters, V.J.M., Stracke, A., 2004. *Composition of the depleted mantle.* Geochem. Geophys. Geosyst. 5 (5). doi:10.1029/2003GC000597.

Schilling, J.-G., Ruppel, C., Davis, A.N., McCully, B., Tighe, S.A., Kingsley, R.H., Lin, J., 1995. *Thermal structure of the mantle beneath the equatorial Mid-Atlantic Ridge: Inferences from the spatial variation of dredged basalt glass compositions.* J. Geophys. Res. 100 (B6), 10057–10076. doi:10.1029/95JB00668.

Schmidt, M.W., Vielzeuf, D., Auzanneau, E., 2004. Melting and dissolution of subducting crust at high pressures: the key role of white mica. Earth and Planetary Science Letters 228 (1-2), 65–84. doi:10.1016/j.epsl.2004.09.020.

Searle, R.C., Thomas, M.V., Jones, E.J.W., 1994. *Morphology and tectonics of the Romanche Transform and its environs.* Mar Geophys Res 16 (6), 427–453. doi:10.1007/BF01270518.

Shaw, D.M., 1970. *Trace element fractionation during anatexis.* Geochimica et Cosmochimica Acta 34 (2), 237–243. doi:10.1016/0016-7037(70)90009-8.

Shen, Y., Forsyth, D.W., 1995. *Geochemical constraints on initial and final depths of melting beneath mid-ocean ridges.* J. Geophys. Res. 100 (B2), 2211–2237.Standish, J.J., Dick, H.J.B., Michael, P.J., Melson, W.G., ’'Hearn, T., 2008. *MORB generation beneath the ultraslow spreading Southwest Indian Ridge (9-25°E): Major element chemistry and the importance of process versus source.* Geochem. Geophys. Geosyst. 9 (5). doi:10.1029/94JB02768.

Sleep, N., H., *Tapping of magmas from ubiquitous mantle heterogeneities: an alternative to mantle plumes?* J. Geophys. Res. 89, 10029–10041 (1984).

Sobolev, A.V., Hofmann, A.W., Sobolev, S.V., Nikogosian, I.K., 2005. *An olivine-free mantle source of Hawaiian shield basalts.* Nature 434 (7033), 590–597. doi:10.1038/nature03411.

Staudigel, H., Plank, T., White, B., Schmincke, H.-U., 1966. *Geochemical Fluxes During Seafloor Alteration of the Basaltic Upper Oceanic Crust: DSDP Sites 417 and 418*, in: , Subduction. American Geophysical Union (AGU), pp. 19–38.

Sun, S.-S., McDonough, W.F., 1989. *Chemical and isotopic systematics of oceanic basalts: implications for mantle composition and processes*. Geological Society, London, Special Publications 42, 313–345. doi:10.1144/GSL.SP.1989.042.01.19.

Sushchevskaya, N., Bonatti, E., Peive, A., Kamenetsky, V., Belyatskii, B.V., Tsekhonya, T.I., Kononkova, N.N., 2002. *Heterogeneity of Rift Magmatism in the Equatorial Province of the Mid-Atlantic Ridge (15°N to 3°S).* Geochemistrt International 40 (1), 26–50.

Trønnes, R.G., 2002. *Stability range and decomposition of potassic richterite and phlogopite end members at 5-15 GPa*. Mineralogy and Petrology 74 (2-4), 129–148. doi:10.1007/s007100200001.

Workman, R.K., Hart, S.R., 2005. *Major and trace element composition of the depleted MORB mantle (DMM).* Earth and Planetary Science Letters 231, 53-72. doi:10.1016/j.epsl.2004.12.005.

Yoder, H.S., Kushiro, I., 1969. *Melting of a hydrous phase: phlogopite*. American Journal of Science 267, 558–582.

Yu, Z., Singh, S.C., Gregory, E.P.M., Maia, M., Wang, Z., Brunelli, D., 2021. *Semibrittle seismic deformation in high-temperature mantle mylonite shear zone along the Romanche transform fault.* Science advances 7 (15). doi:10.1126/sciadv.abf3388.

Zou, H., 1998. *Trace element fractionation during modal and nonmodal dynamic melting and open-system melting: a mathematical treatment.* Geochimica et Cosmochimica Acta 62 (11), 1937–1945. doi:10.1016/S0016-7037(98)00115-X.

## Supplementary material

### Figures

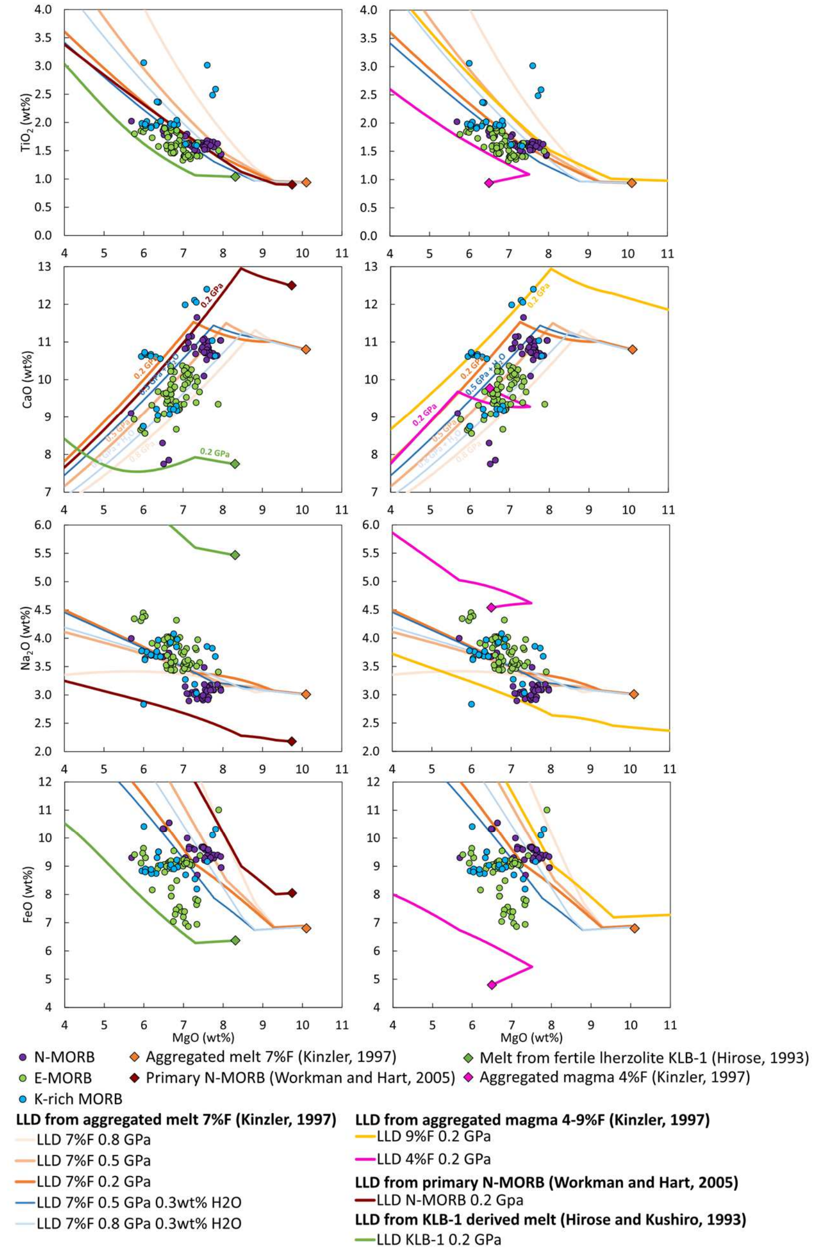

*Figure S 4.1 - L-Ol, L-Ol-Pl, L-Ol-Pl-Cpx LLDs calculated with Petrolog3 using Danyushevsky (2001) model for the calculation of Ol, Pl and Cpx fractionation (see text for details). The first model (left) compares calculated LLDs from various primary liquid: primary N-MORB (Presnall and Hoover (1987) (red line), aggregated melt from a fertile spinel lherzolite (orange and blue lines) (Kinzler, 1997) and a fertile spinel lherzolite (KLB-1) derived melt (Hirose and Kushiro, 1993). The second model (right) compare calculated LLDs from melt derived from the same source but at various degree of melting: near-fractional aggregate melts at average 4% F (pink line), 7% F (orange and blue lines) and 9% F (yellow line) of a fertile spinel-peridotite (Kinzler, 1997).*

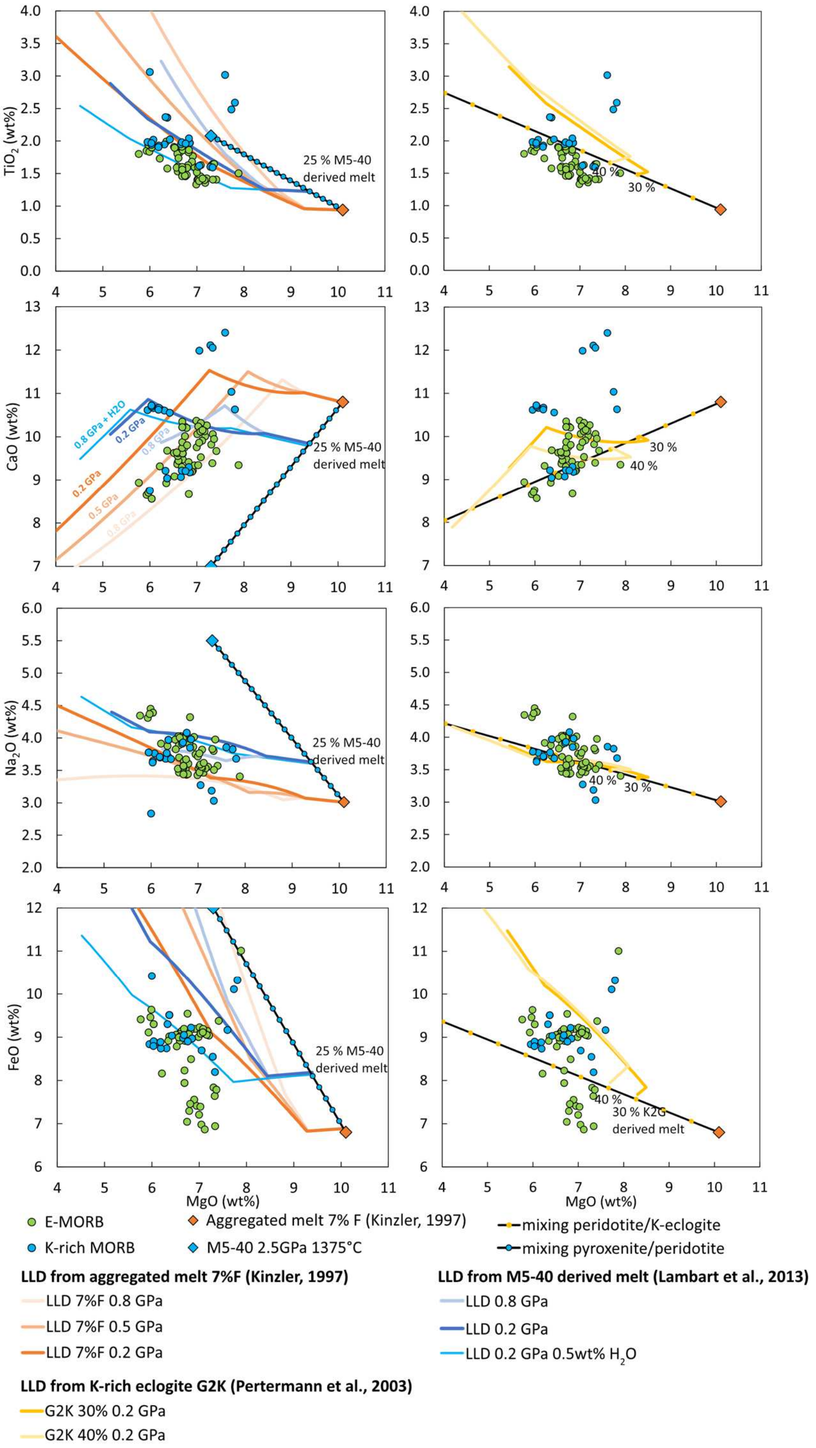

*Figure S 4.2 - L-Ol, L-Ol-Pl, L-Ol-Pl-Cpx LLDs calculated with Petrolog3 using Danyushevsky (2001) model for the calculation of Ol, Pl and Cpx fractionation (see text for details). The first model (left) compares calculated LLDs from various primary liquid: primary N-MORB (Presnall and Hoover (1987) (red line), aggregated melt from a fertile spinel lherzolite (orange and blue lines) (Kinzler, 1997) and a fertile spinel lherzolite (KLB-1) derived melt (Hirose and Kushiro, 1993). The second model (right) compare calculated LLDs from melt derived from the same source but at various degree of melting: near-fractional aggregate melts at average 4% F (pink line), 7% F (orange and blue lines) and 9% F (yellow line) of a fertile spinel-peridotite (Kinzler, 1997).*

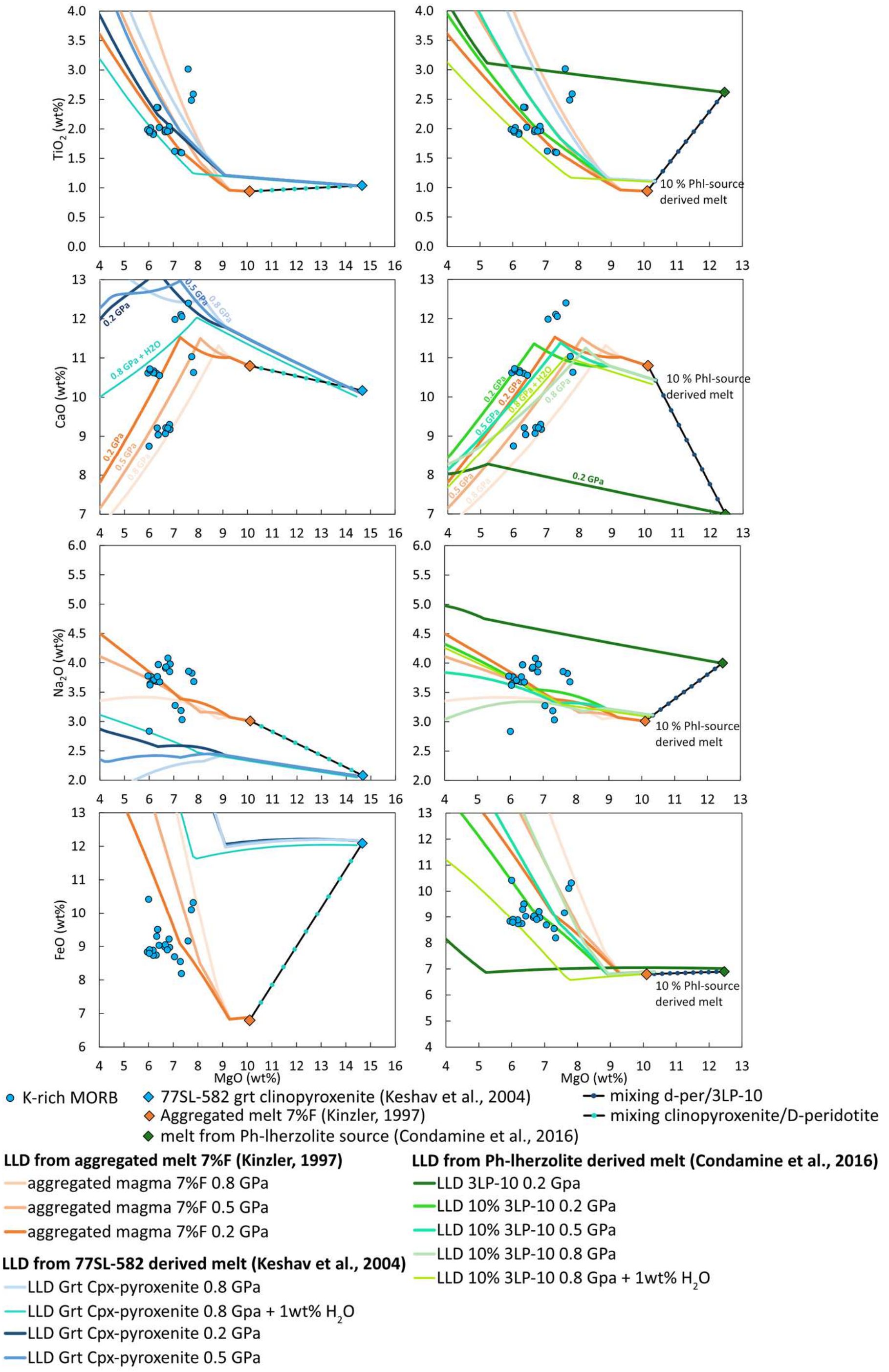

*Figure S 4.3 - Calculated L-Ol, L-Ol-Pl, L-Ol-Pl-Cpx LLD from mixing between aggregated melt at average melting of 7% of a depleted peridotite (data source from Kinzler, 1997) with various source: Left: Experimental melt from partial melting of M5-40 Si-undersaturated pyroxenite at 2.5 GPa 1375 °C (Lambart et al., 2013). Right: Experimental melt from partial melting of garnet clinopyroxenite 77SL-582 at 2.5 GPa and 1430°C (Keshav et al., 2004). (c) Experimental melt from partial melting of phlogopite-bearing lherzolite partially melted at 1250°C (Condamine et al., 2016).*

## Tables

## *Table S4.1- Major elements measured with EMPA*

| **Sample** | **Lat** | **Long** | **Depth** | **Relative distance TF** | **$SiO_2$** | | **$TiO_2$** | | **$Al_2O_3$** | | **FeO** | | **MgO** | | **CaO** | | **$Na_2O$** | | **$K_2O$** | | **$P_2O_5$** | |
|---|---|---|---|---|---|---|---|---|---|---|---|---|---|---|---|---|---|---|---|---|---|---|
| **N-MORB** | | | m | km | wt% | stdev | wt% | stdev | wt% | stdev | wt% | stdev | wt% | stdev | wt% | stdev | wt% | stdev | wt% | stdev | wt% | stdev |
| SMA1977-328 | -0.335 | -16.126 | -4192 | 79.8 | 51.0 | 0.2 | 1.490 | 0.073 | 15.21 | 0.10 | 8.69 | 0.11 | 7.35 | 0.06 | 11.65 | 0.12 | 2.93 | 0.06 | 0.269 | 0.010 | 0.155 | 0.029 |
| SMA1977-329 | -0.335 | -16.126 | -4190 | 79.8 | 50.6 | 0.2 | 1.571 | 0.061 | 15.23 | 0.09 | 9.63 | 0.02 | 7.22 | 0.06 | 11.15 | 0.05 | 3.04 | 0.02 | 0.159 | 0.010 | 0.151 | 0.040 |
| SMA1977-330 | -0.335 | -16.125 | -4146 | 79.8 | 51.1 | 0.2 | 1.638 | 0.030 | 15.45 | 0.05 | 9.68 | 0.05 | 7.14 | 0.08 | 11.14 | 0.08 | 2.89 | 0.03 | 0.176 | 0.009 | 0.154 | 0.010 |
| SMA1977-331 | -0.334 | -16.124 | -4089 | 79.8 | 50.3 | 0.2 | 1.606 | 0.028 | 15.29 | 0.16 | 9.61 | 0.04 | 7.14 | 0.07 | 10.98 | 0.08 | 3.02 | 0.06 | 0.173 | 0.010 | 0.131 | 0.025 |
| SMA1977-334 | -0.333 | -16.121 | -3991 | 79.8 | 50.3 | 0.0 | 1.638 | 0.031 | 15.17 | 0.18 | 9.69 | 0.12 | 7.50 | 0.04 | 10.84 | 0.05 | 2.91 | 0.04 | 0.167 | 0.012 | 0.134 | 0.039 |
| SMA1977-335 | -0.333 | -16.120 | -3948 | 79.7 | 50.5 | 0.2 | 1.625 | 0.042 | 15.18 | 0.14 | 9.59 | 0.09 | 7.54 | 0.09 | 10.93 | 0.07 | 2.95 | 0.02 | 0.169 | 0.008 | 0.147 | 0.044 |
| SMA1977-336 | -0.332 | -16.120 | -3941 | 79.7 | 50.4 | 0.2 | 1.797 | 0.031 | 14.76 | 0.04 | 10.00 | 0.09 | 7.09 | 0.07 | 10.83 | 0.11 | 3.03 | 0.06 | 0.192 | 0.008 | 0.142 | 0.027 |
| SMA1977-337 | -0.332 | -16.120 | -3896 | 79.7 | 50.9 | 0.1 | 1.641 | 0.061 | 15.44 | 0.05 | 9.68 | 0.05 | 7.46 | 0.09 | 10.79 | 0.06 | 2.97 | 0.06 | 0.180 | 0.007 | 0.156 | 0.028 |
| SMA1977-338 | -0.332 | -16.115 | -3883 | 79.8 | 50.5 | 0.3 | 1.598 | 0.050 | 15.13 | 0.09 | 9.65 | 0.09 | 7.49 | 0.02 | 10.86 | 0.03 | 2.94 | 0.07 | 0.169 | 0.003 | 0.166 | 0.045 |
| SMA1977-340 | -0.332 | -16.113 | -3785 | 79.9 | 50.5 | 0.2 | 1.585 | 0.065 | 15.74 | 0.05 | 9.50 | 0.15 | 7.64 | 0.07 | 11.02 | 0.08 | 2.96 | 0.05 | 0.165 | 0.004 | 0.154 | 0.014 |
| SMA1977-341B | -0.333 | -16.110 | -3853 | 80.2 | 50.2 | 0.2 | 1.573 | 0.038 | 15.40 | 0.03 | 9.64 | 0.07 | 7.54 | 0.10 | 11.09 | 0.06 | 2.96 | 0.03 | 0.171 | 0.012 | 0.125 | 0.044 |
| SMA1977-341T | -0.333 | -16.110 | -3853 | 80.2 | 50.6 | 0.2 | 1.575 | 0.048 | 15.29 | 0.12 | 9.65 | 0.14 | 7.50 | 0.02 | 11.05 | 0.01 | 2.99 | 0.03 | 0.170 | 0.011 | 0.149 | 0.026 |
| SMA1977-342 | -0.334 | -16.109 | -3776 | 80.2 | 50.8 | 0.2 | 1.572 | 0.088 | 15.54 | 0.06 | 9.52 | 0.05 | 7.64 | 0.07 | 10.84 | 0.11 | 2.96 | 0.04 | 0.178 | 0.004 | 0.148 | 0.038 |
| SMA1977-343 | -0.334 | -16.109 | -3771 | 80.3 | 50.4 | 0.2 | 1.649 | 0.038 | 15.70 | 0.04 | 9.59 | 0.16 | 7.63 | 0.05 | 10.89 | 0.10 | 2.91 | 0.05 | 0.182 | 0.007 | 0.127 | 0.032 |
| SMA1978-345 | -0.237 | -16.237 | -4322 | 65.5 | 50.8 | 0.2 | 1.586 | 0.032 | 15.43 | 0.08 | 9.33 | 0.07 | 7.68 | 0.07 | 10.73 | 0.04 | 3.17 | 0.08 | 0.209 | 0.009 | 0.192 | 0.023 |
| SMA1978-346 | -0.237 | -16.237 | -4299 | 65.5 | 50.3 | 0.2 | 1.566 | 0.089 | 15.44 | 0.09 | 9.29 | 0.04 | 7.77 | 0.05 | 10.62 | 0.10 | 3.08 | 0.04 | 0.213 | 0.009 | 0.152 | 0.033 |
| SMA1978-348 | -0.237 | -16.237 | -4282 | 65.5 | 50.8 | 0.2 | 1.581 | 0.032 | 15.41 | 0.09 | 9.28 | 0.08 | 7.60 | 0.06 | 10.79 | 0.05 | 3.15 | 0.06 | 0.216 | 0.010 | 0.170 | 0.017 |
| SMA1978-349 | -0.237 | -16.237 | -4282 | 65.5 | 50.8 | 0.3 | 1.656 | 0.043 | 15.25 | 0.13 | 9.40 | 0.13 | 7.76 | 0.10 | 10.70 | 0.14 | 3.09 | 0.05 | 0.214 | 0.015 | 0.157 | 0.030 |
| SMA1978-350 | -0.237 | -16.237 | -4283 | 65.5 | 50.9 | 0.2 | 1.527 | 0.043 | 15.45 | 0.14 | 9.29 | 0.12 | 7.60 | 0.09 | 10.71 | 0.13 | 3.09 | 0.07 | 0.214 | 0.011 | 0.140 | 0.020 |
| SMA1978-352 | -0.238 | -16.235 | -4261 | 65.6 | 50.9 | 0.2 | 1.596 | 0.017 | 15.48 | 0.01 | 9.23 | 0.11 | 7.32 | 0.05 | 10.68 | 0.03 | 3.06 | 0.03 | 0.214 | 0.020 | 0.171 | 0.054 |
| SMA1978-354 | -0.237 | -16.235 | -4258 | 65.6 | 50.6 | 0.2 | 1.662 | 0.042 | 15.10 | 0.09 | 9.23 | 0.05 | 7.66 | 0.11 | 10.72 | 0.07 | 3.11 | 0.09 | 0.218 | 0.008 | 0.173 | 0.041 |
| SMA1978-355 | -0.235 | -16.231 | -4216 | 65.5 | 50.8 | 0.2 | 1.680 | 0.026 | 15.32 | 0.12 | 9.37 | 0.10 | 7.59 | 0.05 | 10.53 | 0.11 | 3.13 | 0.03 | 0.223 | 0.018 | 0.191 | 0.003 |
| SMA1978-356 | -0.235 | -16.230 | -4214 | 65.5 | 51.1 | 0.0 | 1.591 | 0.040 | 15.28 | 0.07 | 9.28 | 0.14 | 7.55 | 0.07 | 10.71 | 0.21 | 3.09 | 0.09 | 0.215 | 0.006 | 0.205 | 0.023 |
| SMA1978-357 | -0.235 | -16.230 | -4192 | 65.5 | 51.0 | 0.2 | 1.757 | 0.066 | 15.21 | 0.09 | 9.30 | 0.02 | 7.05 | 0.06 | 10.82 | 0.08 | 3.15 | 0.08 | 0.225 | 0.017 | 0.191 | 0.037 |
| SMA1978-358 | -0.236 | -16.229 | -4225 | 65.7 | 50.9 | 0.1 | 1.625 | 0.009 | 15.35 | 0.08 | 9.24 | 0.12 | 7.60 | 0.06 | 10.71 | 0.07 | 3.07 | 0.01 | 0.232 | 0.015 | 0.173 | 0.043 |
| SMA1978-360 | -0.237 | -16.229 | -4166 | 65.8 | 50.6 | 0.2 | 1.594 | 0.096 | 15.22 | 0.01 | 9.30 | 0.13 | 7.69 | 0.09 | 10.64 | 0.07 | 3.08 | 0.03 | 0.228 | 0.007 | 0.188 | 0.023 |
| SMA1978-363 | -0.236 | -16.225 | -4130 | 65.8 | 50.7 | 0.4 | 1.566 | 0.036 | 15.51 | 0.06 | 9.21 | 0.05 | 7.53 | 0.01 | 10.72 | 0.09 | 3.19 | 0.05 | 0.203 | 0.006 | 0.174 | 0.041 |
| SMA1978-364 | -0.236 | -16.225 | -4126 | 65.8 | 50.3 | 0.2 | 1.626 | 0.046 | 15.02 | 0.18 | 9.39 | 0.11 | 7.86 | 0.08 | 10.64 | 0.16 | 3.18 | 0.07 | 0.226 | 0.011 | 0.164 | 0.018 |
| S1312-Xa | -0.080 | -16.383 | -2800 | 43.9 | 52.5 | 0.2 | 2.024 | 0.022 | 15.56 | 0.15 | 9.30 | 0.11 | 5.69 | 0.04 | 9.10 | 0.17 | 4.00 | 0.04 | 0.502 | 0.016 | 0.276 | 0.020 |
| S1312-53 | -0.080 | -16.383 | -2800 | 43.9 | 51.3 | | 1.420 | | 15.88 | | 9.34 | | 7.94 | | 11.04 | | 3.11 | | 0.310 | | 0.190 | |
| S1314 | -0.120 | -16.533 | -3000 | 41.3 | 53.2 | | 1.780 | | 14.94 | | 10.32 | | 6.51 | | 7.75 | | 3.68 | | 0.250 | | 0.190 | |
| S1314-X | -0.120 | -16.533 | -3000 | 41.3 | 53.6 | 0.1 | 1.858 | 0.086 | 15.17 | 0.10 | 10.34 | 0.11 | 6.48 | 0.05 | 8.31 | 0.07 | 3.67 | 0.08 | 0.266 | 0.019 | 0.205 | 0.039 |
| S1314-01 | -0.120 | -16.533 | -3000 | 41.3 | 52.9 | | 1.770 | | 14.90 | | 10.55 | | 6.64 | | 7.85 | | 3.74 | | 0.270 | | 0.230 | |

*Table S4.1 (continue)*

| **Sample** | **Lat** | **Long** | **Depth** | **Relative distance TF** | **$SiO_2$** | | **$TiO_2$** | | **$Al_2O_3$** | | **FeO** | | **MgO** | | **CaO** | | **$Na_2O$** | | **$K_2O$** | | **$P_2O_5$** | |
|---|---|---|---|---|---|---|---|---|---|---|---|---|---|---|---|---|---|---|---|---|---|---|
| | | | m | km | wt% | stdev | wt% | stdev | wt% | stdev | wt% | stdev | wt% | stdev | wt% | stdev | wt% | stdev | wt% | stdev | wt% | stdev |
| S1314-01 | -0.120 | -16.533 | -3000 | 41.3 | 52.9 | | 1.770 | | 14.90 | | 10.55 | | 6.64 | | 7.85 | | 3.74 | | 0.27 | | 0.23 | |
| S1627-01 | -0.031 | -16.258 | -2500 | 42.6 | 51.3 | | 1.520 | | 15.30 | | 9.29 | | 7.53 | | 10.10 | | 3.49 | | 0.320 | | 0.190 | |
| S1629-35 | -0.294 | -16.091 | -3100 | 76.7 | 50.3 | | 1.440 | | 15.53 | | 8.95 | | 7.95 | | 11.04 | | 3.08 | | 0.180 | | 0.130 | |
| S1639-03 | -0.405 | -16.827 | -2600 | 62.2 | 50.5 | | 1.516 | | 16.07 | | 9.59 | | 7.28 | | 10.87 | | 3.01 | | 0.248 | | 0.165 | |
| **E-MORB** | | | | | | | | | | | | | | | | | | | | | | |
| SMA1970-191A | 0.021 | -16.815 | -4093 | 17.8 | 50.6 | 0.2 | 1.862 | 0.036 | 17.05 | 0.07 | 9.11 | 0.07 | 6.61 | 0.04 | 9.41 | 0.04 | 3.90 | 0.06 | 0.548 | 0.004 | 0.253 | 0.039 |
| SMA1970-191B | 0.021 | -16.815 | -4093 | 17.8 | 50.2 | 0.2 | 1.819 | 0.046 | 16.93 | 0.10 | 9.15 | 0.09 | 6.63 | 0.05 | 9.46 | 0.06 | 4.03 | 0.07 | 0.561 | 0.021 | 0.262 | 0.030 |
| SMA1970-191C | 0.021 | -16.815 | -4093 | 17.8 | 50.9 | 0.2 | 1.818 | 0.026 | 17.24 | 0.10 | 8.92 | 0.04 | 6.59 | 0.11 | 9.40 | 0.05 | 3.89 | 0.04 | 0.546 | 0.025 | 0.274 | 0.015 |
| SMA1970-191D | 0.021 | -16.815 | -4093 | 17.8 | 50.5 | 0.2 | 1.805 | 0.070 | 16.84 | 0.06 | 9.07 | 0.05 | 6.58 | 0.02 | 9.37 | 0.04 | 4.03 | 0.14 | 0.525 | 0.005 | 0.290 | 0.016 |
| SMA1970-191E | 0.021 | -16.815 | -4093 | 17.8 | 50.8 | 0.2 | 1.909 | 0.016 | 16.90 | 0.07 | 9.06 | 0.08 | 6.51 | 0.06 | 9.63 | 0.13 | 3.97 | 0.06 | 0.525 | 0.005 | 0.254 | 0.060 |
| SMA1970-192 | 0.020 | -16.813 | -4078 | 17.9 | 50.3 | 0.3 | 1.857 | 0.043 | 16.93 | 0.10 | 9.12 | 0.07 | 6.70 | 0.07 | 9.48 | 0.12 | 4.01 | 0.06 | 0.560 | 0.020 | 0.277 | 0.048 |
| SMA1970-193 | 0.020 | -16.813 | -4072 | 17.9 | 50.4 | 0.0 | 1.914 | 0.064 | 16.97 | 0.07 | 9.19 | 0.03 | 6.68 | 0.10 | 9.30 | 0.14 | 3.99 | 0.05 | 0.550 | 0.014 | 0.259 | 0.022 |
| SMA1970-194 | 0.019 | -16.811 | -4041 | 18.1 | 49.9 | 0.3 | 1.765 | 0.061 | 16.74 | 0.11 | 9.19 | 0.10 | 6.91 | 0.07 | 9.22 | 0.04 | 4.02 | 0.09 | 0.574 | 0.018 | 0.293 | 0.057 |
| SMA1970-195 | 0.018 | -16.808 | -4072 | 18.4 | 50.7 | 0.1 | 1.827 | 0.066 | 16.88 | 0.07 | 9.16 | 0.09 | 6.82 | 0.06 | 9.42 | 0.08 | 3.96 | 0.09 | 0.538 | 0.022 | 0.303 | 0.029 |
| SMA1970-199 | 0.013 | -16.796 | -3864 | 19.3 | 50.4 | 0.2 | 1.737 | 0.056 | 17.22 | 0.04 | 8.97 | 0.09 | 6.61 | 0.03 | 9.45 | 0.08 | 4.01 | 0.07 | 0.500 | 0.020 | 0.227 | 0.027 |
| SMA1970-202 | 0.009 | -16.792 | -3779 | 19.8 | 50.0 | 0.1 | 1.629 | 0.075 | 17.07 | 0.07 | 9.13 | 0.06 | 7.08 | 0.09 | 9.53 | 0.06 | 3.82 | 0.06 | 0.424 | 0.015 | 0.222 | 0.015 |
| SMA1973-246 | -0.170 | -16.424 | -4226 | 51.8 | 49.6 | 0.3 | 1.503 | 0.040 | 15.84 | 0.12 | 11.01 | 0.06 | 7.89 | 0.12 | 9.34 | 0.12 | 3.41 | 0.07 | 0.336 | 0.024 | 0.166 | 0.039 |
| SMA1973-248 | -0.169 | -16.423 | -4180 | 51.7 | 51.5 | 0.4 | 1.545 | 0.096 | 16.44 | 0.07 | 8.91 | 0.10 | 6.70 | 0.04 | 9.61 | 0.12 | 3.54 | 0.02 | 0.514 | 0.012 | 0.270 | 0.050 |
| SMA1973-249 | -0.169 | -16.423 | -4138 | 51.7 | 51.3 | 0.1 | 1.457 | 0.041 | 15.84 | 0.12 | 9.54 | 0.12 | 6.76 | 0.06 | 10.23 | 0.14 | 3.43 | 0.03 | 0.402 | 0.012 | 0.228 | 0.015 |
| SMA1973-250 | -0.167 | -16.422 | -4074 | 51.6 | 51.1 | 0.2 | 1.488 | 0.060 | 16.35 | 0.04 | 8.99 | 0.10 | 6.74 | 0.05 | 9.75 | 0.07 | 3.52 | 0.04 | 0.477 | 0.022 | 0.242 | 0.046 |
| SMA1973-251 | -0.167 | -16.422 | -4028 | 51.5 | 51.6 | 0.1 | 1.576 | 0.046 | 16.31 | 0.06 | 9.02 | 0.08 | 6.37 | 0.12 | 9.68 | 0.15 | 3.71 | 0.04 | 0.539 | 0.024 | 0.266 | 0.024 |
| SMA1973-252 | -0.166 | -16.422 | -4006 | 51.5 | 51.5 | 0.2 | 1.532 | 0.052 | 16.49 | 0.10 | 8.91 | 0.05 | 6.59 | 0.11 | 9.56 | 0.06 | 3.47 | 0.05 | 0.515 | 0.011 | 0.232 | 0.044 |
| SMA1973-254 | -0.166 | -16.422 | -3984 | 51.5 | 51.5 | 0.2 | 1.608 | 0.050 | 16.42 | 0.09 | 9.02 | 0.16 | 6.60 | 0.06 | 9.62 | 0.14 | 3.70 | 0.05 | 0.518 | 0.011 | 0.213 | 0.018 |
| SMA1973-255 | -0.166 | -16.422 | -3982 | 51.5 | 51.3 | 0.1 | 1.507 | 0.047 | 16.37 | 0.04 | 8.98 | 0.11 | 6.70 | 0.07 | 9.62 | 0.04 | 3.64 | 0.07 | 0.500 | 0.023 | 0.255 | 0.022 |
| SMA1973-256 | -0.166 | -16.422 | -3939 | 51.5 | 50.9 | 0.1 | 1.459 | 0.067 | 16.29 | 0.04 | 9.00 | 0.10 | 6.69 | 0.05 | 9.74 | 0.09 | 3.54 | 0.08 | 0.477 | 0.019 | 0.187 | 0.051 |
| SMA1973-258 | -0.166 | -16.422 | -3923 | 51.5 | 51.7 | 0.2 | 1.590 | 0.081 | 16.48 | 0.05 | 8.99 | 0.03 | 6.57 | 0.09 | 9.64 | 0.08 | 3.53 | 0.04 | 0.505 | 0.015 | 0.242 | 0.032 |
| SMA1973-261 | -0.161 | -16.421 | -4020 | 51.0 | 50.5 | 0.2 | 1.357 | 0.070 | 16.83 | 0.08 | 9.14 | 0.16 | 7.18 | 0.02 | 10.01 | 0.07 | 3.55 | 0.03 | 0.384 | 0.011 | 0.171 | 0.034 |
| SMA1973-262 | -0.161 | -16.421 | -3993 | 50.9 | 50.0 | 0.4 | 1.406 | 0.057 | 16.66 | 0.11 | 9.38 | 0.03 | 7.42 | 0.13 | 9.67 | 0.08 | 3.57 | 0.03 | 0.357 | 0.015 | 0.187 | 0.028 |
| SMA1973-263 | -0.161 | -16.420 | -3968 | 51.0 | 51.7 | 0.2 | 1.405 | 0.033 | 17.04 | 0.05 | 9.08 | 0.11 | 7.11 | 0.06 | 9.91 | 0.04 | 3.46 | 0.05 | 0.388 | 0.013 | 0.158 | 0.038 |
| SMA1973-264 | -0.158 | -16.419 | -4025 | 50.8 | 51.5 | 0.1 | 1.574 | 0.063 | 16.30 | 0.18 | 9.02 | 0.08 | 6.69 | 0.05 | 9.87 | 0.12 | 3.57 | 0.08 | 0.478 | 0.014 | 0.226 | 0.036 |
| SMA1974-266 | -0.035 | -16.454 | -3871 | 36.5 | 50.9 | 0.1 | 1.401 | 0.027 | 16.55 | 0.10 | 9.23 | 0.07 | 7.01 | 0.03 | 10.06 | 0.08 | 3.53 | 0.06 | 0.391 | 0.011 | 0.188 | 0.034 |
| SMA1974-267 | -0.035 | -16.454 | -3871 | 36.5 | 50.2 | 0.1 | 1.478 | 0.055 | 16.66 | 0.11 | 9.07 | 0.04 | 6.78 | 0.06 | 10.20 | 0.17 | 3.44 | 0.07 | 0.390 | 0.016 | 0.236 | 0.043 |
| SMA1974-271 | -0.038 | -16.453 | -3826 | 36.8 | 51.2 | 0.4 | 1.331 | 0.045 | 17.02 | 0.13 | 9.00 | 0.08 | 6.99 | 0.04 | 10.37 | 0.12 | 3.43 | 0.04 | 0.369 | 0.022 | 0.212 | 0.043 |
| SMA1974-272 | -0.038 | -16.453 | -3826 | 36.8 | 50.4 | 0.1 | 1.425 | 0.030 | 16.65 | 0.14 | 9.04 | 0.11 | 7.21 | 0.02 | 10.26 | 0.06 | 3.56 | 0.06 | 0.367 | 0.014 | 0.161 | 0.034 |

*Table S4.1 (continue)*

| **Sample** | **Lat** | **Long** | **Depth** | **Relative distance TF** | **SiO$_2$** | | **TiO$_2$** | | **Al$_2$O$_3$** | | **FeO** | | **MgO** | | **CaO** | | **Na$_2$O** | | **K$_2$O** | | **P$_2$O$_5$** | |
|---|---|---|---|---|---|---|---|---|---|---|---|---|---|---|---|---|---|---|---|---|---|---|
| | | | m | km | wt% | stdev | wt% | stdev | wt% | stdev | wt% | stdev | wt% | stdev | wt% | stdev | wt% | stdev | wt% | stdev | wt% | stdev |
| SMA1974-273 | -0.038 | -16.453 | -3821 | 36.9 | 50.3 | 0.1 | 1.400 | 0.074 | 16.41 | 0.23 | 9.05 | 0.04 | 7.16 | 0.13 | 10.13 | 0.09 | 3.53 | 0.07 | 0.367 | 0.012 | 0.188 | 0.029 |
| SMA1974-274 | -0.038 | -16.453 | -3820 | 36.9 | 50.7 | 0.1 | 1.417 | 0.047 | 16.71 | 0.09 | 9.19 | 0.05 | 7.08 | 0.09 | 10.32 | 0.04 | 3.53 | 0.03 | 0.368 | 0.009 | 0.140 | 0.033 |
| SMA1974-275 | -0.039 | -16.455 | -3822 | 36.9 | 50.0 | 0.2 | 1.429 | 0.027 | 16.60 | 0.03 | 9.09 | 0.05 | 7.03 | 0.05 | 10.24 | 0.06 | 3.57 | 0.04 | 0.413 | 0.025 | 0.199 | 0.015 |
| SMA1974-276 | -0.039 | -16.455 | -3822 | 36.9 | 50.8 | 0.4 | 1.405 | 0.019 | 16.58 | 0.06 | 9.08 | 0.01 | 7.03 | 0.05 | 10.24 | 0.06 | 3.47 | 0.10 | 0.368 | 0.010 | 0.174 | 0.028 |
| SMA1974-277 | -0.039 | -16.456 | -3812 | 36.9 | 50.6 | 0.2 | 1.455 | 0.086 | 16.56 | 0.11 | 9.11 | 0.06 | 7.08 | 0.05 | 10.12 | 0.06 | 3.55 | 0.09 | 0.377 | 0.015 | 0.176 | 0.027 |
| SMA1979-365 | -0.037 | -16.517 | -4267 | 34.5 | 51.5 | 0.3 | 1.601 | 0.034 | 16.64 | 0.03 | 7.41 | 0.08 | 6.95 | 0.08 | 9.34 | 0.08 | 3.75 | 0.06 | 0.656 | 0.030 | | |
| SMA1979-366 | -0.037 | -16.517 | -4216 | 34.4 | 51.6 | 0.3 | 1.518 | 0.026 | 16.87 | 0.08 | 7.21 | 0.10 | 7.00 | 0.08 | 9.76 | 0.05 | 3.72 | 0.10 | 0.653 | 0.009 | | |
| SMA1979-367 | -0.035 | -16.517 | -4216 | 34.3 | 51.7 | 0.3 | 1.384 | 0.030 | 17.12 | 0.11 | 6.98 | 0.09 | 7.05 | 0.05 | 9.87 | 0.03 | 3.59 | 0.06 | 0.618 | 0.022 | | |
| SMA1979-368 | -0.034 | -16.518 | -4278 | 34.2 | 52.2 | 0.1 | 1.730 | 0.043 | 16.27 | 0.07 | 8.16 | 0.03 | 6.21 | 0.05 | 9.32 | 0.04 | 3.91 | 0.04 | 0.578 | 0.015 | | |
| SMA1979-369 | -0.033 | -16.518 | -4259 | 34.0 | 52.1 | 0.3 | 1.681 | 0.014 | 16.57 | 0.15 | 7.56 | 0.12 | 6.90 | 0.04 | 9.19 | 0.05 | 3.86 | 0.04 | 0.685 | 0.021 | | |
| SMA1979-370 | -0.032 | -16.519 | -4212 | 33.9 | 51.9 | 0.2 | 1.602 | 0.024 | 16.55 | 0.10 | 7.39 | 0.12 | 7.03 | 0.04 | 9.35 | 0.07 | 3.76 | 0.08 | 0.685 | 0.019 | | |
| SMA1979-371 | -0.030 | -16.520 | -4292 | 33.7 | 52.0 | 0.2 | 1.626 | 0.036 | 16.58 | 0.11 | 7.46 | 0.17 | 6.81 | 0.10 | 9.25 | 0.04 | 3.90 | 0.02 | 0.663 | 0.020 | | |
| SMA1979-372 | -0.029 | -16.520 | -4356 | 33.5 | 52.1 | 0.2 | 1.588 | 0.042 | 16.48 | 0.05 | 7.29 | 0.04 | 6.79 | 0.04 | 9.81 | 0.05 | 3.60 | 0.06 | 0.683 | 0.027 | 0.280 | 0.051 |
| SMA1979-373 | -0.026 | -16.522 | -4324 | 33.2 | 51.5 | 0.4 | 1.466 | 0.015 | 16.78 | 0.13 | 7.04 | 0.06 | 6.75 | 0.09 | 10.01 | 0.09 | 3.67 | 0.07 | 0.663 | 0.013 | | |
| SMA1979-374 | -0.027 | -16.522 | -4263 | 33.2 | 52.0 | 0.1 | 1.421 | 0.032 | 16.96 | 0.13 | 6.87 | 0.07 | 7.12 | 0.02 | 10.15 | 0.12 | 3.62 | 0.06 | 0.665 | 0.023 | 0.286 | 0.030 |
| SMA1979-375 | -0.025 | -16.521 | -4332 | 33.1 | 52.1 | 0.3 | 1.406 | 0.040 | 16.93 | 0.07 | 6.94 | 0.07 | 7.34 | 0.07 | 10.06 | 0.06 | 3.51 | 0.02 | 0.668 | 0.017 | 0.297 | 0.052 |
| SMA1979-376 | -0.019 | -16.511 | -4087 | 32.8 | 52.4 | 0.4 | 1.991 | 0.085 | 16.07 | 0.13 | 8.92 | 0.13 | 6.35 | 0.10 | 8.93 | 0.12 | 3.88 | 0.10 | 0.600 | 0.023 | 0.341 | 0.032 |
| SMA1979-377 | -0.018 | -16.511 | -4005 | 32.7 | 52.2 | 0.2 | 1.894 | 0.058 | 16.10 | 0.17 | 8.79 | 0.11 | 6.53 | 0.08 | 9.08 | 0.08 | 3.83 | 0.09 | 0.574 | 0.015 | 0.339 | 0.028 |
| S1313-06 | -0.120 | -16.500 | -3500 | 43.3 | 52.4 | | 1.850 | | 15.41 | | 9.11 | | 5.93 | | 8.65 | | 4.31 | | 0.520 | | 0.320 | |
| S1313-10 | -0.120 | -16.500 | -3500 | 43.3 | 52.6 | 0.3 | 1.835 | 0.020 | 15.48 | 0.04 | 9.64 | 0.01 | 5.99 | 0.08 | 8.75 | 0.03 | 4.45 | 0.04 | 0.510 | 0.030 | 0.310 | 0.040 |
| S1313-11 | -0.017 | -16.433 | -3500 | 43.3 | 52.4 | | 1.900 | | 15.25 | | 9.30 | | 6.04 | | 8.56 | | 4.39 | | 0.540 | | 0.300 | |
| S1313-13 | -0.120 | -16.500 | -3500 | 43.3 | 52.5 | | 1.940 | | 15.37 | | 9.46 | | 5.97 | | 8.70 | | 4.37 | | 0.510 | | 0.260 | |
| S1313-20 | -0.120 | -16.500 | -3500 | 43.3 | 52.1 | | 1.860 | | 15.38 | | 8.49 | | 6.83 | | 8.67 | | 4.32 | | 0.600 | | 0.330 | |
| S1624-21 | -0.093 | -16.658 | -3350 | 35.2 | 51.0 | 0.1 | 1.640 | 0.080 | 16.15 | 0.04 | 7.64 | 0.02 | 7.33 | 0.09 | 9.39 | 0.00 | 3.80 | 0.07 | 0.570 | 0.020 | 0.300 | 0.080 |
| S1625-07 | -0.136 | -16.611 | -2400 | 42.0 | 52.0 | 0.3 | 1.645 | 0.020 | 16.56 | 0.04 | 7.79 | 0.01 | 7.37 | 0.01 | 9.95 | 0.08 | 3.98 | 0.19 | 0.565 | 0.060 | 0.310 | 0.010 |
| S1628-02 | -0.084 | -16.290 | -2600 | 47.3 | 51.6 | | 1.600 | | 16.26 | | 8.23 | | 6.69 | | 10.35 | | 3.44 | | 0.660 | | 0.250 | |
| S1628-02 Dup | -0.084 | -16.290 | -2600 | 47.3 | 51.0 | | 1.560 | | 16.01 | | 7.94 | | 6.69 | | 10.22 | | 3.57 | | 0.620 | | 0.220 | |
| **K-rich MORB** | | | | | | | | | | | | | | | | | | | | | | |
| SMA1966-128 | 0.057 | -16.974 | -5592 | 8.3 | 52.4 | 0.7 | 3.059 | 0.071 | 14.07 | 0.39 | 10.42 | 0.40 | 6.00 | 0.44 | 8.75 | 0.43 | 2.83 | 0.59 | 1.012 | 0.155 | 0.481 | 0.058 |
| SMA1974-283 | -0.042 | -16.462 | -3909 | 36.9 | 49.0 | 0.2 | 1.619 | 0.081 | 16.06 | 0.08 | 8.69 | 0.05 | 7.05 | 0.03 | 11.99 | 0.11 | 3.27 | 0.04 | 0.722 | 0.010 | 0.280 | 0.027 |
| SMA1974-285 | -0.042 | -16.463 | -3836 | 36.9 | 48.9 | 0.0 | 1.603 | 0.034 | 16.47 | 0.06 | 8.55 | 0.06 | 7.29 | 0.06 | 12.11 | 0.03 | 3.19 | 0.03 | 0.750 | 0.014 | 0.283 | 0.028 |

*Table S4.1 (continue)*

| **Sample** | **Lat** | **Long** | **Depth** | **Relative distance TF** | **$SiO_2$** | | **$TiO_2$** | | **$Al_2O_3$** | | **FeO** | | **MgO** | | **CaO** | | **$Na_2O$** | | **$K_2O$** | | **$P_2O_5$** | |
|---|---|---|---|---|---|---|---|---|---|---|---|---|---|---|---|---|---|---|---|---|---|---|
| | | | m | km | wt% | stdev | wt% | stdev | wt% | stdev | wt% | stdev | wt% | stdev | wt% | stdev | wt% | stdev | wt% | stdev | wt% | stdev |
| SMA1974-287 | -0.042 | -16.463 | -3799 | 36.9 | 48.4 | 0.1 | 1.593 | 0.074 | 16.78 | 0.05 | 8.19 | 0.06 | 7.33 | 0.09 | 12.05 | 0.09 | 3.03 | 0.01 | 0.751 | 0.009 | 0.291 | 0.028 |
| SMA1976-315 | -0.003 | -16.649 | -3969 | 26.1 | 50.1 | 0.2 | 1.947 | 0.065 | 16.12 | 0.04 | 8.74 | 0.03 | 6.31 | 0.06 | 10.60 | 0.06 | 3.68 | 0.05 | 0.857 | 0.014 | 0.393 | 0.055 |
| SMA1976-317 | -0.003 | -16.648 | -3922 | 26.2 | 49.8 | 0.2 | 2.019 | 0.043 | 16.20 | 0.08 | 8.87 | 0.08 | 6.08 | 0.11 | 10.66 | 0.05 | 3.76 | 0.04 | 0.858 | 0.019 | 0.416 | 0.040 |
| SMA1976-319 | -0.003 | -16.642 | -3880 | 26.5 | 50.2 | 0.3 | 1.929 | 0.060 | 16.39 | 0.11 | 8.74 | 0.10 | 6.19 | 0.09 | 10.67 | 0.09 | 3.70 | 0.07 | 0.857 | 0.030 | 0.381 | 0.069 |
| SMA1976-320 | -0.003 | -16.643 | -3869 | 26.4 | 50.0 | 0.2 | 1.905 | 0.066 | 16.43 | 0.11 | 8.89 | 0.06 | 6.18 | 0.06 | 10.62 | 0.04 | 3.71 | 0.05 | 0.823 | 0.019 | 0.379 | 0.037 |
| SMA1976-321 | -0.006 | -16.642 | -3918 | 26.7 | 50.1 | 0.1 | 1.985 | 0.048 | 16.37 | 0.11 | 8.84 | 0.10 | 5.95 | 0.09 | 10.62 | 0.12 | 3.78 | 0.04 | 0.923 | 0.007 | 0.390 | 0.063 |
| SMA1976-323 | -0.006 | -16.641 | -3868 | 26.8 | 50.5 | 0.4 | 1.941 | 0.089 | 16.15 | 0.10 | 8.90 | 0.10 | 6.04 | 0.02 | 10.69 | 0.17 | 3.64 | 0.05 | 0.843 | 0.011 | 0.419 | 0.039 |
| SMA1976-324 | -0.007 | -16.642 | -3891 | 26.9 | 49.9 | 0.1 | 2.023 | 0.106 | 16.03 | 0.08 | 9.03 | 0.10 | 6.42 | 0.06 | 10.55 | 0.10 | 3.68 | 0.06 | 0.888 | 0.006 | 0.407 | 0.017 |
| SMA1976-325 | -0.008 | -16.641 | -3847 | 27.0 | 50.5 | 0.1 | 1.968 | 0.033 | 16.41 | 0.06 | 8.79 | 0.12 | 6.03 | 0.05 | 10.72 | 0.07 | 3.62 | 0.05 | 0.868 | 0.026 | 0.397 | 0.020 |
| S1311-03 | -0.017 | -16.433 | -3500 | 35.2 | 47.6 | 0.1 | 2.485 | 0.060 | 14.51 | 0.19 | 10.11 | 0.01 | 7.74 | 0.15 | 11.04 | 0.02 | 3.83 | 0.01 | 1.250 | 0.000 | 0.605 | 0.090 |
| S1312-45 | -0.080 | -16.383 | -2800 | 43.9 | 51.2 | | 2.360 | | 15.13 | | 9.51 | | 6.37 | | 9.04 | | 3.97 | | 1.000 | | 0.550 | |
| S1312-49 | -0.080 | -16.383 | -2800 | 43.9 | 44.3 | 0.1 | 3.015 | 0.010 | 14.89 | 0.00 | 9.17 | 0.06 | 7.60 | 0.06 | 12.40 | 0.08 | 3.86 | 0.05 | 1.945 | 0.040 | 0.870 | 0.040 |
| S1312-B | -0.080 | -16.383 | -2800 | 43.9 | 47.5 | | 2.590 | | 14.48 | | 10.32 | | 7.81 | | 10.63 | | 3.68 | | 1.180 | | 0.590 | |
| S1312-Xb | -0.080 | -16.383 | -2800 | 43.9 | 51.0 | 0.3 | 2.366 | 0.091 | 15.06 | 0.21 | 9.30 | 0.06 | 6.33 | 0.12 | 9.21 | 0.07 | 3.77 | 0.09 | 1.000 | 0.004 | 0.487 | 0.039 |
| S1626-15 A | -0.018 | -16.333 | -3000 | 39.1 | 50.5 | | 1.970 | | 15.35 | | 8.97 | | 6.85 | | 9.18 | | 3.98 | | 0.870 | | 0.340 | |
| S1626-15 F | -0.018 | -16.333 | -3000 | 39.1 | 50.5 | | 1.970 | | 15.35 | | 8.97 | | 6.85 | | 9.18 | | 3.98 | | 0.870 | | 0.340 | |
| S1626-15 F | -0.018 | -16.333 | -3000 | 39.1 | 50.5 | | 1.970 | | 15.35 | | 8.97 | | 6.85 | | 9.18 | | 3.98 | | 0.870 | | 0.340 | |
| S1626-21 | -0.018 | -16.333 | -3000 | 39.1 | 50.4 | | 1.950 | | 15.16 | | 8.98 | | 6.66 | | 9.07 | | 3.91 | | 0.850 | | 0.380 | |
| S1626-22 | -0.018 | -16.333 | -3000 | 39.1 | 51.1 | | 2.040 | | 15.51 | | 9.22 | | 6.83 | | 9.30 | | 3.85 | | 0.900 | | 0.320 | |
| S1626-22 Dup | -0.018 | -16.333 | -3000 | 39.1 | 50.4 | | 1.980 | | 15.21 | | 9.05 | | 6.68 | | 9.22 | | 3.93 | | 0.850 | | 0.450 | |
| S1626-23 | -0.018 | -16.333 | -3000 | 39.1 | 50.0 | | 1.960 | | 15.15 | | 8.90 | | 6.76 | | 9.21 | | 4.08 | | 0.860 | | 0.410 | |

*Data without standard deviation are from the first set of samples previously analysed at Lamont Doherty Earth Observatory (Cipriani, A.).*

## *Table S4.2 - Trace elements measured with LA-ICP-MS*

| **Sample** | | **Rb** | | **Sr** | | **Y** | | **Zr** | | **Nb** | | **Mo** | | **Cs** | | **Ba** | | **La** | | **Ce** | |
|---|---|---|---|---|---|---|---|---|---|---|---|---|---|---|---|---|---|---|---|---|---|
| **N-MORB** | | ppm | stdev | ppm | stdev | ppm | stdev | ppm | stdev | ppm | stdev | ppm | stdev | ppm | stdev | ppm | stdev | ppm | stdev | ppm | stdev |
| SMA1977-328 | B | 4.014 | 0.052 | 150.7 | 0.3 | 25.161 | 0.122 | 85.892 | 0.089 | 7.289 | 0.056 | 0.434 | 0.009 | 0.048 | 0.007 | 46.780 | 0.466 | 5.688 | 0.025 | 15.25 | 0.15 |
| SMA1977-329 | B | 2.708 | 0.056 | 124.4 | 0.5 | 30.747 | 0.290 | 102.620 | 0.683 | 4.973 | 0.012 | 0.365 | 0.002 | | | 28.148 | 0.117 | 4.670 | 0.026 | 13.46 | 0.09 |
| SMA1977-330 | B | 2.765 | 0.026 | 124.7 | 0.4 | 30.848 | 0.386 | 103.966 | 0.953 | 5.172 | 0.010 | 0.357 | 0.014 | 0.018 | 0.013 | 28.923 | 0.038 | 4.798 | 0.019 | 13.99 | 0.03 |
| SMA1977-331 | B | 2.742 | 0.037 | 123.8 | 0.6 | 30.281 | 0.164 | 102.769 | 0.416 | 5.073 | 0.027 | 0.372 | 0.012 | | | 28.551 | 0.210 | 4.635 | 0.020 | 13.68 | 0.09 |
| SMA1977-334 | B | 2.880 | 0.016 | 124.4 | 0.8 | 29.721 | 0.119 | 101.893 | 0.678 | 5.322 | 0.030 | 0.388 | 0.034 | 0.025 | 0.004 | 29.598 | 0.118 | 4.715 | 0.020 | 14.08 | 0.10 |
| SMA1977-335 | B | 2.925 | 0.034 | 125.6 | 0.4 | 31.125 | 0.092 | 105.708 | 0.306 | 5.377 | 0.009 | 0.367 | 0.031 | | | 29.954 | 0.102 | 4.870 | 0.011 | 14.25 | 0.02 |
| SMA1977-336 | B | 2.709 | 0.024 | 120.8 | 0.3 | 31.676 | 0.235 | 99.859 | 1.225 | 5.360 | 0.086 | 0.371 | 0.027 | 0.032 | 0.003 | 29.937 | 0.185 | 5.027 | 0.037 | 14.49 | 0.15 |
| SMA1977-337 | B | 3.102 | 0.037 | 123.2 | 0.7 | 30.030 | 0.575 | 102.599 | 2.113 | 5.617 | 0.019 | 0.413 | 0.050 | | | 31.148 | 0.302 | 4.858 | 0.058 | 14.88 | 0.11 |
| SMA1977-338 | B | 2.865 | 0.045 | 123.9 | 0.1 | 31.174 | 0.143 | 107.572 | 0.751 | 5.284 | 0.031 | 0.359 | 0.008 | | | 29.193 | 0.151 | 4.816 | 0.013 | 14.03 | 0.05 |
| SMA1977-340 | B | 2.870 | 0.018 | 122.9 | 0.4 | 31.602 | 0.166 | 108.105 | 0.543 | 5.347 | 0.013 | 0.373 | 0.001 | | | 28.918 | 0.084 | 4.810 | 0.018 | 14.00 | 0.08 |
| SMA1977-341B | B | 2.703 | 0.022 | 124.1 | 0.3 | 30.041 | 0.524 | 102.165 | 1.855 | 5.014 | 0.018 | 0.340 | 0.010 | | | 28.058 | 0.068 | 4.568 | 0.023 | 13.49 | 0.07 |
| SMA1977-341T | B | 2.680 | 0.035 | 124.6 | 0.2 | 30.186 | 0.241 | 102.849 | 0.880 | 4.997 | 0.011 | 0.359 | 0.015 | | | 28.055 | 0.161 | 4.562 | 0.024 | 13.44 | 0.05 |
| SMA1977-342 | B | 2.942 | 0.009 | 121.5 | 0.4 | 31.061 | 0.183 | 107.667 | 0.649 | 5.376 | 0.042 | 0.375 | 0.027 | | | 29.223 | 0.042 | 4.765 | 0.024 | 13.93 | 0.09 |
| SMA1977-343 | B | 2.878 | 0.011 | 121.4 | 0.4 | 31.137 | 0.022 | 107.189 | 0.340 | 5.328 | 0.034 | 0.393 | 0.006 | | | 29.253 | 0.093 | 4.757 | 0.030 | 13.92 | 0.06 |
| SMA1978-345 | B | 3.192 | 0.040 | 150.2 | 0.9 | 27.955 | 0.250 | 96.691 | 1.236 | 6.037 | 0.023 | 0.386 | 0.010 | 0.039 | 0.002 | 37.026 | 0.296 | 5.468 | 0.041 | 14.60 | 0.06 |
| SMA1978-346 | B | 3.168 | 0.022 | 148.9 | 0.4 | 26.136 | 0.355 | 91.725 | 0.936 | 6.040 | 0.013 | 0.404 | 0.020 | 0.030 | 0.001 | 36.772 | 0.070 | 5.294 | 0.030 | 14.51 | 0.04 |
| SMA1978-348 | B | 3.611 | 0.028 | 151.5 | 0.9 | 29.074 | 0.272 | 109.082 | 0.901 | 6.409 | 0.028 | 0.474 | 0.015 | | | 38.627 | 0.067 | 5.511 | 0.011 | 15.38 | 0.11 |
| SMA1978-349 | B | 3.746 | 0.017 | 144.2 | 0.6 | 30.948 | 0.085 | 116.377 | 0.277 | 6.756 | 0.071 | 0.451 | 0.006 | | | 38.947 | 0.313 | 5.797 | 0.018 | 16.23 | 0.10 |
| SMA1978-350 | B | 3.386 | 0.065 | 159.6 | 1.7 | 25.313 | 0.118 | 102.383 | 0.321 | 5.907 | 0.063 | 0.483 | 0.045 | 0.041 | 0.008 | 39.280 | 0.449 | 5.216 | 0.009 | 15.33 | 0.15 |
| SMA1978-352 | B | 3.342 | 0.025 | 151.9 | 0.6 | 26.026 | 0.265 | 104.903 | 1.302 | 5.758 | 0.051 | 0.433 | 0.050 | 0.040 | 0.003 | 38.505 | 0.141 | 5.282 | 0.027 | 15.19 | 0.04 |
| SMA1978-354 | B | 3.755 | 0.028 | 144.8 | 0.7 | 30.584 | 0.746 | 108.454 | 1.693 | 6.444 | 0.011 | | 0.000 | 0.049 | 0.005 | 39.171 | 0.124 | 5.871 | 0.075 | 16.37 | 0.07 |
| SMA1978-355 | B | 3.320 | 0.197 | 140.8 | 1.7 | 29.374 | 0.257 | 100.671 | 1.236 | 6.306 | 0.009 | 0.441 | 0.016 | 0.044 | 0.003 | 37.031 | 0.183 | 5.645 | 0.017 | 15.51 | 0.08 |
| SMA1978-356 | B | 3.642 | 0.019 | 143.3 | 0.5 | 30.108 | 0.269 | 106.498 | 0.238 | 6.409 | 0.019 | | 0.000 | 0.047 | 0.002 | 26.291 | 18.592 | 5.884 | 0.037 | 16.58 | 0.15 |
| SMA1978-357 | B | 3.824 | 0.072 | 146.6 | 1.6 | 30.360 | 0.438 | 112.663 | 1.111 | 6.648 | 0.143 | | 0.000 | 0.047 | 0.003 | 38.671 | 0.764 | 5.784 | 0.067 | 16.28 | 0.36 |
| SMA1978-358 | B | 3.812 | 0.051 | 145.0 | 0.4 | 29.477 | 0.128 | 109.411 | 0.325 | 6.558 | 0.023 | | 0.000 | 0.048 | 0.006 | 38.211 | 0.147 | 5.675 | 0.025 | 16.07 | 0.07 |
| SMA1978-360 | B | 3.814 | 0.039 | 144.2 | 0.1 | 29.045 | 0.221 | 108.483 | 0.491 | 6.567 | 0.046 | | 0.000 | 0.048 | 0.003 | 38.383 | 0.057 | 5.598 | 0.048 | 15.99 | 0.02 |
| SMA1978-363 | B | 3.582 | 0.043 | 152.8 | 0.8 | 27.017 | 0.152 | 101.272 | 0.770 | 6.279 | 0.008 | | 0.000 | 0.030 | 0.021 | 38.474 | 0.475 | 5.301 | 0.061 | 15.25 | 0.11 |
| SMA1978-364 | B | 3.098 | 0.013 | 143.7 | 0.6 | 29.443 | 0.033 | 100.236 | 0.188 | 6.323 | 0.040 | 0.411 | 0.027 | 0.037 | 0.001 | 37.682 | 0.256 | 5.742 | 0.028 | 15.82 | 0.04 |
| S1312-Xa | L | 9.818 | 0.130 | 223.9 | 2.4 | 55.674 | 0.997 | 226.729 | 4.220 | 18.399 | 0.380 | 1.013 | 0.086 | 0.108 | 0.007 | 118.329 | 1.495 | 15.364 | 0.258 | 32.23 | 0.34 |
| S1312-53 | L | 3.700 | | 168.0 | | 27.700 | | 100.000 | | 8.700 | | | | 0.070 | | 61.000 | | 7.100 | | 16.60 | |
| S1314 | L | 4.900 | | 192.1 | | 27.830 | | 101.990 | | 7.090 | | 0.780 | | 0.080 | | 43.010 | | 6.190 | | 15.30 | |

*Table S4.2 (continue)*

| **Sample** | | **Rb** | | **Sr** | | **Y** | | **Zr** | | **Nb** | | **Mo** | | **Cs** | | **Ba** | | **La** | | **Ce** | |
|---|---|---|---|---|---|---|---|---|---|---|---|---|---|---|---|---|---|---|---|---|---|
| | | ppm | stdev | ppm | stdev | ppm | stdev | ppm | stdev | ppm | stdev | ppm | stdev | ppm | stdev | ppm | stdev | ppm | stdev | ppm | stdev |
| S1314-X | | 5.307 | 0.098 | 193.6 | 0.5 | 23.993 | 0.182 | 106.445 | 1.159 | 8.007 | 0.030 | 0.815 | 0.053 | 0.054 | 0.009 | 46.217 | 0.237 | 6.048 | 0.002 | 16.11 | 0.08 |
| S1314-01 | L | 5.240 | | 193.7 | | 28.930 | | 104.210 | | 7.250 | | 0.780 | | 0.080 | | 43.710 | | 6.410 | | 15.25 | |
| S1314-01 Dup | L | 4.50 | | 189.00 | | 27.50 | | 113.00 | | 7.60 | | | | 0.09 | | 47.00 | | 6.08 | | 16.30 | |
| S1627-01 | L | 6.50 | | 169.00 | | 32.00 | | 112.00 | | 8.40 | | | | 0.09 | | 65.00 | | 7.20 | | 18.70 | |
| S1629-35 | L | 2.62 | | 131.07 | | 31.57 | | 92.56 | | 4.78 | | 0.39 | | 0.03 | | 28.05 | | 4.94 | | 13.28 | |
| S1629-35 Dup | L | 2.50 | | 129.00 | | 31.00 | | 98.00 | | 4.50 | | | | 0.05 | | 29.00 | | 4.98 | | 13.20 | |
| S1639-03 | L | 7.20 | | 171.91 | | 32.99 | | 120.53 | | 8.52 | | | | 0.06 | | 53.07 | | 7.16 | | 19.96 | |
| **E-MORB** | | | | | | | | | | | | | | | | | | | | | |
| SMA1970-191A | B | 9.188 | 0.228 | 249.8 | 0.4 | 27.014 | 0.206 | 130.304 | 1.145 | 15.035 | 0.069 | 0.833 | 0.029 | 0.109 | 0.010 | 104.494 | 0.363 | 11.032 | 0.031 | 25.92 | 0.28 |
| SMA1970-191B | B | 8.950 | 0.018 | 251.6 | 0.8 | 27.594 | 0.241 | 132.702 | 0.810 | 15.255 | 0.060 | 0.825 | 0.018 | 0.102 | 0.004 | 106.376 | 0.875 | 11.295 | 0.057 | 26.48 | 0.23 |
| SMA1970-191C | B | 10.359 | 0.240 | 245.2 | 1.8 | 26.656 | 0.205 | 141.808 | 0.646 | 15.735 | 0.379 | 1.035 | 0.004 | 0.097 | 0.014 | 105.131 | 0.932 | 10.788 | 0.100 | 26.41 | 0.35 |
| SMA1970-191D | B | 9.978 | 0.122 | 244.9 | 1.7 | 27.923 | 0.095 | 145.992 | 0.854 | 15.299 | 0.181 | 0.776 | 0.069 | 0.111 | 0.006 | 103.607 | 0.729 | 10.998 | 0.070 | 26.15 | 0.12 |
| SMA1970-191E | B | 9.365 | 0.084 | 246.7 | 1.6 | 27.773 | 0.037 | 133.888 | 0.455 | 15.516 | 0.010 | 0.885 | 0.083 | 0.089 | 0.005 | 106.124 | 0.311 | 11.255 | 0.047 | 26.75 | 0.12 |
| SMA1970-192 | B | 9.236 | | 244.4 | 0.7 | 27.259 | 0.346 | 132.096 | 1.243 | 15.188 | 0.011 | 0.841 | 0.032 | 0.086 | 0.008 | 105.108 | 0.594 | 11.052 | 0.098 | 26.30 | 0.31 |
| SMA1970-193 | B | 8.924 | 0.078 | 239.1 | 1.3 | 26.411 | 0.255 | 129.629 | 1.192 | 15.124 | 0.145 | 0.848 | 0.033 | 0.084 | 0.005 | 104.147 | 0.520 | 10.903 | 0.090 | 25.82 | 0.26 |
| SMA1970-194 | B | 8.711 | 0.016 | 236.4 | 0.6 | 25.459 | 0.142 | 125.132 | 0.512 | 14.784 | 0.045 | 0.821 | 0.017 | 0.083 | 0.002 | 101.353 | 0.354 | 10.445 | 0.028 | 24.83 | 0.13 |
| SMA1970-195 | B | 8.888 | 0.024 | 242.5 | 0.4 | 26.930 | 0.137 | 131.381 | 0.910 | 15.016 | 0.050 | 0.839 | 0.019 | 0.082 | 0.006 | 104.007 | 0.381 | 11.022 | 0.059 | 25.89 | 0.10 |
| SMA1970-199 | B | 8.371 | 0.172 | 240.7 | 0.4 | 26.203 | 0.130 | 125.377 | 0.404 | 14.051 | 0.040 | 0.775 | 0.034 | 0.096 | 0.003 | 97.241 | 0.610 | 10.415 | 0.034 | 24.83 | 0.11 |
| SMA1970-202 | B | 6.951 | 0.014 | 230.3 | 0.3 | 23.978 | 0.164 | 111.164 | 1.039 | 11.895 | 0.020 | 0.644 | 0.025 | 0.067 | 0.002 | 81.166 | 0.362 | 8.845 | 0.014 | 21.46 | 0.17 |
| SMA1973-246 | B | 5.481 | 0.038 | 234.6 | 0.3 | 20.292 | 0.094 | 76.870 | 0.457 | 8.715 | 0.032 | 0.633 | 0.001 | 0.050 | 0.004 | 65.192 | 0.190 | 6.995 | 0.012 | 17.61 | 0.01 |
| SMA1973-248 | B | 9.574 | 0.063 | 190.7 | 0.8 | 24.344 | 0.167 | 104.596 | 0.765 | 15.846 | 0.076 | 0.909 | 0.025 | 0.111 | 0.003 | 103.944 | 0.442 | 10.655 | 0.033 | 25.00 | 0.11 |
| SMA1973-249 | B | 7.631 | 0.039 | 186.5 | 1.0 | 21.321 | 0.146 | 79.411 | 0.684 | 12.153 | 0.166 | 0.657 | 0.024 | 0.081 | 0.002 | 81.559 | 0.809 | 7.947 | 0.117 | 18.65 | 0.18 |
| SMA1973-250 | B | 10.124 | 0.164 | 199.9 | 1.4 | 26.674 | 0.377 | 112.626 | 0.774 | 16.424 | 0.164 | 0.943 | 0.011 | 0.113 | 0.004 | 106.693 | 1.173 | 11.025 | 0.134 | 25.13 | 0.24 |
| SMA1973-251 | B | 10.860 | 0.510 | 201.3 | 3.3 | 25.814 | 0.889 | 112.369 | 3.586 | 17.840 | 0.576 | 1.042 | 0.064 | 0.122 | 0.004 | 113.611 | 3.505 | 11.589 | 0.316 | 27.29 | 1.16 |
| SMA1973-252 | B | 9.166 | 0.303 | 185.8 | 0.2 | 25.540 | 0.125 | 108.639 | 0.300 | 15.192 | 0.201 | 0.855 | 0.035 | 0.108 | 0.008 | 98.506 | 0.727 | 10.371 | 0.046 | 23.47 | 0.14 |
| SMA1973-254 | B | 10.739 | 0.052 | 197.5 | 3.4 | 27.141 | 0.419 | 123.538 | 1.465 | 17.712 | 0.276 | 1.021 | 0.018 | 0.121 | 0.002 | 109.348 | 2.029 | 11.324 | 0.203 | 26.20 | 0.20 |
| SMA1973-255 | B | 10.595 | 0.137 | 193.6 | 2.6 | 25.402 | 0.425 | 115.756 | 1.833 | 17.364 | 0.157 | 1.006 | 0.021 | 0.118 | 0.003 | 105.512 | 1.767 | 10.666 | 0.110 | 25.50 | 0.62 |
| SMA1973-256 | B | 9.818 | 0.313 | 194.0 | 2.2 | 25.150 | 0.732 | 113.499 | 3.099 | 16.178 | 0.428 | 0.939 | 0.017 | 0.109 | 0.004 | 101.840 | 1.711 | 10.185 | 0.261 | 24.18 | 0.65 |
| SMA1973-258 | B | 9.953 | 0.072 | 190.3 | 0.7 | 27.162 | 0.233 | 122.709 | 0.527 | 16.738 | 0.020 | 0.953 | 0.021 | 0.108 | 0.002 | 103.623 | 0.093 | 10.824 | 0.006 | 24.71 | 0.10 |
| SMA1973-261 | B | 7.004 | 0.087 | 223.2 | 1.6 | 22.654 | 0.141 | 98.077 | 0.137 | 10.724 | 0.041 | 0.709 | 0.021 | 0.072 | 0.004 | 72.614 | 0.389 | 7.551 | 0.033 | 19.21 | 0.13 |
| SMA1973-262 | B | 6.516 | 0.060 | 212.5 | 1.2 | 21.724 | 0.270 | 92.735 | 1.094 | 9.825 | 0.043 | 0.650 | 0.014 | 0.066 | 0.002 | 67.156 | 0.224 | 7.003 | 0.051 | 18.30 | 0.17 |

*Table S4.2 (continue)*

| **Sample** | | **Rb** | | **Sr** | | **Y** | | **Zr** | | **Nb** | | **Mo** | | **Cs** | | **Ba** | | **La** | | **Ce** | |
|---|---|---|---|---|---|---|---|---|---|---|---|---|---|---|---|---|---|---|---|---|---|
| | | ppm | stdev | ppm | stdev | ppm | stdev | ppm | stdev | ppm | stdev | ppm | stdev | ppm | stdev | ppm | stdev | ppm | stdev | ppm | stdev |
| SMA1973-263 | B | 7.024 | 0.169 | 217.6 | 1.7 | 21.722 | 0.213 | 93.022 | 0.877 | 10.619 | 0.064 | 0.730 | 0.010 | 0.075 | 0.007 | 73.371 | 1.110 | 7.392 | 0.039 | 19.24 | 0.22 |
| SMA1973-264 | B | 9.187 | 0.143 | 192.1 | 2.7 | 24.598 | 0.586 | 104.684 | 1.501 | 15.273 | 0.300 | 0.864 | 0.003 | 0.107 | 0.001 | 100.015 | 1.179 | 10.264 | 0.191 | 23.79 | 0.44 |
| SMA1974-266 | B | 7.774 | 0.043 | 192.0 | 0.9 | 22.986 | 0.392 | 91.947 | 1.433 | 12.225 | 0.062 | 0.767 | 0.034 | 0.085 | 0.002 | 78.492 | 0.369 | 8.279 | 0.064 | 20.92 | 0.15 |
| SMA1974-267 | B | 7.946 | 0.054 | 193.9 | 0.8 | 23.301 | 0.357 | 93.114 | 1.420 | 12.536 | 0.043 | 0.800 | 0.020 | 0.085 | 0.002 | 80.907 | 0.464 | 8.533 | 0.149 | 21.94 | 0.24 |
| SMA1974-271 | B | 7.351 | 0.064 | 196.4 | 0.2 | 22.266 | 0.113 | 87.395 | 0.341 | 11.399 | 0.090 | 0.725 | 0.025 | 0.074 | 0.003 | 77.814 | 0.244 | 7.878 | 0.013 | 19.99 | 0.15 |
| SMA1974-272 | B | 7.445 | 0.071 | 197.8 | 0.9 | 23.279 | 0.129 | 97.585 | 0.217 | 11.474 | 0.083 | 0.748 | 0.014 | 0.079 | 0.001 | 74.134 | 0.564 | 7.733 | 0.032 | 19.24 | 0.14 |
| SMA1974-273 | B | 7.360 | 0.040 | 189.0 | 1.3 | 22.570 | 0.043 | 95.098 | 0.660 | 11.315 | 0.023 | 0.739 | 0.005 | 0.079 | 0.002 | 73.705 | 0.617 | 7.578 | 0.032 | 19.07 | 0.10 |
| SMA1974-274 | B | 7.434 | 0.080 | 196.9 | 2.0 | 23.385 | 0.203 | 99.907 | 0.635 | 11.414 | 0.048 | 0.760 | 0.001 | 0.078 | 0.004 | 74.804 | 0.195 | 7.624 | 0.037 | 19.12 | 0.01 |
| SMA1974-275 | B | 7.583 | 0.070 | 194.2 | 2.0 | 24.319 | 0.405 | 105.614 | 1.796 | 11.899 | 0.120 | 0.766 | 0.020 | 0.080 | 0.002 | 77.925 | 0.711 | 8.065 | 0.142 | 19.88 | 0.13 |
| SMA1974-276 | B | 7.929 | 0.120 | 194.0 | 3.5 | 23.015 | 0.492 | 102.093 | 1.911 | 12.058 | 0.167 | 0.812 | 0.011 | 0.082 | 0.003 | 80.624 | 1.436 | 7.902 | 0.147 | 20.53 | 0.14 |
| SMA1974-277 | B | 8.056 | 0.064 | 193.1 | 0.7 | 22.426 | 0.181 | 99.677 | 0.219 | 11.860 | 0.088 | 0.791 | 0.016 | 0.081 | 0.002 | 80.032 | 0.524 | 7.743 | 0.010 | 20.46 | 0.13 |
| SMA1979-365 | M | 13.797 | 0.087 | 219.2 | 1.1 | 27.673 | 0.546 | 143.133 | 3.027 | 20.293 | 0.083 | 1.299 | 0.040 | | | 140.600 | 0.668 | 14.017 | 0.101 | 31.08 | 0.22 |
| SMA1979-366 | M | 13.373 | 0.167 | 223.6 | 0.6 | 25.237 | 0.273 | 131.767 | 1.302 | 20.167 | 0.076 | 1.288 | 0.031 | | | 136.667 | 0.492 | 13.763 | 0.098 | 29.44 | 0.12 |
| SMA1979-367 | M | 13.560 | 0.060 | 233.7 | 0.0 | 24.935 | 0.005 | 130.300 | 0.400 | 20.475 | 0.025 | 1.154 | 0.040 | | | 141.450 | 0.650 | 14.140 | 0.010 | 29.53 | 0.11 |
| SMA1979-367 Dup | B | 11.561 | 0.139 | 215.1 | 0.6 | 22.415 | 0.178 | 117.070 | 0.872 | 19.435 | 0.100 | 1.107 | 0.022 | 0.130 | 0.001 | 130.711 | 0.784 | 12.815 | 0.059 | 27.71 | 0.18 |
| SMA1979-368 | B | 10.265 | 0.051 | 196.8 | 0.5 | 30.462 | 0.215 | 146.657 | 0.470 | 16.979 | 0.149 | 0.968 | 0.011 | 0.108 | 0.002 | 111.864 | 0.380 | 12.194 | 0.076 | 28.32 | 0.22 |
| SMA1979-369 | B | 13.091 | 0.083 | 217.2 | 0.8 | 26.803 | 0.266 | 137.748 | 1.639 | 20.355 | 0.105 | 1.252 | 0.005 | 0.150 | 0.002 | 137.647 | 0.449 | 13.640 | 0.003 | 31.45 | 0.09 |
| SMA1979-370 | B | 13.118 | 0.240 | 220.3 | 1.8 | 24.977 | 0.315 | 130.205 | 1.507 | 20.473 | 0.042 | 1.222 | 0.032 | 0.148 | 0.007 | 140.335 | 1.069 | 13.510 | 0.098 | 31.26 | 0.44 |
| SMA1979-371 | B | 12.756 | 0.125 | 216.2 | 0.7 | 26.154 | 0.329 | 136.266 | 1.982 | 20.159 | 0.022 | 1.184 | 0.045 | 0.138 | 0.005 | 135.639 | 0.210 | 13.349 | 0.086 | 30.69 | 0.06 |
| SMA1979-372 | B | 12.381 | 0.203 | 215.3 | 0.8 | 25.435 | 0.182 | 129.840 | 1.135 | 20.088 | 0.037 | 1.153 | 0.038 | 0.129 | 0.004 | 134.232 | 1.433 | 13.236 | 0.087 | 30.32 | 0.26 |
| SMA1979-373 | B | 12.843 | 0.167 | 216.1 | 2.0 | 20.722 | 0.578 | 107.590 | 3.320 | 20.814 | 0.406 | 1.196 | 0.054 | 0.141 | 0.004 | 139.713 | 1.885 | 12.793 | 0.259 | 29.69 | 0.38 |
| SMA1979-374 | B | 12.450 | 0.075 | 220.5 | 1.7 | 21.313 | 0.442 | 111.322 | 2.097 | 20.251 | 0.115 | 1.166 | 0.007 | 0.133 | 0.000 | 137.815 | 0.620 | 12.923 | 0.184 | 29.15 | 0.06 |
| SMA1979-375 | B | 14.088 | 0.265 | 226.2 | 3.1 | 22.923 | 0.183 | 127.273 | 1.476 | 20.371 | 0.074 | 1.168 | 0.053 | 0.166 | 0.006 | 138.481 | 0.942 | 13.055 | 0.117 | 29.29 | 0.42 |
| SMA1979-376 | B | 12.615 | 0.078 | 197.1 | 0.5 | 36.973 | 0.391 | 190.235 | 0.769 | 19.211 | 0.156 | 1.255 | 0.034 | 0.145 | 0.009 | 112.093 | 0.544 | 13.424 | 0.092 | 32.91 | 0.34 |
| SMA1979-377 | B | 12.674 | 0.076 | 205.1 | 0.8 | 32.868 | 0.334 | 169.982 | 2.375 | 18.715 | 0.030 | 1.338 | 0.128 | 0.145 | 0.010 | 110.074 | 0.372 | 12.633 | 0.038 | 31.78 | 0.05 |
| S1313-06 | L | 9.47 | | 208.14 | | 36.84 | | 151.63 | | 14.51 | | 1.12 | | 0.11 | | 95.70 | | 11.72 | | 26.18 | |
| S1313-06 Dup | L | 9.00 | | 202.00 | | 36.00 | | 164.00 | | 12.50 | | | | 0.06 | | 100.00 | | 10.50 | | 27.40 | |
| S1313-10 | L | 9.10 | | 204.00 | | 36.00 | | 167.00 | | 13.00 | | | | 0.10 | | 105.00 | | 10.70 | | 27.80 | |
| S1313-11 | L | 9.45 | | 205.47 | | 37.25 | | 153.46 | | 14.25 | | 1.07 | | 0.11 | | 96.20 | | 11.91 | | 26.68 | |
| S1313-11 Dup | L | 9.00 | | 211.00 | | 34.00 | | 168.00 | | 15.30 | | | | 0.05 | | 104.00 | | 11.00 | | 27.60 | |
| S1313-13 | L | 9.25 | | 204.33 | | 36.26 | | 151.48 | | 14.13 | | 1.05 | | 0.11 | | 95.57 | | 11.73 | | 26.30 | |

*Table S4.2 (continue)*

| **Sample** | | **Rb** | | **Sr** | | **Y** | | **Zr** | | **Nb** | | **Mo** | | **Cs** | | **Ba** | | **La** | | **Ce** | |
|---|---|---|---|---|---|---|---|---|---|---|---|---|---|---|---|---|---|---|---|---|---|
| | | ppm | stdev | ppm | stdev | ppm | stdev | ppm | stdev | ppm | stdev | ppm | stdev | ppm | stdev | ppm | stdev | ppm | stdev | ppm | stdev |
| S1624-21 | L | 10.640 | | 219.3 | | 29.930 | | 130.830 | | 15.830 | | 0.970 | | 0.120 | | 116.400 | | 12.470 | | 27.03 | |
| S1624-21 Dup | L | 9.700 | | 216.0 | | 30.000 | | 143.000 | | 15.000 | | | | 0.090 | | 122.000 | | 11.800 | | 28.20 | |
| S1625-07 | L | 10.800 | | 219.0 | | 30.000 | | 149.000 | | 14.000 | | | | 0.240 | | 129.000 | | 11.000 | | 30.00 | |
| S1628-02 | L | 11.430 | | 254.8 | | 29.200 | | 131.250 | | 19.130 | | 1.160 | | 0.150 | | 133.210 | | 14.430 | | 30.27 | |
| S1628-02 Dup | L | 11.500 | | 256.9 | | 29.100 | | 131.050 | | 19.350 | | 1.230 | | 0.140 | | 134.030 | | 14.430 | | 30.39 | |
| **K-rich MORB** | | | | | | | | | | | | | | | | | | | | | |
| SMA1966-128 | M | 19.473 | 0.596 | 487.1 | 5.5 | 22.017 | 0.315 | 193.433 | 1.893 | 30.830 | 0.213 | 2.119 | 0.059 | | | 239.200 | 2.238 | 22.233 | 0.336 | 48.07 | 0.61 |
| SMA1974-283 | M | 13.783 | 0.149 | 300.0 | 2.8 | 21.090 | 0.008 | 115.033 | 0.713 | 22.207 | 0.327 | 1.148 | 0.004 | | | 165.467 | 1.543 | 15.397 | 0.109 | 32.28 | 0.27 |
| SMA1974-285 | M | 13.413 | 1.133 | 333.2 | 16.0 | 17.730 | 1.153 | 103.870 | 6.600 | 20.553 | 1.093 | 1.051 | 0.073 | | | 163.633 | 6.440 | 14.840 | 0.850 | 31.12 | 1.58 |
| SMA1974-287 | M | 13.917 | 0.135 | 314.6 | 4.2 | 18.423 | 0.271 | 107.633 | 1.666 | 21.950 | 0.286 | 1.144 | 0.014 | | | 171.700 | 1.499 | 15.323 | 0.222 | 32.90 | 0.26 |
| SMA1976-315 | M | 16.517 | 0.816 | 390.6 | 2.1 | 25.057 | 0.483 | 144.833 | 2.641 | 30.363 | 0.176 | 1.617 | 0.059 | | | 204.600 | 0.283 | 19.863 | 0.082 | 42.34 | 0.12 |
| SMA1976-317 | M | 15.783 | 0.523 | 378.8 | 0.3 | 26.213 | 0.221 | 153.433 | 1.592 | 30.733 | 0.048 | 1.571 | 0.051 | | | 203.567 | 1.644 | 20.143 | 0.091 | 42.26 | 0.25 |
| SMA1976-317 Dup | B | 17.064 | 0.033 | 373.9 | 0.7 | 25.211 | 0.162 | 160.458 | 1.895 | 32.228 | 0.180 | 1.620 | 0.007 | 0.191 | 0.006 | 207.728 | 1.421 | 19.889 | 0.189 | 43.57 | 0.16 |
| SMA1976-319 | M | 15.563 | 0.555 | 386.5 | 9.7 | 25.013 | 0.832 | 146.000 | 4.528 | 29.777 | 0.483 | 1.516 | 0.032 | | | 199.533 | 2.327 | 19.443 | 0.487 | 41.05 | 0.70 |
| SMA1976-320 | M | 15.533 | 0.083 | 380.5 | 2.3 | 26.453 | 0.773 | 152.000 | 4.031 | 30.370 | 0.594 | 1.523 | 0.082 | | | 201.500 | 2.736 | 20.040 | 0.446 | 41.67 | 0.70 |
| SMA1976-321 | M | 17.810 | 0.615 | 381.7 | 2.2 | 25.483 | 0.508 | 153.367 | 2.831 | 34.213 | 0.443 | 1.633 | 0.049 | | | 221.533 | 2.949 | 21.783 | 0.340 | 45.72 | 0.60 |
| SMA1976-323 | M | 15.063 | 0.484 | 348.2 | 2.8 | 25.760 | 0.369 | 147.367 | 1.634 | 30.390 | 0.392 | 1.522 | 0.073 | | | 199.133 | 3.103 | 19.753 | 0.275 | 41.55 | 0.72 |
| SMA1976-324 | M | 16.283 | 0.062 | 400.0 | 3.3 | 27.297 | 0.255 | 159.133 | 1.236 | 31.820 | 0.258 | 1.655 | 0.064 | | | 213.000 | 2.362 | 21.470 | 0.130 | 45.01 | 0.41 |
| SMA1976-325 | M | 16.413 | 0.521 | 379.5 | 8.4 | 25.020 | 0.897 | 151.200 | 5.339 | 32.247 | 0.818 | 1.618 | 0.092 | | | 210.100 | 6.227 | 20.720 | 0.732 | 43.10 | 1.56 |
| S1311-03 | L | 22.300 | | 594.0 | | 27.000 | | 227.000 | | 38.100 | | | | 0.230 | | 350.000 | | 32.000 | | 75.00 | |
| S1312-45 | L | 32.840 | | 262.1 | | 39.420 | | 206.090 | | 29.000 | | 1.710 | | 0.700 | | 194.830 | | 21.790 | | 44.54 | |
| S1312-45 Dup | L | 22.820 | | 322.5 | | 40.240 | | 210.150 | | 30.340 | | 1.760 | | 0.710 | | 210.220 | | 23.250 | | 47.50 | |
| S1312-49 | L | 36.000 | | 943.0 | | 30.000 | | 351.000 | | 66.000 | | | | 0.470 | | 631.000 | | 58.000 | | 132.00 | |
| S1312 | L | 27.000 | | 620.0 | | 25.200 | | 215.000 | | 47.000 | | | | 0.440 | | 387.000 | | 33.300 | | 69.50 | |
| S1312-Xb | L | 19.906 | 0.155 | 348.9 | 2.9 | 42.388 | 0.779 | 247.500 | 4.055 | 34.615 | 0.299 | 1.673 | 0.008 | 0.205 | 0.022 | 241.050 | 2.731 | 25.088 | 0.313 | 51.11 | 0.59 |
| S1626-15 | L | 16.920 | | 296.0 | | 33.300 | | 163.830 | | 27.740 | | 1.720 | | 0.200 | | 198.690 | | 20.000 | | 40.95 | |
| S1626-15 Dup | L | 17.140 | | 294.7 | | 32.940 | | 162.090 | | 27.470 | | 1.570 | | 0.210 | | 199.620 | | 19.910 | | 40.47 | |
| S1626-21 | L | 17.290 | | 296.7 | | 33.730 | | 163.770 | | 27.840 | | 1.630 | | 0.200 | | 201.800 | | 20.150 | | 40.64 | |
| S1626-22 | L | 16.950 | | 291.8 | | 32.840 | | 160.080 | | 27.180 | | 1.630 | | 0.200 | | 196.720 | | 19.760 | | 40.64 | |
| S1626-23 | L | 17.100 | | 299.8 | | 33.430 | | 164.440 | | 27.650 | | 1.680 | | 0.200 | | 199.970 | | 20.080 | | 40.48 | |

*The letters correspond to the place where the analyses have been done: P: PSO Plouzané; M: CIGS Modena; L: previously measured at Lamont Doherty Earth Observatory (Cipriani, A.).*

*Table S4.2 (continue)*

| **Sample** | **Pr** | | **Nd** | | **Sm** | | **Eu** | | **Gd** | | **Tb** | | **Dy** | | **Ho** | | **Er** | | **Yb** | | **Lu** | |
|---|---|---|---|---|---|---|---|---|---|---|---|---|---|---|---|---|---|---|---|---|---|---|
| **N-MORB** | ppm | stdev | ppm | stdev | ppm | stdev | ppm | stdev | ppm | stdev | ppm | stdev | ppm | stdev | ppm | stdev | ppm | stdev | ppm | stdev | ppm | stdev |
| SMA1977-328 | 2.177 | 0.017 | 10.798 | 0.026 | 3.311 | 0.019 | 1.225 | 0.008 | 4.116 | 0.019 | 0.698 | 0.001 | 4.608 | 0.022 | 0.977 | 0.002 | 2.809 | 0.013 | 2.733 | 0.014 | 0.387 | 0.002 |
| SMA1977-329 | 2.116 | 0.012 | 10.971 | 0.049 | 3.604 | 0.029 | 1.318 | 0.010 | 4.624 | 0.047 | 0.796 | 0.010 | 5.249 | 0.023 | 1.124 | 0.013 | 3.248 | 0.033 | 3.151 | 0.036 | 0.460 | 0.006 |
| SMA1977-330 | 2.161 | 0.006 | 11.164 | 0.111 | 3.654 | 0.055 | 1.344 | 0.005 | 4.614 | 0.063 | 0.798 | 0.012 | 5.314 | 0.059 | 1.129 | 0.007 | 3.227 | 0.040 | 3.112 | 0.048 | 0.460 | 0.003 |
| SMA1977-331 | 2.125 | 0.010 | 11.022 | 0.077 | 3.536 | 0.013 | 1.312 | 0.005 | 4.556 | 0.013 | 0.784 | 0.002 | 5.196 | 0.028 | 1.101 | 0.005 | 3.155 | 0.014 | 3.072 | 0.027 | 0.439 | 0.007 |
| SMA1977-334 | 2.159 | 0.010 | 11.088 | 0.062 | 3.534 | 0.020 | 1.311 | 0.011 | 4.485 | 0.027 | 0.770 | 0.005 | 5.054 | 0.033 | 1.075 | 0.005 | 3.080 | 0.048 | 3.062 | 0.014 | 0.434 | 0.006 |
| SMA1977-335 | 2.190 | 0.008 | 11.420 | 0.046 | 3.622 | 0.014 | 1.346 | 0.001 | 4.704 | 0.021 | 0.816 | 0.006 | 5.344 | 0.010 | 1.145 | 0.002 | 3.260 | 0.010 | 3.190 | 0.021 | 0.467 | 0.004 |
| SMA1977-336 | 2.245 | 0.015 | 11.657 | 0.127 | 3.857 | 0.048 | 1.381 | 0.008 | 4.994 | 0.058 | 0.861 | 0.005 | 5.791 | 0.043 | 1.234 | 0.014 | 3.585 | 0.032 | 3.473 | 0.014 | 0.499 | 0.001 |
| SMA1977-337 | 2.229 | 0.011 | 11.448 | 0.111 | 3.607 | 0.071 | 1.349 | 0.006 | 4.571 | 0.075 | 0.787 | 0.013 | 5.161 | 0.112 | 1.094 | 0.022 | 3.107 | 0.070 | 3.116 | 0.064 | 0.446 | 0.012 |
| SMA1977-338 | 2.151 | 0.009 | 11.272 | 0.026 | 3.617 | 0.006 | 1.327 | 0.001 | 4.656 | 0.044 | 0.809 | 0.009 | 5.318 | 0.061 | 1.129 | 0.014 | 3.273 | 0.046 | 3.168 | 0.037 | 0.461 | 0.003 |
| SMA1977-340 | 2.161 | 0.006 | 11.282 | 0.027 | 3.602 | 0.023 | 1.321 | 0.001 | 4.681 | 0.050 | 0.817 | 0.007 | 5.341 | 0.012 | 1.136 | 0.001 | 3.284 | 0.038 | 3.205 | 0.014 | 0.463 | 0.002 |
| SMA1977-341B | 2.071 | 0.014 | 10.827 | 0.086 | 3.526 | 0.054 | 1.295 | 0.009 | 4.475 | 0.049 | 0.770 | 0.011 | 5.068 | 0.090 | 1.082 | 0.018 | 3.128 | 0.046 | 3.035 | 0.021 | 0.437 | 0.007 |
| SMA1977-341T | 2.058 | 0.013 | 10.799 | 0.106 | 3.541 | 0.014 | 1.299 | 0.010 | 4.444 | 0.048 | 0.771 | 0.005 | 5.098 | 0.059 | 1.085 | 0.004 | 3.109 | 0.014 | 3.015 | 0.029 | 0.443 | 0.004 |
| SMA1977-342 | 2.159 | 0.008 | 11.245 | 0.111 | 3.595 | 0.003 | 1.302 | 0.005 | 4.616 | 0.021 | 0.791 | 0.007 | 5.250 | 0.066 | 1.124 | 0.006 | 3.243 | 0.030 | 3.141 | 0.025 | 0.456 | 0.004 |
| SMA1977-343 | 2.144 | 0.005 | 11.240 | 0.044 | 3.599 | 0.007 | 1.300 | 0.005 | 4.625 | 0.016 | 0.796 | 0.004 | 5.234 | 0.019 | 1.125 | 0.004 | 3.222 | 0.007 | 3.174 | 0.037 | 0.453 | 0.001 |
| SMA1978-345 | 2.242 | 0.033 | 11.289 | 0.093 | 3.635 | 0.054 | 1.300 | 0.007 | 4.530 | 0.058 | 0.775 | 0.010 | 5.047 | 0.041 | 1.093 | 0.019 | 3.085 | 0.031 | 2.961 | 0.016 | 0.435 | 0.004 |
| SMA1978-346 | 2.204 | 0.004 | 10.976 | 0.056 | 3.469 | 0.034 | 1.276 | 0.001 | 4.314 | 0.061 | 0.735 | 0.007 | 4.781 | 0.074 | 1.032 | 0.015 | 2.905 | 0.042 | 2.831 | 0.015 | 0.410 | 0.007 |
| SMA1978-348 | 2.291 | 0.016 | 11.691 | 0.066 | 3.582 | 0.004 | 1.307 | 0.014 | 4.457 | 0.015 | 0.764 | 0.009 | 5.018 | 0.059 | 1.060 | 0.005 | 2.991 | 0.026 | 2.940 | 0.025 | 0.424 | 0.002 |
| SMA1978-349 | 2.428 | 0.011 | 12.405 | 0.051 | 3.797 | 0.011 | 1.360 | 0.015 | 4.756 | 0.017 | 0.805 | 0.004 | 5.344 | 0.009 | 1.126 | 0.006 | 3.246 | 0.017 | 3.139 | 0.006 | 0.452 | 0.005 |
| SMA1978-350 | 2.214 | 0.024 | 11.211 | 0.131 | 3.373 | 0.027 | 1.254 | 0.025 | 3.980 | 0.103 | 0.695 | 0.012 | 4.527 | 0.061 | 0.950 | 0.017 | 2.730 | 0.011 | 2.506 | 0.117 | 0.383 | 0.009 |
| SMA1978-352 | 2.208 | 0.004 | 11.327 | 0.097 | 3.404 | 0.018 | 1.250 | 0.005 | 4.234 | 0.016 | 0.719 | 0.005 | 4.703 | 0.038 | 0.982 | 0.015 | 2.840 | 0.037 | 2.626 | 0.119 | 0.399 | 0.008 |
| SMA1978-354 | 2.469 | 0.013 | 12.480 | 0.196 | 3.859 | 0.049 | 1.384 | 0.014 | 4.870 | 0.063 | 0.834 | 0.021 | 5.407 | 0.195 | 1.157 | 0.030 | 3.337 | 0.093 | 3.169 | 0.064 | 0.472 | 0.015 |
| SMA1978-355 | 2.346 | 0.016 | 11.861 | 0.008 | 3.745 | 0.018 | 1.336 | 0.010 | 4.748 | 0.025 | 0.812 | 0.009 | 5.334 | 0.059 | 1.145 | 0.011 | 3.292 | 0.048 | 3.124 | 0.019 | 0.459 | 0.006 |
| SMA1978-356 | 2.485 | 0.019 | 12.416 | 0.100 | 3.830 | 0.007 | 1.362 | 0.022 | 4.885 | 0.105 | 0.839 | 0.010 | 5.389 | 0.062 | 1.167 | 0.012 | 3.363 | 0.059 | 3.117 | 0.174 | 0.474 | 0.009 |
| SMA1978-357 | 2.465 | 0.036 | 12.269 | 0.134 | 3.859 | 0.054 | 1.373 | 0.008 | 4.698 | 0.140 | 0.800 | 0.018 | 5.313 | 0.084 | 1.119 | 0.029 | 3.241 | 0.061 | 3.011 | 0.078 | 0.447 | 0.010 |
| SMA1978-358 | 2.415 | 0.022 | 12.037 | 0.015 | 3.783 | 0.036 | 1.335 | 0.027 | 4.553 | 0.032 | 0.800 | 0.004 | 5.208 | 0.029 | 1.108 | 0.010 | 3.176 | 0.046 | 2.932 | 0.094 | 0.443 | 0.011 |
| SMA1978-360 | 2.378 | 0.024 | 11.944 | 0.087 | 3.702 | 0.032 | 1.354 | 0.016 | 4.524 | 0.053 | 0.769 | 0.004 | 5.098 | 0.051 | 1.078 | 0.004 | 3.028 | 0.032 | 3.003 | 0.026 | 0.422 | 0.006 |
| SMA1978-363 | 2.263 | 0.028 | 11.313 | 0.172 | 3.564 | 0.074 | 1.297 | 0.022 | 4.235 | 0.062 | 0.719 | 0.006 | 4.728 | 0.061 | 0.990 | 0.011 | 2.846 | 0.071 | 2.834 | 0.029 | 0.402 | 0.004 |
| SMA1978-364 | 2.395 | 0.017 | 11.950 | 0.011 | 3.759 | 0.020 | 1.350 | 0.004 | 4.758 | 0.018 | 0.815 | 0.003 | 5.333 | 0.004 | 1.149 | 0.001 | 3.292 | 0.012 | 3.149 | 0.029 | 0.463 | 0.004 |
| S1312-Xa | 4.877 | 0.112 | 24.404 | 0.510 | 7.218 | 0.256 | 2.329 | 0.031 | 9.041 | 0.316 | 1.541 | 0.038 | 10.215 | 0.238 | 2.184 | 0.038 | 6.276 | 0.179 | 6.032 | 0.133 | 0.906 | 0.022 |
| S1312-53 | | | 13.400 | | 3.810 | | 1.200 | | 5.010 | | | | 5.010 | | | | 3.130 | | 2.740 | | | |
| S1314 | 2.330 | | 12.120 | | 4.040 | | 1.410 | | 5.550 | | 0.880 | | 5.310 | | 1.010 | | 2.800 | | 2.300 | | 0.350 | |

*Table S4.2 (continue)*

| **Sample** | **Pr** | | **Nd** | | **Sm** | | **Eu** | | **Gd** | | **Tb** | | **Dy** | | **Ho** | | **Er** | | **Yb** | | **Lu** | |
|---|---|---|---|---|---|---|---|---|---|---|---|---|---|---|---|---|---|---|---|---|---|---|
| | ppm | stdev | ppm | stdev | ppm | stdev | ppm | stdev | ppm | stdev | ppm | stdev | ppm | stdev | ppm | stdev | ppm | stdev | ppm | stdev | ppm | stdev |
| S1314-X | 2.343 | 0.023 | 11.705 | 0.061 | 3.804 | 0.058 | 1.420 | 0.011 | 4.376 | 0.047 | 0.726 | 0.013 | 4.472 | 0.015 | 0.896 | 0.007 | 2.437 | 0.029 | 2.143 | 0.079 | 0.314 | 0.003 |
| S1314-01 | 2.340 | | 12.020 | | 3.940 | | 1.420 | | 5.200 | | 0.860 | | 5.300 | | 1.010 | | 2.850 | | 2.350 | | 0.360 | |
| S1314-01 Dup | | | 12.400 | | 3.780 | | 1.390 | | 5.270 | | | | 5.070 | | | | 2.910 | | 2.670 | | | |
| S1627-01 | | | 13.000 | | 3.600 | | 1.180 | | 4.810 | | | | 5.320 | | | | 3.180 | | 2.990 | | | |
| S1629-35 | 2.110 | | 10.760 | | 3.630 | | 1.230 | | 4.980 | | 0.890 | | 5.760 | | 1.160 | | 3.270 | | 2.870 | | 0.440 | |
| S1629-35 Dup | | | 10.900 | | 3.440 | | 1.370 | | 4.610 | | | | 5.280 | | | | 3.120 | | 3.110 | | | |
| S1639-03 | | | 13.590 | | 3.940 | | 1.430 | | 4.770 | | | | 5.420 | | | | 3.250 | | 3.140 | | | |
| **E-MORB** | | | | | | | | | | | | | | | | | | | | | | |
| SMA1970-191A | 3.402 | 0.004 | 14.968 | 0.133 | 3.964 | 0.006 | 1.446 | 0.011 | 4.493 | 0.039 | 0.761 | 0.004 | 4.861 | 0.026 | 1.022 | 0.002 | 2.928 | 0.011 | 2.835 | 0.036 | 0.417 | 0.002 |
| SMA1970-191B | 3.456 | 0.012 | 15.189 | 0.084 | 4.064 | 0.041 | 1.477 | 0.004 | 4.628 | 0.040 | 0.784 | 0.007 | 5.043 | 0.017 | 1.063 | 0.004 | 3.014 | 0.045 | 2.938 | 0.040 | 0.435 | 0.006 |
| SMA1970-191C | 3.451 | 0.042 | 15.319 | 0.135 | 4.007 | 0.023 | 1.468 | 0.017 | 4.355 | 0.026 | 0.729 | 0.011 | 4.697 | 0.065 | 0.987 | 0.003 | 2.824 | 0.036 | 2.737 | 0.030 | 0.404 | 0.014 |
| SMA1970-191D | 3.423 | 0.009 | 15.271 | 0.174 | 4.012 | 0.036 | 1.451 | 0.024 | 4.625 | 0.037 | 0.754 | 0.010 | 4.923 | 0.006 | 1.032 | 0.009 | 2.951 | 0.030 | 2.849 | 0.026 | 0.419 | 0.005 |
| SMA1970-191E | 3.480 | 0.013 | 15.418 | 0.078 | 4.074 | 0.018 | 1.467 | 0.006 | 4.640 | 0.017 | 0.785 | 0.006 | 5.070 | 0.038 | 1.060 | 0.008 | 3.059 | 0.028 | 2.974 | 0.018 | 0.430 | 0.002 |
| SMA1970-192 | 3.412 | 0.010 | 15.142 | 0.126 | 3.995 | 0.036 | 1.455 | 0.008 | 4.614 | 0.034 | 0.771 | 0.012 | 4.943 | 0.053 | 1.054 | 0.007 | 3.023 | 0.027 | 2.932 | 0.029 | 0.428 | 0.005 |
| SMA1970-193 | 3.364 | 0.015 | 14.898 | 0.097 | 3.991 | 0.048 | 1.434 | 0.016 | 4.504 | 0.054 | 0.750 | 0.011 | 4.842 | 0.071 | 1.027 | 0.013 | 2.950 | 0.020 | 2.874 | 0.050 | 0.419 | 0.006 |
| SMA1970-194 | 3.211 | 0.006 | 14.101 | 0.061 | 3.780 | 0.008 | 1.371 | 0.011 | 4.291 | 0.018 | 0.717 | 0.006 | 4.576 | 0.032 | 0.982 | 0.013 | 2.779 | 0.009 | 2.771 | 0.036 | 0.397 | 0.003 |
| SMA1970-195 | 3.401 | 0.011 | 15.096 | 0.030 | 4.019 | 0.011 | 1.450 | 0.004 | 4.552 | 0.045 | 0.758 | 0.006 | 4.865 | 0.031 | 1.037 | 0.008 | 2.952 | 0.029 | 2.887 | 0.011 | 0.422 | 0.002 |
| SMA1970-199 | 3.252 | 0.007 | 14.496 | 0.079 | 3.879 | 0.031 | 1.405 | 0.008 | 4.391 | 0.003 | 0.737 | 0.002 | 4.763 | 0.013 | 1.000 | 0.002 | 2.844 | 0.015 | 2.791 | 0.016 | 0.404 | 0.002 |
| SMA1970-202 | 2.833 | 0.015 | 12.688 | 0.112 | 3.493 | 0.015 | 1.298 | 0.018 | 4.069 | 0.021 | 0.673 | 0.007 | 4.363 | 0.025 | 0.920 | 0.014 | 2.660 | 0.023 | 2.555 | 0.013 | 0.378 | 0.003 |
| SMA1973-246 | 2.429 | 0.006 | 11.321 | 0.039 | 3.234 | 0.003 | 1.219 | 0.008 | 3.669 | 0.023 | 0.609 | 0.002 | 3.843 | 0.016 | 0.785 | 0.001 | 2.209 | 0.017 | 2.129 | 0.023 | 0.303 | 0.002 |
| SMA1973-248 | 3.213 | 0.009 | 14.018 | 0.038 | 3.775 | 0.031 | 1.366 | 0.005 | 4.227 | 0.021 | 0.704 | 0.005 | 4.499 | 0.019 | 0.938 | 0.004 | 2.666 | 0.025 | 2.603 | 0.028 | 0.369 | 0.001 |
| SMA1973-249 | 2.389 | 0.036 | 10.785 | 0.201 | 3.065 | 0.028 | 1.193 | 0.007 | 3.640 | 0.011 | 0.612 | 0.002 | 4.040 | 0.027 | 0.830 | 0.007 | 2.304 | 0.006 | 2.241 | 0.023 | 0.328 | 0.004 |
| SMA1973-250 | 3.178 | 0.041 | 14.101 | 0.137 | 3.893 | 0.032 | 1.394 | 0.028 | 4.580 | 0.041 | 0.748 | 0.007 | 4.829 | 0.064 | 0.998 | 0.012 | 2.884 | 0.032 | 2.697 | 0.033 | 0.395 | 0.007 |
| SMA1973-251 | 3.401 | 0.113 | 14.685 | 0.504 | 3.964 | 0.114 | 1.437 | 0.036 | 4.430 | 0.163 | 0.723 | 0.023 | 4.692 | 0.139 | 0.951 | 0.030 | 2.761 | 0.089 | 2.579 | 0.067 | 0.373 | 0.012 |
| SMA1973-252 | 3.052 | 0.029 | 13.680 | 0.068 | 3.732 | 0.034 | 1.335 | 0.004 | 4.370 | 0.026 | 0.734 | 0.003 | 4.701 | 0.028 | 0.983 | 0.005 | 2.803 | 0.005 | 2.703 | 0.012 | 0.392 | 0.003 |
| SMA1973-254 | 3.302 | 0.026 | 14.800 | 0.195 | 3.886 | 0.085 | 1.392 | 0.025 | 4.415 | 0.063 | 0.735 | 0.012 | 4.656 | 0.079 | 0.977 | 0.018 | 2.744 | 0.064 | 2.584 | 0.022 | 0.378 | 0.008 |
| SMA1973-255 | 3.150 | 0.071 | 13.817 | 0.249 | 3.611 | 0.086 | 1.329 | 0.035 | 4.086 | 0.120 | 0.678 | 0.016 | 4.309 | 0.124 | 0.907 | 0.027 | 2.554 | 0.090 | 2.395 | 0.062 | 0.350 | 0.012 |
| SMA1973-256 | 3.058 | 0.077 | 13.675 | 0.351 | 3.632 | 0.095 | 1.334 | 0.031 | 4.157 | 0.116 | 0.695 | 0.021 | 4.408 | 0.118 | 0.923 | 0.028 | 2.605 | 0.071 | 2.484 | 0.076 | 0.360 | 0.011 |
| SMA1973-258 | 3.160 | 0.006 | 14.307 | 0.072 | 3.857 | 0.014 | 1.380 | 0.002 | 4.470 | 0.011 | 0.747 | 0.004 | 4.783 | 0.036 | 0.998 | 0.005 | 2.822 | 0.004 | 2.664 | 0.013 | 0.393 | 0.001 |
| SMA1973-261 | 2.556 | 0.015 | 11.779 | 0.075 | 3.277 | 0.012 | 1.245 | 0.013 | 3.760 | 0.018 | 0.620 | 0.006 | 3.999 | 0.044 | 0.832 | 0.004 | 2.340 | 0.029 | 2.244 | 0.008 | 0.322 | 0.003 |
| SMA1973-262 | 2.428 | 0.014 | 11.190 | 0.045 | 3.129 | 0.020 | 1.199 | 0.001 | 3.576 | 0.030 | 0.594 | 0.003 | 3.852 | 0.039 | 0.792 | 0.008 | 2.252 | 0.029 | 2.170 | 0.021 | 0.310 | 0.001 |

*Table S4.2 (continue)*

| **Sample** | **Pr** | | **Nd** | | **Sm** | | **Eu** | | **Gd** | | **Tb** | | **Dy** | | **Ho** | | **Er** | | **Yb** | | **Lu** | |
|---|---|---|---|---|---|---|---|---|---|---|---|---|---|---|---|---|---|---|---|---|---|---|
| | ppm | stdev | ppm | stdev | ppm | stdev | ppm | stdev | ppm | stdev | ppm | stdev | ppm | stdev | ppm | stdev | ppm | stdev | ppm | stdev | ppm | stdev |
| SMA1973-263 | 2.508 | 0.018 | 11.509 | 0.030 | 3.230 | 0.012 | 1.220 | 0.006 | 3.664 | 0.025 | 0.606 | 0.005 | 3.870 | 0.023 | 0.799 | 0.008 | 2.270 | 0.024 | 2.183 | 0.033 | 0.314 | 0.004 |
| SMA1973-264 | 3.066 | 0.048 | 13.474 | 0.292 | 3.727 | 0.053 | 1.347 | 0.024 | 4.195 | 0.042 | 0.707 | 0.013 | 4.538 | 0.086 | 0.953 | 0.018 | 2.710 | 0.061 | 2.611 | 0.071 | 0.377 | 0.009 |
| SMA1974-266 | 2.672 | 0.015 | 12.039 | 0.096 | 3.374 | 0.033 | 1.252 | 0.007 | 3.839 | 0.043 | 0.651 | 0.008 | 4.114 | 0.039 | 0.858 | 0.013 | 2.476 | 0.024 | 2.342 | 0.026 | 0.340 | 0.005 |
| SMA1974-267 | 2.723 | 0.026 | 12.247 | 0.138 | 3.395 | 0.038 | 1.270 | 0.008 | 3.889 | 0.081 | 0.648 | 0.013 | 4.140 | 0.076 | 0.864 | 0.016 | 2.471 | 0.055 | 2.331 | 0.050 | 0.341 | 0.006 |
| SMA1974-271 | 2.603 | 0.010 | 11.795 | 0.034 | 3.281 | 0.009 | 1.223 | 0.006 | 3.784 | 0.020 | 0.638 | 0.004 | 4.081 | 0.041 | 0.850 | 0.002 | 2.395 | 0.010 | 2.279 | 0.014 | 0.331 | 0.001 |
| SMA1974-272 | 2.585 | 0.030 | 11.864 | 0.091 | 3.273 | 0.019 | 1.232 | 0.007 | 3.761 | 0.016 | 0.632 | 0.006 | 4.043 | 0.031 | 0.852 | 0.007 | 2.423 | 0.009 | 2.325 | 0.014 | 0.334 | 0.003 |
| SMA1974-273 | 2.524 | 0.018 | 11.465 | 0.047 | 3.200 | 0.020 | 1.209 | 0.006 | 3.668 | 0.027 | 0.612 | 0.009 | 3.936 | 0.024 | 0.824 | 0.004 | 2.361 | 0.024 | 2.244 | 0.029 | 0.324 | 0.002 |
| SMA1974-274 | 2.527 | 0.008 | 11.720 | 0.102 | 3.233 | 0.033 | 1.220 | 0.008 | 3.758 | 0.016 | 0.627 | 0.001 | 4.029 | 0.036 | 0.842 | 0.004 | 2.401 | 0.026 | 2.317 | 0.031 | 0.330 | 0.001 |
| SMA1974-275 | 2.622 | 0.042 | 12.220 | 0.251 | 3.377 | 0.022 | 1.257 | 0.008 | 3.923 | 0.080 | 0.662 | 0.011 | 4.244 | 0.097 | 0.883 | 0.018 | 2.512 | 0.038 | 2.422 | 0.058 | 0.353 | 0.003 |
| SMA1974-276 | 2.625 | 0.004 | 11.955 | 0.063 | 3.266 | 0.036 | 1.220 | 0.009 | 3.698 | 0.039 | 0.617 | 0.004 | 3.973 | 0.041 | 0.827 | 0.012 | 2.328 | 0.013 | 2.307 | 0.052 | 0.328 | 0.008 |
| SMA1974-277 | 2.596 | 0.007 | 11.783 | 0.080 | 3.221 | 0.032 | 1.216 | 0.009 | 3.665 | 0.025 | 0.606 | 0.003 | 3.930 | 0.019 | 0.805 | 0.004 | 2.270 | 0.006 | 2.255 | 0.022 | 0.320 | 0.001 |
| SMA1979-365 | 3.972 | 0.032 | 17.457 | 0.190 | 4.493 | 0.089 | 1.432 | 0.024 | 4.879 | 0.114 | 0.794 | 0.025 | 5.093 | 0.108 | 1.073 | 0.021 | 3.067 | 0.131 | 2.909 | 0.045 | 0.423 | 0.010 |
| SMA1979-366 | 3.755 | 0.045 | 16.410 | 0.106 | 4.110 | 0.127 | 1.387 | 0.036 | 4.461 | 0.090 | 0.735 | 0.009 | 4.624 | 0.125 | 0.975 | 0.024 | 2.834 | 0.042 | 2.639 | 0.079 | 0.381 | 0.005 |
| SMA1979-367 | 3.743 | 0.055 | 16.310 | 0.140 | 4.089 | 0.018 | 1.363 | 0.002 | 4.399 | 0.001 | 0.740 | 0.027 | 4.679 | 0.048 | 0.980 | 0.013 | 2.837 | 0.001 | 2.649 | 0.042 | 0.384 | 0.003 |
| SMA1979-367 Dup | 3.418 | 0.020 | 14.757 | 0.064 | 3.606 | 0.015 | 1.248 | 0.006 | 3.906 | 0.010 | 0.641 | 0.002 | 4.107 | 0.014 | 0.871 | 0.005 | 2.471 | 0.012 | 2.368 | 0.012 | 0.343 | 0.001 |
| SMA1979-368 | 3.749 | 0.023 | 16.990 | 0.112 | 4.555 | 0.052 | 1.490 | 0.014 | 5.188 | 0.063 | 0.856 | 0.015 | 5.596 | 0.087 | 1.189 | 0.016 | 3.345 | 0.035 | 3.260 | 0.036 | 0.474 | 0.006 |
| SMA1979-369 | 3.940 | 0.011 | 16.930 | 0.114 | 4.321 | 0.009 | 1.420 | 0.002 | 4.614 | 0.027 | 0.767 | 0.004 | 4.893 | 0.032 | 1.016 | 0.007 | 2.889 | 0.041 | 2.817 | 0.010 | 0.407 | 0.004 |
| SMA1979-370 | 3.867 | 0.031 | 16.390 | 0.090 | 4.175 | 0.033 | 1.372 | 0.027 | 4.370 | 0.073 | 0.721 | 0.010 | 4.592 | 0.066 | 0.963 | 0.009 | 2.729 | 0.011 | 2.691 | 0.022 | 0.377 | 0.008 |
| SMA1979-371 | 3.922 | 0.021 | 16.815 | 0.118 | 4.228 | 0.051 | 1.425 | 0.007 | 4.643 | 0.088 | 0.762 | 0.012 | 4.878 | 0.041 | 1.011 | 0.012 | 2.894 | 0.024 | 2.797 | 0.052 | 0.405 | 0.005 |
| SMA1979-372 | 3.841 | 0.027 | 16.341 | 0.096 | 4.101 | 0.051 | 1.411 | 0.008 | 4.542 | 0.031 | 0.745 | 0.007 | 4.787 | 0.042 | 0.991 | 0.010 | 2.832 | 0.035 | 2.752 | 0.006 | 0.396 | 0.003 |
| SMA1979-373 | 3.563 | 0.073 | 14.743 | 0.275 | 3.584 | 0.084 | 1.264 | 0.017 | 3.685 | 0.108 | 0.599 | 0.016 | 3.841 | 0.112 | 0.797 | 0.021 | 2.263 | 0.067 | 2.235 | 0.068 | 0.315 | 0.007 |
| SMA1979-374 | 3.523 | 0.015 | 14.727 | 0.208 | 3.606 | 0.053 | 1.259 | 0.010 | 3.795 | 0.058 | 0.616 | 0.016 | 3.962 | 0.079 | 0.824 | 0.015 | 2.337 | 0.053 | 2.275 | 0.042 | 0.327 | 0.007 |
| SMA1979-375 | 3.555 | 0.031 | 15.049 | 0.062 | 3.708 | 0.070 | 1.264 | 0.024 | 3.973 | 0.018 | 0.651 | 0.004 | 4.163 | 0.013 | 0.863 | 0.004 | 2.478 | 0.026 | 2.349 | 0.070 | 0.348 | 0.002 |
| SMA1979-376 | 4.378 | 0.021 | 19.938 | 0.198 | 5.427 | 0.041 | 1.706 | 0.023 | 6.179 | 0.118 | 1.009 | 0.003 | 6.732 | 0.093 | 1.384 | 0.023 | 3.991 | 0.027 | 3.864 | 0.025 | 0.562 | 0.010 |
| SMA1979-377 | 4.186 | 0.022 | 18.775 | 0.141 | 4.968 | 0.057 | 1.640 | 0.022 | 5.469 | 0.095 | 0.900 | 0.019 | 5.839 | 0.039 | 1.209 | 0.023 | 3.492 | 0.013 | 3.335 | 0.065 | 0.482 | 0.003 |
| S1313-06 | 3.760 | | 17.240 | | 4.880 | | 1.580 | | 5.670 | | 0.980 | | 6.180 | | 1.240 | | 3.540 | | 3.180 | | 0.460 | |
| S1313-06 Dup | | | 17.600 | | 4.630 | | 1.430 | | 5.740 | | | | 6.090 | | | | 3.680 | | 3.360 | | | |
| S1313-10 | | | 17.700 | | 4.630 | | 1.630 | | 5.910 | | | | 6.200 | | | | 3.810 | | 3.390 | | | |
| S1313-11 | 3.750 | | 17.370 | | 4.900 | | 1.560 | | 5.670 | | 0.990 | | 6.190 | | 1.240 | | 3.650 | | 3.250 | | 0.490 | |
| S1313-11 Dup | | | 18.400 | | 5.140 | | 1.570 | | 6.140 | | | | 5.900 | | | | 3.710 | | 3.450 | | | |
| S1313-13 | 3.760 | | 17.340 | | 4.940 | | 1.590 | | 5.580 | | 1.020 | | 6.320 | | 1.290 | | 3.580 | | 3.300 | | 0.480 | |

*Table S4.2 (continue)*

| **Sample** | **Pr** | | **Nd** | | **Sm** | | **Eu** | | **Gd** | | **Tb** | | **Dy** | | **Ho** | | **Er** | | **Yb** | | **Lu** | |
|---|---|---|---|---|---|---|---|---|---|---|---|---|---|---|---|---|---|---|---|---|---|---|
| | ppm | stdev | ppm | stdev | ppm | stdev | ppm | stdev | ppm | stdev | ppm | stdev | ppm | stdev | ppm | stdev | ppm | stdev | ppm | stdev | ppm | stdev |
| S1624-21 | 3.670 | | 16.900 | | 4.430 | | 1.440 | | 5.390 | | 0.920 | | 5.470 | | 1.050 | | 3.060 | | 2.750 | | 0.410 | |
| S1624-21 Dup | | | 16.100 | | 4.250 | | 1.380 | | 5.140 | | | | 5.240 | | | | 3.000 | | 2.760 | | | |
| S1625-07 | | | 16.500 | | 4.270 | | 1.450 | | 4.430 | | | | 5.240 | | | | 3.040 | | 2.780 | | | |
| S1628-02 A | 4.000 | | 17.540 | | 4.430 | | 1.480 | | 5.190 | | 0.890 | | 5.110 | | 1.060 | | 2.980 | | 2.660 | | 0.400 | |
| S1628-02 | 3.980 | | 17.330 | | 4.340 | | 1.450 | | 5.040 | | 0.870 | | 5.160 | | 1.020 | | 2.900 | | 2.660 | | 0.380 | |
| **K-rich MORB** | | | | | | | | | | | | | | | | | | | | | | |
| SMA1966-128 | 6.053 | 0.061 | 26.800 | 0.398 | 6.688 | 0.142 | 2.302 | 0.018 | 6.475 | 0.063 | 0.915 | 0.020 | 4.970 | 0.030 | 0.889 | 0.007 | 2.221 | 0.085 | 1.714 | 0.052 | 0.228 | 0.004 |
| SMA1974-283 | 4.151 | 0.059 | 17.630 | 0.102 | 4.262 | 0.059 | 1.446 | 0.026 | 4.197 | 0.053 | 0.669 | 0.004 | 4.153 | 0.027 | 0.841 | 0.021 | 2.266 | 0.045 | 2.138 | 0.060 | 0.305 | 0.002 |
| SMA1974-285 | 3.869 | 0.181 | 16.490 | 0.882 | 3.720 | 0.200 | 1.320 | 0.061 | 3.761 | 0.216 | 0.590 | 0.033 | 3.597 | 0.164 | 0.709 | 0.041 | 1.967 | 0.154 | 1.804 | 0.099 | 0.253 | 0.023 |
| SMA1974-287 | 4.014 | 0.032 | 17.410 | 0.367 | 3.914 | 0.093 | 1.362 | 0.033 | 3.941 | 0.038 | 0.588 | 0.007 | 3.606 | 0.026 | 0.721 | 0.018 | 1.963 | 0.046 | 1.767 | 0.037 | 0.252 | 0.004 |
| SMA1976-315 | 5.168 | 0.032 | 22.033 | 0.148 | 5.193 | 0.126 | 1.747 | 0.017 | 5.194 | 0.096 | 0.812 | 0.018 | 4.899 | 0.080 | 0.978 | 0.026 | 2.747 | 0.052 | 2.570 | 0.101 | 0.356 | 0.009 |
| SMA1976-317 | 5.200 | 0.024 | 22.197 | 0.298 | 5.295 | 0.085 | 1.751 | 0.054 | 5.396 | 0.092 | 0.837 | 0.006 | 5.058 | 0.028 | 1.025 | 0.011 | 2.847 | 0.012 | 2.596 | 0.017 | 0.377 | 0.005 |
| SMA1976-317 Dup | 5.220 | 0.022 | 21.899 | 0.119 | 4.986 | 0.059 | 1.722 | 0.012 | 4.851 | 0.048 | 0.762 | 0.006 | 4.612 | 0.048 | 0.911 | 0.000 | 2.505 | 0.012 | 2.311 | 0.023 | 0.330 | 0.003 |
| SMA1976-319 | 5.055 | 0.133 | 21.320 | 0.570 | 5.130 | 0.100 | 1.726 | 0.011 | 5.077 | 0.058 | 0.798 | 0.046 | 4.920 | 0.155 | 0.967 | 0.037 | 2.726 | 0.094 | 2.540 | 0.052 | 0.361 | 0.004 |
| SMA1976-320 | 5.151 | 0.090 | 22.083 | 0.514 | 5.200 | 0.182 | 1.742 | 0.035 | 5.148 | 0.104 | 0.837 | 0.019 | 5.124 | 0.112 | 1.029 | 0.037 | 2.848 | 0.071 | 2.658 | 0.107 | 0.380 | 0.012 |
| SMA1976-321 | 5.560 | 0.095 | 23.307 | 0.395 | 5.337 | 0.177 | 1.798 | 0.033 | 5.166 | 0.122 | 0.817 | 0.023 | 5.034 | 0.108 | 0.975 | 0.008 | 2.747 | 0.076 | 2.547 | 0.080 | 0.359 | 0.004 |
| SMA1976-323 | 5.140 | 0.058 | 21.733 | 0.259 | 5.113 | 0.035 | 1.748 | 0.023 | 5.276 | 0.031 | 0.818 | 0.022 | 5.006 | 0.088 | 0.989 | 0.010 | 2.845 | 0.054 | 2.597 | 0.051 | 0.376 | 0.010 |
| SMA1976-324 | 5.565 | 0.049 | 23.750 | 0.185 | 5.571 | 0.010 | 1.884 | 0.018 | 5.749 | 0.056 | 0.893 | 0.013 | 5.460 | 0.051 | 1.081 | 0.014 | 2.968 | 0.031 | 2.818 | 0.081 | 0.396 | 0.010 |
| SMA1976-325 | 5.229 | 0.175 | 22.327 | 0.905 | 5.104 | 0.196 | 1.719 | 0.032 | 5.086 | 0.211 | 0.790 | 0.042 | 4.975 | 0.154 | 0.979 | 0.035 | 2.743 | 0.187 | 2.541 | 0.116 | 0.363 | 0.013 |
| S1311-03 | | | 36.000 | | 7.070 | | 2.260 | | 6.850 | | | | 5.400 | | | | 2.600 | | 2.030 | | | |
| S1312-45 | 5.830 | | 25.530 | | 6.260 | | 1.900 | | 6.690 | | 1.130 | | 6.860 | | 1.390 | | 3.790 | | 3.300 | | 0.480 | |
| S1312-45 Dup | 6.160 | | 26.890 | | 6.520 | | 1.930 | | 6.890 | | 1.150 | | 6.980 | | 1.430 | | 3.980 | | 3.470 | | 0.490 | |
| S1312-49 | | | 58.000 | | 10.500 | | 3.210 | | 8.350 | | | | 6.110 | | | | 2.940 | | 2.260 | | | |
| S1312 | | | 36.500 | | 7.030 | | 2.300 | | 6.270 | | | | 5.230 | | | | 2.610 | | 2.220 | | | |
| S1312-Xb | 6.817 | 0.099 | 30.981 | t.17414 | 7.523 | 0.143 | 2.340 | 0.083 | 8.249 | 0.234 | 1.324 | 0.029 | 8.219 | 0.148 | 1.720 | 0.039 | 4.892 | 0.164 | 4.533 | 0.096 | 0.649 | 0.015 |
| S1626-15 | 5.230 | | 22.470 | | 5.350 | | 1.760 | | 6.050 | | 1.000 | | 5.950 | | 1.190 | | 3.270 | | 2.980 | | 0.440 | |
| S1626-15 Dup | 5.170 | | 22.620 | | 5.360 | | 1.750 | | 6.270 | | 1.010 | | 5.960 | | 1.170 | | 3.250 | | 2.920 | | 0.430 | |
| S1626-21 | 5.190 | | 22.740 | | 5.570 | | 1.790 | | 6.270 | | 1.000 | | 6.140 | | 1.180 | | 3.440 | | 3.010 | | 0.450 | |
| S1626-22 | 5.180 | | 22.530 | | 5.390 | | 1.710 | | 6.080 | | 1.020 | | 6.100 | | 1.160 | | 3.180 | | 2.780 | | 0.430 | |
| S1626-23 | 5.180 | | 22.500 | | 5.310 | | 1.760 | | 6.040 | | 1.000 | | 6.060 | | 1.190 | | 3.350 | | 2.980 | | 0.430 | |

*Table S4.2 (continue)*

| **Sample** | **Hf** | | **Ta** | | **Pb** | | **Th** | | **U** | |
|---|---|---|---|---|---|---|---|---|---|---|
| **N-MORB** | ppm | stdev | ppm | stdev | ppm | stdev | ppm | stdev | ppm | stdev |
| SMA1977-328 | 2.220 | 0.003 | 0.402 | 0.001 | 0.549 | 0.006 | 0.498 | 0.001 | 0.162 | 0.003 |
| SMA1977-329 | 2.401 | 0.064 | 0.274 | 0.002 | 0.521 | 0.006 | 0.318 | 0.001 | 0.117 | 0.001 |
| SMA1977-330 | 2.416 | 0.008 | 0.279 | 0.001 | 0.536 | 0.002 | 0.323 | 0.002 | 0.119 | 0.001 |
| SMA1977-331 | 2.346 | 0.009 | 0.272 | 0.002 | 0.524 | 0.004 | 0.321 | 0.004 | 0.118 | 0.001 |
| SMA1977-334 | 2.340 | 0.016 | 0.278 | 0.001 | 0.541 | 0.004 | 0.328 | 0.001 | 0.125 | 0.001 |
| SMA1977-335 | 2.485 | 0.020 | 0.294 | 0.003 | 0.520 | 0.001 | 0.346 | 0.002 | 0.122 | 0.001 |
| SMA1977-336 | 2.682 | 0.024 | 0.308 | 0.005 | 0.526 | 0.013 | 0.374 | 0.003 | 0.123 | 0.001 |
| SMA1977-337 | 2.408 | 0.048 | 0.291 | 0.005 | 0.535 | 0.006 | 0.342 | 0.007 | 0.132 | 0.002 |
| SMA1977-338 | 2.432 | 0.015 | 0.287 | 0.001 | 0.528 | 0.013 | 0.340 | 0.001 | 0.123 | 0.001 |
| SMA1977-340 | 2.469 | 0.024 | 0.285 | 0.002 | 0.517 | 0.011 | 0.344 | 0.002 | 0.123 | 0.002 |
| SMA1977-341B | 2.348 | 0.043 | 0.273 | 0.003 | 0.514 | 0.003 | 0.318 | 0.008 | 0.117 | 0.001 |
| SMA1977-341T | 2.343 | 0.018 | 0.272 | 0.002 | 0.512 | 0.002 | 0.321 | 0.006 | 0.117 | 0.001 |
| SMA1977-342 | 2.430 | 0.010 | 0.291 | 0.001 | 0.522 | 0.001 | 0.347 | 0.004 | 0.121 | 0.001 |
| SMA1977-343 | 2.434 | 0.018 | 0.293 | 0.002 | 0.517 | 0.002 | 0.347 | 0.001 | 0.124 | 0.002 |
| SMA1978-345 | 2.540 | 0.030 | 0.352 | 0.004 | 0.555 | 0.005 | 0.422 | 0.005 | 0.136 | 0.003 |
| SMA1978-346 | 2.379 | 0.018 | 0.341 | 0.004 | 0.568 | 0.003 | 0.409 | 0.004 | 0.136 | 0.001 |
| SMA1978-348 | 2.433 | 0.019 | 0.351 | 0.002 | 0.600 | 0.002 | 0.417 | 0.002 | 0.149 | 0.002 |
| SMA1978-349 | 2.609 | 0.028 | 0.370 | 0.004 | 0.620 | 0.006 | 0.442 | 0.004 | 0.155 | 0.001 |
| SMA1978-350 | 2.192 | 0.040 | 0.321 | 0.003 | 0.574 | 0.020 | 0.359 | 0.007 | 0.144 | 0.002 |
| SMA1978-352 | 2.309 | 0.011 | 0.324 | 0.003 | 0.591 | 0.002 | 0.369 | 0.004 | 0.145 | 0.003 |
| SMA1978-354 | 2.674 | 0.061 | 0.378 | 0.006 | 0.599 | 0.002 | 0.455 | 0.013 | 0.159 | 0.004 |
| SMA1978-355 | 2.664 | 0.014 | 0.363 | 0.004 | 0.575 | 0.009 | 0.439 | 0.007 | 0.134 | 0.018 |
| SMA1978-356 | 2.726 | 0.067 | 0.371 | 0.011 | 0.595 | 0.016 | 0.452 | 0.006 | 0.163 | 0.004 |
| SMA1978-357 | 2.629 | 0.029 | 0.366 | 0.002 | 0.607 | 0.020 | 0.437 | 0.002 | 0.156 | 0.003 |
| SMA1978-358 | 2.557 | 0.027 | 0.363 | 0.006 | 0.602 | 0.005 | 0.425 | 0.006 | 0.156 | 0.003 |
| SMA1978-360 | 2.482 | 0.052 | 0.350 | 0.005 | 0.587 | 0.015 | 0.416 | 0.003 | 0.147 | 0.005 |
| SMA1978-363 | 2.296 | 0.022 | 0.331 | 0.002 | 0.567 | 0.013 | 0.394 | 0.005 | 0.144 | 0.003 |
| SMA1978-364 | 2.652 | 0.009 | 0.362 | 0.001 | 0.589 | 0.008 | 0.438 | 0.002 | 0.149 | 0.002 |
| S1312-Xa | 5.734 | 0.090 | 1.162 | 0.034 | 1.363 | 0.042 | 1.515 | 0.047 | 0.352 | 0.016 |
| S1312-53 | | | | | | | | | | |
| S1314 | 2.810 | | 0.460 | | 0.720 | | 0.620 | | 0.180 | |

*Table S4.2 (continue)*

| **Sample** | **Hf** | | **Ta** | | **Pb** | | **Th** | | **U** | |
|---|---|---|---|---|---|---|---|---|---|---|
| | ppm | stdev | ppm | stdev | ppm | stdev | ppm | stdev | ppm | stdev |
| S1314-X | 2.467 | 0.012 | 0.418 | 0.004 | 0.851 | 0.013 | 0.590 | 0.008 | 0.205 | 0.001 |
| S1314-01 | 2.880 | | 0.470 | | 0.800 | | 0.590 | | 0.180 | |
| S1314-01 Dup | | | | | | | | | | |
| S1627-01 | | | | | | | | | | |
| S1629-35 | 2.520 | | 0.330 | | 0.450 | | 0.340 | | 0.110 | |
| S1629-35 Dup | | | | | | | | | | |
| S1639-03 | | | | | | | | | | |
| **E-MORB** | | | | | | | | | | |
| SMA1970-191A | 2.902 | 0.017 | 0.806 | 0.004 | 0.971 | 0.019 | 0.985 | 0.006 | 0.321 | 0.006 |
| SMA1970-191B | 3.005 | 0.040 | 0.831 | 0.008 | 1.009 | 0.008 | 1.020 | 0.007 | 0.335 | 0.004 |
| SMA1970-191C | 2.793 | 0.044 | 0.804 | 0.012 | 0.970 | 0.013 | 0.976 | 0.005 | 0.346 | 0.013 |
| SMA1970-191D | 2.934 | 0.057 | 0.810 | 0.010 | 0.931 | 0.012 | 0.988 | 0.003 | 0.334 | 0.004 |
| SMA1970-191E | 3.000 | 0.042 | 0.837 | 0.000 | 0.984 | 0.014 | 1.019 | 0.010 | 0.331 | 0.000 |
| SMA1970-192 | 2.955 | 0.043 | 0.824 | 0.009 | 0.970 | 0.022 | 1.015 | 0.006 | 0.333 | 0.006 |
| SMA1970-193 | 2.904 | 0.046 | 0.828 | 0.013 | 0.969 | 0.011 | 1.002 | 0.012 | 0.328 | 0.001 |
| SMA1970-194 | 2.758 | 0.003 | 0.793 | 0.001 | 1.000 | 0.014 | 0.954 | 0.005 | 0.313 | 0.001 |
| SMA1970-195 | 2.941 | 0.033 | 0.826 | 0.007 | 0.968 | 0.010 | 1.003 | 0.008 | 0.317 | 0.005 |
| SMA1970-199 | 2.830 | 0.026 | 0.755 | 0.004 | 0.958 | 0.009 | 0.910 | 0.005 | 0.303 | 0.002 |
| SMA1970-202 | 2.539 | 0.031 | 0.649 | 0.003 | 0.844 | 0.009 | 0.772 | 0.012 | 0.249 | 0.006 |
| SMA1973-246 | 1.981 | 0.004 | 0.467 | 0.006 | 1.093 | 0.004 | 0.680 | 0.004 | 0.220 | 0.001 |
| SMA1973-248 | 2.533 | 0.018 | 0.835 | 0.002 | 0.917 | 0.017 | 1.126 | 0.003 | 0.384 | 0.006 |
| SMA1973-249 | 1.960 | 0.036 | 0.620 | 0.010 | 0.723 | 0.011 | 0.796 | 0.015 | 0.277 | 0.005 |
| SMA1973-250 | 2.779 | 0.013 | 0.866 | 0.008 | 0.913 | 0.018 | 1.171 | 0.016 | 0.379 | 0.003 |
| SMA1973-251 | 2.639 | 0.084 | 0.874 | 0.030 | 0.947 | 0.039 | 1.168 | 0.038 | 0.415 | 0.009 |
| SMA1973-252 | 2.679 | 0.003 | 0.837 | 0.004 | 0.859 | 0.024 | 1.139 | 0.012 | 0.352 | 0.009 |
| SMA1973-254 | 2.620 | 0.057 | 0.877 | 0.018 | 0.925 | 0.005 | 1.144 | 0.017 | 0.385 | 0.004 |
| SMA1973-255 | 2.398 | 0.099 | 0.816 | 0.027 | 0.898 | 0.036 | 1.075 | 0.042 | 0.380 | 0.016 |
| SMA1973-256 | 2.459 | 0.072 | 0.813 | 0.022 | 0.902 | 0.021 | 1.069 | 0.030 | 0.367 | 0.011 |
| SMA1973-258 | 2.683 | 0.011 | 0.858 | 0.004 | 0.923 | 0.020 | 1.152 | 0.003 | 0.371 | 0.003 |
| SMA1973-261 | 2.106 | 0.013 | 0.540 | 0.006 | 0.948 | 0.008 | 0.740 | 0.006 | 0.258 | 0.006 |
| SMA1973-262 | 2.006 | 0.019 | 0.493 | 0.005 | 0.940 | 0.005 | 0.673 | 0.005 | 0.245 | 0.003 |

*Table S4.2 (continue)*

| **Sample** | **Hf** | | **Ta** | | **Pb** | | **Th** | | **U** | |
|---|---|---|---|---|---|---|---|---|---|---|
| | ppm | stdev | ppm | stdev | ppm | stdev | ppm | stdev | ppm | stdev |
| SMA1973-263 | 2.057 | 0.022 | 0.532 | 0.009 | 1.007 | 0.003 | 0.717 | 0.004 | 0.256 | 0.006 |
| SMA1973-264 | 2.556 | 0.063 | 0.807 | 0.015 | 0.869 | 0.017 | 1.106 | 0.024 | 0.357 | 0.002 |
| SMA1974-266 | 2.155 | 0.033 | 0.588 | 0.004 | 0.872 | 0.012 | 0.771 | 0.018 | 0.276 | 0.003 |
| SMA1974-267 | 2.152 | 0.059 | 0.582 | 0.003 | 0.879 | 0.018 | 0.774 | 0.013 | 0.285 | 0.003 |
| SMA1974-271 | 2.124 | 0.003 | 0.561 | 0.004 | 0.848 | 0.012 | 0.763 | 0.004 | 0.271 | 0.004 |
| SMA1974-272 | 2.120 | 0.018 | 0.570 | 0.004 | 0.860 | 0.004 | 0.762 | 0.004 | 0.265 | 0.003 |
| SMA1974-273 | 2.057 | 0.022 | 0.557 | 0.001 | 0.857 | 0.003 | 0.736 | 0.003 | 0.264 | 0.005 |
| SMA1974-274 | 2.094 | 0.007 | 0.563 | 0.006 | 0.854 | 0.003 | 0.748 | 0.001 | 0.271 | 0.002 |
| SMA1974-275 | 2.244 | 0.047 | 0.607 | 0.010 | 0.881 | 0.007 | 0.811 | 0.013 | 0.287 | 0.002 |
| SMA1974-276 | 2.094 | 0.040 | 0.578 | 0.003 | 0.919 | 0.019 | 0.760 | 0.007 | 0.285 | 0.004 |
| SMA1974-277 | 2.040 | 0.019 | 0.566 | 0.002 | 0.927 | 0.002 | 0.745 | 0.002 | 0.289 | 0.003 |
| SMA1979-365 | 3.284 | 0.069 | 1.134 | 0.019 | 1.330 | 0.034 | 1.578 | 0.045 | 0.498 | 0.004 |
| SMA1979-366 | 3.044 | 0.062 | 1.102 | 0.017 | 1.410 | 0.048 | 1.537 | 0.024 | 0.476 | 0.008 |
| SMA1979-367 | 3.059 | 0.074 | 1.155 | 0.014 | 1.346 | 0.001 | 1.607 | 0.021 | 0.494 | 0.015 |
| SMA1979-367 Dup | 2.651 | 0.006 | 1.050 | 0.006 | 0.991 | 0.007 | 1.444 | 0.009 | 0.449 | 0.004 |
| SMA1979-368 | 3.443 | 0.040 | 0.935 | 0.005 | 1.057 | 0.011 | 1.269 | 0.014 | 0.392 | 0.001 |
| SMA1979-369 | 3.151 | 0.023 | 1.103 | 0.013 | 1.165 | 0.012 | 1.526 | 0.013 | 0.497 | 0.004 |
| SMA1979-370 | 2.965 | 0.071 | 1.095 | 0.002 | 1.150 | 0.008 | 1.507 | 0.006 | 0.505 | 0.006 |
| SMA1979-371 | 3.111 | 0.061 | 1.057 | 0.013 | 1.145 | 0.002 | 1.459 | 0.011 | 0.481 | 0.006 |
| SMA1979-372 | 2.998 | 0.023 | 1.051 | 0.006 | 1.095 | 0.008 | 1.460 | 0.011 | 0.483 | 0.007 |
| SMA1979-373 | 2.430 | 0.070 | 1.048 | 0.024 | 1.072 | 0.016 | 1.432 | 0.040 | 0.490 | 0.007 |
| SMA1979-374 | 2.526 | 0.071 | 1.046 | 0.017 | 1.047 | 0.005 | 1.450 | 0.013 | 0.479 | 0.001 |
| SMA1979-375 | 2.680 | 0.005 | 1.090 | 0.010 | 1.059 | 0.014 | 1.463 | 0.027 | 0.499 | 0.012 |
| SMA1979-376 | 4.145 | 0.030 | 1.015 | 0.016 | 1.262 | 0.006 | 1.375 | 0.007 | 0.466 | 0.002 |
| SMA1979-377 | 3.437 | 0.051 | 0.943 | 0.004 | 1.197 | 0.037 | 1.232 | 0.026 | 0.458 | 0.003 |
| S1313-06 | 3.640 | | 0.910 | | 1.060 | | 1.060 | | 0.350 | |
| S1313-06 Dup | | | | | | | | | | |
| S1313-10 | | | | | | | | | | |
| S1313-11 | 3.650 | | 0.900 | | 1.150 | | 1.090 | | 0.320 | |
| S1313-11 Dup | | | | | | | | | | |
| S1313-13 | 3.610 | | 0.920 | | 1.450 | | 1.040 | | 0.330 | |

*Table S4.2 (continue)*

| **Sample** | **Hf** | | **Ta** | | **Pb** | | **Th** | | **U** | |
|---|---|---|---|---|---|---|---|---|---|---|
| | ppm | stdev | ppm | stdev | ppm | stdev | ppm | stdev | ppm | stdev |
| S1624-21 | 3.220 | | 1.000 | | 0.970 | | 1.200 | | 0.340 | |
| S1624-21 Dup | | | | | | | | | | |
| S1625-07 | | | | | | | | | | |
| S1628-02 A | 3.140 | | 1.240 | | 1.230 | | 1.460 | | 0.430 | |
| S1628-02 | 3.150 | | 1.210 | | 1.040 | | 1.520 | | 0.430 | |
| **K-rich MORB** | | | | | | | | | | |
| SMA1966-128 | 4.999 | 0.060 | 1.715 | 0.017 | 1.936 | 0.035 | 2.332 | 0.013 | 0.675 | 0.005 |
| SMA1974-283 | 2.845 | 0.023 | 1.213 | 0.018 | 1.133 | 0.024 | 1.659 | 0.026 | 0.502 | 0.013 |
| SMA1974-285 | 2.584 | 0.179 | 1.189 | 0.062 | 1.164 | 0.075 | 1.627 | 0.116 | 0.486 | 0.022 |
| SMA1974-287 | 2.554 | 0.048 | 1.198 | 0.024 | 1.159 | 0.020 | 1.630 | 0.038 | 0.508 | 0.004 |
| SMA1976-315 | 3.461 | 0.082 | 1.613 | 0.035 | 1.543 | 0.045 | 2.058 | 0.035 | 0.626 | 0.012 |
| SMA1976-317 | 3.592 | 0.030 | 1.619 | 0.014 | 1.641 | 0.012 | 2.082 | 0.023 | 0.620 | 0.007 |
| SMA1976-317 Dup | 3.118 | 0.054 | 1.525 | 0.015 | 1.437 | 0.006 | 1.886 | 0.020 | 0.659 | 0.003 |
| SMA1976-319 | 3.399 | 0.105 | 1.533 | 0.010 | 1.478 | 0.021 | 1.985 | 0.066 | 0.613 | 0.005 |
| SMA1976-320 | 3.515 | 0.058 | 1.587 | 0.046 | 1.604 | 0.019 | 2.062 | 0.059 | 0.612 | 0.006 |
| SMA1976-321 | 3.487 | 0.025 | 1.734 | 0.035 | 1.649 | 0.019 | 2.230 | 0.036 | 0.719 | 0.042 |
| SMA1976-323 | 3.429 | 0.057 | 1.577 | 0.031 | 1.508 | 0.044 | 2.048 | 0.056 | 0.623 | 0.006 |
| SMA1976-324 | 3.861 | 0.056 | 1.732 | 0.008 | 1.665 | 0.022 | 2.309 | 0.005 | 0.696 | 0.008 |
| SMA1976-325 | 3.456 | 0.166 | 1.695 | 0.076 | 1.573 | 0.080 | 2.153 | 0.102 | 0.660 | 0.036 |
| S1311-03 | | | | | | | | | | |
| S1312-45 | 4.720 | | 1.800 | | 1.560 | | 2.130 | | 0.650 | |
| S1312-45 Dup | 4.910 | | 1.870 | | 1.530 | | 2.180 | | 0.640 | |
| S1312-49 | | | | | | | | | | |
| S1312 | | | | | | | | | | |
| S1312-Xb | 6.198 | 0.174 | 2.130 | 0.036 | 1.855 | 0.141 | 2.806 | 0.060 | 0.725 | y.023148 |
| S1626-15 | 3.87 | | 1.71 | | 1.37 | | 1.99 | | 0.54 | |
| S1626-15 Dup | 3.87 | | 1.71 | | 1.27 | | 2.03 | | 0.53 | |
| S1626-21 | 3.99 | | 1.70 | | 1.26 | | 2.01 | | 0.56 | |
| S1626-22 | 3.87 | | 1.68 | | 1.23 | | 2.03 | | 0.58 | |
| S1626-23 | 3.97 | | 1.69 | | 1.26 | | 1.95 | | 0.52 | |

*Table S4.3 – Calculated normative compositions (%).*

| Sample | Qz | Pl | Or | Nph | Di | Hyp | Ol | Ilm | Ap |
|---|---|---|---|---|---|---|---|---|---|
| **N-MORB** | | | | | | | | | |
| SMA1977-328 | 0 | 52.3 | 1.60 | 0 | 23.93 | 10.8 | 7 | 2.83 | 0.37 |
| SMA1977-329 | 0 | 53.2 | 0.95 | 0 | 22.14 | 10.53 | 8.8 | 2.98 | 0.35 |
| SMA1977-330 | 0 | 53.1 | 1.06 | 0 | 21.11 | 15.24 | 5.56 | 3.11 | 0.35 |
| SMA1977-331 | 0 | 53.2 | 1 | 0 | 21.37 | 11.08 | 8.45 | 3.06 | 0.3 |
| SMA1977-334 | 0 | 52.5 | 1 | 0 | 20.64 | 12.84 | 8.18 | 3.11 | 0.3 |
| SMA1977-335 | 0 | 52.6 | 1 | 0 | 21.01 | 12.48 | 8.21 | 3.1 | 0.35 |
| SMA1977-336 | 0 | 51.8 | 1.12 | 0 | 22.01 | 12.38 | 7.48 | 3.42 | 0.32 |
| SMA1977-337 | 0 | 53.4 | 1.06 | 0 | 19.91 | 14.25 | 7.28 | 3.11 | 0.37 |
| SMA1977-338 | 0 | 52.5 | 1 | 0 | 20.7 | 13.48 | 7.61 | 3.04 | 0.39 |
| SMA1977-340 | 0 | 54.2 | 0.95 | 0 | 20.12 | 11.18 | 9.61 | 3 | 0.35 |
| SMA1977-341B | 0 | 53.3 | 1 | 0 | 21.37 | 9.56 | 10.36 | 2.98 | 0.28 |
| SMA1977-341T | 0 | 53.1 | 1 | 0 | 21.41 | 11.24 | 9.08 | 2.98 | 0.35 |
| SMA1977-342 | 0 | 53.6 | 1.06 | 0 | 19.89 | 13.17 | 8.28 | 2.98 | 0.35 |
| SMA1977-343 | 0 | 53.9 | 1.06 | 0 | 19.66 | 12.13 | 9.12 | 3.13 | 0.3 |
| SMA1978-345 | 0 | 54.1 | 1.24 | 0 | 20.3 | 9.92 | 10.31 | 3.02 | 0.44 |
| SMA1978-346 | 0 | 53.8 | 1.24 | 0 | 19.7 | 9.95 | 10.63 | 2.98 | 0.35 |
| SMA1978-348 | 0 | 53.9 | 1.3 | 0 | 20.65 | 10.17 | 9.8 | 3 | 0.39 |
| SMA1978-349 | 0 | 53.3 | 1.24 | 0 | 20.44 | 11.54 | 9.22 | 3.15 | 0.37 |
| SMA1978-350 | 0 | 53.8 | 1.24 | 0 | 20.15 | 11.76 | 8.89 | 2.91 | 0.32 |
| SMA1978-352 | 0 | 53.8 | 1.24 | 0 | 19.71 | 13.73 | 6.93 | 3.04 | 0.39 |
| SMA1978-354 | 0 | 52.9 | 1.3 | 0 | 20.89 | 10.86 | 9.12 | 3.15 | 0.39 |
| SMA1978-355 | 0 | 53.6 | 1.3 | 0 | 19.61 | 12.37 | 8.54 | 3.19 | 0.44 |
| SMA1978-356 | 0 | 53.4 | 1.24 | 0 | 20.21 | 13.44 | 7.46 | 3.02 | 0.46 |
| SMA1978-357 | 0 | 53.3 | 1.36 | 0 | 21.17 | 12.67 | 6.58 | 3.34 | 0.44 |
| SMA1978-358 | 0 | 53.4 | 1.36 | 0 | 20.18 | 12.67 | 8.02 | 3.08 | 0.39 |
| SMA1978-360 | 0 | 53.1 | 1.36 | 0 | 20.11 | 11.67 | 9.07 | 3.02 | 0.44 |
| SMA1978-363 | 0 | 54.4 | 1.18 | 0 | 20.24 | 9.93 | 9.89 | 2.98 | 0.39 |
| SMA1978-364 | 0 | 52.9 | 1.36 | 0 | 21.08 | 7.78 | 11.94 | 3.1 | 0.37 |
| S1312-Xa | 0 | 56.9 | 2.95 | 0 | 16.79 | 12.75 | 5.31 | 3.84 | 0.65 |
| S1312-53 | 0 | 54.8 | 1.83 | 0 | 20.56 | 8.37 | 12.04 | 2.7 | 0.44 |
| S1314 | 0.61 | 54.7 | 1.48 | 0 | 11.33 | 26.85 | 0 | 3.38 | 0.44 |
| S1314-X | 0.33 | 55.2 | 1.60 | 0 | 13.07 | 25.9 | 0 | 3.53 | 0.46 |
| S1314-01 | 0 | 54.7 | 1.60 | 0 | 11.9 | 25.61 | 1.34 | 3.36 | 0.53 |
| S1627-01 | 0 | 54.7 | 1.89 | 0 | 19.49 | 8.43 | 11.49 | 2.89 | 0.44 |
| S1629-35 | 0 | 54.1 | 1.06 | 0 | 21.2 | 7.38 | 11.95 | 2.73 | 0.3 |
| S1639-03 | 0 | 55.1 | 1.48 | 0 | 19.16 | 10.39 | 10.08 | 2.89 | 0.37 |
| **E-MORBs** | | | | | | | | | |
| SMA1973-246 | 0 | 55.8 | 2.01 | 0 | 15.11 | 3.45 | 19.69 | 2.85 | 0.39 |
| SMA1973-261 | 0 | 58.9 | 2.25 | 0 | 16.19 | 3.08 | 15.89 | 2.58 | 0.39 |
| SMA1973-262 | 0 | 58.6 | 2.13 | 0 | 15.09 | 2.41 | 17.47 | 2.68 | 0.44 |
| SMA1973-263 | 0 | 59.1 | 2.30 | 0 | 15.05 | 10.02 | 10.93 | 2.68 | 0.37 |
| SMA1974-272 | 0 | 58.5 | 2.19 | 0 | 17.66 | 1.57 | 16.29 | 2.7 | 0.37 |
| SMA1974-273 | 0 | 57.7 | 2.19 | 0 | 17.41 | 3 | 15.32 | 2.66 | 0.44 |
| SMA1974-274 | 0 | 58.5 | 2.19 | 0 | 17.79 | 2.72 | 15.39 | 2.7 | 0.32 |
| S1313-06 | 0 | 58.2 | 3.07 | 0 | 17.21 | 6.76 | 10.11 | 3.42 | 0.79 |
| S1313-10 | 0 | 58.4 | 3.01 | 0 | 17.07 | 4.56 | 12.46 | 3.49 | 0.72 |
| S1313-11 | 0 | 57.5 | 3.19 | 0 | 16.68 | 6.5 | 10.69 | 3.61 | 0.7 |
| S1313-13 | 0 | 57.8 | 3.01 | 0 | 17.06 | 6.59 | 10.49 | 3.68 | 0.6 |
| SMA1974-275 | 0 | 58.3 | 2.42 | 0 | 17.63 | 0.05 | 17.2 | 2.72 | 0.46 |
| SMA1970-191A | 0 | 60.4 | 3.25 | 0 | 14.53 | 0.37 | 16.8 | 3.53 | 0.58 |

*Table S4.3 (continue)*

| Sample | Qz | Pl | Or | Nph | Di | Hyp | Ol | Ilm | Ap |
|---|---|---|---|---|---|---|---|---|---|
| SMA1970-191B | 0 | 58.3 | 3.31 | 1.21 | 15.46 | 0 | 16.87 | 3.46 | 0.6 |
| SMA1970-191C | 0 | 60.9 | 3.25 | 0 | 13.91 | 2.15 | 15.45 | 3.46 | 0.63 |
| SMA1970-191D | 0 | 59.7 | 3.13 | 0.36 | 15.06 | 0 | 16.85 | 3.42 | 0.67 |
| SMA1970-191E | 0 | 60.0 | 3.13 | 0.16 | 15.98 | 0 | 16.25 | 3.63 | 0.58 |
| SMA1970-192 | 0 | 58.6 | 3.31 | 1.01 | 15.35 | 0 | 16.94 | 3.53 | 0.65 |
| SMA1970-193 | 0 | 59.7 | 3.25 | 0.48 | 14.54 | 0 | 17.25 | 3.63 | 0.6 |
| SMA1970-194 | 0 | 57.7 | 3.37 | 1.22 | 14.71 | 0 | 17.74 | 3.36 | 0.67 |
| SMA1970-195 | 0 | 60.1 | 3.19 | 0.05 | 14.87 | 0 | 17.44 | 3.48 | 0.7 |
| SMA1970-199 | 0 | 60.1 | 2.95 | 0.72 | 14.7 | 0 | 16.96 | 3.3 | 0.53 |
| SMA1970-202 | 0 | 60.0 | 2.48 | 0.3 | 14.51 | 0 | 18.24 | 3.1 | 0.51 |
| SMA1973-248 | 0 | 57.4 | 3.01 | 0 | 15.18 | 10.92 | 9.1 | 2.94 | 0.63 |
| SMA1973-249 | 0 | 55.7 | 2.36 | 0 | 18.65 | 9.19 | 10.19 | 2.77 | 0.53 |
| SMA1973-250 | 0 | 57.2 | 2.84 | 0 | 15.97 | 9.12 | 10.38 | 2.83 | 0.56 |
| SMA1973-251 | 0 | 57.7 | 3.19 | 0 | 16.49 | 8.21 | 10.11 | 3 | 0.63 |
| SMA1973-252 | 0 | 57.3 | 3.01 | 0 | 14.83 | 12.61 | 7.83 | 2.91 | 0.53 |
| SMA1973-254 | 0 | 58.0 | 3.07 | 0 | 16.21 | 7.37 | 11.22 | 3.06 | 0.49 |
| SMA1973-255 | 0 | 57.7 | 2.95 | 0 | 15.78 | 7.93 | 11.22 | 2.87 | 0.6 |
| SMA1973-256 | 0 | 57.1 | 2.84 | 0 | 16.42 | 7.73 | 11.21 | 2.77 | 0.44 |
| SMA1973-258 | 0 | 57.5 | 3.01 | 0 | 15.35 | 11.57 | 8.39 | 3.02 | 0.56 |
| SMA1973-264 | 0 | 57.2 | 2.84 | 0 | 16.82 | 9 | 10.01 | 2.98 | 0.53 |
| SMA1974-266 | 0 | 58.0 | 2.3 | 0 | 16.88 | 5.42 | 13.69 | 2.66 | 0.44 |
| SMA1974-267 | 0 | 58.0 | 2.3 | 0 | 16.6 | 5.09 | 13.31 | 2.81 | 0.56 |
| SMA1974-271 | 0 | 59.0 | 2.19 | 0 | 16.55 | 7.06 | 12.36 | 2.53 | 0.49 |
| SMA1974-276 | 0 | 57.9 | 2.19 | 0 | 17.37 | 5.28 | 13.42 | 2.68 | 0.39 |
| SMA1974-277 | 0 | 58.2 | 2.25 | 0 | 17.19 | 3.77 | 14.67 | 2.77 | 0.42 |
| SMA1979-365 | 0 | 58.4 | 3.90 | 0 | 16.09 | 5.5 | 11.09 | 3.04 | 0 |
| SMA1979-366 | 0 | 58.9 | 3.84 | 0 | 17.12 | 4.12 | 11.62 | 2.89 | 0 |
| SMA1979-367 | 0 | 59.1 | 3.66 | 0 | 16.45 | 6.44 | 10.1 | 2.62 | 0 |
| SMA1979-368 | 0 | 58.2 | 3.43 | 0 | 17.34 | 7.75 | 8.5 | 3.29 | 0 |
| SMA1979-369 | 0 | 58.5 | 4.08 | 0 | 16.12 | 6.18 | 10.55 | 3.19 | 0 |
| SMA1979-370 | 0 | 58.1 | 4.08 | 0 | 16.43 | 6.32 | 10.45 | 3.04 | 0 |
| SMA1979-371 | 0 | 58.8 | 3.90 | 0 | 16.42 | 5.5 | 10.75 | 3.1 | 0 |
| SMA1979-372 | 0 | 57.3 | 4.02 | 0 | 16.35 | 10.89 | 6.63 | 3.02 | 0.65 |
| SMA1979-373 | 0 | 58.4 | 3.90 | 0 | 18.18 | 3.96 | 10.74 | 2.79 | 0 |
| SMA1979-374 | 0 | 58.7 | 3.90 | 0 | 16.58 | 7.36 | 9.32 | 2.7 | 0.67 |
| SMA1979-375 | 0 | 58.2 | 3.96 | 0 | 15.85 | 9.64 | 8.44 | 2.68 | 0.7 |
| SMA1979-376 | 0 | 57.5 | 3.55 | 0 | 14.33 | 12.96 | 6.75 | 3.78 | 0.79 |
| SMA1979-377 | 0 | 57.5 | 3.37 | 0 | 14.61 | 12.3 | 7.43 | 3.59 | 0.79 |
| S1313-06 | 0 | 57.6 | 3.07 | 0 | 16.23 | 8.45 | 9.04 | 3.51 | 0.74 |
| S1313-11 | 0 | 57.5 | 3.19 | 0 | 16.68 | 6.5 | 10.69 | 3.61 | 0.7 |
| S1313-20 | 0 | 57.4 | 3.55 | 0 | 16.44 | 4.34 | 12.75 | 3.53 | 0.76 |
| S1624-21 | 0 | 57.5 | 3.37 | 0 | 15.74 | 5.25 | 12.35 | 3.11 | 0.7 |
| S1625-07 | 0 | 59.3 | 3.37 | 0 | 17.7 | 1.38 | 14.75 | 3.13 | 0.72 |
| S1628-02 | 0 | 56.1 | 3.90 | 0 | 18.65 | 7.83 | 9.12 | 3.04 | 0.58 |

*Table S4.3 (continue)*

| Sample | Qz | Pl | Or | Nph | Di | Hyp | Ol | Ilm | Ap |
|---|---|---|---|---|---|---|---|---|---|
| **K-rich MORBs** | | | | | | | | | |
| SMA1966-128 | 3.03 | 46.7 | 5.97 | 0 | 14.52 | 22.12 | 0 | 5.81 | 1.11 |
| SMA1976-315 | 0 | 53.4 | 5.08 | 1.47 | 20.65 | 0 | 13.71 | 3.7 | 0.9 |
| SMA1976-317 | 0 | 52.7 | 5.08 | 2.11 | 20.88 | 0 | 13.26 | 3.84 | 0.97 |
| SMA1976-319 | 0 | 54.0 | 5.08 | 1.59 | 20.47 | 0 | 13.55 | 3.67 | 0.88 |
| SMA1976-320 | 0 | 54.0 | 4.85 | 1.71 | 20.14 | 0 | 13.91 | 3.63 | 0.88 |
| SMA1976-321 | 0 | 53.1 | 5.44 | 2.08 | 20.74 | 0 | 13.11 | 3.76 | 0.9 |
| SMA1976-323 | 0 | 54.9 | 4.96 | 0.61 | 20.64 | 0 | 13.47 | 3.68 | 0.97 |
| SMA1976-324 | 0 | 52.4 | 5.26 | 1.78 | 20.63 | 0 | 14.23 | 3.84 | 0.95 |
| SMA1976-325 | 0 | 55.3 | 5.14 | 0.69 | 20.27 | 0 | 13.37 | 3.74 | 0.93 |
| S1311-03 | 0 | 35.6 | 7.39 | 8.39 | 26.31 | 0 | 15.49 | 4.73 | 1.41 |
| S1312-45 | 0 | 54.1 | 5.91 | 0 | 17.09 | 2.81 | 13.67 | 4.48 | 1.27 |
| S1312-49 | 0 | 19.7 | 11.52 | 16.52 | 31.23 | 0 | 11.53 | 5.74 | 2.02 |
| S1312-B | 0 | 38.5 | 6.97 | 6.57 | 24.09 | 0 | 16.51 | 4.92 | 1.37 |
| S1312-Xb | 0 | 53.1 | 5.91 | 0 | 17.51 | 5.15 | 11.35 | 4.5 | 1.14 |
| S1626-15 | 0 | 54.1 | 5.14 | 0.58 | 17.96 | 0 | 15.9 | 3.74 | 0.79 |
| S1626-21 | 0 | 54.4 | 5.02 | 0 | 17.43 | 1.09 | 15 | 3.7 | 0.88 |
| S1626-22 | 0 | 55.0 | 5.32 | 0 | 17.8 | 1.12 | 15.39 | 3.87 | 0.74 |
| S1626-23 | 0 | 52.3 | 5.08 | 1.44 | 18.5 | 0 | 15.46 | 3.72 | 0.95 |
| SMA1974-283 | 0 | 48.8 | 4.25 | 3.19 | 25.13 | 0 | 13.76 | 3.08 | 0.65 |
| SMA1974-285 | 0 | 49.0 | 4.43 | 3.45 | 24.44 | 0 | 14.25 | 3.04 | 0.65 |
| SMA1974-287 | 0 | 50.3 | 4.43 | 2.86 | 22.83 | 0 | 14.46 | 3.02 | 0.67 |

*Qz: quartz; Pl.: plagioclase; Or: orthoclase; Nph: nepheline; Di: diopside; Hyp: hypersthene; Ol: olivine: Ilm: ilmenite; Ap: apatite.*

*Table S4.4 – Different compositions and parameters used for LLD calculations*

| | **Starting major composition for LLD calculations** | **Mixing** | **$P_i$** | **$P_i$ with $H_2O$** | **Figures** |
|---|---|---|---|---|---|
| N-MORB | Primary N-MORB (Presnall and Hoover, 1987) | - | 0.2 GPa | - | Fig. 4.10<br>Fig. 4.10 |
| | Aggregated melt 4%-9% F from a fertile spinel lherzolite (Kinzler, 1997) | - | 0.2 GPa<br>0.5 GPa<br>0.8 GPa | 0.8 GPa<br>0.3 wt% $H_2O$ | Fig. 4.10<br>Fig. 4.10 |
| | Melt from fertile spinel lherzolite (KLB-1) (Hirose and Kushiro, 1993) | - | 0.2 GPa | - | Fig. 4.10<br>Fig. 4.11 |
| E-MORB | Aggregated melt 4%-9% F from a fertile spinel lherzolite (Kinzler, 1997) | - | 0.2 GPa<br>0.5 GPa<br>0.8 GPa | 0.8 GPa<br>0.3 wt% $H_2O$ | Fig. 4.10 |
| | Experimental melt from partial melting of M5-40 Si-undersaturated pyroxenite at 2.5 GPa 1375 °C (Lambart et al., 2013) | 25% melt from M5-40 pyroxenite (Lambart et al., 2013) + 75% aggregated melt 7% F from a fertile spinel lherzolite (Kinzler, 1997) | 0.2 Ga<br>0.8 Gpa | 0.8 Gpa<br>0.5 wt% $H_2O$ | Fig. 4.14 |
| | Experimental melt from partial melting of K-rich eclogite (G2K) at 2 GPa and 1325°C (Pertermann et al., 2003) | 30% melt from G2K eclogite (Pertermann et al., 2003) + 70% aggregated melt 7% F from a fertile spinel lherzolite (Kinzler, 1997) | 0.2 GPa | - | Fig. 4.14 |
| K-rich MORB | Experimental melt from partial melting of M5-40 Si-undersaturated pyroxenite at 2.5 GPa 1375 °C (Lambart et al., 2013) | 25% melt from M5-40 pyroxenite (Lambart et al., 2013) + 75% aggregated melt 7% F from a fertile spinel lherzolite (Kinzler, 1997) | 0.2 GPa<br>0.8 GPa | 0.2 GPa<br>0.5 wt% $H_2O$ | Fig. 4.14 |
| | Experimental melt from partial melting of garnet clinopyroxenite 77SL-582 at 2.5 GPa and 1430°C (Keshav et al., 2004) | - | 0.2 GPa<br>0.5 GPa<br>0.8 GPa | 0.8 GPa<br>1 wt% $H_2O$ | Fig. 4.18 |
| | Experimental melt from partial melting of phlogopite-bearing lherzolite partially melted at 1250°C (Condamine et al., 2016) | 10% melt from Phl. lherzolite (Condamine et al., 2016) + 90% aggregated melt 7% F from a fertile spinel lherzolite (Kinzler, 1997) | 0.2 GPa<br>0.5 GPa<br>0.8 GPa | 0.8 GPa 1 wt% $H_2O$ | Fig. 4.18 |

*Table S4.5 – Different fractional non-modal aggregated melt calculated for trace element modelling*

| | **Starting trace compositiong for REE melting models** | **Mineral abundance** | **F (%)** | **Mixing** | **Melting mode** | **Partition coefficients** | **Figure** |
|---|---|---|---|---|---|---|---|
| N-MORB | D-DMM<br>(Workmann et al., 2005) | 0.57 Ol + 0.28 Opx + 0.13 Cpx + 0.02 Sp<br>(Workmann et al., 2005) | 4% | - | (Hellebrand et al., 2002) | Brunelli et al. (2006) | Fig. 4.12 |
| | E-DMM<br>(Workmann et al., 2005) | 0.53 Ol + 0.27 Opx + 0.17 Cpx + 0.03 Sp<br>(Hellebrand et al., 2002) | 9% | - | | | Fig. 4.12 |
| E-MORB | E-DMM<br>(Workmann et al., 2005) | 0.53 Ol + 0.27 Opx + 0.17 Cpx + 0.03 Sp<br>(Hellebrand et al., 2002) | 3% | - | | | Fig. 4.13 |
| | Altered MORB<br>(Staudigel et al., 1996) | 0.61 Cpx + 0.18 Grt + 0.21 Opx<br>(Borghini et al., 2016) | 7% | Aggregated melt from 2%F D-DMM<br>(Workmann et al., 2005) | Borghini et al. (2017) | Pertermann et al. (2002, 2004) | Fig. 4.15 |
| K-rich MORB | Subducted oceanic crust garnet pyroxenite<br>(Donelly et al., 2004) | 0.61 Cpx + 0.18 Grt + 0.21 Opx<br>(Borghini et al., 2016) | 2% | Aggregated melt from 2%F D-DMM<br>(Workmann et al., 2005) | Borghini et al. (2017) | | Fig. 4.19 |
| | Phlogopite-bearing lherzolite source<br>(Grégoire et al., 2002). | 0.67 Ol + 0.29 Opx + 0.01 Cpx + 0.01 Sp + 0.03 Phl<br>(Grégoire et al., 2002) | 4% | Aggregated melt from 2%F D-DMM<br>(Workmann et al., 2005) | Condamine et al. (2014) | Condamine et al. (2022) | Fig. 4.20 |

# CHAPTER 5 Unblended MORBs at a Mid-Ocean Ridge cold spot

## Abstract

Mid-Ocean-Ridge Basalts have highly variable isotopic signatures ranging from enriched, linked to the influence of hotspots, to depleted, where ancient, depleted domains are scattered in the source. However, the majority of MORB results from mixing of these multiple isotopic components hiding the true diversity of the mantle source. Here we measure the Sr, Nd, Pb and Hf isotope composition of basaltic glasses from the Eastern Romanche Ridge Transform Intersection, in the Equatorial Mid-Atlantic Ridge region, where cold lithosphere faces the warm axial segment tip creating a progressively colder thermal regime along the ridge axis moving towards the transform domain. Within 100 km we identify four extreme mantle components in the data, Depleted-MORB Mantle, Ultra-Depleted Mantle, HIMU and EMII, which cover most of the global isotope variability documented in MORBs. The geographical distribution of melt compositions along the ridge axis correlates with mantle potential temperature, evidence that unblending of the mantel source signatures is efficient in cold thermal regimes.

We argue that in cold spots, i.e., regions with colder-than-average mantle temperatures, individual components are preferentially extracted revealing that the mantle is heterogeneous at a smaller scale than previously thought. Moreover, isotopically ultra-depleted components scattered in the mantle source, which are generally expected to have elemental ultra-depleted composition, could instead be fertile in composition. This is evidence for variable compositions of long-time integrated heterogeneities that have experienced ancient partial melting events.

## Introduction

The evidence is overwhelming that the mantle contains multiple components that are chemically distinct especially from an isotopic point of view (Zindler et al., 1979, Hart, 1984, Stracke, 2021, and references therein). However, during melting at Mid-Ocean Ridges, mantle heterogeneities are generally smoothed out and skewed towards the Depleted MORB Mantle (DMM) endmember (Stracke and Bourdon, 2009, Rudge et al., 2013, Liu and Liang, 2020, Stracke, 2021). This smoothing phenomenon is evident when considering the extreme isotopic difference between MORB and mantle rocks (Salters and Dick, 2002, Liu et al., 2008, Cipriani et al., 2004, 2011, Salters et al., 2011, Brunelli et al., 2018, Willig et al., 2020) or the residual variability in incompletely aggregated gabbroics (Lambart et al., 2019) and melt inclusion (Saal et al., 2005, Sobolev et al., 2011, Koornneef et al., 2015, Reinhard et al., 2016, Stracke et al., 2019). Thus, MORBs are globally characterized by depleted isotopic signatures, i.e., high εNd and εHf and low $^{87}Sr/^{86}Sr$ and $^{206}Pb/^{204}Pb$, with more enriched signatures related to portion of the MOR system affected by hot spot influence. The spatial distribution of the isotope composition of MORBs along the MAR (Figure 5.1) shows a great variability with εHf ranging from -2.758 to 26.205, εNd from -5.325 to 13.109, $^{87}Sr/^{86}Sr$ from 0.702125 to 0.705878 and $^{206}Pb/^{204}Pb$ from 17.496 to 20.090 (Agranier et al., 2005). Along the MAR, highly enriched signatures, i.e., lower εNd and εHf and higher $^{87}Sr/^{86}Sr$ and $^{206}Pb/^{204}Pb$ show up in ridge sectors close to Iceland, Azores, Ascension, Sierra Leone, Discovery and Shona hot spot locations (Figure 5.1). Highly depleted signatures are instead present at the Mohns and Knipovitch ridges and in the Lucky Strike region, close to the Azores, attesting for ancient parcels of mantle preserved through time during mantle convection stirring and progressive solid-state mixing (Figure 5.1) (Salters et al., 2011, Hamelin et al., 2013, Willig et al., 2020, Sanfilippo et al., 2021).

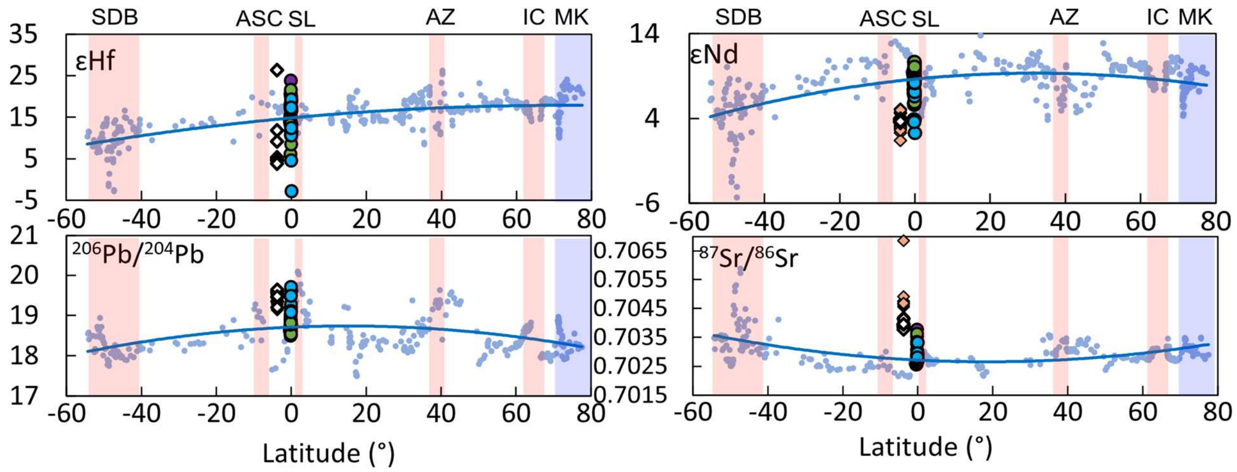

*Figure 5.1- ERRTI (Eastern Romanche Ridge-Transform Intersection) isotopic systematic (red dots) compared to the entire MAR (blue dots, Agranier et al., 2005, Dosso et al., 1993). The blue line is a second order polynomial regression of the MAR data. Red area are hot spot locations. SDB: Shona-Discovery-Bouvet hotspot; ASC: Ascension hot spot; SL: Sierra Leone hotspot; AZ: Azores hotspot; IC: Iceland hotspot. The blue area marks the Monhs-Knipovitch (MK) axis where an ultra-depleted signature has been observed. We also plot data of Fernando de Noronha lavas from this study (white) and from Gerlach et al. (1987; pink) for comparison (see text for details).*

Ridge-scale fluctuation of the isotopic fingerprint along the MAR is evidence for large-scale heterogeneity of the mantle source mainly controlled by ridge/hot spot interactions (White, 1985, Hanan et al., 1986, Schilling et al., 1994, Agranier et al., 2005). Conversely, the small scale (ridge segment) isotopic fluctuation of the MORB source is not yet defined. Distinguishing the contribution of single heterogeneities to the extracted melt is a major challenge. We contribute to this understanding by studying a MAR segment characterized by an extreme lateral thermal gradient where the ridge centre has a "normal" thermal setting comparable to average MAR portions and the ridge tips have significantly lower-than-average mantle potential temperatures. This natural-scale experiment is thought to take advantage of the heat diffusion effects acting in a lithologically heterogenous source during partial melting (Sleep, 1984; Phipps Morgan, 2001, Brunelli et al., 2018). In fact, at average mantle potential temperatures (1350 °C), the size of the sub-ridge melting region is large enough to induce an extensive partial melting of the most refractory components (Phipps Morgan, 2001, Brunelli et al., 2018). Hence, any fertile heterogeneity dispersed in the source produces melts that are strongly diluted into those abundantly produced by the prevalent depleted portion of the source (the DM). This results in a chemically smooth MORB blend where the enriched components are only occasionally showing up or generate local shift in the isotopic signature when the degree of melting is reduced (Haase, 1996 and 2011). If mantle potential temperature locally decreases, the melting region shrinks proportionally then reducing the number of separated heterogeneities (hence different reservoirs/components) entering the melting region and sampled by partial melting (Shorttle and Maclennan, 2011, Stracke and Bourdon, 2009, Brunelli et al., 2018). In this case, the thermodynamic effect of heat diffusion into the low-solidus, first melting lithology, should make it possible to extract melts from individual component or with a significantly reduced degree of mixing. This is because the reservoir with lower solidus experiences enhanced melting due to heat diffusion into the melting heterogeneity from the more refractory screen (Sleep, 1984; Phipps Morgan, 2001; Katz and Rudge, 2011; Brunelli et al., 2018). Heat diffusion induces over-melting of the low-solidus components while reducing the degree of melting of the more refractory one, independently from the relative melt productivity of the two units (Brunelli et al., 2018; Lambart et al., 2016).

We expect this effect to be enhanced in ridge portions whose temperature is significantly lower than average MORs, hereafter called cold spots, according to the definition given by Bonatti et al. (2001). Cold spots have been identified in the context of oceanic mega-transforms (Ligi et al., 2002), which not only create large offsets in the MOR system but also juxtapose oceanic lithosphere with different age. A rather old, thick, and cold lithosphere faces the warm axial segment tips on both sides of the transform, creating a high age contrast (Figure S5.1). The former progressively cools the mantle beneath the ridge axis, resulting in enhanced lateral mantle thermal gradient (Ligi et al., 2002 and 2005; Bonatti, 1996). This makes Ridge-Transform Intersections (RTI) at oceanic mega-transforms natural laboratories for the study of MORB generation at different mantle temperatures.

The Romanche transform fault (RTF) is one of these large mega-transforms with a left stepping offset of the MAR axis of 950 km resulting in an age contrast of about 40 Ma. We focused on the Eastern Romanche Ridge-Transform Intersection (ERRTI) (Figure S5.1). Here, the presence of a thermal minimum has been first hypothesized based on the decrease in the degree of melting of mantle residua (Bonatti et al., 1993 and 2001, Schilling et al., 1994, Le Voyer et al., 2015), the peculiar RTI morphology (Bonatti, 1996) and extreme MORB compositions (Schilling et al., 1994; 1995; Ligi et al., 2005; Sushchevskaya et al., 2002; Le Voyer et al., 2015).

## Chemical variability observed at Romanche transform fault

In order to characterize the compositional variability along the lateral thermal gradient at the ERRTI, high-resolution sampling has been carried out by 25 dives with the manned submersible Nautile dives (SMARTIES 2019 expedition, *Smooth regions at the Mid-Atlantic Ridge Transform-Intersections under extreme thermal gradients*). This expedition complements and integrates an existing scattered conventional dredge sampling from previous expeditions (PRIMAR expeditions, *Russian-Italian project for the study of the MAR*; Gasperini et al., 1997, Bonatti et al., 1991, 1994).

Major and trace elements on the ERRTI basaltic glasses (Verhoest et al., in prep.; see chapter 4) have shown that the composition of MORB glasses approaching the ERRTI shows a dramatic increase of the alkaline and incompatible element contents: $Na_2O$ up to 4.45 wt%, $K_2O$ up to 1.95 wt% and $La/Sm_{PM}$ (Primitive Mantle normalized, Sun and McDonough, 1989) up to 3.6 confirming previous studies' observations (Schilling et al., 1995; Ligi et al., 2005; Le Voyer et al., 2015). Overall, sampled MORBs deviate from the N-MORB, tholeiitic compositional field, by a strong alkali enrichment extending into the alkali-basalt field and its unusual (for MORBs) potassium enrichment. In In this study, “alkaline MORBs” are defined as those samples plotting beyond the McDonald-Katsura line in the TAS plot (Figure 5.2) (Verhoest et al., in prep.; see chapter 4). They are nepheline normative (0.3 % to 16.5 %) and have high $La/Sm_{PM}$ (Primitive

Mantle normalised) and a marked enrichment in potassium with respect to MORBs worldwide (Figure 5.2). The potassium enrichment represents a unique feature in the MOR record. Moreover, as discussed later, K-rich alkaline MORBs have a common HIMU isotopic flavour, hence the K content in addition to the $La/Sm_{PM}$ ratio has been used to classify the basaltic glasses into three groups: N-MORB, E-MORB and K-rich MORB (Figure 5.2) (Verhoest et al., in prep.; see chapter 4). N- and E- MORB are separated based on Gale et al. (2013) $La/Sm_{PM}$ arbitrary value of 1.5. They form two distinct groups in the K vs. Si plot (Figure 5.2) forming trends possibly deriving by progressive fractional crystallization. K-rich MORB here defined, have $K_2O$ content plotting in the high-$K_2O$ field of Middlemost (1975) (>0.7 wt% in our sample set) clearly forming a separate family of rocks (Figure 5.2).

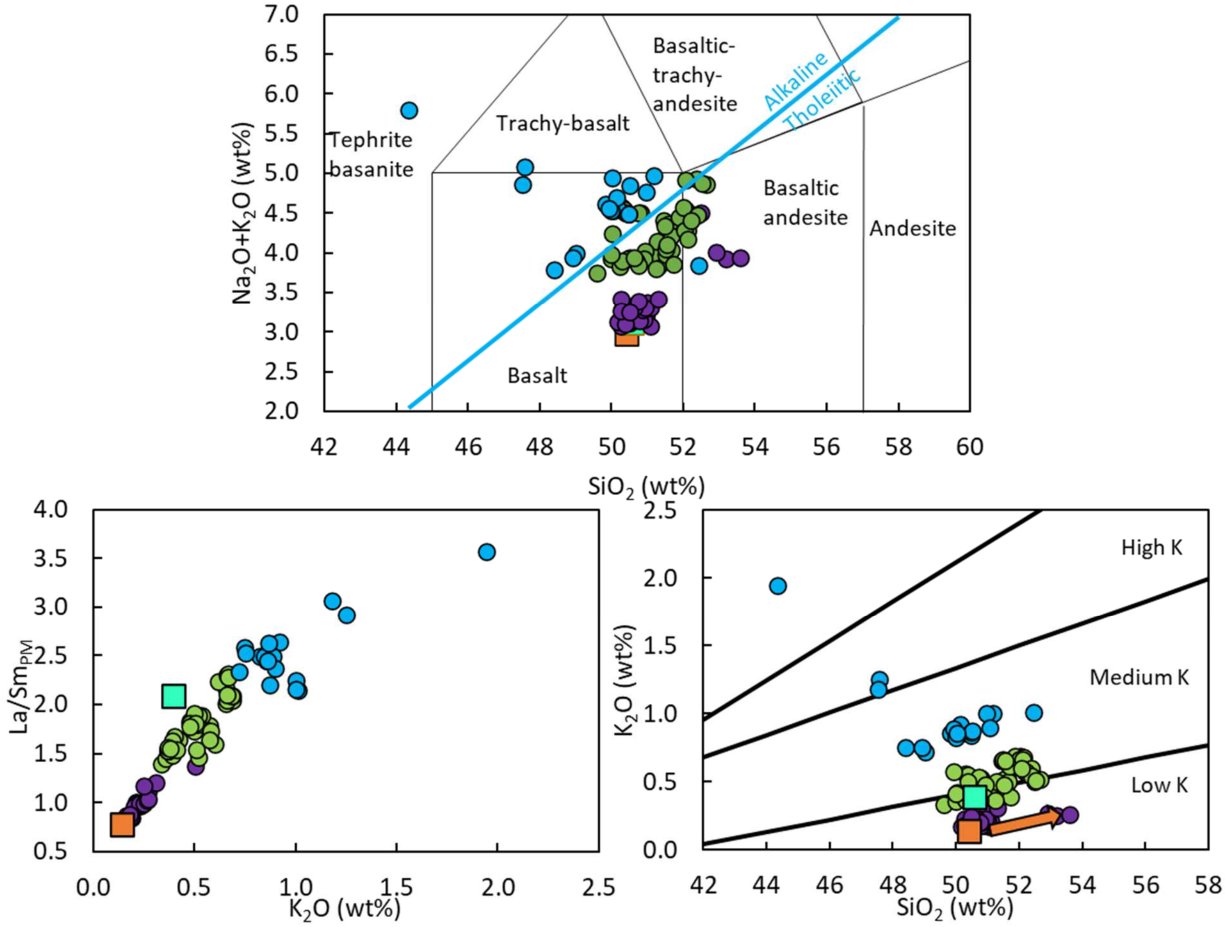

*Figure 5.2 - $La/Sm_{PM}$ PM normalised (Sun and McDonough, 1989) vs $K_2O$ diagram and $K_2O$ vs. $SiO_2$ (wt%). The K fields are from Middlemost (1975). By looking at both trace element compositions and potassium content three groups of samples have been identified (Verhoest et al., in prep.; see chapter 4): 1- normal-MORB (N-MORB, violet solid circle): compositionally homogeneous and slightly enriched in LREE and depleted in HREE compared to N-MORB. 2-*

*Enriched MORB (E-MORB, solid green circle) with La/SmPM>1.5 as defined by Gale et al (2013). 3- K-rich MORB, they have higher $K_2O$ content (>0.7 wt%) and very enriched LREE. Orange and green squares are respectively N-MORB and E-MORB from Gale et al. (2013). The arrow represents the evolution during fractional crystallization.*

## Identification of the endmembers

The Sr, Pb, Nd and Hf isotope composition of the basaltic glasses at the ERRTI is highly variable over a very short distance (Figure 5.1, 5.3). The εHf varies from -2.880 to 23.734, a range almost covering the variability observed along the entire Mid Atlantic Ridge system (-2.758 at 47.3°S and 26.205 at 40.2°N, Agranier et al., 2005). The other isotope systematics are also highly variable with εNd varying from 2.262 to 11.525, $^{87}$Sr/$^{86}$Sr from 0.702398 to 0.703758 and $^{206}$Pb/$^{204}$Pb from 18.503 to 19.700 at the ERRTI. The ERRTI isotope variability is extreme considering the length of our sampling area (ca. 100 km) compared to the total extent of the MAR system (16 000 km). This variability is evidence for an efficient separation of melts from the source reservoirs during sub-ridge partial melting and melt extraction.

To define the type of sources contributing to the magmatism in the mantle region below the ERRTI, we compare our data with known isotopic mantle domains and account for variable extent of melt mixing by simple mixing models. A large portion of the samples plots near the Depleted-MORB Mantle (DMM) (Figure 5.3 and S5.2, the DMM endmember has been defined based on literature data from Woodhead et al., 2012, Armienti and Longo, 2011, Salters and Stracke, 2004). However, to explain the overall dispersion of the data we need to consider three additional endmembers that we identified in EMII, HIMU, as well as an ultra-depleted component (Figure 5.3 and S5.2, Table 1) (Zindler and Hart, 1986, Hart, 1988, Stracke et al., 2005, Salters et al., 2011).

The N-MORB group has very heterogeneous isotopic signatures, with $^{87}$Sr/$^{86}$Sr ranging from 0.702541 to 0.703758, $^{206}$Pb/$^{204}$Pb from 18.506 to 18.799, εNd from 5.738 to 10.654 and εHf from 11.552 to 23.734. Even if most of these samples plot close to the DMM pole, few samples plot towards the EMII-type and UDM-type endmembers (Figure 5.3 and S5.2). The EMII-flavoured glasses from the N-MORB group are characterized by higher $^{87}$Sr/$^{86}$Sr (0.703758), and $^{206}$Pb/$^{204}$Pb (18.800) and lower εNd (5.738) and εHf (11.552). These samples plot together with a group of lavas from the Fernando de Noronha archipelagos (FN, Brazilian coastline) in all the isotope systematics (Figure 5.3 and S5.2). The isotopic signatures of FN lavas have been ascribed to an EMII signature derived from recycling of Brazilian continental material and/or to mixing between melts deriving from DMM, HIMU and EMII type mantle components (Gerlach et al., 1987, Rivalenti et al., 2000 and 2007). In our binary mixing model, less than 5% of the EMII endmember needs to be added to the DMM to fit the sample with the highest Sr isotope ratio.

A peculiar sample from the N-MORB group is highly radiogenic in εHf at εNd lower than expected compared to the mantle array (Figure S5.2) (respectively 23.734 and 10.654). Its $^{206}Pb/^{204}Pb$ is 18.506 and $^{87}Sr/^{86}Sr$ 0.702783, close to the DMM signature. The existence of high εHf signatures in the MOR mantle is becoming more evident (Salters et al., 2011; Willig et al., 2020; Sanfilippo et al., 2021; Stracke, 2021) and has been ascribed to the presence of Ultra-Depleted Mantle domains (UDM) within the DMM. Melts extracted from an old (at least 1 Ga) UDM residue by partial melting, exhibit high εHf and εNd isotope signatures. These are generally not observed in MORBs, but have been described in melt inclusions and, to a bigger extent, in clinopyroxenes from residual abyssal peridotites (Cipriani et al., 2004, 2011; Stracke et al. 2011, 2019, Brunelli et al 2018). In our model, the UDM-derived melt has been calculated from 10 % partial melting of a 1 Ga residual mantle from Sanfilippo et al. (2021). The addition of a very small amount (< 1%) of this UDM-derived melt to the DMM ones, changes significantly the εHf and, to a lesser extent, the εNd but has a very small effect on the DMM Sr and Pb isotope ratios (Figure 5.3 and S5.2) (Salters et al., 2011, Sanfilippo et al., 2019 and 2021).

The E-MORB group is also isotopically highly variable, with $^{87}Sr/^{86}Sr$ ranging from 0.702653 to 0.703624, $^{206}Pb/^{204}Pb$ from 18.488 to 19.472, εNd from 3.835 to 10.663 and εHf from 6.001 to 21.481, plotting within the range of variability of the N-MORB group in all the isotope systematics. However, the Sr isotope ratios of the E-MORB group do not reach the radiogenic values of the N-MORBs and the involvement of the DMM component is generally slightly lower.

The K-rich MORB group is the most isotopically enriched and therefore the farthest away from the DMM pole, with $^{87}Sr/^{86}Sr$ ranging from 0.702752 to 0.703309, $^{206}Pb/^{204}Pb$ from 19.089 to 19.700, εNd from 2.262 to 8.177 and εHf from -2.880 to 19.227. Their isotope signatures result from mixing various amounts of the four different endmembers. These lavas plot together with samples affected by the Sierra Leone hotspot, impacting the MAR at 1°7N (Schilling et al., 1994), along a trend closer to the HIMU endmember in all the isotope systematics (Figure 5.3 and S5.2). One sample from the K-rich group is very peculiar and characterized by very low εHf compared to the expected εNd (respectively -2.880 and 2.262), plotting far below the mantle array in the εNd-εHf isotope space (Figure 5.3, S5.2). Its $^{87}Sr/^{86}Sr$ is 0.703309 and the $^{206}Pb/^{204}Pb$ is 19.604, close to a HIMU-type signature (Stracke et al., 2005) (Figure 5.3 and S5.2). Until recently, the most accepted model for the HIMU signature was the melting of old recycled oceanic crust ± continental material (Woodhead, 1996, Hanyu and Kaneoka, 1997, Stracke et al., 2003, Willig et al., 2020). Another hypothesis calls upon K-rich Archean sub-continental lithospheric mantle (SCLM) metasomatized by a carbonatitic liquid (Weiss et al., 2016, Thomson et al., 2016, Castillo, 2015, Hanyu et al., 2019). Such source has been used to explain the alkaline carbonatitic magmatism in Brazil (Comin-Chiaramonti et al., 2014) and the origin of kimberlites in Labrador, Greenland and Africa (Tappe et al., 2011). Here, we will not discuss which is more likely and we use the term HIMU considering that it can derive from either one of them.

Various relative amounts of each component can explain the variability observed in isotope ratios of the ERRTI basaltic glasses, with generally small involvement of the EMII, HIMU and UDM endmembers. Thus, in our mixing model, the glasses with the most enriched isotopic signatures originate from a dominant DMM signature mixed with ~10-12% of the HIMU component and 1%-5% of EMII (green line and orange lines in Figure 5.3 and S5.2). Less than 1% of the UDM component is needed to produce the higher εHf values observed. This value may be highly underestimated due to the extreme elemental depletion of the UDM component used in the model. The addition of a small amount of enriched material to the UDM would drastically change the signature of the melt, making it difficult to quantify the amount of UDM.

Only the one basaltic glass with the lower εHf does not fit the mixing model. To our knowledge, oceanic basalts with such a low εHf for a given εNd have never been observed. The only natural samples with this isotope signature are the group I kimberlites from South Africa of Nowell (2004). However, it is possible to fit this isotope signature by mixing a high amount (50%-70%) of the present-day ratios of a 2 Ga recycled oceanic crust (calculated after Stracke et al., 2003 model; Figure 5.3 and S5.3) with the DMM.

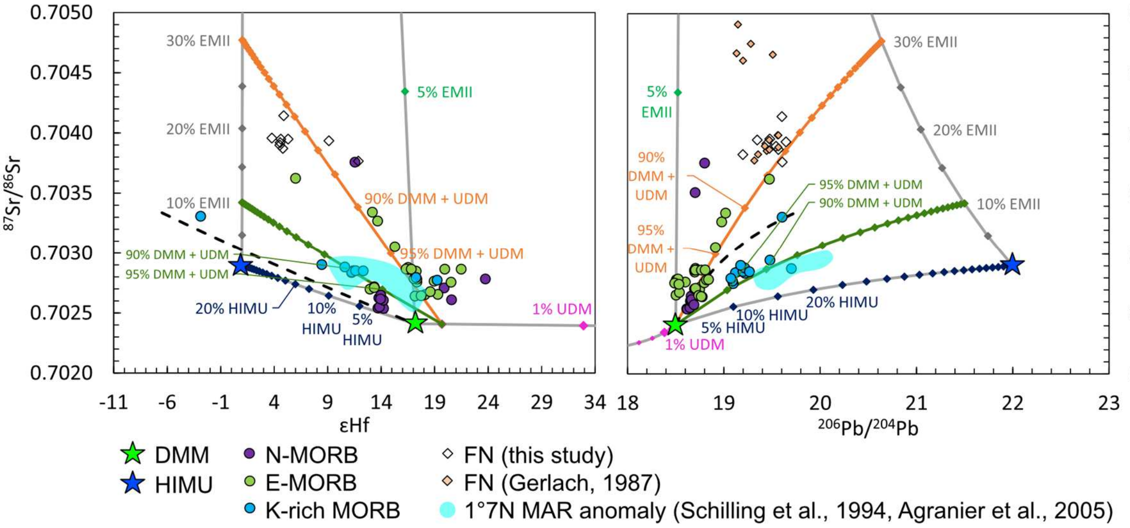

*Figure 5.3 - ERRTI Sr-Hf and Sr-Pb isotopes and simple binary mixing models. The UDM endmember has been calculated from 10% melting of a residual mantle following Sanfilippo et al. (2021) model. Endmember compositions are given in Table 1. The grey lines represent simple binary mixing lines between melts from the different endmembers, calculated with a step interval of 5% mixing. The green and orange lines represent mixings between DMM-UDM-HIMU-derived melts with variable proportions of EMII. The dashed line is a simple binary mixing between the DMM and actual ratios calculated from a 2 Ga recycled oceanic crust (after Stracke et al., 2003). Samples from the 1°7N anomaly (Sierra Leone) described by Schilling et al. (1994) and from Fernando de Noronha archipelago are plotted for comparison (see text for details).*

Simple binary mixing between different mantle endmembers are commonly used to explain the high variability in basalt isotopic ratios. However, this assumes that the mantellic components are partially melted, and that the whole aggregated melts participate to the mixing. This is not a realistic scenario, and it has been shown that melt extraction from different depth (Rudge et al., 2013, Liang, 2020) and/or incomplete melt mixing (Koornneef et al., 2012) can have a large impact on the isotopic variability of the erupted melts, even if only two mantle endmembers are considered. Indeed, the curvature of a mixing line in isotope systematics is defined by the ratio between the two elements considered for each mantle endmembers, as Sr/Hf or Sr/Pb in figure 5.3 (Langmuir et al., 1978, Liang, 2020). These ratios can significantly change during partial melting due to the difference in incompatibility of the elements. Thus, mixing instantaneous melts extracted at different degrees of melting derived from two mantle components partially melted at different depths results in a large variability, i.e., numerous possibilities of curvatures for the simple binary mixing lines (Rudge et al., 2013, Liang, 2020). The same effect occurs when considering incomplete melt mixing: a given amount of melt produced from two components can result in high variability in isotopic ratios by mixing only part of the melt generated by each component (Koornneef et al., 2012). Both processes could occur at the ERRTI, meaning that possibly only two endmembers are at the origin the observed isotopic variability instead of the four previously identified. This process can be checked by studying simple binary mixing in isotope systematics with the same element, as Pb-Pb, which gives rise to straight mixing lines as the trace element ratio is equal to 1 (Rudge et al., 2013).

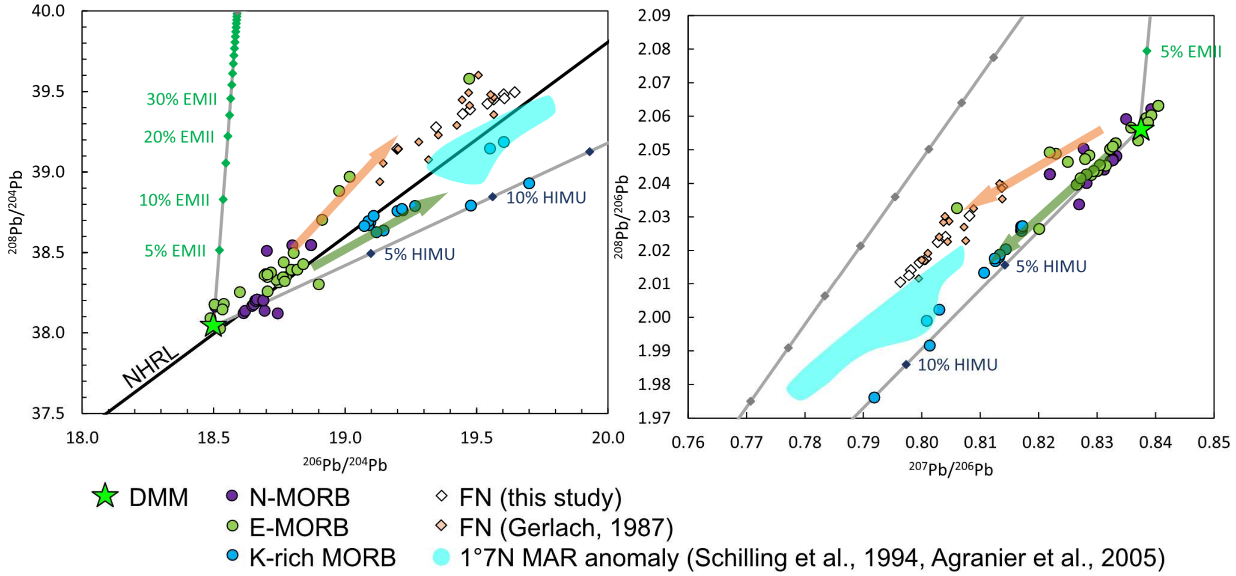

*Figure 5.4 – Pb isotope systematics and simple binary mixing model. Endmember compositions are given in Table 1. The grey lines represent simple binary mixing lines between the different endmembers, calculated with a step interval of 5%.*

Two trends are observed in the $^{208}Pb/^{204}Pb$ vs. $^{206}Pb/^{204}Pb$ and $^{208}Pb/^{206}Pb$ vs. $^{207}Pb/^{206}Pb$ diagrams (Figure 5.4), corresponding to mixing between DMM and EMII- and HIMU-type signatures previously described (Figure 5.3, 5.4 and S5.2). Thus, even if incomplete melt mixing and partial melting at different depths occurs in the region, these processes are not the driving mechanisms for the measured isotopic distribution.

*Table 1 – Endmembers composition*

| | εHf | Hf (ppm) | $^{206}$Pb/$^{204}$Pb | Pb (ppm) | εNd | Nd (ppm) | $^{87}$Sr/$^{86}$Sr | Sr (ppm) |
|---|---|---|---|---|---|---|---|---|
| DMM | 17.15[a] | 0.199[c] | 18.5[b] | 0.023[c] | 11.0[b] | 0.71[c] | 0.70241[b] | 9.8[c] |
| UDM | 203.37[d] | 0.91[d] | 16.57[d] | 0.01[d] | 133.6[d] | 1.91[d] | 0.702134[d] | 27.4[d] |
| HIMU | 0.99[e] | 1.78[e] | 22[e] | 0.09[e] | 3.2[e] | 7.449[e] | 0.7029[f] | 80.542[e] |
| EMII | 1.56[f] | 0.24[g] | 18.59[b] | 0.14[g] | -10.49[f] | 1.14[g] | 0.722[f] | 20.4[g] |
| Recycled oceanic crust | -6.49[e] | 1.78[e] | 19.7[e] | 0.09[e] | 1.6[e] | 7.449[e] | 0.703337[e] | 80.542[e] |

[a] Woodhead, 2012
[b] Armienti and Longo, 2011
[c] Salters and Stracke, 2004
[d] calculated after Sanfilippo et al., 2021
[e] Stracke and Salters, 2003
[f] Rollinson and Pease, 2021
[g] Workman et al., 2004

### Nature of the heterogeneities

The isotope variability of the ERRTI glasses shows a correlation with the relative distance from the transform fault, used here as a proxy of the mantle potential temperature evolution (Figure S5.1, S5.3). Along the central segment, at more than 50 km from the transform fault, the mantle potential temperature is proposed to be comparable with the average MAR subaxial temperature (Bonatti et al., 2001, Ligi et al., 2005). Here, all samples are N-MORBs with isotopic signatures close to the DMM component. Approaching the ERRTI, i.e., decreasing the mantle potential temperature (Figure S5.1), the isotopic variability significantly increases. Thus, while the N-MORB group is present all along the ridge axis, its extreme isotopic values, samples with the higher $^{87}$Sr/$^{86}$Sr and the sample with the higher εHf, are observed at lower mantle potential temperature closer to the ERRTI (Figure S5.1 and S5.3). Similarly, the E-MORBs and K-rich MORBs are only observed at lower mantle potential temperature, and the sample from the K-rich group with the most enriched isotope signature, the lowest εHf value, is the one closest to the transform fault at ~10 km to the south. The correlation of the isotopic dispersion/enrichment with the mantle temperature gives a clear indication on the nature of the heterogeneities. A fine-scale scattered, stochastic, distribution of enriched components (Meibom and Anderson, 2004) cannot explain the correlation between temperature and isotopic composition. On the other hand, a lithological heterogeneity, resulting from recycling and stirring fertile and depleted distinct domains, will result in a temperature-dependent isotopic distribution (Brunelli et al., 2018, Haase et al., 2011). This hypothesis can be tested by looking at the correlation between isotopes and major/trace elements in the analysed lavas. Overall, $SiO_2$ and MgO show a negative correlation with $^{87}Sr/^{86}Sr$ and $^{206}Pb/^{204}Pb$ and a positive correlation with εNd and εHf (Figure 5.5, S5.4). On the contrary, $TiO_2$, FeO, $Na_2O$ and $K_2O$ show a positive correlation with $^{87}Sr/^{86}Sr$ and $^{206}Pb/^{204}Pb$ and a negative correlation with εNd and εHf. In Figures 5.5 and S5.5 we consider the behaviour of Nb/Zr vs. the measured isotope ratios. This trace element ratio has been chosen because it is little affected by fractional crystallization and is thus a good indicator of the source enrichment (Gee et al., 1998, Hanan et al., 2000, Shorttle et al., 2014). The Nb/Zr ratios of the ERRTI samples show a general positive correlation with $^{206}Pb/^{204}Pb$ and $^{87}Sr/^{86}Sr$ and a negative correlation with εNd and εHf (Figure 5.5, S5.5). Generally, two trends are observed in major and trace element vs. isotopic ratios: the first corresponds to the K-rich samples, which have the higher $^{206}Pb/^{204}Pb$, close to HIMU-type mantle signature, the second contains the sample from the N-MORB group with the higher $^{87}Sr/^{86}Sr$ and few E-MORBs, pointing toward EMII mantle signature (Figure 5.5, S5.4, S5.5).

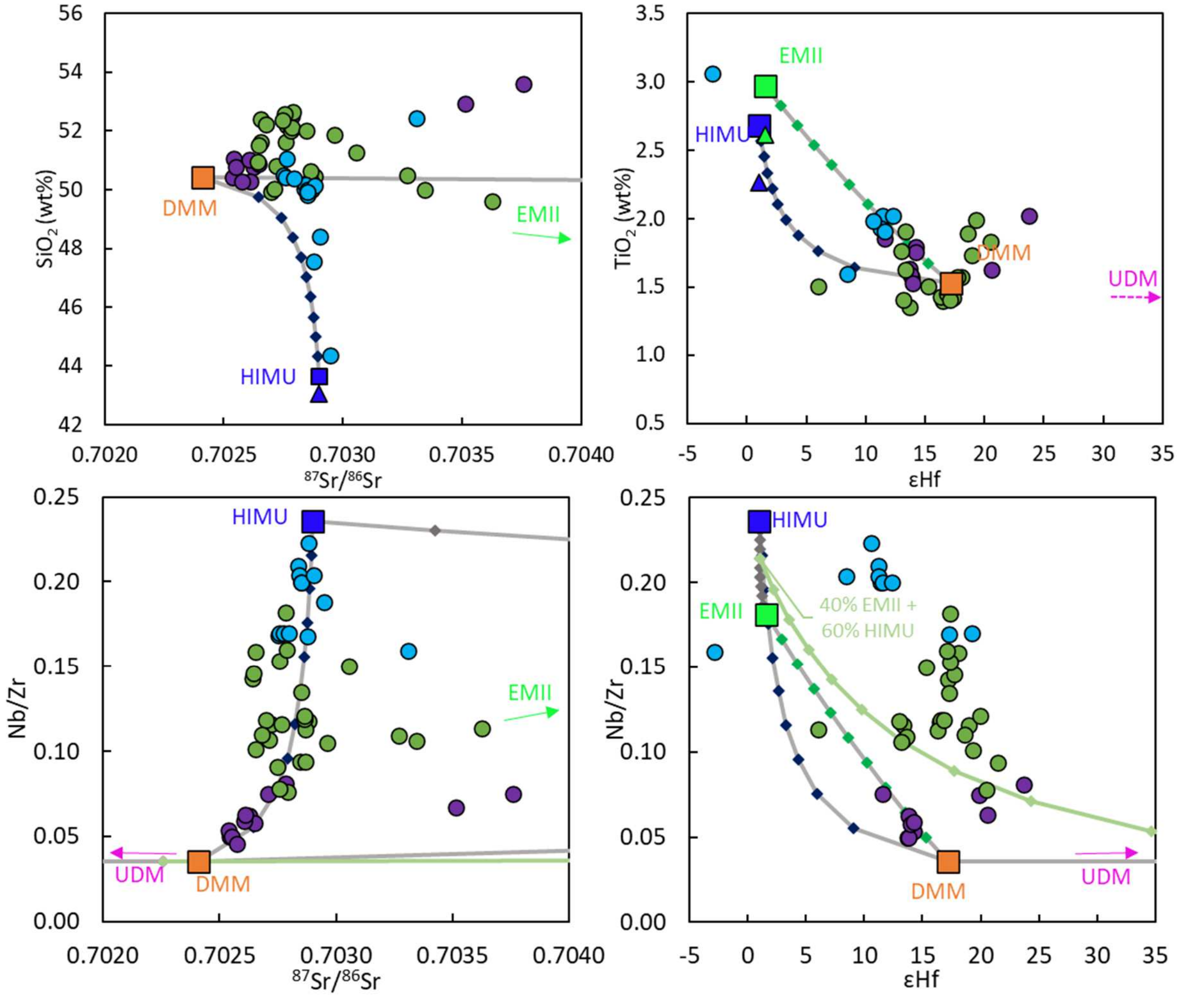

*Figure 5.5 - Major and trace element correlations with $^{87}Sr/^{86}Sr$ and εHf. Lines represent simple binary mixing between the various endmembers calculated at 10% mixing step (markers). The green line represents mixing between all the endmembers (mixing between a melt derived from EMII and HIMU mixing respectively 40% and 60% and a melt derived from DMM and UDM mixing respectively 95% and 5%). Isotopes data of the mantle endmembers are given in table 5.1. Major elements data of the enriched endmembers are from Jackson and Dasgupta (2008). For comparison, triangles are HIMU (blue) and EMII (green) major element data corrected for olivine fractionation (Jackson and Dasgupta, 2008). Trace element data are average values from Willbold and Stracke (2006). Major and trace elements data of DMM are N-MORB of Gale et al. (2013).*

K-rich MORBs major and trace elements show a correlation with all the isotope ratios going toward enriched signatures (Figure 5.5, S5.4, S5.5). This implies that the specific major element composition of this group is directly inherited from the source, as their high $CaO/Al_2O_3$, $K_2O/TiO_2$ and Nb/Zr (Figure 5.5, S5.4, S5.5). Thus, the source at the origin of the HIMU-type signature has low $SiO_2$, $Al_2O_3$, MgO and high $TiO_2$ and FeO content. For the most part, these compositions correspond to the HIMU major element reference, which is generally characterised by higher FeO, CaO, and CaO/$Al_2O_3$ and lower $SiO_2$ and $Al_2O_3$ than EM mantle endmember (Jackson and Dasgupta, 2008). The $K_2O$ content of this group is much higher than the mean HIMU value (Figure S5.4). This K enrichment has been previously suggested to originate from a phlogopite (or amphibole) -bearing metasomatized mantle (Verhoest et al., in prep.; see chapter 4). In the subridge recent melting, this lithology has undergone higher degree of partial melting than the surrounding lherzolitic mantle at lower mantle temperature because of its higher degree of fertility (Verhoest et al., in prep.; see chapter 4). The samples with the highest $^{87}Sr/^{86}Sr$ are characterised by higher FeO and $Na_2O$ content than N-MORB (Figures 5.5, S5.4) and have intermediate Nb/Zr ratio between N-MORB and HIMU (Figure 5.5, S5.5). These major and trace element compositions all correlate with an isotopic signature driven by an EMII mantle endmember composition.

UDM isotopic signature is generally associated to highly REE depleted melts resulting from partial melting of ancient residual DMM (Sanfilippo et al., 2019, Stracke et al., 2019, Willig et al., 2020). However, here, the higher εHf sample has La/$Sm_{PM}$ and Nb/Zr higher than N-MORBs, respectively 1.38 and 0.081 (Figures 5.2, 5.5) and higher $SiO_2$ (52.5 wt%), $Na_2O$ (4 wt%) and $K_2O$ (0.5 wt%) and lower MgO (5.7 wt%) (Figures 5.5, S5.4, S5.5). These chemical characters are consistent with partial melting of a relatively fertile material, which does not fit the definition of UDM (Sanfilippo et al., 2019, Stracke et al., 2019), thus suggesting that the source material of the ancient melting event may have been significantly more fertile than the DMM. For instance, a garnet/pyroxene-rich source experiencing a moderate degree of melting would produce a residue more fertile than DMM. The ultra-depleted isotopic signature is then the result of the long time-integrated (at least 1 Ga) radiogenic ingrowth (Stracke et al., 2019). This suggests that distinct ultra-depleted components, with variable degrees of fertility, are present within the mantle.

Major and trace element simple binary mixing models have been calculated between the various endmembers (Figures 5.5, S5.4, S5.5). The general mixing rule inferred from the isotopic systematic is also recognizable in the major and trace element distribution. ERRTI lavas appear as mixing of a main DMM component with a mixture of HIMU-EMII-UDM derived melts. Correlation between the isotope ratios and the major and trace compositions have shown that these various mantle signatures correspond to various lithologies. As previously suggested (Verhoest et al., in prep.; see chapter 4), these lithologies are partially melted all together or independently of the DMM depending on the mantle temperature. While, at higher mantle temperature, the melts derived from each lithology are blended together to give N-MORB erupted melts compositions, at the ERRTI these melts are "unblended", i.e., the erupted melts are less mixed, due to the preferential partial melting of the lower solidus source at lower mantle potential temperature

(Figures 5.3, 5.4, 5.5, and supplementary figures). This lower degree of mixing between the melts extracted from the different sources is possible because of the very low degree of melting of the mantle. This colder than normal regime has induced very small volumes of melts compared to the "normal" amount of melt erupted at MOR, i.e., 0-1 km of oceanic crust generated at cold spots by contrast to the 5-6 km of oceanic crust generally observed. Thus, even if a low degree of mixing occurs, the very small volumes of erupted magmas are more concentrated in melts extracted from the more fertile, preferentially melted, lithologies.

At MOR, the presence, in small amount, of material with the same isotopic signature of the large-scale isotopic anomalies (hot spots), i.e., HIMU and EMII, suggests a fine scale distribution of these heterogeneities within the upper mantle. However, it is difficult to define whether these small-scale heterogeneities are present periodically as blobs, directly coming from the deeper mantle (Agius et al., 2021), or as thin filament resulting from long time delamination and stirring within the upper mantle (Meibom and Anderson, 2004).

## Conclusions

Four isotopic mantle signatures have been highlighted: Depleted-MORBs Mantle (DMM), Ultra-Depleted Mantle (UDM), HIMU and EMII. All these signatures contribute to the extreme isotopic heterogeneity observed at ERRTI by various degree of mixing of a large amount of DMM with a small contribution of other components.

These extreme isotopic signatures correlate with the major and trace element compositions of the MORBs, evidence that they are directly inherited from various lithologies present within the peridotitic mantle.

A link has been made between the suggested decrease of the mantle potential temperature and an increase of the compositional and isotopic variability of the MORBs. Thus, DMM signatures are essentially observed at higher mantle potential temperature, at the central segment, while the enriched signatures can be observed closer to the transform fault, at lower mantle potential temperature. This repartition suggests that the lithologies at the origin of the HIMU and EMII signatures are more fertile than the surrounding mantle, allowing their partial melting to the detriment of the more refractory peridotitic mantle (Phipps Morgan, 2001, Brunelli et al., 2018). This is also true for the UDM component, whose signature is observed only at colder mantle temperature similarly to the enriched components, implying a higher fertility for the UDM than its surrounding mantle.

Our finding shows that long time-integrated heterogeneities that experienced ancient partial melting, i.e., isotopically ultra-depleted, are possibly variable in composition. This may reflect variable extent of melting from compositionally different sources, resulting in several ultra-depleted components with distinct degrees of fertility. These ultra-depleted components are dispersed at fine spatial scale within the mantle source of MORBs, in the same way as the isotopically enriched lithologies are.

## References

Agius, M.R., Rychert, C.A., Harmon, N., Tharimena, S., Kendall, J.-M., 2021. A thin mantle transition zone beneath the equatorial Mid-Atlantic Ridge. Nature 589 (7843), 562–566. doi:10.1038/s41586-020-03139-x.

Agranier, A., Blichert-Toft, J., Graham, D., Debaille, V., Schianio, P., Albarede, F., 2005. *The spectra of isotopic heterogeneities along the mid-Atlantic Ridge.* Earth and Planetary Science Letters 238 (1-2), 96–109. doi:10.1016/j.epsl.2005.07.011.

Armienti, P., Longo, P., 2011. *Three-Dimensional Representation of Geochemical Data from a Multidimensional Compositional Space.* IJG 02 (03), 231–239. doi:10.4236/ijg.2011.23025.

Blichert-Toft, J., Chauvel, C., Albarède, F., 1997. *Separation of Hf and Lu for high-precision isotope analysis of rock samples by magnetic sector-multiple collector ICP-MS.* Contributions to Mineralogy and Petrology 127 (3), 248–260. doi:10.1007/s004100050278.

Bonatti, E., 1996. *Anomalous opening of the Equatorial Atlantic due to an equatorial mantle thermal minimum.* Earth and Planetary Science Letters 143, 147–160.

Bonatti, E., Brunelli, D., Fabretti, P., Ligi, M., Portaro R. A., Seyler, M., 2001. *Steady-state creation of crust-free lithosphere at cold spot in mid-ocean ridges.* Geology 29 (11), 979–982.

Bonatti, E., Ligi, M., Gasperini, L., Peyve, A., Raznitsin, Y., Chen, Y.J., 1994. *Transform migration and vertical tectonics at the Romanche fracture zone, equatorial Atlantic.* Journal of Geophysical Research 99 (B11), 21779–21802. doi:10.1029/94JB01178.

Bonatti, E., Raznitzin, Y., Bortoluzzi, G., Budillon, F., Alteriis, G. de, Gasperini, L., Gasperini, M., Giacquinto, G., Ligi, M., Lodolo, E., Mazarovich, A., Peyve, A., Sacchi, M., Skolotnev, S., Trofimov, V., Turko, N., Zacharov, M., Auzende, J.-M., Mamaloukas-Frangoulis, V., Searle, R.C., 1991. *Geological studies of the eastern part of the Romanche transform (equatorial Atlantic): a first report.* Giornale di Geologia 53/2, 31–48.

Bonatti, E., Seyler, M., Sushchevskaya, N.M., 1993. *A cold suboceanic mantle belt at the Earth's equator.* Science 261 (5119), 315–320. doi:10.1126/science.261.5119.315.

Brunelli, D., Cipriani, A., Bonatti, E., 2018. *Thermal effects of pyroxenites on mantle melting below mid-ocean ridges.* Nature Geosci 11 (7), 520–525. doi:10.1038/s41561-018-0139-z.

Castillo, P.R., 2015. *The recycling of marine carbonates and sources of HIMU and FOZO ocean island basalts.* Lithos 216-217, 254–263. doi:10.1016/j.lithos.2014.12.005.

Chauvel, C., Bureau, S., Poggi, C., 2011. *Comprehensive Chemical and Isotopic Analyses of Basalt and Sediment Reference Materials.* Geostandards and Geoanalytical Research 35 (1), 125–143. doi:10.1111/j.1751-908X.2010.00086.x.

Cipriani, A., Bonatti, E., Carlson, R.W., 2011. *Nonchondritic 142 Nd in suboceanic mantle peridotites.* Geochem. Geophys. Geosyst. 12 (3). doi:10.1029/2010GC003415.

Cipriani, A., Brueckner, H.K., Bonatti, E., Brunelli, D., 2004. *Oceanic crust generated by elusive parents: Sr and Nd isotopes in basalt-peridotite pairs from the Mid-Atlantic Ridge.* Geology 32 (8), 657–660. doi:10.1130/G20560.1.

Comin-Chiaramonti, P., Gomes, C., Min, A., Ruberti, E., Girardi, V.A.V., Slejko, F., Neder, R.D., Pinho, F., 2014. *Petrology of potassic alkaline ultramafic and carbonatitic rocks from Planalto da Serra (Mato Grosso State), Brazil.* Open Geosciences 6 (4), 565–587. doi:10.2478/s13533-012-0196-6.

Deniel, C., Pin, C., 2001. *Single-stage method for the simultaneous isolation of lead and strontium from silicate samples for isotopic measurements.* Analytica Chimica Acta 426 (1), 95–103. doi:10.1016/S0003-2670(00)01185-5.

Dosso, L., Bougault, H., Joron, J.-L., 1993. *Geochemical morphology of the North Mid-Atlantic Ridge 10°-24°N: trace element-isotope complementary.* Earth and Planetary Science Letters 120, 443–462.

Gale, A., Dalton, C.A., Langmuir, C.H., Su, Y., Schilling, J.-G., 2013. *The mean composition of ocean ridge basalts.* Geochem. Geophys. Geosyst. 14 (3), 489–518. doi:10.1029/2012GC004334.

Gasperini, L., Bonatti, E., Brunelli, D., Carrara, G., Cipriani, A., Fabretti, P., Gilod, D., Ligi, M., Peyve, A., Skolotnev, S., Susini, S., Tartarotti, P., Turko, N., 1997. *New data on the geology of the Romanche FZ, equatorial Atlantic: PRIMAR-96 cruise report.* Giornale di Geologia 59/1-2, 3–18.

Gee, M., Taylor, R.N., Thirlwall, M.F., Murton, B.J., 1998. *Glacioisostacy controls chemical and isotopic characteristics of tholeiites from the Reykjanes Peninsula, SW Iceland.* Earth and Planetary Science Letters 164 (1-2), 1–5. doi:10.1016/S0012-821X(98)00246-5.

Gerlach, D.C., Stormer, J.C., Mueller, P.A., 1987. *Isotopic geochemistry of Fernando de Noronha.* Earth and Planetary Science Letters 85, 129–144.

Haase, K. M., 1996. *The relationship between the age of the lithosphere and the composition of oceanic magmas: Constraints on partial melting, mantle sources and the thermal structure of the plates*, Earth Planet. Sci. Lett., 144, 75–92, doi:10.1016/0012-821X(96)00145-8.

Haase, K.M., Regelous, M., Duncan, R.A., Brandl, P.A., Stroncik, N., Grevemeyer, I., 2011. *Insights into mantle composition and mantle melting beneath mid-ocean ridges from postspreading volcanism on the fossil Galapagos Rise.* Geochem. Geophys. Geosyst. 12 (5). doi:10.1029/2010GC003482.

Hamelin, C., Bezos, A., Dosso, L., Escartin, J., Cannat, M., Mevel, C., 2013. *Atypically depleted upper mantle component revealed by Hf isotopes at Lucky Strike segment.* Chemical Geology 341, 128–139. doi:10.1016/j.chemgeo.2013.01.013.

Hanan, B.B., Blichert-Toft, J., Kingsley, R., Schilling, J.-G., 2000. *Depleted Iceland mantle plume geochemical signature: Artifact of multicomponent mixing?* Geochem. Geophys. Geosyst. 1 (4). doi:10.1029/1999GC000009.

Hanan, B.B., Kingsley, R.H., Schilling, J.-G., 1986. *Pb isotope evidence in the South Atlantic for migrating ridge—hotspot interactions.* Nature 322 (6075), 137–144. doi:10.1038/322137a0.

Hanyu, T., Kaneoka, I., 1997. *The uniform and low 3He/4He ratios of HIMU basalts as evidence for their origin as recycled materials.* Nature 390 (6657), 273–276. doi:10.1038/36835.

Hanyu, T., Shimizu, K., Ushikubo, T., Kimura, J.-I., Chang, Q., Hamada, M., Ito, M., Iwamori, H., Ishikawa, T., 2019. *Tiny droplets of ocean island basalts unveil Earth's deep chlorine cycle.* Nature communications 10 (1), 60. doi:10.1038/s41467-018-07955-8.

Hart, S.R., 1984. *A large-scale isotope anomaly in the Southern Hemisphere mantle.* Nature 309 (5971), 753–757. doi:10.1038/309753a0.

Hart, S.R., 1988. *Heterogeneous mantle domains: signatures, genesis and mixing chronologies.* Earth and Planetary Science Letters 90 (3), 273–296.

Jackson, M.G., Dasgupta, R., 2008. *Compositions of HIMU, EM1, and EM2 from global trends between radiogenic isotopes and major elements in ocean island basalts.* Earth and Planetary Science Letters 276 (1-2), 175–186. doi:10.1016/j.epsl.2008.09.023.

Katz, R.F., Rudge, J.F., 2011. *The energetics of melting fertile heterogeneities within the depleted mantle.* Geochem. Geophys. Geosyst. 12 (10). doi:10.1029/2011GC003834.

Koornneef, J.M., Nikogosian, I., van Bergen, M.J., Smeets, R., Bouman, C., Davies, G.R., 2015. *TIMS analysis of Sr and Nd isotopes in melt inclusions from Italian potassium-rich lavas using prototype 1013Ω amplifiers.* Chemical Geology 397, 14–23. doi:10.1016/j.chemgeo.2015.01.005.

Koornneef, J.M., Stracke, A., Bourdon, B., Meier, M.A., Jochum, K.P., Stoll, B., Grönvold, K., 2012. Melting of a Two-component Source beneath Iceland. Journal of Petrology 53 (1), 127–157. doi:10.1093/petrology/egr059.

Lambart, S., Baker, M.B., Stolper, E.M., 2016. *The role of pyroxenite in basalt genesis: Melt-PX, a melting parameterization for mantle pyroxenites between 0.9 and 5 GPa.* J. Geophys. Res. Solid Earth 121 (8), 5708–5735. doi:10.1002/2015JB012762.

Lambart, S., Koornneef, J.M., Millet, M.-A., Davies, G.R., Cook, M., Lissenberg, C.J., 2019. *Highly heterogeneous depleted mantle recorded in the lower oceanic crust.* Nature Geosci 12 (6), 482–486. doi:10.1038/s41561-019-0368-9.

Langmuir, C.H., Vocke, R.D., Hanson, G.N., Hart, S.R., 1978. A general mixing equation with applications to Icelandic basalts. Earth and Planetary Science Letters 37 (3), 380–392. doi:10.1016/0012-821X(78)90053-5.

Le Voyer, M., Cottrell, E., Kelley, K.A., Brounce, M., Hauri, E.H., 2015. *The effect of primary versus secondary processes on the volatile content of MORB glasses: An example from the equatorial Mid-Atlantic Ridge (5°N–3°S).* J. Geophys. Res. Solid Earth 120 (1), 125–144. doi:10.1002/2014JB011160.

Liang, Y., 2020. Trace element fractionation and isotope ratio variation during melting of a spatially distributed and lithologically heterogeneous mantle. Earth and Planetary Science Letters 552, 116594. doi:10.1016/j.epsl.2020.116594.

Ligi, M., Bonatti, E., Cipriani, A., Ottolini, L., 2005. *Water-rich basalts at mid-ocean-ridge cold spots.* Nature 434 (7029), 66–69. doi:10.1038/nature03264.

Ligi, M., Bonatti, E., Gasperini, L., Poliakov, A.N.B., 2002. *Oceanic broad multifault transform plate boundaries.* Geology 30 (1), 11–14.

Liu, B., Liang, Y., 2020. *Importance of the size and distribution of chemical heterogeneities in the mantle source to the variations of isotope ratios and trace element abundances in mid-ocean ridge basalts.* Geochimica et Cosmochimica Acta 268, 383–404. doi:10.1016/j.gca.2019.10.013.

Liu, C.-Z., Snow, J.E., Hellebrand, E., Brügmann, G., Handt, A. von der, Büchl, A., Hofmann, A.W., 2008. *Ancient, highly heterogeneous mantle beneath Gakkel ridge, Arctic Ocean.* Nature 452 (7185), 311–316. doi:10.1038/nature06688.

Meibom, A., Anderson, D.L., 2004. *The statistical upper mantle assemblage.* Earth and Planetary Science Letters 217 (1-2), 123–139. doi:10.1016/S0012-821X(03)00573-9.

Middlemost, E.A., 1975. *The basalt clan.* Earth-Science Reviews 11 (4), 337–364. doi:10.1016/0012-8252(75)90039-2.

Nowell, G.M., 2004. *Hf Isotope Systematics of Kimberlites and their Megacrysts: New Constraints on their Source Regions.* Journal of Petrology 45 (8), 1583–1612. doi:10.1093/petrology/egh024.

Phipps Morgan, J., 2001. *Thermodynamics of pressure release melting of a veined plum pudding mantle.* Geochem. Geophys. Geosyst. 2.

Reinhard, A.A., Jackson, M.G., Harvey, J., Brown, C.R., Koornneef, J.M., 2016. *Extreme differences in 87Sr/86Sr between Samoan lavas and the magmatic olivines they host: Evidence for highly heterogeneous 87Sr/86Sr in the magmatic plumbing system sourcing a single lava.* Chemical Geology 439, 120–131. doi:10.1016/j.chemgeo.2016.05.017.

Richard, P., Shimizu, N., Allègre, C.J., 1976. *143Nd/146Nd, a natural tracer: an application to oceanic basalts.* Earth and Planetary Science Letters 31 (2), 269–278. doi:10.1016/0012-821X(76)90219-3.

Rivalenti, G., Mazzucchelli, M., Girardi, V.A.V., Vannuci, R., Barbieri, M.A., Zanetti, A., Goldstein, S.L., 2000. *Composition and processes of the mantle lithosphere in northeastern Brazil and Fernando de Noronha: evidence from mantle xenoliths.* Contributions to Mineralogy and Petrology 138, 308–325.

Rivalenti, G., Zanetti, A., Girardi, V.A., Mazzucchelli, M., Tassinari, C.C., Bertotto, G.W., 2007. *The effect of the Fernando de Noronha plume on the mantle lithosphere in north-eastern Brazil.* Lithos 94 (1-4), 111–131. doi:10.1016/j.lithos.2006.06.012.

Rollinson, H., Pease, V., 2021. *Using Geochemical Data: To Understand Geological Processes.* Cambridge University Press.

Rudge, J.F., Maclennan, J., Stracke, A., 2013. *The geochemical consequences of mixing melts from a heterogeneous mantle.* Geochimica et Cosmochimica Acta 114, 112–143. doi:10.1016/j.gca.2013.03.042.

Saal, A.E., Hart, S.R., Shimizu, N., Hauri, E.H., Layne, G.D., Eiler, J.M., 2005. *Pb isotopic variability in melt inclusions from the EMI–EMII–HIMU mantle end-members and the role of the oceanic lithosphere.* Earth and Planetary Science Letters 240 (3-4), 605–620. doi:10.1016/j.epsl.2005.10.002.

Salters, V.J.M., Dick, H.J.B., 2002. *Mineralogy of the mid-ocean-ridge basalt source from neodymium isotopic composition of abyssal peridotites.* Nature 418 (6893), 68–72. doi:10.1038/nature00798.

Salters, V.J.M., Mallick, S., Hart, S.R., Langmuir, C.E., Stracke, A., 2011. *Domains of depleted mantle: New evidence from hafnium and neodymium isotopes.* Geochem. Geophys. Geosyst. 12 (8). doi:10.1029/2011GC003617.

Salters, V.J.M., Stracke, A., 2004. *Composition of the depleted mantle.* Geochem. Geophys. Geosyst. 5 (5). doi:10.1029/2003GC000597.

Sanfilippo, A., Salters, V., Tribuzio, R., Zanetti, A., 2019. *Role of ancient, ultra-depleted mantle in Mid-Ocean-Ridge magmatism.* Earth and Planetary Science Letters 511, 89–98. doi:10.1016/j.epsl.2019.01.018.

Sanfilippo, A., Salters, V.J., Sokolov, S.Y., Peyve, A.A., Stracke, A., 2021. *Ancient refractory asthenosphere revealed by mantle re-melting at the Arctic Mid Atlantic Ridge.* Earth and Planetary Science Letters 566, 116981. doi:10.1016/j.epsl.2021.116981.

Schilling, J.-G., C. Ruppel, C., Davis, A.N., McCully, B., Tighe, S.A., Kingsley, R.H., Lin, J., 1995. *Thermal structure of the mantle beneath the equatorial Mid-Atlantic Ridge: Inferences from the spatial variation of dredged basalt glass compositions.* Journal of Geophysical Research 100 (B7), 10,057-10,073.

Schilling, J.-G., Hanan, B.B., McCully, B., Kingsley, R.H., Fontignie, D., 1994. *Influence of the Sierra Leone mantle plume on the equatorial Mid-Atlantic Ridge: A Nd-Sr-Pb isotopic study.* Journal of Geophysical Research 99 (B6), 12,005-12,028.

Shorttle, O., Maclennan, J., Lambart, S., 2014. *Quantifying lithological variability in the mantle.* Earth and Planetary Science Letters 395, 24–40. doi:10.1016/j.epsl.2014.03.040.

Shorttle, O., Maclennan, J., 2011. *Compositional trends of Icelandic basalts: Implications for short-length scale lithological heterogeneity in mantle plumes*. Geochem. Geophys. Geosyst. 12 (11), n/a-n/a. doi:10.1029/2011GC003748.

Sleep, N.H., 1984. *Tapping of magmas from ubiquitous mantle heterogeneities: An alternative to mantle plumes?* J. Geophys. Res. 89 (B12), 10029–10041. doi:10.1029/JB089iB12p10029.

Sobolev, A.V., Hofmann, A.W., Jochum, K.P., Kuzmin, D.V., Stoll, B., 2011. *A young source for the Hawaiian plume.* Nature 476 (7361), 434–437. doi:10.1038/nature10321.

Stracke, A., 2021. *A process-oriented approach to mantle geochemistry.* Chemical Geology 579, 120350. doi:10.1016/j.chemgeo.2021.120350.

Stracke, A., Bizimis, M., Salters, V.J.M., 2003. *Recycling oceanic crust: Quantitative constraints.* Geochem. Geophys. Geosyst. 4 (3). doi:10.1029/2001GC000223.

Stracke, A., Bourdon, B., 2009. *The importance of melt extraction for tracing mantle heterogeneity.* Geochimica et Cosmochimica Acta 73 (1), 218–238. doi:10.1016/j.gca.2008.10.015.

Stracke, A., Genske, F., Berndt, J., Koornneef, J.M., 2019. *Ubiquitous ultra-depleted domains in Earth's mantle.* Nat. Geosci. 12 (10), 851–855. doi:10.1038/s41561-019-0446-z.

Stracke, A., Hofmann, A.W., Hart, S.R., 2005. *FOZO, HIMU, and the rest of the mantle zoo.* Geochem. Geophys. Geosyst. 6 (5), n/a-n/a. doi:10.1029/2004GC000824.

Stracke, A., Snow, J.E., Hellebrand, E., Handt, A. von der, Bourdon, B., Birbaum, K., Günther, D., 2011. *Abyssal peridotite Hf isotopes identify extreme mantle depletion.* Earth and Planetary Science Letters 308 (3-4), 359–368. doi:10.1016/j.epsl.2011.06.012.

Sun, S.S., McDonough, W.F., 1989. *Chemical and isotopic systematics of oceanic basalts: implications for mantle composition and processes.* Geological Society, London, Special Publications 42 (1), 313–345. doi:10.1144/GSL.SP.1989.042.01.19.

Sushchevskaya, N.M., Bonatti, E., Peive, A.A., Kamenetskii, V.S., Belyatskii, B.V., Tsekhonya, T.I., Kononkova, N.N., 2002. *Heterogeneity of Rift Magmatism in the Equatorial Province of the Mid-Atlantic Ridge (15° N to 3° S).* Geochemistry International 40, 26–50.

Tappe, S., Pearson, D.G., Nowell, G., Nielsen, T., Milstead, P., Muehlenbachs, K., 2011. *A fresh isotopic look at Greenland kimberlites: Cratonic mantle lithosphere imprint on deep source signal.* Earth and Planetary Science Letters 305 (1-2), 235–248. doi:10.1016/j.epsl.2011.03.005.

Thomson, A.R., Walter, M.J., Kohn, S.C., Brooker, R.A., 2016. *Slab melting as a barrier to deep carbon subduction.* Nature 529 (7584), 76–79. doi:10.1038/nature16174.

Weiss, Y., Class, C., Goldstein, S.L., Hanyu, T., 2016. *Key new pieces of the HIMU puzzle from olivines and diamond inclusions.* Nature 537 (7622), 666–670. doi:10.1038/nature19113.

White, W.M., 1985. *Sources of oceanic basalts: Radiogenic isotopic evidence.* Geology 13 (2), 115. doi:10.1130/0091-7613(1985)13<115:SOOBRI>2.0.CO;2.

Willbold, M., Stracke, A., 2006. *Trace element composition of mantle end-members: Implications for recycling of oceanic and upper and lower continental crust.* Geochem. Geophys. Geosyst. 7 (4). doi:10.1029/2005GC001005.

Willig, M., Stracke, A., Beier, C., Salters, V.J., 2020. *Constraints on mantle evolution from Ce-Nd-Hf isotope systematics.* Geochimica et Cosmochimica Acta 272, 36–53. doi:10.1016/j.gca.2019.12.029.

Woodhead, J., Stern, R.J., Pearce, J., Hergt, J., Vervoort, J., 2012. *Hf-Nd isotope variation in Mariana Trough basalts: The importance of "ambient mantle" in the interpretation of subduction zone magmas.* Geology 40 (6), 539–542. doi:10.1130/G32963.1.

Woodhead, J.D., 1996. *Extreme HIMU in an oceanic setting: the geochemistry of Mangaia Island (Polynesia), and temporal evolution of the Cook—Austral hotspot.* Journal of Volcanology and Geothermal Research 72 (1-2), 1–19. doi:10.1016/0377-0273(96)00002-9.

Workman, R.K., Hart, S.R., Jackson, M., Regelous, M., Farley, K.A., Blusztajn, J., Kurz, M., Staudigel, H., 2004. *Recycled metasomatized lithosphere as the origin of the Enriched Mantle II (EM2) end-member: Evidence from the Samoan Volcanic Chain.* Geochem. Geophys. Geosyst. 5 (4). doi:10.1029/2003GC000623.

Yu, Z., Singh, S.C., Gregory, E.P.M., Maia, M., Wang, Z., Brunelli, D., 2021. *Semibrittle seismic deformation in high-temperature mantle mylonite shear zone along the Romanche transform fault.* Science Advances 7.

Zindler, A., Hart, S.R., 1986. *Chemical geodynamics.* Ann. Rev. Earth Planet. 14 (1), 493–571.

Zindler, A., Hart, S.R., Frey, F.A., Jakobsson, S.P., 1979. *Nd and Sr isotope ratios and rare earth element abundances in Reykjanes Peninsula basalts evidence for mantle heterogeneity beneath Iceland.* Earth and Planetary Science Letters 45 (2), 249–262. doi:10.1016/0012-821X(79)90127-4.

## Supplementary material

### Figures

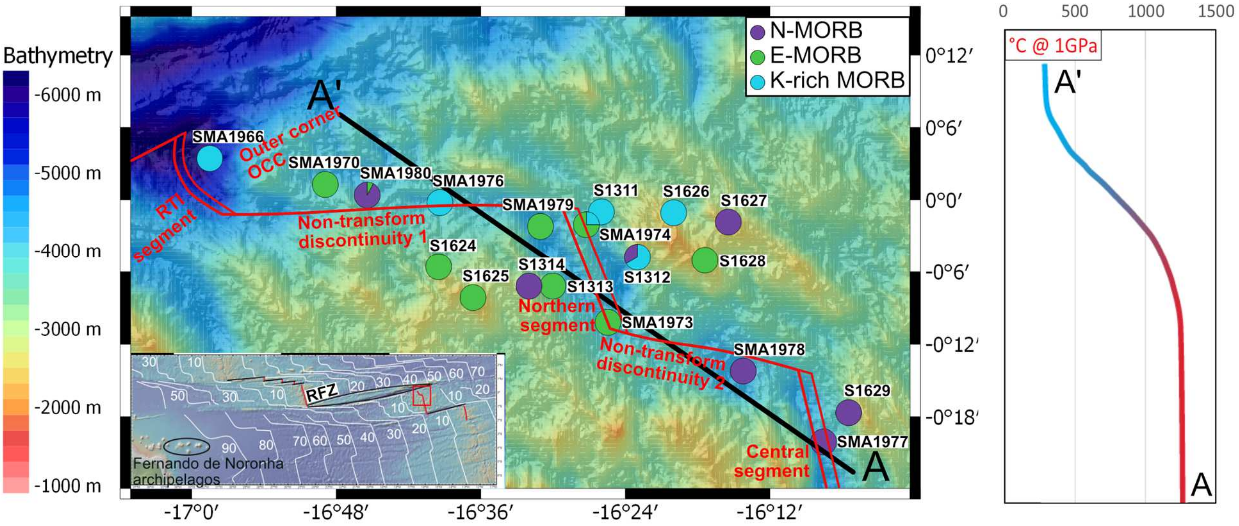

*Figure S 5.1 - Bathymetric map with the location of the sampling sites considered in this study. The white lines indicate the age of the oceanic lithosphere (from Yu et al., 2021). The thermal profile shows the thermal gradient along the A-A' section. Temperature is calculated according to Ligi et al. (2005) at the pressure of 1 GPa. RFZ: Romanche Fracture Zone.*

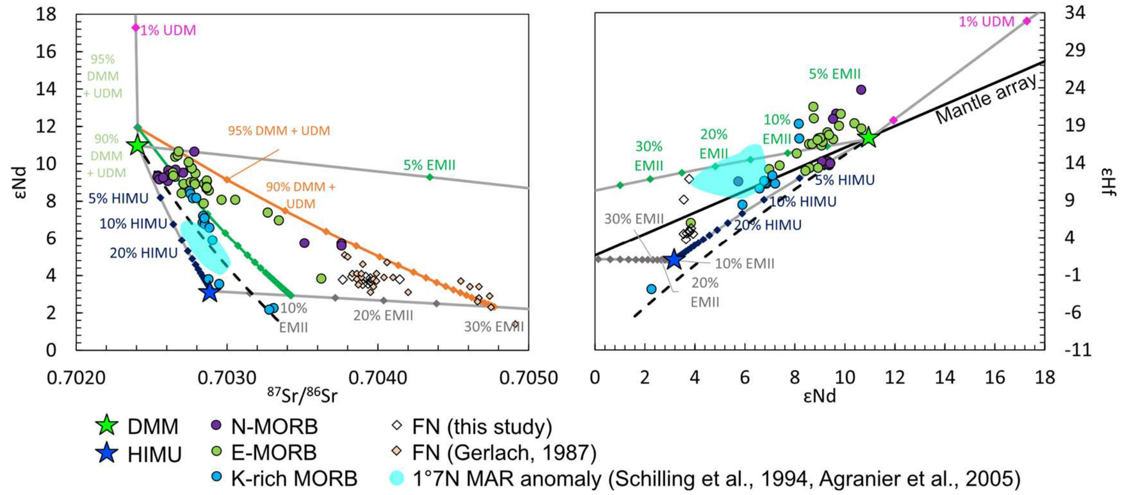

*Figure S 5.2 - Nd-Sr and Hf-Nd isotopes systematics and simple binary mixing model. The UDM endmember has been calculated from 10% melting of a residual mantle following Sanfilippo et al. (2021) model. Endmember compositions are given in Table 1. The grey lines represent simple binary mixing lines between the different endmembers, calculated with a step interval of 5%. The* *green and orange lines represent mixings between DMM-UDM-HIMU-derived melts with variable proportions of EMII. The dashed line is a simple binary mixing between the DMM and actual ratios calculated from a 2 Ga recycled oceanic crust (after Stracke et al., 2003). Samples from the 1°7N anomaly (Sierra Leone) described by Schilling et al. (1994) and from Fernando de Noronha archipelago are plotted for comparison.*

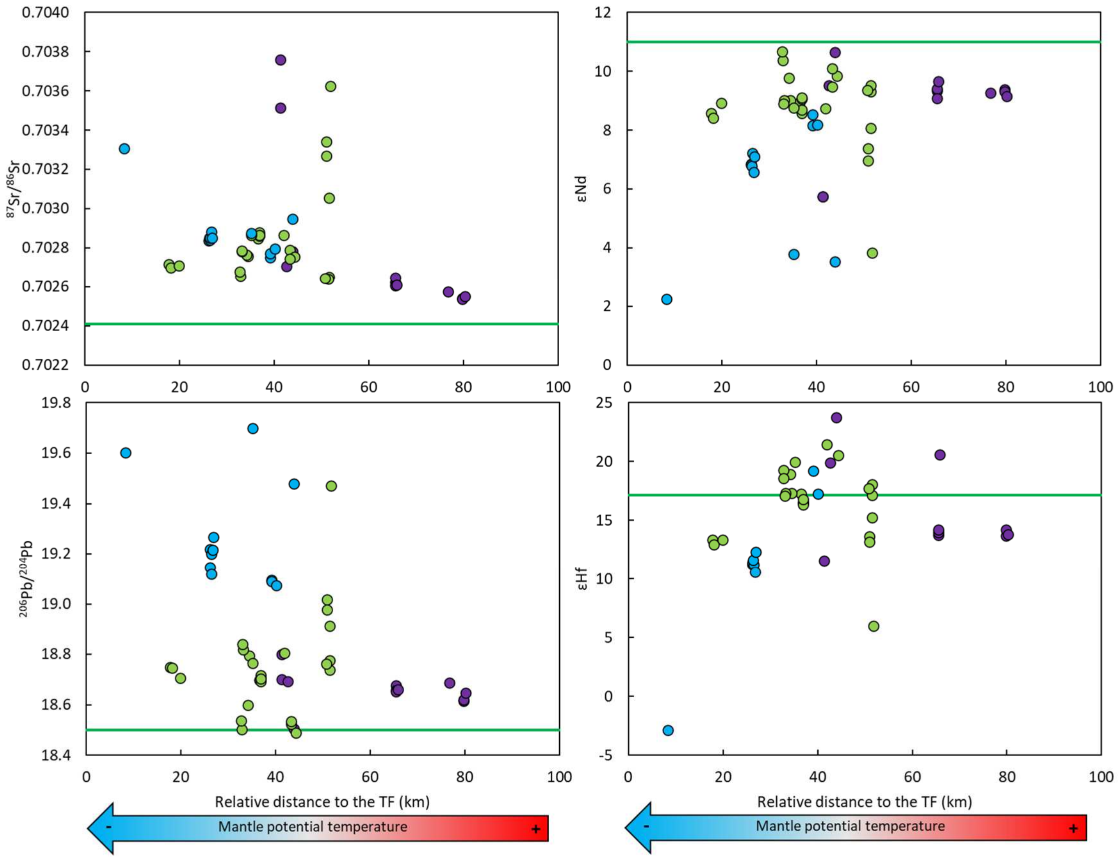

*Figure S 5.3 - Isotope ratios vs relative distance to the transform fault, proxy of the mantle potential temperature. The green line represents the DMM isotope ratios used in our mixing model.*

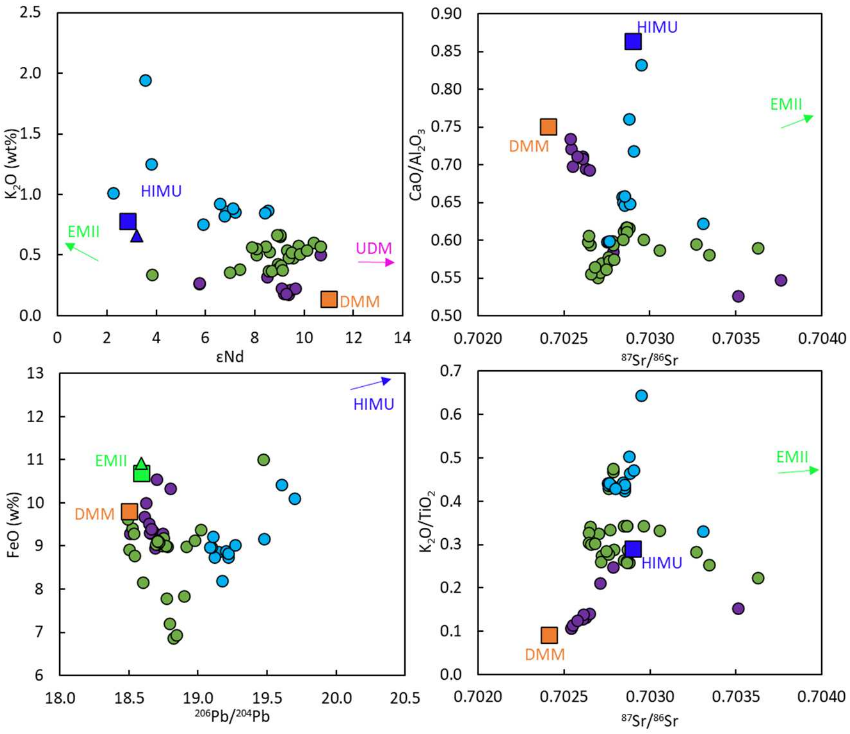

*Figure S 5.4 - Major element correlations with $^{87}Sr/^{86}Sr$ and εHf. Major elements data of the enriched endmembers are from Jackson and Dasgupta (2008). For comparison, triangles are HIMU (blue) and EMII (green) major element data corrected for olivine fractionation (Jackson and Dasgupta, 2008). Trace element data are average values from Willbold and Stracke (2006). Major and trace elements data of DMM are N-MORB of Gale et al. (2013).*

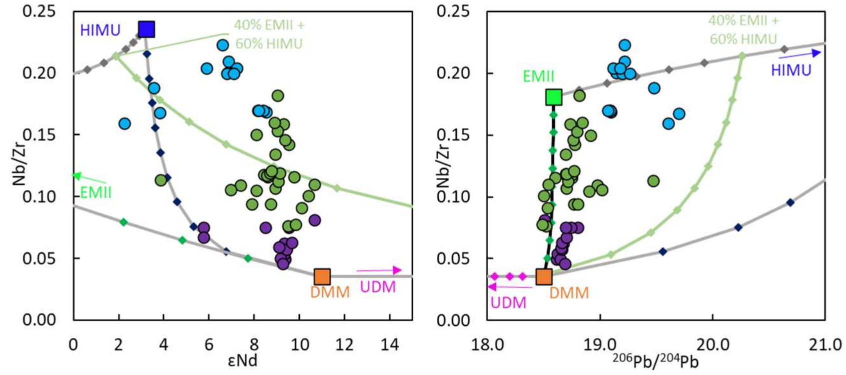

*Figure S 5.5 - Trace element correlations with εNd and $^{206}Pb/^{204}Pb$. Lines represent simple binary mixing between the various endmembers calculated at 10% mixing step (markers). The green line represent mixing between all the endmembers (mixing between a melt derived from EMII and HIMU mixing respectively 40% and 60% and a melt derived from DMM and UDM mixing respectively 95% and 5%). Isotopes data of the mantle endmembers are given in table 5.1. Major and trace elements data of the enriched endmembers are from Willbold and Stracke (2006). The ones of DMM are N-MORB data from Gale et al. (2013).*

## Analytical methods

### *Major elements and trace elements*

The major element compositions have been analysed by the Electron Probe Micro Analysis (EPMA) using the Microsonde Ouest (operated by Université de Bretagne Occidentale, IFREMER, Institut Universitaire Européen de la Mer, INSA Rennes, Université de Rennes1 and Université de Nantes). Analyses consist of 4 spots of 5 µm diameter on each sample.

The trace element distribution has been measured using Laser Ablation Inductively Coupled Plasma Mass Spectrometry (LA-ICP-MS ThermoFisher Scientific XSeries$^{II}$) at the Centro Interdipartimentale Grandi Strumenti (Modena) and by LA-HR-ICP-MS ThermoFisher Scientific Element XR at Pole Spectrométrie Océan (IUEM, Plouzané, France). Dwell times on each isotope during one run was 30 ms per amu. One run consists of 50 replicates per analysis. The standard reference materials NIST612 and NIST614 have been analysed following the sequence of analysis: NIST614 - NIST612 - NIST614 - 3 x sample #1 – 3 x sample #2. The natural reference sample BHVO2 has been regularly measured.

### *Pb, Sr, Nd and Hf isotopes analysis*

About 100 - 200 mg of basaltic glasses chip, carefully handpicked under a binocular microscope to avoid any alteration, have been leached by $H_2O_2$, followed by 2.5N HCl, in an ultrasonic bath for ~ 1h for each step. Samples have been then dissolved with a HF+HNO3 solution on a hotplate at ~ 90°C for two days and regularly put in an ultrasonic bath for 30 minutes each time.

The Pb, Sr, Hf and Nd elements have been separated from the same batch of sample. The combined Pb-Sr chemistry was performed at the Dipartimento di Scienze Chimiche e Geologiche (DSCG, Modena, Italy) after Deniel and Pin (2001) protocol. Samples were loaded on 150 µL teflon columns filled with Sr-spec resin in 2N HNO3. The cut containing Hf and Nd was first eluted with about 2 ml of 2N HNO3, followed by Ba cut with 7N HNO3 and 2N HNO3. Sr was collected with MilliQ and Pb with 6N HCl. Acids used in the leaching, dissolution and chemistry were all of suprapure grade.

The Hf and Nd chemistry has been made at the Laboratory Géo-Océan (IUEM Plouzané, France). The REE fraction is separated from the fraction containing Hf in 2 mL teflon columns filled with AG50W-X8 (200-400mesh) resin (Chauvel et al., 2011). Hf was then recovered following the two columns procedure of Blichert-Toft et al. (1997), which uses a 1st set of columns containing an anionic resin AG1-X8 (100-200 mesh) and then a 2nd set of columns containing a cationic resin AG50W-X8 (200-400 mesh).

Nd was separated from the REE fraction in 2 mL Teflon columns containing LN-spec resin (LaNthanides Specification) and 0.25N HCl (Richard et al., 1976).

Pb, Sr isotopes have been analysed at the Centro Interdipartimentale Grandi Strumenti (Modena) and Hf isotopes at the Pole Spectrométrie Océan (Plouzané, France), with a Multi-Collector Inductively Coupled Plasma Mass Spectrometer (MC-ICPMS ThermoFisher Scientific NEPTUNE). Nd isotope ratios have been analysed with a Multi-Collector Thermo-Ionisation Mass Spectrometer (MC TI-MS ThermoFisher Scientific Triton) at the Pole Spectrométrie Océan (Plouzané, France). The average values of all standards used during the analytical sessions is reported in supplementary table S5.1. Chemical blanks have been measured for each set of chemistry, the maximum values are inferior at 0.8 ng, 0.9 ng, 40 pg and 0.9 ng respectively for Nd, Sr, Hf and Pb.

## *Table S5.1 – Pb, Sr, Nd and Hf isotope ratios.*

| **Sample** | **Latitude** | **Longitude** | | **$^{87}$Sr/$^{86}$Sr** | | **$^{143}$Nd/$^{144}$Nd** | | **εNd** | **$^{206}$Pb/$^{204}$Pb** | | **$^{176}$Hf/$^{177}$Hf** | | **εHf** |
|---|---|---|---|---|---|---|---|---|---|---|---|---|---|
| **N-MORB** | | | | | **2σ** | | **2σ** | | | **2σ** | | **2σ** | |
| SMA1977-330 | -0.335 | -16.125 | M/P | 0.702541 | 0.000006 | 0.513119 | 0.000007 | 9.4 | 18.614 | 0.001 | 0.283159 | 0.000009 | 13.692 |
| SMA1977-336 | -0.332 | -16.120 | M/P | 0.702539 | 0.000006 | 0.513115 | 0.000007 | 9.3 | 18.620 | 0.001 | 0.283174 | 0.000021 | 14.224 |
| SMA1977-342 | -0.334 | -16.109 | M/P | 0.702551 | 0.000012 | 0.513108 | 0.000017 | 9.2 | 18.647 | 0.001 | 0.283163 | 0.000014 | 13.831 |
| SMA1978-345 | -0.237 | -16.237 | M/P | 0.702625 | 0.000006 | 0.513117 | 0.000006 | 9.3 | 18.677 | 0.001 | 0.283162 | 0.000010 | 13.780 |
| SMA1978-350 | -0.237 | -16.237 | M/P | 0.702648 | 0.000006 | 0.513121 | 0.000007 | 9.4 | 18.658 | 0.001 | 0.283167 | 0.000018 | 13.967 |
| SMA1978-357 | -0.235 | -16.230 | M/P | 0.702606 | 0.000009 | 0.513104 | 0.000006 | 9.1 | 18.652 | 0.001 | 0.283174 | 0.000014 | 14.207 |
| SMA1978-364 | -0.236 | -16.225 | M/P | 0.702610 | 0.000008 | 0.513133 | 0.000008 | 9.6 | 18.661 | 0.002 | 0.283354 | 0.000017 | 20.573 |
| SMA1978-364 Dup | | | M/P | 0.702617 | 0.000008 | 0.513121 | 0.000010 | 9.4 | 18.665 | 0.003 | 0.283166 | 0.000022 | 13.932 |
| S1312-Xa | -0.080 | -16.383 | P | 0.702783 | 0.000004 | 0.513184 | 0.000004 | 10.7 | 18.506 | 0.001 | 0.283443 | 0.000009 | 23.734 |
| S1314-X | -0.120 | -16.533 | P | | | 0.512932 | 0.000008 | 5.7 | 18.800 | 0.002 | 0.283099 | 0.000006 | 11.552 |
| S13-14-X Dup | -0.120 | -16.533 | P | 0.703758 | 0.000005 | 0.512925 | 0.000004 | 5.6 | 18.870 | 0.003 | 0.283074 | 0.000006 | 10.683 |
| S1314-X Dup1 | -0.120 | -16.533 | P | 0.703775 | 0.000007 | | | | | | | | |
| S1314-X Dup2 | -0.120 | -16.533 | P | 0.703919 | 0.000004 | | | | | | | | |
| S1314-01 | -0.120 | -16.533 | L | 0.703513 | 0.000013 | 0.512933 | 0.000009 | 5.7 | 18.702 | 0.001 | | | |
| S1627-01B | -0.031 | -16.258 | L | | | 0.513073 | 0.000019 | 8.5 | 18.744 | 0.003 | | | |
| S1627-01 | -0.031 | -16.258 | P | 0.702708 | 0.000005 | 0.513126 | 0.000006 | 9.5 | 18.694 | 0.003 | 0.283334 | 0.000006 | 19.879 |
| S1627-01 | -0.031 | -16.258 | M | 0.702658 | 0.000008 | 0.513135 | 0.000009 | 9.7 | | | | | |
| S1629-35 | -0.294 | -16.091 | L | 0.702576 | 0.000013 | 0.513113 | 0.000007 | 9.3 | 18.689 | 0.001 | | | |
| **E-MORB** | | | | | | | | | | | | | |
| SMA1970-191E | 0.021 | -16.815 | M/P | 0.702719 | 0.000008 | 0.513078 | 0.000007 | 8.6 | 18.749 | 0.001 | 0.283149 | 0.000012 | 13.344 |
| SMA1970-194 | 0.019 | -16.811 | M/P | 0.702699 | 0.000007 | 0.513070 | 0.000008 | 8.4 | 18.747 | 0.001 | 0.283138 | 0.000009 | 12.958 |
| SMA1970-202 | 0.009 | -16.792 | M/P | 0.702712 | 0.000008 | 0.513096 | 0.000012 | 8.9 | 18.705 | 0.001 | 0.283149 | 0.000012 | 13.342 |
| SMA1973-246 | -0.170 | -16.424 | M/P | 0.703624 | 0.000007 | 0.512835 | 0.000003 | 3.8 | 19.472 | 0.001 | 0.282942 | 0.000012 | 6.001 |
| SMA1973-251 | -0.167 | -16.422 | M/P | 0.702653 | 0.000007 | 0.513115 | 0.000007 | 9.3 | 18.738 | 0.001 | 0.283283 | 0.000008 | 18.073 |
| SMA1973-255 | -0.166 | -16.422 | M/P | 0.703054 | 0.000005 | 0.513052 | 0.000006 | 8.1 | 18.913 | 0.001 | 0.283204 | 0.000008 | 15.276 |
| SMA1973-256 | -0.166 | -16.422 | M/P | 0.702641 | 0.000008 | 0.513127 | 0.000006 | 9.5 | 18.775 | 0.001 | 0.283257 | 0.000009 | 17.166 |
| SMA1973-261 | -0.161 | -16.421 | M/P | 0.703269 | 0.000008 | 0.513017 | 0.000006 | 7.4 | 18.977 | 0.001 | 0.283158 | 0.000010 | 13.660 |
| SMA1973-262 | -0.161 | -16.421 | M/P | 0.703343 | 0.000008 | 0.512995 | 0.000006 | 7.0 | 19.017 | 0.002 | 0.283145 | 0.000009 | 13.175 |
| SMA1973-264 | -0.158 | -16.419 | M/P | 0.702644 | 0.000012 | 0.513118 | 0.000009 | 9.4 | 18.764 | 0.001 | 0.283273 | 0.000008 | 17.734 |
| SMA1973-264 bis | | | | | | | | | | | 0.283251 | 0.000009 | 16.923 |
| SMA1974-267 | -0.035 | -16.454 | M/P | 0.702848 | 0.000006 | 0.513096 | 0.000007 | 8.9 | 18.698 | 0.001 | 0.283260 | 0.000009 | 17.266 |
| SMA1974-272 | -0.038 | -16.453 | M/P | 0.702879 | 0.000007 | 0.513077 | 0.000006 | 8.6 | 18.705 | 0.001 | 0.283239 | 0.000013 | 16.511 |
| SMA1974-273 | -0.038 | -16.453 | M/P | 0.702862 | 0.000008 | 0.513084 | 0.000006 | 8.7 | 18.694 | 0.001 | 0.283239 | 0.000007 | 16.530 |
| SMA1974-275 | -0.039 | -16.455 | M/P | 0.702867 | 0.000005 | 0.513103 | 0.000010 | 9.1 | 18.718 | 0.001 | 0.283234 | 0.000016 | 16.327 |
| SMA1974-277 | -0.039 | -16.456 | M/P | 0.702865 | 0.000005 | 0.513105 | 0.000020 | 9.1 | 18.705 | 0.002 | 0.283247 | 0.000010 | 16.809 |
| SMA1979-366 | -0.037 | -16.517 | M/P | 0.702758 | 0.000007 | 0.513101 | 0.000006 | 9.0 | 18.796 | 0.001 | 0.283262 | 0.000011 | 17.334 |
| SMA1979-368 | -0.034 | -16.518 | M/P | 0.702764 | 0.000006 | 0.513139 | 0.000008 | 9.8 | 18.600 | 0.001 | 0.283308 | 0.000013 | 18.947 |
| SMA1979-374 | -0.027 | -16.522 | M/P | 0.702782 | 0.000007 | 0.513100 | 0.000006 | 9.0 | 18.818 | 0.001 | 0.283262 | 0.000008 | 17.341 |

*Table S5.1 (continue)*

| **Sample** | **Latitude** | **Longitude** | | **$^{87}Sr/^{86}Sr$** | **2σ** | **$^{143}Nd/^{144}Nd$** | **2σ** | **εNd** | **$^{206}Pb/^{204}Pb$** | **2σ** | **$^{176}Hf/^{177}Hf$** | **2σ** | **εHf** |
|---|---|---|---|---|---|---|---|---|---|---|---|---|---|
| SMA1979-375 | -0.025 | -16.521 | M/P | 0.702786 | 0.000011 | 0.513095 | 0.000010 | 8.9 | 18.841 | 0.001 | 0.283255 | 0.000011 | 17.073 |
| SMA1979-376 | -0.019 | -16.511 | M/P | 0.702656 | 0.000004 | 0.513170 | 0.000006 | 10.4 | | | 0.283317 | 0.000006 | 19.291 |
| SMA1979-376 dup | | | M/P | 0.702672 | 0.000007 | 0.513174 | 0.000003 | 10.5 | 18.503 | 0.0004 | 0.283306 | 0.000006 | 18.9 |
| SMA1979-377 | -0.018 | -16.511 | M/P | 0.702678 | 0.000012 | 0.513185 | 0.000007 | 10.7 | 18.538 | 0.001 | 0.283298 | 0.000009 | 18.6 |
| S1313-06 | -0.120 | -16.500 | L | 0.702790 | 0.000008 | 0.513124 | 0.000009 | 9.5 | 18.524 | 0.003 | | | |
| S1313-10 | -0.120 | -16.500 | P | 0.702756 | 0.000004 | 0.513142 | 0.000006 | 9.8 | 18.488 | 0.001 | 0.283352 | 0.000006 | 20.5 |
| S1313-10 Dup | -0.120 | -16.500 | M | 0.702766 | 0.000008 | 0.513138 | 0.000007 | 9.8 | | | | | |
| S1313-11 | -0.017 | -16.433 | L | 0.702745 | 0.000013 | 0.513155 | 0.000009 | 10.1 | 18.533 | 0.001 | | | |
| S1624-21 | -0.093 | -16.658 | L | 0.702963 | 0.000008 | 0.513052 | 0.000011 | 8.1 | 18.900 | 0.011 | | | |
| S1624-21 Dup | -0.093 | -16.658 | P | 0.702864 | 0.000005 | 0.513087 | 0.000004 | 8.8 | 18.766 | 0.001 | 0.283336 | 0.000004 | 19.9 |
| S1625-07 | -0.136 | -16.611 | L | 0.702845 | 0.000015 | 0.513042 | 0.000011 | 7.9 | 18.770 | 0.003 | | | |
| S1625-07 Dup | -0.136 | -16.611 | P | 0.702866 | 0.000004 | 0.513086 | 0.000008 | 8.7 | 18.804 | 0.002 | 0.283379 | 0.000006 | 21.5 |
| **K-rich MORB** | | | | | | | | | | | | | |
| SMA1966-128 | 0.057 | -16.974 | M/P | 0.703309 | 0.000008 | 0.512754 | 0.000006 | 2.3 | 19.604 | 0.001 | 0.282691 | 0.000010 | -2.9 |
| SMA1966-128 Dup | | | M/P | 0.703280 | 0.000008 | 0.512750 | 0.000006 | 2.2 | 19.551 | 0.001 | 0.282658 | 0.000006 | -4.0 |
| SMA1974-287 | -0.042 | -16.463 | M/P | 0.702903 | 0.000005 | 0.512941 | 0.000007 | 5.9 | 19.174 | 0.003 | 0.283011 | 0.000009 | 8.4 |
| SMA1976-315 | -0.003 | -16.649 | M/P | 0.702837 | 0.000007 | 0.512989 | 0.000007 | 6.9 | 19.219 | 0.001 | 0.283090 | 0.000013 | 11.2 |
| SMA1976-317 | -0.003 | -16.648 | M/P | 0.702852 | 0.000004 | 0.512988 | 0.000006 | 6.8 | 19.146 | 0.002 | 0.283094 | 0.000008 | 11.4 |
| SMA1976-319 | -0.003 | -16.642 | M/P | 0.702841 | 0.000005 | 0.513008 | 0.000009 | 7.2 | 19.119 | 0.002 | 0.283090 | 0.000009 | 11.2 |
| SMA1976-320 | -0.003 | -16.643 | M/P | 0.702852 | 0.000005 | 0.512985 | 0.000006 | 6.8 | 19.199 | 0.001 | 0.283100 | 0.000009 | 11.6 |
| SMA1976-321 | -0.006 | -16.642 | M/P | 0.702883 | 0.000008 | 0.512976 | 0.000007 | 6.6 | 19.216 | 0.001 | 0.283071 | 0.000008 | 10.6 |
| SMA1976-324 | -0.007 | -16.642 | M/P | 0.702851 | 0.000008 | 0.513002 | 0.000007 | 7.1 | 19.266 | 0.001 | 0.283121 | 0.000015 | 12.3 |
| S1311-03 | -0.017 | -16.433 | L | 0.702877 | 0.000010 | 0.512833 | 0.000008 | 3.8 | 19.700 | 0.003 | | | |
| S1312-49 | -0.080 | -16.383 | L | 0.702947 | 0.000015 | 0.512820 | 0.000008 | 3.6 | 19.478 | 0.002 | | | |
| S1626-15 | -0.018 | -16.333 | L | 0.702752 | 0.000012 | 0.513076 | 0.000009 | 8.5 | 19.096 | 0.001 | | | |
| S1626-21 | -0.018 | -16.333 | L | 0.702758 | 0.000013 | 0.513069 | 0.000009 | 8.4 | 19.088 | 0.006 | | | |
| S1626-21 Dup | -0.018 | -16.333 | P | 0.702773 | 0.000005 | 0.513056 | 0.000004 | 8.2 | 19.089 | 0.001 | 0.283316 | 0.000006 | 19.2 |
| S1626-22 | -0.018 | -16.333 | L | 0.702762 | 0.000013 | | | | | | | | |
| S1626-22 Dup | -0.018 | -16.333 | P | 0.702795 | 0.000004 | 0.513057 | 0.000004 | 8.2 | 19.073 | 0.0004 | 0.283260 | 0.000008 | 17.3 |

The letters correspond to the place where the ratios have been analysed: P: chemical separation and analysed all made at GO (Plouzané), Sr and Nd measured with TIMS, Pb and Hf with HR-ICP-MS; M/P: Pb-Sr chemical separation and analyses made at DSCG and at CIGS Modena (HR-ICP-MS), Nd and Hf chemical separation and analyses made at GO Plouzané (respectively TIMS and HR-ICP-MS); L: previously existing data analysed at Lamont Doherty Earth Observatory (Cipriani, A.).

# CHAPTER 6 Evidence for re-melting of impregnated peridotite below an Oceanic Core Complex

## Abstract

Mid-Ocean Ridge Basalts (MORBs) from the Eastern Romanche Ridge Transform Intersection (ERRTI) are characterised by extreme compositional heterogeneity with highly variable major and trace elements and isotopic signatures (Schilling et al., 1994, 1995, Bonatti et al., 2001, Sushchevskaya et al., 2002, Ligi et al., 2005, Le Voyer et al., 2015, Verhoest et al., in prep.). A regional thermal low, resulting in a strong reduction of the degree of partial melting, is the main cause of the observed variability overprinted by melt mixing and fractional crystallization processes. Here we discuss a peculiar group of lavas characterized by positive europium and strontium anomalies along with high $SiO_2$ and $Al_2O_3$ and low $TiO_2$, CaO and FeO contents. We show that these rocks are generated by partial melting of the lithospheric mantle, previously impregnated in the plagioclase stability field during the relocation of the spreading axis in oscillatory Core Complex tectonics. In spite of the marked compositional variability of the melts erupted at the ERRTI, the Eu-Sr bearing anomalies MORBs unveil homogeneous compositions generated by the melting process.

## Introduction

MORBs erupted along Mid Ocean Ridges frequently exhibit an incompatible element pattern with negative Eu and Sr anomalies due to the subtraction of these elements by fractionating plagioclase in shallow magma chambers (Kay et al., 1970, Schilling et al., 1976, Puchelt and Emmermann, 1977). The mantle source is generally assumed to bear no or weakly negative Eu and Sr anomalies (Salters and Stracke, 2004, Workman et al., 2005). MORBs with positive Eu and Sr anomalies have also been reported and associated to various processes: (1) source effects due to recycled heterogeneities in the mantle source (Hofmann and Jochum, 1996, Chauvel and Hémond, 2000, Yaxley and Sobolov, 2007), (2) disequilibrium melting with fast Eu-Sr diffusion from pyroxenes during partial melting (Tang et al., 2017) or (3) assimilation via melt reaction with consolidated or partially consolidated gabbroic crystal mushes (Danyushevsky 2003 and 2004, Laubier et al., 2012, Gale, Laubier et al., 2013, Lissenberg and Dick, 2008, Yang et al., 2019, Sobolev et al. 2000, Anderson et al., 2021).

Here we present major and trace elements compositions and Sr, Pb, Nd and Hf isotope ratios of a group of MORBs from the Eastern Romanche Ridge Transform Intersection (ERRTI) with peculiar positive Sr ad Eu anomalies. These basalts were recovered with the Nautile submersible during the SMARTIES (*Smooth regions at the Mid-Atlantic Ridge Transform-Intersections under extreme thermal gradients*) oceanographic expedition and are mainly located close to a large Oceanic Core Complex (OCC) (Figure 6.1). This structure shows a peculiar extension, resulting from a discontinuous spreading process. While the crust exhumed at the OCC spreads eastward, the active spreading line is dragged westward, till the spreading centre jumps back into the middle of the OCC breaking the shoulders of the detachment fault surface. This jump reactivates the spreading in a partially cooled region.

A second peculiarity of this region is the reported large presence of plagioclase-bearing peridotites resulting from melt retention/percolation in the plagioclase stability field (Seyler and Bonatti, 1997, Tartarotti et al., 2002, Santi, 2014). These peridotites are widespread in the ERRTI indicating they are a major constituent of the local lithosphere, then exhumed by the OCC itself and the large normal faults resulting from the reduced magma budget at the ridge axis (Bonatti et al 2001).

Ridge relocation in the middle of the core complex, reactivation and thermal rejuvenation of its roots, and re-melting of Pl-bearing peridotites are here presented as a new mechanism to generate basalts with a particular major element signature and positive anomalies in Eu and Sr. This mechanism maybe active in other cold-spreading regions, where thick lithosphere, reduced magma budget and ridge instability results in melt retention in the plagioclase field and possible re-heating due to ridge axes relocation.

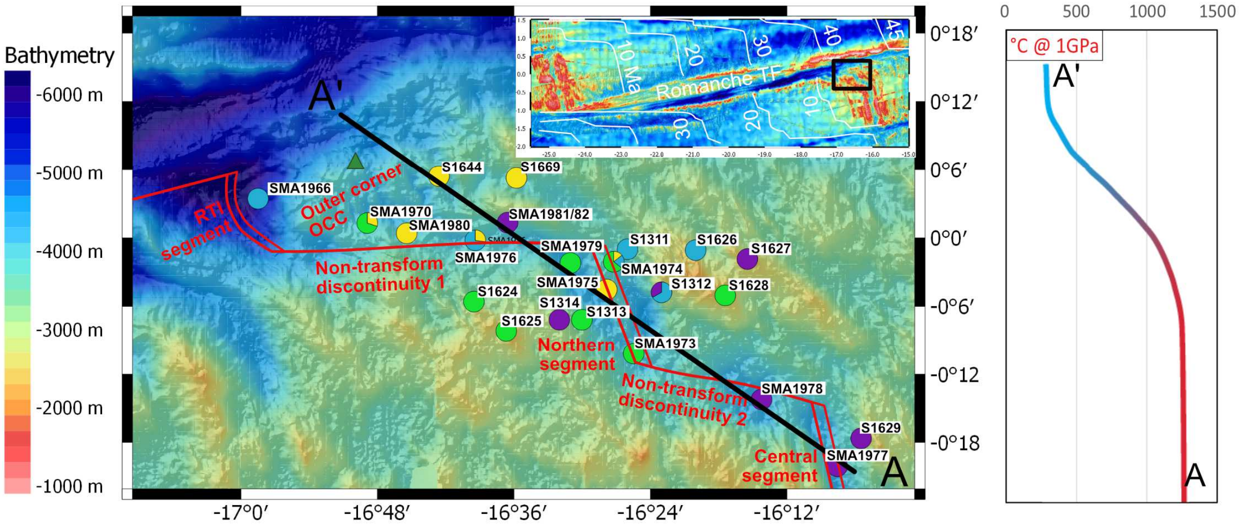

*Figure 6.1 - Bathymetric map of the ERRTI with the location of the sampling sites. In yellow, MORBs with a plagioclase fingerprint studied in this paper. Purple, green and blue circles colours*

*represent N-MORBs, E-MORBs and K-rich MORBs respectively, according to the grouping of Verhoest et al. (in prep.). The right inset shows the thermal profile calculated at 1 GPa along the A-A' section according to the thermal model of Ligi et al. (2005). The dark green triangle represents the location of the plagioclase-bearing peridotite discussed in this study.*

## Methods

### Major elements analysis

The major element compositions have been analysed by the Electron Probe Micro Analysis (EPMA) using the Microsonde Ouest (operated by Université de Bretagne Occidentale, IFREMER, Institut Universitaire Européen de la Mer, INSA Rennes, Université de Rennes1 and Université de Nantes). Analyses consist of 4 spots of 5 µm diameter on each sample.

### Trace element analysis

The trace element distribution has been measured using Laser Ablation Inductively Coupled Plasma Mass Spectrometry (LA-ICP-MS ThermoFisher Scientific XSeriesII) at the Centro Interdipartimentale Grandi Strumenti (Modena) and by LA-HR-ICP-MS ThermoFisher Scientific Element XR at Pole Spectrométrie Océan (IUEM, Plouzané, France). Dwell times on each isotope during one run was 30 ms per amu. One run consists of 50 replicates per analysis. The standard reference materials NIST612 and NIST614 have been analysed following the sequence of analysis: NIST614 - NIST612 - NIST614 - 3 x sample #1 – 3 x sample #2. The natural reference sample BHVO2 has been regularly measured.

### Pb, Sr, Nd and Hf isotopes analysis

After picking about 100 - 200 mg of clean basaltic glass chips, the samples have been leached by $H_2O_2$, followed by 2.5N HCl, in an ultrasonic bath for ~ 1h for each step. Samples have then been dissolved with a HF+HNO3 solution.

The Pb, Sr, Hf and Nd elements have been separated from the same batch of sample. The combined Pb-Sr chemistry was performed at the Dipartimento di Scienze Chimiche e Geologiche (DSCG, Modena, Italy) after Deniel and Pin (2001) protocol. Samples were loaded on 150 µL teflon columns filled with Sr-spec resin in 2N HNO3. The cut containing Hf and Nd was first eluted with about 2 ml of 2N HNO3, followed by Ba cut with 7N HNO3 and 2N HNO3. Sr was collected with MilliQ and Pb with 6N HCl. Acids used in the leaching, dissolution and chemistry were all of suprapure grade.

The Hf and Nd chemistry has been made at the Laboratory Géo-Océan (IUEM Plouzané, France). The REE fraction is separated from the fraction containing Hf in 2 mL teflon columns filled with AG50W-X8 (200-400mesh) resin (Chauvel et al., 2011). Hf was then recovered following the two columns procedure of Blichert-Toft et al. (1997), which uses a first set of columns containing an anionic resin AG1-X8 (100-200 mesh) and then a second set of columns containing a cationic resin AG50W-X8 (200-400 mesh).

Nd was separated from the REE fraction in 2 mL Teflon columns containing LN-spec resin (LaNthanides Specification) and 0.25N HCl (Richard et al., 1976).

Pb, Sr isotopes have been analysed at the Centro Interdipartimentale Grandi Strumenti (Modena) and Hf isotopes at the Pole Spectrométrie Océan (Plouzané, France), with a Multi-Collector Inductively Coupled Plasma Mass Spectrometer (MC-ICPMS ThermoFisher Scientific NEPTUNE). Nd isotope ratios have been analysed with a Multi-Collector Thermo-Ionisation Mass Spectrometer (MC TI-MS ThermoFisher Scientific Triton) at the Pole Spectrométrie Océan (Plouzané, France). Chemical blanks have been measured for each set of chemistry, the maximum values are inferior at 0.8 ng, 0.9 ng, 40 pg and 0.9 ng respectively for Nd, Sr, Hf and Pb.

## Results

### Major elements compositions

ERRTI MORBs here considered are characterised by high $SiO_2$ content, 49.25 wt% to 54.22 wt%, and $Al_2O_3$, 15.56 wt% to 17.09 wt%, and low $TiO_2$ content, 0.88 wt% to 1.68 wt% compared to global MAR MORBs (Figure 6.2). They also have low CaO and FeO, respectively from 9.03 wt% to 10.68 wt% and from 7.64 wt% to 9.34 wt%. Their MgO content varies from 6.99 wt% to

8.95 wt%, $Na_2O$ from 2.68 wt% to 3.5 wt%, $K_2O$ from 0.09 wt% to 0.39 wt% and $P_2O_5$ from 0.05 wt% to 0.21 wt%.

### Trace element compositions

The REE element patterns of the samples vary from flat to enriched LREE (Figure 6.3a) with low HREE compared to N-MORB signature (Gale et al., 2013). They are characterised by positive $Eu_N$ and $Sr_N$ (chondrite normalised) anomalies.

The extended trace element patterns show a slightly positive $Ba_{PM}$ (Primitive Mantle normalised) anomaly, particularly in the samples most enriched in highly incompatible element. $Th_{PM}$ presents a marked negative anomaly, irrespective of the relative enrichments. $K_{PM}$ has no anomaly or slightly positive anomaly, this is peculiar given the constant negative K anomaly in the global (and specifically MAR) MORB record. $Sr_{PM}$ shows a strong positive anomaly (Figure 6.3b).

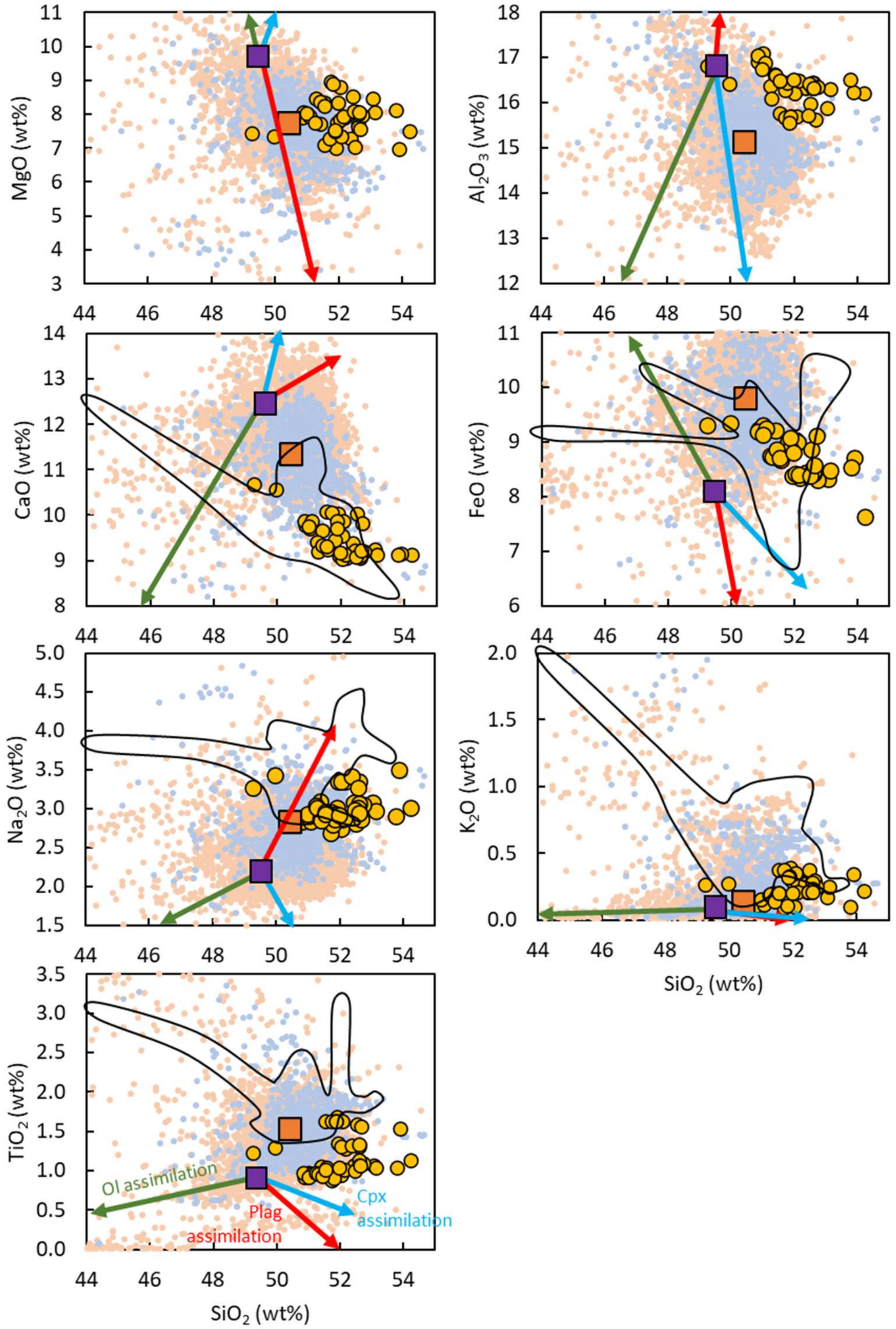

*Figure 6.2 – Major elements compositions vs. $SiO_2$. Black field represents the local MORB compositional variability (data from Verhoest et al., in prep). Orange square is the average N-MORB reference from Gale et al. (2013). Purple square is the primitive N-MORB reference from Presnall and Hoover (1987). The arrows show the compositional trends due to assimilation of olivine (green), plagioclase (red) or clinopyroxene (blue). They represent the effect of reaction between a MORB melt and cumulate or crystal mush. Mineral compositions are from olivine gabbros from the Vema Fracture Zone (Brunelli et al., 2020). Orange and purple dots are North and South MAR MORB respectively.*

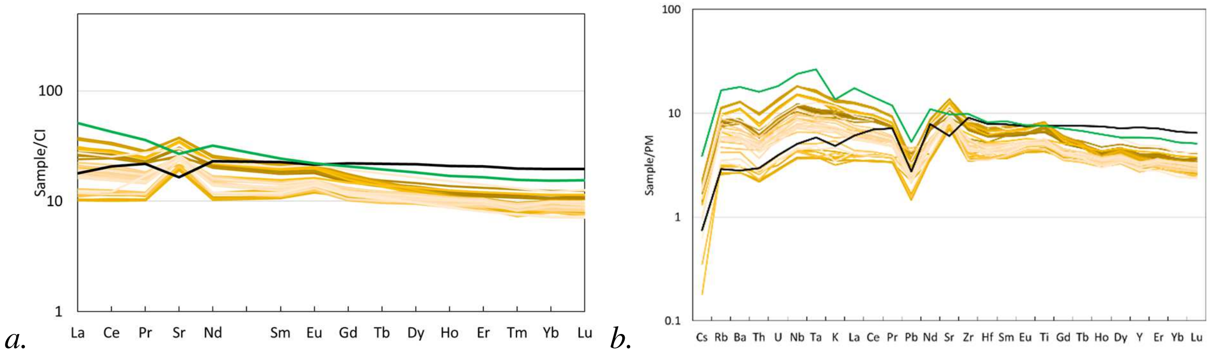

*Figure 6.3 – (a) REE + Sr patterns normalised to CI chondrite (Barrat et al., 2012) and (b) extended trace element patterns normalize to primitive mantle of Sun and McDonough (1989). Black and green lines represent respectively N-MORB and E-MORB references from Gale et al. (2013).*

## Radiogenic isotope signatures

The isotopic signature of these samples is close to the Depleted MORB Mantle (DMM) endmember with $^{87}$Sr/$^{86}$Sr varying from 0.702420 to 0.702929, εNd from 7.22 to 11.45, $^{206}$Pb/$^{204}$Pb from 18.614 to 19.312, $^{207}$Pb/$^{206}$Pb from 15.494 to 15.641, $^{208}$Pb/$^{204}$Pb from 38.123 to 38.754 and εHf from 10.11 to 19.2. These signatures are markedly more homogeneous and closer to the DMM pole when compared to the extreme isotopic variability measured in the regional MORBs (Figure 6.4).

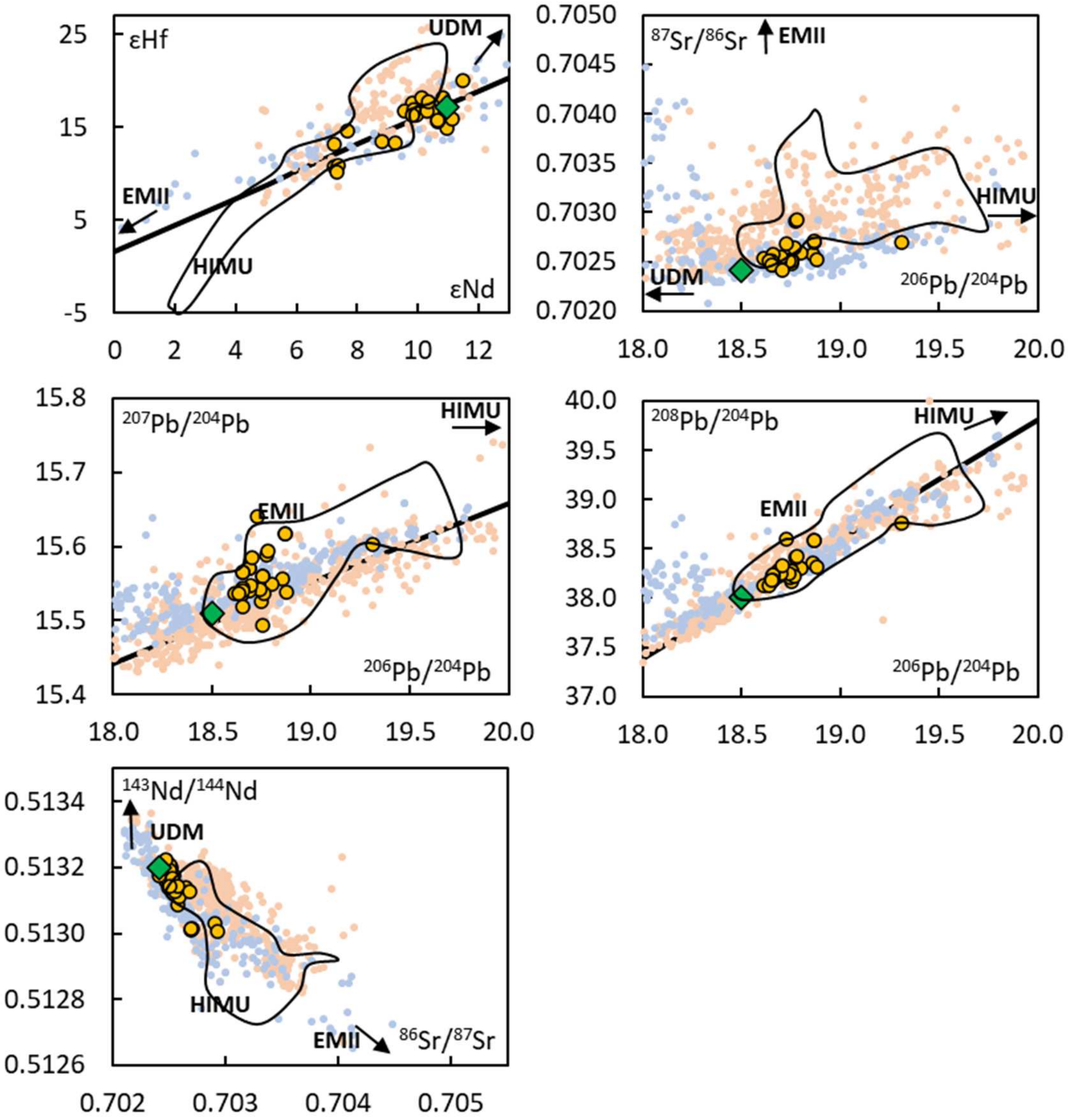

*Figure 6.4 – Isotopes systematics. Black lines bracket the local MORBs compositional field (data from Verhoest et al., in prep.). Green diamond represents DMM signature.*

## Discussion

### Role of plagioclase

The presence of coupled Eu-Sr anomalies in lavas is generally interpreted as the effect of plagioclase separation (negative anomalies) or assimilation (positive anomalies) during fractional crystallization or melt/rock reaction (Kay et al., 1970, Schilling et al., 1976, Puchelt and Emmermann, 1977, Danyushevsky 2003 and 2004, Gale, Laubier et al., 2013, Lissenberg and Dick, 2008, Yang et al., 2017, Yang et al., 2019). Europium presents two valence states (+2 and

+3) in basaltic systems (e.g., Tang et al., 2017) where $Eu^{2+}$ behaves like $Sr^{2+}$ due to their similar ionic radii. In the upper mantle and oceanic crust where plagioclase is stable (Borghini et al., 2010), Eu and Sr are strongly partitioned into plagioclase and thus fractionated from their nearby incompatible elements (e.g., Ce, Sm …). In the lavas here discussed, these anomalies are positive and positively correlated (Figure 6.5) with Eu/Eu* and Sr/Sr*, used to identify Eu and Sr anomaly (see Figure 6.5 caption for details), varying respectively from 1.06 to 1.20 and 1.09 to 1.96. Source processes, pointing to inheritance or disequilibrium melting, have also been proposed to account for positive Eu-Sr anomalies like those here observed (Niu and O'Hara, 2009, Tang et al., 2017). The possible causes with different implications on the magmatic process are:

- Inheritance from recycled heterogeneities in the mantle source
- Kinetic effects on Eu-Sr diffusion from pyroxenes resulting in disequilibrium partial melting
- Assimilation via melt/rock reaction in the lower crust with consolidated or partially consolidated gabbroic crystal mushes

In the following, we show that none of these factors are possible for the ERRTI basalts and propose a new mechanism supported by sampling and local tectonics.

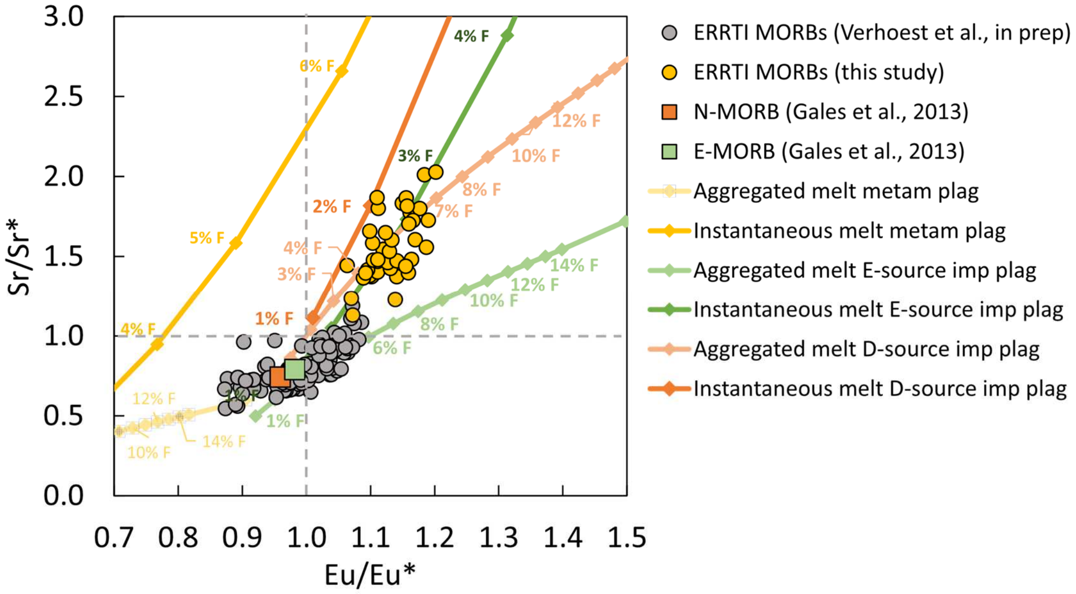

*Figure 6.5 – Correlation between Sr/Sr* and Eu/Eu*, calculated to identify positive Sr and Eu anomalies (Sr/Sr* and Eu/Eu* > 1).* $Sr/Sr^{*} = \frac{Sr}{\sqrt{Pr \times Nd}}$; $Eu/Eu^{*} = \frac{Eu}{\sqrt{Sm \times Gd}}$ *where all the trace element values are normalised to CI chondrite (Barrat et al., 2012). The lines represent the*

*compositional evolution of the aggregated and instantaneous melts obtained by partial melting of different sources: an enriched source bearing metamorphic plagioclase (yellow lines); an enriched source with magmatic plagioclase (green lines) and a depleted source with magmatic plagioclase (orange lines). Sources bearing a metamorphic plagioclase, i.e., where plagioclase is not deriving from magmatic impregnation, do not have Eu-Sr anomalies because originated by equilibration of a spinel peridotites in the plagioclase stability field. Source with plagioclase deriving from magmatic impregnation do have a positive Eu-Sr anomaly because of the equilibration with a transient melt. Source bulk compositions have been calculated from the modal and mineral compositions of the ERRTI pl-peridotites from Tartarotti et al., 2002 and Santi (2014).*

Source effects can be hypothesized assuming that non-DMM lithologies dispersed in the mantle source bear a positive Eu-Sr anomaly inherited from the recycled material brought into subduction. MORBs sampled in the region with no Eu-Sr anomalies (black line fields in Figures 6.2, 6.4), compositionally span to extremely enriched terms, both for radiogenic isotope and incompatible element systematics (Verhoest et al., in prep.) (Figure 6.6). They attest for mixing of DMM-derived melts with enriched and depleted components including EMII, HIMU and UDM (Ultra Depleted Mantle) (Figure 6.4.) (Verhoest et al., in prep). Hence a correlation between Eu-Sr coupled anomalies and the isotopic distribution would appear if one or more of these non-DM components would bear a primary Eu-Sr anomaly. Simple correlations between radiogenic isotope ratios and Eu-Sr anomalies (Figure 6.6 and S6.1) show that this fingerprint in the ERRTI MORBs does not form an unequivocal trend with the N- to E-MORBs collected in the region. In other words, none of the enriched, or partially enriched (mixing related) components sampled in the region show a clear correlation with the extent of the coupled Eu-Sr anomalies, even though some partial correlations with one of the anomalies occasionally appears (Figure 6.6 and S6.1). The low-solidus lithologies hypothesized to be the source of the enriched component erupted in the region (Verhoest et al., in prep., i.e., chapter 5) are therefore unlikely to be the carrier of the observed Eu-Sr anomalies. This conclusion is in agreement with the trace element composition of mantle endmember estimated from erupted basalts (Willbold and Stracke, 2006), which do not bear significant Eu-Sr anomalies. This also rule out the possibility that positive Eu-Sr anomalies are inherited from a normal DMM source although suggested by Jenner and O'Neill (2012). However, the lack of anomalies in the erupted products may derive from large extents of melting or mixing events (see discussion in Tang et al., 2017).

A second possible origin of the coupled Eu-Sr anomalies may be represented by fast Eu-Sr diffusion during disequilibrium melting. Tang et al. (2017) evaluated this kinetic effect for Sm–Eu–Gd and Pr–Sr–Nd fractionations during peridotite partial melting in the spinel field. They show that Eu and Sr under reducing conditions diffuse four orders of magnitude faster than adjacent elements in clino- and orthopyroxenes. This effect is particularly significant at low degrees of melting and decreases during progressive melt aggregation. The total Eu-Sr enrichment in the melt strictly depends on the oxidation state of the source and hence on the $Eu^{2+}/Eu^{3+}$ ratio and melt productivity. Here we observe that if such effect would be active in the subaxial melting region, residual peridotites sampled in the vicinity should show coupled negative Eu-Sr anomalies in the residual clinopyroxene patterns. This is not observed in general along MORs and neither locally at the ERRTI (Seyler and Bonatti, 1997, Tartarotti et al., 2002, Santi, 2014).

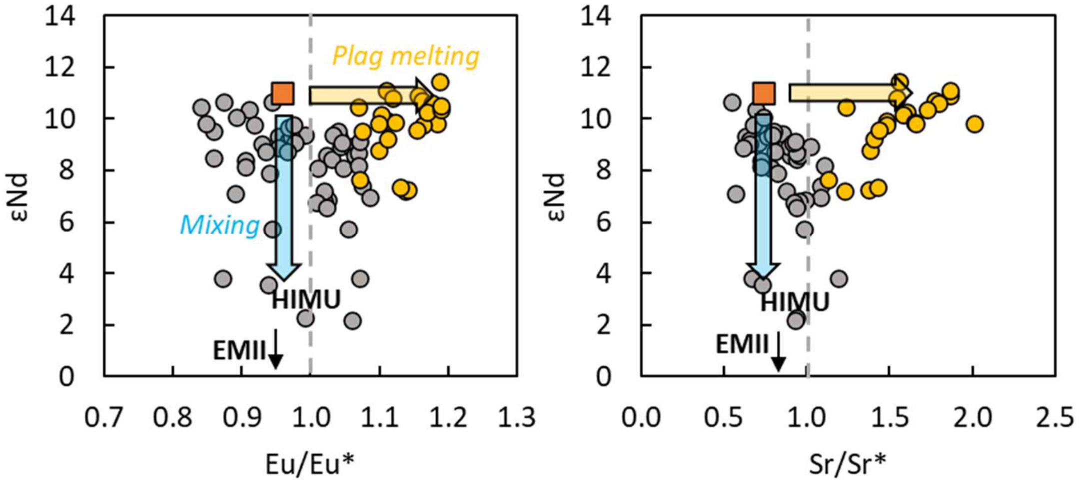

*Figure 6.6 - εNd vs. Eu/Eu* and Sr/Sr*. Symbols are the same as in figure 6.5. The blue arrows show the direction of mixing Dm-derived melts with enriched (HIMU- or EMII-derived) melts. The yellow arrow represents the effect of melting a Pl-bearing source. All other correlation between isotopes and Eu-Sr anomalies are reported in supplementary figure S6.1.*

Moreover, Eu-Sr bearing anomalies MORBs from the ERRTI being the closest to the DM pole in the various radiogenic isotopic spaces, we expect spinel field melting to result in N-MORB compositions. This is clearly not the case, excluding spinel field (disequilibrium) melting of a DM-type source as potential cause for the observed anomalies.

The third scenario concerns the assimilation of lower crustal rocks. This process has been discussed in a number of studies based on melt inclusions and bulk lava compositions. They show that melt-rock reaction frequently occurs between raising variably aggregated melts and cooler wall rocks in the lower crust (peridotites, gabbros or gabbroic crystal mushes) (Danyushevsky

2003, 2004, Gale, Laubier et al., 2013, Lissenberg and Dick, 2008, Yang et al., 2017, Yang et al., 2019). Partial assimilation of gabbroic rocks is here approximated by the olivine, plagioclase and clinopyroxene assimilation vectors in figure 6.2 (simple binary mixing between primitive MORB from Presnall and Hoover, 1987 and troctolitic gabbroic minerals, average compositions are from Brunelli et al., 2020). Resulting chemical assimilation trajectories cannot explain the measured compositions of the ERRTI basalts (Figure 6.2). Reaction and partial assimilation of a cumulate or crystal mush is hence unlikely to cause the Eu-Sr anomalies. This observation is possibly supported by the general lack of gabbroic samples from the ERRTI region, where a bimodal lithological distribution characterized by peridotite and basalts is common in almost all sampled sites close to the transform fault.

### A peculiar tectonic context allowing re-melting of plagio-impregnated mantle peridotites

Plagioclase-bearing peridotites have been reported from the ERRTI and testify for shallow depth (plagioclase field) melt impregnation of mantle peridotites mainly by melt-rock reaction processes between an ascending basaltic melt and the peridotite, resulting in crystallization of plagioclase (±ol ±cpx ±sp) (Seyler and Bonatti, 1997, Tartarotti et al., 2002, Santi, 2014) (Figure 6.7). Factors concurring to the generation of plagioclase impregnation at the ERRTI are the presence of a regional thermal low that significantly reduces the extent of mantle partial melting, and the presence of a thick lithosphere with a strong thermal gradient at its base preventing the small amount of melt produced to efficiently accumulate in magma chambers and reach the surface (Bonatti et al., 1996, 2001, Seyler and Bonatti, 1997, Tartarotti et al., 2002, Ligi et al., 2005). The melt is instead partially retained at the base of the brittle lithosphere (Seyler and Bonatti, 1997; Tartarotti et al., 2002, Santi, 2014). This thermal setting is similar to that present in the polar Gakkel ridge where similar Pl-impregnated peridotites and processes have been described (Laukert et al., 2014).

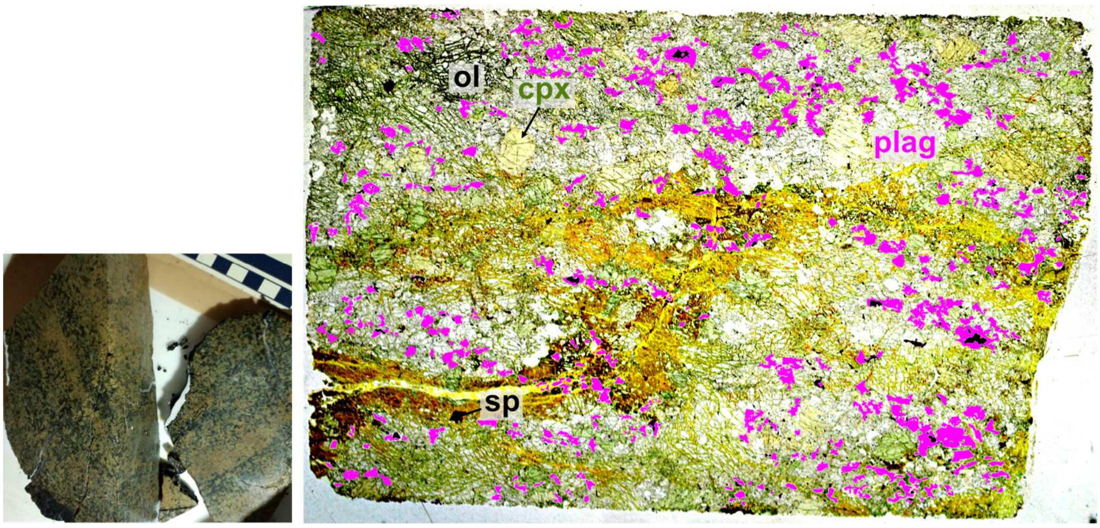

*Figure 6.7 - Plagioclase-impregnated peridotite (sample SMA1968-169) from the ERRTI recovered during the SMARTIES 2019 expedition (dive SMA1968, dark green triangle in figure 6.1). Plagioclases are coloured in pink for easier visibility. Pl: plagioclase; Ol: olivine; Cpx: clinopyroxene; Sp: spinel.*

Plagioclase-impregnated peridotites are widespread in the Eastern Romanche region but systematically recovered in the RTI massif (Bonatti et al., 2001). The geometry of this region has been revealed by high quality bathymetric data during the SMARTIES 2019 oceanographic expedition (R/V Pourquoi Pas?) (Figure 6.8a). A sequence of oblique subparallel ridges exhuming Pl-impregnated mantle rocks have been discovered facing the active detachment fault of a large core complex at the RTI (Figure 6.8). OCC spreading is asymmetric by nature (MacLeod et al., 2009) resulting in a progressive migration of the detachment termination, i.e., the active spreading line, away from the detachment, in a westward direction in the ERRTI geometry. This migration cannot be sustained far from the equilibrium line and results in the relocation of the ridge axis backwards with the consequent cut-off of the active detachment (MacLeod et al., 2009) (Figure 6.8b). The inactive chopped “nose” of the detachment is then dragged away by plate spreading. What is significant to the genesis of the Eu-Sr basalts, is the thermal resetting and consequent partial melting events occurring after the relocation of the active spreading line in correspondence of the new graben formed inside the old body of the, now extinct, core complex.

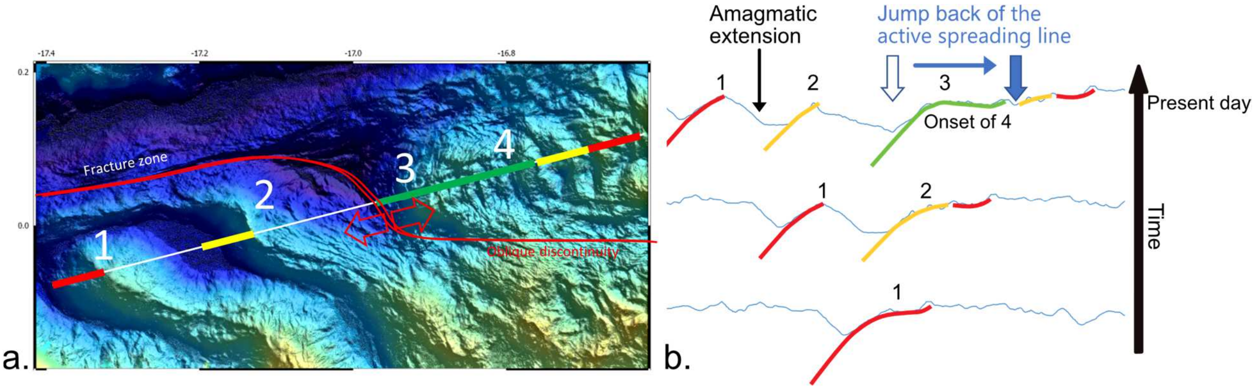

*Figure 6.8 - Schematic model of the Oceanic Core Complex breaking and ridge jump. (a) Bathymetric map showing the various parallel seamounts exhuming mantle rocks (1, 2 and 3). (b) Schematic cartoon showing the evolution of the OCC at the ERRTI. The red line represents the initial OCC. When the plate separation line extends too far in the western direction the OCC breaks and the extension is relocated backwards splitting the OCC detachment fault. An amagmatic extensional component stretches the exhumed crust. The process repeats three times forming the succession of oblique ridges. At present, a fourth breaking is occurring marked by a growing graben on the OCC shoulder.*

The ERRTI bathymetry revealed that three relocation events have occurred in the region. A fourth one is presently occurring and still in evolution (Figure 6.8) (Brunelli et al., in prep.). The lithospheric thickness in correspondence of the ERRTI can be approximated by the elastic thickness revealed by OBS data acquired during the SMARTIES oceanographic expedition (Yu et al., 2021). Seismic activity in the OCC region extends down to more than 15 km (Yu et al., 2021). The brittle/ductile transition between 15 to 20 km depth is the probable region where the impregnation of the mantle rocks occurs. The extensive rock sampling of the OCC done during several oceanographic expeditions reveals that these structures are made almost exclusively of variably impregnated Pl-bearing peridotites spotted by few occurrences of basalts (Bonatti et al., 2001, Tartarotti et al., 2002, Santi, 2014, SMARTIES cruise report). During the active OCC spreading, the upper termination of the mantle flow lines is partially dragged westward due to the westward migration of the active spreading line and extension of the OCC (Figure 6.9a) During this time the base of the lithosphere is partially impregnated by rising melts. Once the system reaches the limit to its asymmetry, the spreading line jumps back, and the mantle flow lines re-equilibrate to the vertical position (Figure 6.9b). This results in a re-heating of the base of the lithosphere because of the combined effects of the upwelling residual hot mantle and the local delivery of melts produced at depth (Figure 6.9b). The temperature increase is possibly enough to temporary induce partial melting of the impregnated Pl-bearing peridotite and the generation of a basalt with the peculiar major element composition and the Eu-Sr positive anomalies observed at the ERRTI. The shallow melting region can only persist over a short time representing a transient step to a complete resetting of the system with two possible evolutions: back to Pl-impregnation if a new OCC is formed or direct extrusion to the seafloor if a normal ridge axis develops.

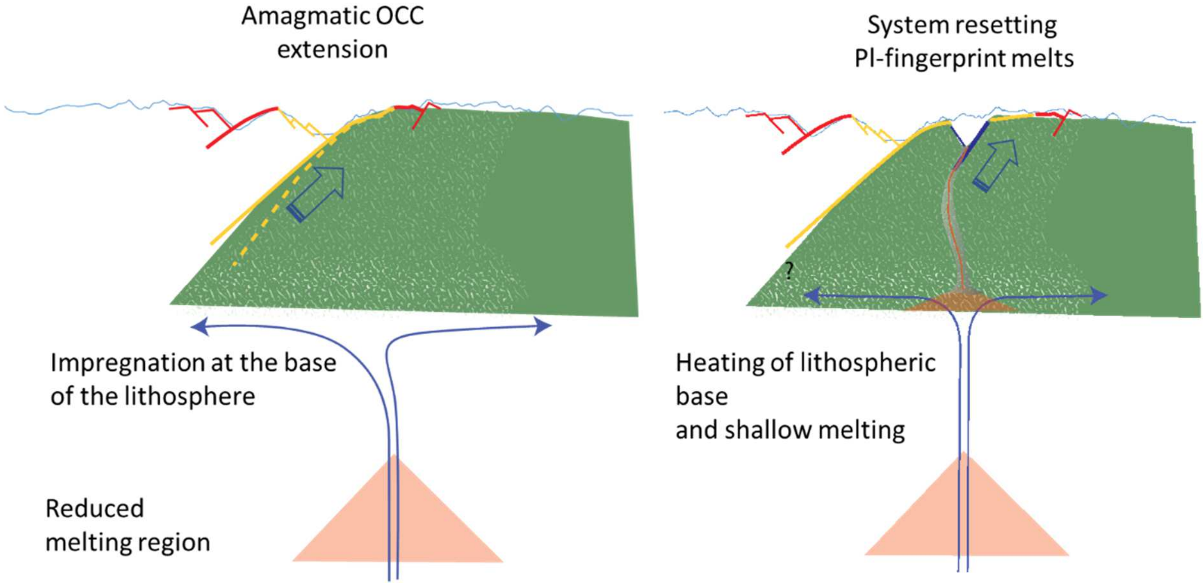

*Figure 6.9 - Cartoon showing the impregnation of the lithospheric mantle followed by melting of the plagioclase-bearing peridotite. The regional thermal minimum results in a thicken lithosphere and a shrunk melting region with low amount of melt delivered upward. Melts arriving in the cold lithospheric base react and impregnate the lithospheric mantle (left panel) forming the Pl-bearing peridotites systematically sampled in the ERRTI region. When the active spreading line relocates backward, the impregnated lithosphere is reheated (right panel) and partially molten generating melts with the Pl-fingerprint. The development of a shallow melting region is transient short-lived step in the tectonic evolution of the system.*

## Constraints on partial melting of Pl-impregnated mantle peridotites at the ERRTI

Partial melting of a Pl-equilibrated mantle peridotite is not extensively explored by experimental petrology, as mantle peridotite is mainly melting in the spinel and garnet stability fields. The few available studies present a variety of source fertility and relative incompatible element enrichment that makes it hard to draw consistent trend lines for progressive extents of partial melting (Jaques and Green, 1980; Fujii and Bougault, 1983; Till et al., 2012; Chalot-Prat et al., 2010 and 2013). Moreover, a number of these experimental runs explored extremely high degrees of melting, which are not consistent with our case study. High degrees of melting drag the silica contents to low values and MgO to very high contents (id.). Nonetheless, all runs with a low degree of melting (<15% F) show a compositional character coherent with what we observed in the ERRTI plagioclase-signature basalts and particularly the high Al/Ca ratio (e.g., Chalot-Prat et al., 2013).

In order to explore the evolution of Eu and Sr anomalies during partial melting, we test the compositional effects due to fractional melting of a Pl-bearing peridotite calculating the evolution of the residual mantle, instantaneous and partially aggregated melts (Figure 6.10). The small degrees of melting of the primary, sub-axial, melting region results in impregnating melts spanning a large range of enrichment (Bonatti et al., 1992; Ligi et al., 2005; Verhoest et al., in prep). Consistently the composition of the Pl-impregnated peridotites varies from depleted to relatively enriched members (Santi, 2014). We have therefore modelled the effects of fractional non-modal melting of different sources: (a) an enriched source where plagioclase is of metamorphic origin, i.e., a source where plagioclase is not of magmatic origin, hence a source bearing no bulk Eu-Sr anomalies even though the single minerals bear both positive (Pl) and negative (Cpx) anomalies; (b) an enriched source impregnated in the Pl-stability field, and (c) a depleted source similarly impregnated in the Pl- stability field. In the Pl-impregnated enriched and depleted sources, the addition of mineral phases in equilibrium with an exotic melt generates positive Eu-Sr anomalies of the bulk rock as measured by Santi (2014) on regional impregnated peridotites. Bulk compositions have been reconstructed based on average modal and mineral compositions from Tartarotti et al. (2002) and Santi (2014). Partition coefficients of olivine, orthopyroxene, clinopyroxene and spinel are from Brunelli et al. (2006) and those of plagioclase are from Sun et al. (2017), melting modes are from Falloon et al. (2008). Source mineral abundances are 64 % olivine, 22% orthopyroxene, 7% clinopyroxene, 5% plagioclase and 2% spinel.

Partial melting of a source bearing no Eu-Sr anomalies, i.e., with metamorphic plagioclase, represents the less favourable case for the generation of the Eu-Sr anomalies. The calculated incompatible element patterns of the aggregated melts show marked negative Eu and Sr anomalies (Figure 6.10, left column, orange lines). The preferential Eu-Sr partition into the residual plagioclase during the first degrees of melting persists during the progressive aggregation because of the diluted nature of the following instantaneous melt contributions. It is worth noting, however, that the relative enrichment of both Eu and Sr in the residual bulk rock steadily increases (Figure 6.10, left column, blue lines). As a result, positive Eu and Sr anomalies develop in the instantaneous melt after ~ 6% F (Figure 6.10, left column, yellow lines). This behaviour can be readily represented by the variation of $Sr/Ce_N$ and $Eu/Sm_N$ ratios (CI chondrite normalised) with respect to the degree of melting F (insets in the lower raw of Figure 6.10). In the residual source both chondrite normalised ratios are >1 immediately after the first degree of melting, while the aggregated melt never crosses the positive anomaly line (=1).

Melting a variably enriched source but with magmatic plagioclase, develops positive Eu-Sr anomalies in the aggregated melt after 7% F starting with and enriched source and after 3% F starting with a depleted source (Figure 6.10, central and right columns, orange lines). The anomalies appear in the instantaneous melts only after 2% F and 1% F respectively. The presence of positive anomalies in the bulk source generated by the impregnation process boosts the Eu-Sr accumulation in the residue at values that are easily transferred to the instantaneous and aggregated melts (Figure 6.10, central and right columns). At each step of melting a higher proportion of Sr and Eu are transferred into the melt compared to the adjacent elements Ce and Sm.

Model Eu and Sr anomalies of the aggregated melt calculated from the enriched impregnated source fit the ERRTI samples at about 3% F. The depleted impregnated source model reproduces the Eu/Eu* and Sr/Sr* for an aggregated melt at about 4%-8% F (Figure 6.5).

Model Eu and Sr anomalies are plotted in Figure 6.5 and compared with the ERRTI basalts here studied. Aggregated melts (light lines) and instantaneous melts trends (dark lines) are plotted together for the three model sources. It clearly appears that melting a source with no starting Eu-Sr anomaly, i.e., bearing metamorphic plagioclase, does not reproduce the observed ERRTI variability. In contrast, the inherited Eu-Sr anomalies measured in the regional impregnated peridotites allow compositional trends to cross the field of the ERRTI Eu-Sr positive bearing anomalies basalts. The required degrees of melting are reasonably low, as expected in a tectonic setting dominated by amagmatic extension and a thick cold axial lithosphere. However, it appears that these compositions are possibly the result of the extraction of near-instantaneous melts or a mixing of melts with different but low, degree of aggregation. We stress that extraction of near-instantaneous melts in this setting is not unlikely because of the shallow depth of the shallow melting region. The extreme and deep tectonics related to the OCC breakout and formation of a new graben in an old-cold lithosphere result in deep faulting interacting with magma accumulation. This represents an extreme case of the general enhanced tectonic interaction between magma accumulation and normal faulting at the ridge tips, as described for the Vema Eastern Ridge Transform Intersection (Brunelli et al., 2020). At the ERRTI, however, lacking any evidence of gabbroic rocks, an extremely efficient and rapid extraction must be hypothesized possibly accounting for the tectonic-induced extraction of melt fractions not completely aggregated.

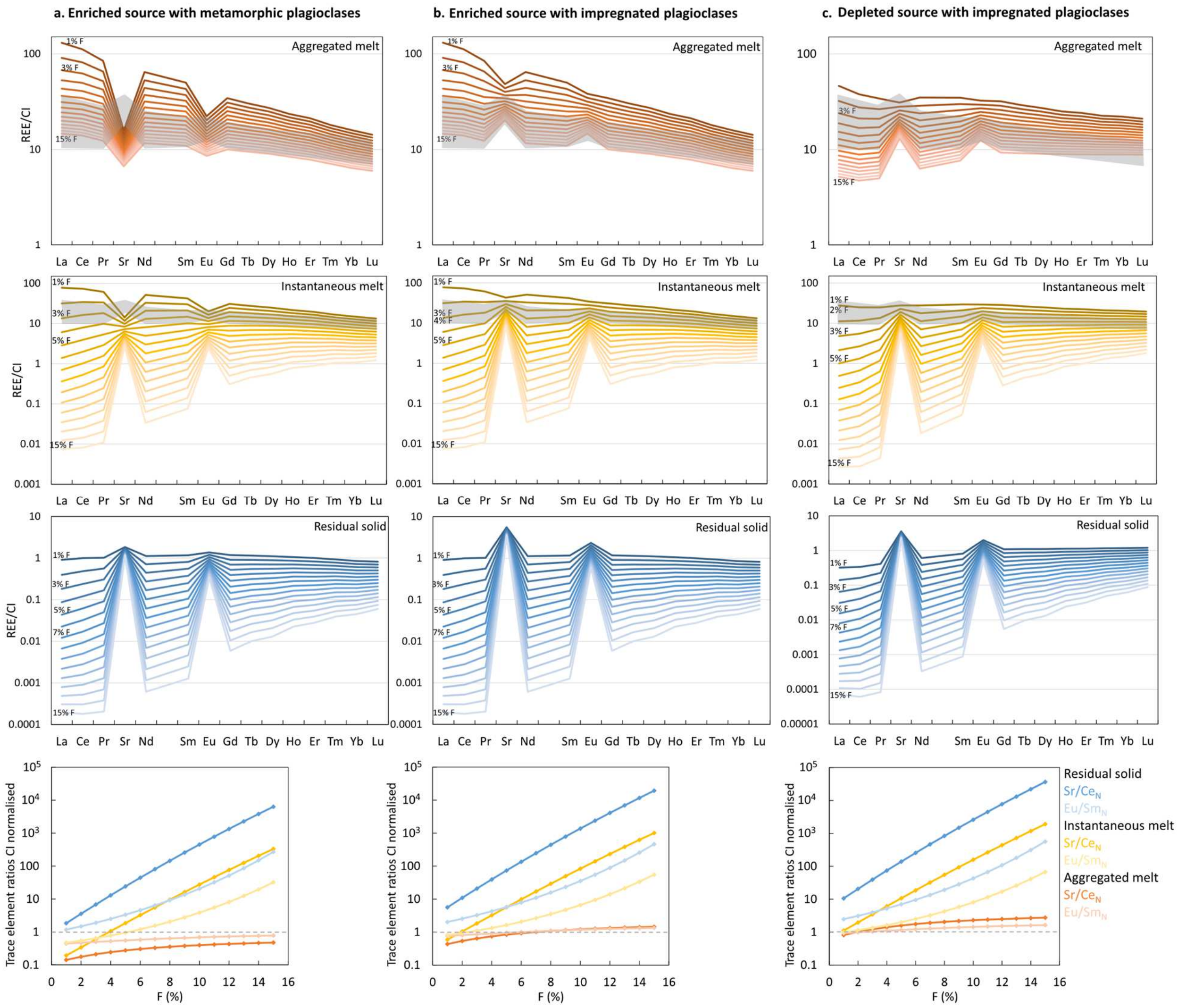

*Figure 6.10 - Evolution of the trace element patterns during non-modal fractional melting of a Pl-bearing peridotite. Orange, yellow and blue lines represent respectively aggregated melt, instantaneous melt and residual solid calculated from three sources: (a) Enriched source with metamorphic plagioclases; (b) Enriched source with impregnated plagioclases and (c) Depleted*

*source with impregnated plagioclases. See text and caption of figure 6.5. Grey areas represent the range of the ERRTI MORBs studied here.*

Re-melting of an impregnated mantle residue also accounts for the peculiar isotopic signature of the ERRTI basalts here studied. Indeed, a large isotopic variability has been described at the ERRTI due to the regional low degrees of melting. Low mantle potential temperature only allows melting of the low solidus mantle components, whose isotopic signatures show up in the erupted, extremely enriched, basalts (Verhoest et al., in prep.). Mantle residua are therefore closer to the DMM end-member being the low solidus heterogeneities extracted first. In the ERRTI setting, the low amount of melt produced in the primary melting region may bear an enriched signature. However, its rising is slowed in the cold regime driven by the thick cold overlying lithosphere. We stress that enhanced melt/rock reaction and melt re-distribution during impregnation results in a general isotopic homogenisation, an inverse process than the un-blending extraction observed in the region leading to the separation of isolated mantle components. This process may explain why the isotopic fingerprint of the MORBs bearing Eu-Sr positive anomalies from the ERRTI is generally more homogeneous and closer to the DMM pole with respect to all other MORBs erupted in the region (figure 6.4).

However, shallow melting has a transient character because occurring during the evolution of the system toward a new equilibrium state, either the formation of a new OCC or the evolution toward a “normal” axial valley. This transitory state is a possible explication why these basalts are found close to variably enriched MORBs showing no Eu-Sr anomaly (figure 6.1).

## Conclusions

A group of MORBs from the ERRTI show peculiar compositions with high $SiO_2$ and $Al_2O_3$ and low $TiO_2$, CaO and FeO content compared to the global MAR MORBs (Figure 6.2). They also exhibit positive Sr and Eu anomalies suggesting a role for plagioclase during melting or melt extraction.

Positive Eu-Sr anomalies are generally associated to the presence of recycled heterogeneities in the mantle source, disequilibrium melting due to fast Eu-Sr diffusion from pyroxenes during partial melting or melt reaction with lower crustal rocks. None of these processes is likely to occur at the ERRTI that instead is characterized by a peculiar tectonic setting that allows melting of Pl-impregnated peridotites. Plagioclase-bearing peridotites, generated by melt-rock reaction and retention, are indeed widespread in the ERRTI region (Seyler and Bonatti, 1997, Tartarotti et al., 2002, Santi, 2014) (Figure 6.7).

The ERRTI tectonics present a large OCC that repeatedly breaks, relocating the ridge axis on its shoulders and generating a local re-heating of the base of the lithosphere where Pl-impregnation has occurred during OCC extension. We propose that during the backward active ridge relocation, the Pl-impregnated lower lithosphere peridotites partially melt due to local re-heating.

Fractional non-modal melting of variably enriched plagioclase-bearing peridotitic sources account for the observed Eu-Sr anomalies under the condition that the plagioclase is of magmatic origin, i.e., the bulk rock bears positive Eu-Sr anomalies inherited during the magmatic impregnation. Metamorphic equilibration of spinel bearing peridotites at low pressure, results in rocks with no original Eu-Sr anomalies that hardly develop coupled positive anomalies during partial melting. Instantaneous melts generated by an enriched impregnated source can reproduce the Eu-Sr anomalies at very low degrees of melting (3% F). Aggregated melts from the depleted impregnated source acquire the Eu-Sr anomalies after 3% F, and fit the ERRTI compositions between 4%-8% F.

## References

Anderson, O.E., Jackson, M.G., Rose-Koga, E.F., Marske, J.P., Peterson, M.E., Price, A.A., Byerly, B.L., Reinhard, A.A., 2021. *Testing the Recycled Gabbro Hypothesis for the Origin of "Ghost Plagioclase" Melt Signatures Using 87 Sr/ 86 Sr of Individual Olivine-Hosted Melt Inclusions From Hawai'i.* Geochem. Geophys. Geosyst. 22 (4), e2020GC009260. doi:10.1029/2020GC009260.

Asimow, P.D., Dixon, J.E., Langmuir, C.H., 2004. *A hydrous melting and fractionation model for mid-ocean ridge basalts: Application to the Mid-Atlantic Ridge near the Azores.* Geochem. Geophys. Geosyst. 5 (1). doi:10.1029/2003GC000568.

Barrat, J.A., Zanda, B., Moynier, F., Bollinger, C., Liorzou, C., Bayon, G., 2012. *Geochemistry of CI chondrites: Major and trace elements, and Cu and Zn Isotopes.* Geochimica et Cosmochimica Acta 83, 79–92. doi:10.1016/j.gca.2011.12.011.

Blichert-Toft, J., Chauvel, C., Albarède, F., 1997. *Separation of Hf and Lu for high-precision isotope analysis of rock samples by magnetic sector-multiple collector ICP-MS.* Contrib Mineral Petrol 127 (3), 248–260. doi:10.1007/s004100050278.

Bonatti, E., Brunelli, D., Fabretti, P., Ligi, M., Asunta Portaro, R., Seyler, M., 2001. *Steady-state creation of crust-free lithosphere at cold spots in mid-ocean ridges.* Geol 29 (11), 979. doi:10.1130/0091-7613(2001)029<0979:SSCOCF>2.0.CO;2.

Bonatti, E., 1996. *Anomalous opening of the Equatorial Atlantic due to an equatorial mantle thermal minimum.* Earth and Planetary Science Letters 143 (1-4), 147–160. doi:10.1016/0012-821X(96)00125-2.

Bonatti, E., Peyve, A., Kepezhinskas, P., Kurentsova, N., Seyler, M., Skolotnev, S., Udintsev, G., 1992. *Upper mantle heterogeneity below the Mid-Atlantic Ridge, 0°–15°N.* J. Geophys. Res. 97 (B4), 4461. doi:10.1029/91JB02838.

Borghini, G., Fumagalli, P., Rampone, E., 2010. *The Stability of Plagioclase in the Upper Mantle: Subsolidus Experiments on Fertile and Depleted Lherzolite.* Journal of Petrology 51 (1-2), 229–254. doi:10.1093/petrology/egp079.

Brunelli, D., Sanfilippo, A., Bonatti, E., Skolotnev, S., Escartin, J., Ligi, M., Ballabio, G., Cipriani, A., 2020. *Origin of oceanic ferrodiorites by injection of nelsonitic melts in gabbros at the Vema Lithospheric Section, Mid Atlantic Ridge.* Lithos 368-369, 105589. doi:10.1016/j.lithos.2020.105589.

Brunelli, D., Seyler, M., Cipriani, A., Ottolini, L., Bonatti, E., 2006. *Discontinuous Melt Extraction and Weak Refertilization of Mantle Peridotites at the Vema Lithospheric Section (Mid-Atlantic Ridge).* Journal of Petrology 47 (4), 745–771. doi:10.1093/petrology/egi092.

Chalot-Prat, F., Falloon, T.J., Green, D.H., Hibberson, W.O., 2013. *Melting of plagioclase+spinel lherzolite at low pressures (0.5GPa): An experimental approach to the evolution of basaltic melt during mantle refertilisation at shallow depths.* Lithos 172-173, 61–80. doi:10.1016/j.lithos.2013.03.012.

Chalot-Prat, F., Falloon, T.J., Green, D.H., Hibberson, W.O., 2010. *An Experimental Study of Liquid Compositions in Equilibrium with Plagioclase + Spinel Lherzolite at Low Pressures (0.75 GPa).* J Petrology 51 (11), 2349–2376. doi:10.1093/petrology/egq060.

Chauvel, C., Bureau, S., Poggi, C., 2011. *Comprehensive Chemical and Isotopic Analyses of Basalt and Sediment Reference Materials.* Geostandards and Geoanalytical Research 35 (1), 125–143. doi:10.1111/j.1751-908X.2010.00086.x.

Chauvel, C., Hémond, C., 2000. *Melting of a complete section of recycled oceanic crust: Trace element and Pb isotopic evidence from Iceland.* Geochem. Geophys. Geosyst. 1 (2). doi:10.1029/1999GC000002.

Danyushevsky, L.V., Leslie, R.A.J., Crawford, A.J., Durance, P., 2004. *Melt Inclusions in Primitive Olivine Phenocrysts: the Role of Localized Reaction Processes in the Origin of Anomalous Compositions.* Journal of Petrology 45 (12), 2531–2553. doi:10.1093/petrology/egh080.

Danyushevsky, L.V., Perfit, M.R., Eggins, S.M., Falloon, T.J., 2003. *Crustal origin for coupled 'ultra-depleted' and 'plagioclase' signatures in MORB olivine-hosted melt inclusions: evidence from the Siqueiros Transform Fault, East Pacific Rise.* Contrib Mineral Petrol 144 (5), 619–637. doi:10.1007/s00410-002-0420-3.

Falloon, T.J., Green, D.H., Danyushevsky, L.V., McNeill, A.W., 2008. *The Composition of Near-solidus Partial Melts of Fertile Peridotite at 1 and 1·5 GPa: Implications for the Petrogenesis of MORB.* Journal of Petrology 49 (4), 591–613. doi:10.1093/petrology/egn009.

Fujii, T., Bougault, H., 1983. *Melting relations of a magnesian abyssal tholeiite and the origin of MORBs.* Earth and Planetary Science Letters 62 (2), 283–295. doi:10.1016/0012-821X(83)90091-2.

Gale, A., Dalton, C.A., Langmuir, C.H., Su, Y., Schilling, J.-G., 2013. *The mean composition of ocean ridge basalts.* Geochem. Geophys. Geosyst. 14 (3), 489–518. doi:10.1029/2012GC004334.

Gale, A., Laubier, M., Escrig, S., Langmuir, C.H., 2013. *Constraints on melting processes and plume-ridge interaction from comprehensive study of the FAMOUS and North Famous segments, Mid-Atlantic Ridge.* Earth and Planetary Science Letters 365, 209–220. doi:10.1016/j.epsl.2013.01.022.

Hofmann, A.W., Jochum, K.P., 1996. *Source characteristics derived from very incompatible trace elements in Mauna Loa and Mauna Kea basalts, Hawaii Scientific Drilling Project.* J. Geophys. Res. Solid Earth 101 (B5), 11831–11839. doi:10.1029/95JB03701.

Jaques, A.L., Green, D.H., 1980. *Anhydrous melting of peridotite at 0.15 Kb pressure and the genesis of tholeiitic basalts.* Contrib Mineral Petrol 73 (3), 287–310. doi:10.1007/BF00381447.

Jenner, F.E., St. O'Neill, H.C., 2012. *Analysis of 60 elements in 616 ocean floor basaltic glasses.* Geochem. Geophys. Geosyst. 13 (2). doi:10.1029/2011GC004009.

Kay, R., Hubbard, N.J., Gast, P.W., 1970. Chemical characteristics and origin of oceanic ridge volcanic rocks 1. J. Geophys. Res. 75 (8), 1585–1613. doi:10.1029/JB075i008p01585.

Laubier, M., Gale, A., Langmuir, C.H., 2012. *Melting and Crustal Processes at the FAMOUS Segment (Mid-Atlantic Ridge): New Insights from Olivine-hosted Melt Inclusions from Multiple Samples.* Journal of Petrology 53 (4), 665–698. doi:10.1093/petrology/egr075.

Laukert, G., Handt, A. von der, Hellebrand, E., Snow, J.E., Hoppe, P., Klügel, A., 2014. *High-pressure Reactive Melt Stagnation Recorded in Abyssal Pyroxenites from the Ultraslow-spreading Lena Trough, Arctic Ocean.* J Petrology 55 (2), 427–458. doi:10.1093/petrology/egt073.

Le Voyer, M., Cottrell, E., Kelley, K.A., Brounce, M., Hauri, E.H., 2015. *The effect of primary versus secondary processes on the volatile content of MORB glasses: An example from the equatorial Mid-Atlantic Ridge (5°N–3°S).* J. Geophys. Res. Solid Earth 120 (1), 125–144. doi:10.1002/2014JB011160.

Ligi, M., Bonatti, E., Cipriani, A., Ottolini, L., 2005. *Water-rich basalts at mid-ocean-ridge cold spots.* Nature 434 (7029), 66–69. doi:10.1038/nature03264.

Lissenberg, C.J., Dick, H.J., 2008. *Melt–rock reaction in the lower oceanic crust and its implications for the genesis of mid-ocean ridge basalt.* Earth and Planetary Science Letters 271 (1-4), 311–325. doi:10.1016/j.epsl.2008.04.023.

MacLeod, C.J., Searle, R.C., Murton, B.J., Casey, J.F., Mallows, C., Unsworth, S.C., Achenbach, K.L., Harris, M., 2009. *Life cycle of oceanic core complexes.* Earth and Planetary Science Letters 287 (3-4), 333–344. doi:10.1016/j.epsl.2009.08.016.

Niu, Y., Gilmore, T., Mackie, S., Greig, A., Bach, W. 2002. *Mineral chemistry, whole-rock compositions, and petrogenesis of leg 176 gabbros: Data and discussion*, in: , Proceedings of the Ocean Drilling Program, Scientific Results, vol. 176.

Niu, Y., O'Hara, M.J., 2009. *MORB mantle hosts the missing Eu (Sr, Nb, Ta and Ti) in the continental crust: New perspectives on crustal growth, crust–mantle differentiation and chemical structure of oceanic upper mantle.* Lithos 112 (1-2), 1–17. doi:10.1016/j.lithos.2008.12.009.

Presnall, D.C., Hoover, J.D., 1987. *High pressure phase equilibrium constraints on the origin of mid-ocean ridge basalts.* Geochem. Soc. Spec. Publ., Magmatic Processes : Physicochemical Principles 1, 75–89.

Puchelt, H., Emmermann, R., 1977. *REE characteristics of ocean floor basalts from the MAR 37 N (Leg 37 DSDP).* Contrib Mineral Petrol 62 (1), 43–52. doi:10.1007/BF00371026.

Richard, P., Shimizu, N., Allègre, C.J., 1976. *143Nd/146Nd, a natural tracer: an application to oceanic basalts.* Earth and Planetary Science Letters 31 (2), 269–278. doi:10.1016/0012-821X(76)90219-3.

Salters, V.J.M., Stracke, A., 2004. *Composition of the depleted mantle.* Geochem. Geophys. Geosyst. 5 (5). doi:10.1029/2003GC000597.

Santi, D., 2014. *Structure and petrogenesis of plagioclase-bearing mantle peridotites from the Romanche Transform (Equatorial Atlantic Ocean)*, 197 pp. PhD.

Schilling, J.G., Ruppel, C., Davis, A.N., McCully, B., Tighe, S.A., Kingsley, R.H., Linc, J., 1995. *Thermal structure of the mantle beneath the equatorial Mid-Atlantic Ridge: Inferences from the spatial variation of dredged basalt glass compositions.* Journal of Geophysical Research 100 (B7), 10,057-10,076.

Schilling, J.-G., Anderson, R.N., Vogt, P., 2022. *Rare earth, Fe and Ti variations along the Galapagos spreading centre, and their relationship to the Galapagos mantle plume.* Nature Publishing Group. https://www.nature.com/articles/261108a0#citeas. Accessed 30 June 2022. doi:1976.

Schilling, J.-G., Hanan, B.B., McCully, B., Kingsley, R.H., Fontignie, D., 1994. *Influence of the Sierra Leone mantle plume on the equatorial Mid-Atlantic Ridge: A Nd-Sr-Pb isotopic study.* Journal of Geophysical Research 99 (B6), 12,005-12,028.

Schilling, J.-G., Anderson, R.N., Vogt, P., 1976. *Rare earth, Fe and Ti variations along the Galapagos spreading centre, and their relationship to the Galapagos mantle plume*. Nature 261 (5556), 108–113. doi:10.1038/261108a0.

Seyler, M., Bonatti, E., 1997. *Regional-scale melt-rock interaction in lherzolitic mantle in the Romanche Fracture Zone (Atlantic Ocean).* Earth and Planetary Science Letters 146, 273–287.

Sobolev, A.V., Hofmann, A.W., Nikogosian, I.K., 2000. *Recycled oceanic crust observed in 'ghost plagioclase' within the source of Mauna Loa lavas.* Nature 404 (6781), 986–990. doi:10.1038/35010098.

Sun, C., Graff, M., Liang, Y., 2017. *Trace element partitioning between plagioclase and silicate melt: The importance of temperature and plagioclase composition, with implications for terrestrial and lunar magmatism*. Geochimica et Cosmochimica Acta 206, 273–295. doi:10.1016/j.gca.2017.03.003.

Sun, S., McDonough, W.F., 1989. *Chemical and isotopic systematics of oceanic basalts: implications for mantle composition and processes.* Geological Society, London, Special Publications 42 (1), 313–345. doi:10.1144/GSL.SP.1989.042.01.19.

Sushchevskaya, N.M., Bonatti, E., Peive, A.A., Kamenetskii, V.S., Belyatskii, B.V., Tsekhonya, T.I., Kononkova, N.N., 2002. *Heterogeneity of rift magmatism in the equatorial province of the mid-atlantic ridge (15°N to 3°S).* Geochemistry International 40 (1), 26–50.

Tang, M., McDonough, W.F., Ash, R.D., 2017. *Europium and strontium anomalies in the MORB source mantle.* Geochimica et Cosmochimica Acta 197, 132–141. doi:10.1016/j.gca.2016.10.025.

Tartarotti, P., Susini, S., Nimis, P., Ottolini, L., 2002. *Melt migration in the upper mantle along the Romanche Fracture Zone (Equatorial Atlantic).* Lithos 63, 125–149.

Till, C.B., Grove, T.L., Krawczynski, M.J., 2012. *A melting model for variably depleted and enriched lherzolite in the plagioclase and spinel stability fields*. J. Geophys. Res. Solid Earth 117 (B6), n/a-n/a. doi:10.1029/2011JB009044.

Verhoest, L., Cipriani, A., Hémond, C., Nonnotte, P., Maia, M., Brunelli, D. *Unblended MORBs at a Mid-Ocean Ridge cold spot.* in prep.

Willbold, M., Stracke, A., 2006. *Trace element composition of mantle end-members: Implications for recycling of oceanic and upper and lower continental crust*. Geochem. Geophys. Geosyst. 7 (4). doi:10.1029/2005GC001005.

Yang, A.Y., Wang, C., Liang, Y., Lissenberg, C.J., 2019. *Reaction Between Mid-Ocean Ridge Basalt and Lower Oceanic Crust: An Experimental Study.* Geochem. Geophys. Geosyst. 20 (9), 4390–4407. doi:10.1029/2019GC008368.

Yang, A.Y., Zhao, T.-P., Zhou, M.-F., Deng, X.-G., 2017. *Isotopically enriched N-MORB: A new geochemical signature of off-axis plume-ridge interaction—A case study at 50°28'E, Southwest Indian Ridge.* J. Geophys. Res. Solid Earth 122 (1), 191–213. doi:10.1002/2016JB013284.

Yaxley, G.M., Sobolev, A.V., 2007. *High-pressure partial melting of gabbro and its role in the Hawaiian magma source.* Contrib Mineral Petrol 154 (4), 371–383. doi:10.1007/s00410-007-0198-4.

Yu, Z., Singh, S.C., Gregory, E.P.M., Maia, M., Wang, Z., Brunelli, D., 2021. *Semibrittle seismic deformation in high-temperature mantle mylonite shear zone along the Romanche transform fault*. Science advances 7 (15). doi:10.1126/sciadv.abf3388.

## Supplementary material

### Figure

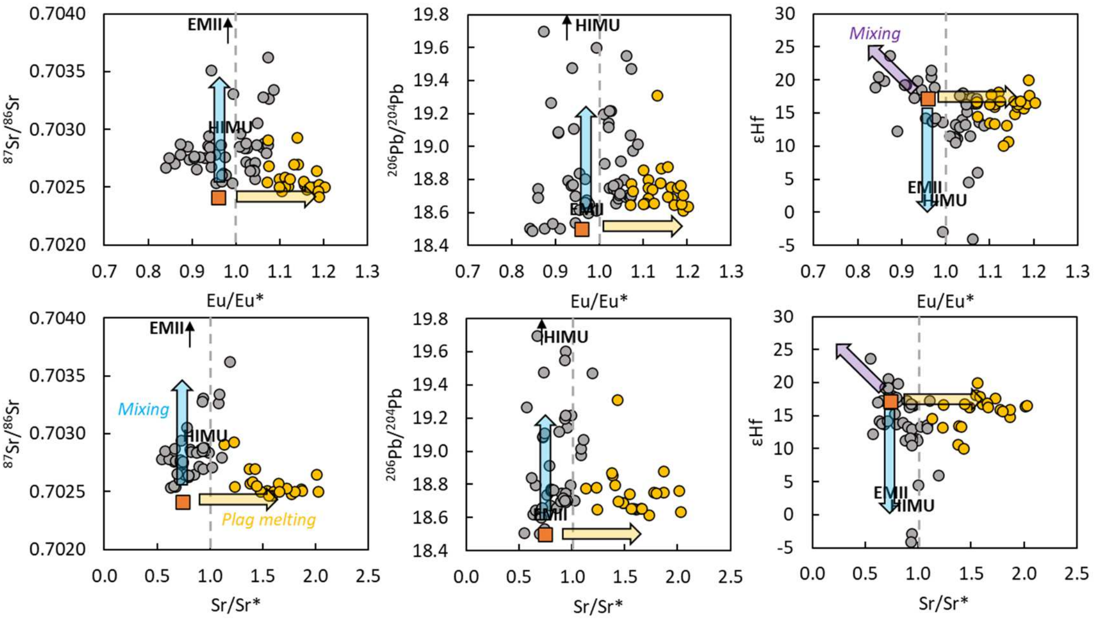

*Figure S 6.1 - Correlation between the isotopes ratios and Eu/Eu* and Sr/Sr*. Symbols are the same as in figure 6.5. The blues arrow show the direction of mixing DMM-derived melts with enriched (HIMU- or EMII-derived) melts. The yellow arrow represents the effect of melting a Pl-bearing source.*

### Tables

## *Table S6.1 - Sr-Nd-Pb-Hf isotope ratios*

| Sample | Lat | Long | | $^{87}Sr/^{86}Sr$ | 2σ | $^{143}Nd/^{144}Nd$ | 2σ | εNd | $^{206}Pb/^{204}Pb$ | 2σ | $^{207}Pb/^{204}Pb$ | 2σ | $^{208}Pb/^{204}Pb$ | 2σ | $^{176}Hf/^{177}Hf$ | 2σ | εHf |
|---|---|---|---|---|---|---|---|---|---|---|---|---|---|---|---|---|---|
| SMA1970-203C | 0.007 | -16.789 | M/P | 0.702575 | 0.000008 | 0.513088 | 0.000007 | 8.8 | 18.859 | 0.001 | 15.557 | 0.001 | 38.358 | 0.002 | 0.283153 | 0.000013 | 13.5 |
| SMA1970-204 | 0.007 | -16.789 | M/P | 0.702587 | 0.000007 | 0.513112 | 0.000006 | 9.2 | 18.799 | 0.001 | 15.550 | 0.001 | 38.298 | 0.002 | 0.283150 | 0.000011 | 13.4 |
| SMA1974-265 | -0.035 | -16.454 | M/P | 0.702911 | 0.000007 | 0.513031 | 0.000007 | 7.7 | 18.776 | 0.001 | 15.588 | 0.001 | 38.415 | 0.003 | 0.283184 | 0.000056 | 14.6 |
| SMA1974-268 | -0.035 | -16.454 | M/P | 0.702929 | 0.000005 | 0.513008 | 0.000006 | 7.2 | 18.783 | 0.003 | 15.593 | 0.002 | 38.428 | 0.006 | 0.283146 | 0.000010 | 13.2 |
| SMA1975-290 | -0.076 | -16.464 | M/P | 0.702697 | 0.000007 | 0.513010 | 0.000009 | 7.3 | | | | | | | 0.283075 | 0.000062 | 10.7 |
| SMA1975-290 Dup | | | M/P | 0.702703 | 0.000005 | 0.513016 | 0.000007 | 7.4 | 18.869 | 0.001 | 15.617 | 0.001 | 38.587 | 0.002 | 0.283080 | 0.000013 | 10.9 |
| SMA1975-294 | -0.075 | -16.462 | M/P | 0.702701 | 0.000006 | 0.513014 | 0.000006 | 7.3 | 19.312 | 0.001 | 15.603 | 0.001 | 38.754 | 0.003 | 0.283058 | 0.000011 | 10.1 |
| SMA1975-301 | -0.071 | -16.458 | M/P | 0.702524 | 0.000007 | 0.513198 | 0.000008 | 10.9 | 18.879 | 0.001 | 15.538 | 0.001 | 38.320 | 0.003 | 0.283192 | 0.000008 | 14.8 |
| SMA1975-302 | -0.070 | -16.457 | M/P | 0.702507 | 0.000006 | 0.513208 | 0.000017 | 11.1 | 18.753 | 0.002 | 15.494 | 0.002 | 38.165 | 0.005 | 0.283222 | 0.000017 | 15.9 |
| SMA1975-305 | -0.068 | -16.455 | M/P | 0.702481 | 0.000008 | 0.513186 | 0.000009 | 10.7 | | | | | | | 0.283222 | 0.000018 | 15.9 |
| SMA1975-305 Dup | | | M/P | 0.702523 | 0.000007 | 0.513182 | 0.000007 | 10.6 | 18.754 | 0.001 | 15.559 | 0.001 | 38.281 | 0.002 | 0.283213 | 0.000005 | 15.6 |
| SMA1975-307 | -0.065 | -16.455 | M/P | 0.702548 | 0.000008 | 0.513175 | 0.000010 | 10.5 | 18.649 | 0.001 | 15.534 | 0.001 | 38.190 | 0.002 | 0.283244 | 0.000012 | 16.7 |
| SMA1975-308 | -0.065 | -16.455 | M/P | 0.702504 | 0.000012 | 0.513183 | 0.000008 | 10.6 | 18.750 | 0.001 | 15.526 | 0.001 | 38.213 | 0.002 | 0.283217 | 0.000009 | 15.7 |
| SMA1976-310 | -0.004 | -16.657 | M/P | 0.702647 | 0.000008 | 0.513140 | 0.000005 | 9.8 | 18.765 | 0.001 | 15.537 | 0.001 | 38.220 | 0.003 | 0.283237 | 0.000031 | 16.4 |
| SMA1976-312 | -0.004 | -16.655 | M/P | 0.702511 | 0.000007 | 0.513192 | 0.000005 | 10.8 | 18.742 | 0.001 | 15.542 | 0.001 | 38.242 | 0.002 | 0.283287 | 0.000027 | 18.2 |
| SMA1980-378 | 0.007 | -16.757 | M/P | 0.702515 | 0.000008 | 0.513141 | 0.000006 | 9.8 | 18.689 | 0.001 | 15.571 | 0.001 | 38.277 | 0.002 | 0.283269 | 0.000004 | 17.6 |
| SMA1980-378 Dup | | | M/P | 0.702504 | 0.000004 | 0.513147 | 0.000007 | 9.9 | | | | | | | 0.283234 | 0.000011 | 16.3 |
| SMA1980-379 | 0.007 | -16.757 | M/P | 0.702502 | 0.000005 | 0.513140 | 0.000006 | 9.8 | 18.689 | 0.002 | 15.540 | 0.002 | 38.220 | 0.005 | 0.283233 | 0.000014 | 16.3 |
| SMA1980-381 | 0.006 | -16.752 | M/P | 0.702553 | 0.000007 | 0.513128 | 0.000008 | 9.6 | 18.698 | 0.002 | 15.547 | 0.002 | 38.245 | 0.004 | 0.283247 | 0.000027 | 16.8 |
| SMA1980-383 | 0.003 | -16.750 | M/P | 0.702501 | 0.000010 | 0.513165 | 0.000006 | 10.3 | 18.649 | 0.001 | 15.536 | 0.001 | 38.173 | 0.003 | 0.283247 | 0.000028 | 16.8 |
| SMA1980-385 | | | M/P | 0.702500 | 0.000007 | 0.513157 | 0.000003 | 10.1 | 18.657 | 0.001 | 15.565 | 0.001 | 38.231 | 0.002 | 0.283284 | 0.000006 | 18.1 |
| SMA1980-385 Dup | -0.001 | -16.750 | M/P | 0.702468 | 0.000006 | 0.513158 | 0.000005 | 10.1 | | | | | | | 0.283277 | 0.000011 | 17.9 |
| SMA1980-386 | -0.003 | -16.749 | M/P | 0.702528 | 0.000009 | 0.513169 | 0.000030 | 10.4 | 18.614 | 0.001 | 15.537 | 0.001 | 38.133 | 0.002 | 0.283273 | 0.000067 | 17.7 |
| SMA1980-387 | -0.005 | -16.747 | M/P | 0.702574 | 0.000013 | 0.513143 | 0.000011 | 9.9 | 18.658 | 0.001 | 15.544 | 0.001 | 38.175 | 0.003 | 0.283249 | 0.000012 | 16.9 |
| SMA1980-388 | -0.006 | -16.747 | M/P | 0.702505 | 0.000007 | 0.513142 | 0.000034 | 9.8 | 18.654 | 0.002 | 15.541 | 0.001 | 38.169 | 0.003 | 0.283234 | 0.000022 | 16.3 |
| SMA1980-389 | -0.007 | -16.746 | M/P | 0.702501 | 0.000010 | | | | 18.637 | 0.002 | 15.536 | 0.001 | 38.123 | 0.003 | 0.283241 | 0.000012 | 16.6 |
| SMA1981-405 | 0.030 | -16.600 | M/P | 0.702469 | 0.000007 | 0.513225 | 0.000007 | 11.4 | 18.653 | 0.001 | 15.519 | 0.001 | 38.181 | 0.003 | 0.283337 | 0.000016 | 20.0 |
| S1644 | 0.090 | -16.709 | L | 0.702685 | | 0.513127 | | 9.5 | 18.729 | | 15.641 | | 38.595 | | | | |
| S1669 | 0.088 | -16.596 | L | 0.702420 | | 0.513176 | | 10.5 | 18.705 | | 15.585 | | 38.336 | | | | |

*The letters correspond to the place where the ratios have been analysed: M/P: Pb-Sr chemical separation and analyses made at DSCG and at CIGS Modena (HR-ICP-MS), Nd and Hf chemical separation and analyses made at GO Plouzané (respectively TIMS and HR-ICP-MS); L: previously existing data analysed at Lamont Doherty Earth Observatory (Cipriani, A.).*

## *Table S6.2 - Major elements measured with EMPA*

| **Sample** | **Lat** | **Long** | **Relative distance TF** | **$SiO_2$** | | **$TiO_2$** | | **$Al_2O_3$** | | **$Cr_2O_3$** | | **FeO** | | **MnO** | | **MgO** | | **CaO** | | **$Na_2O$** | | **$K_2O$** | | **$P_2O_5$** | |
|---|---|---|---|---|---|---|---|---|---|---|---|---|---|---|---|---|---|---|---|---|---|---|---|---|---|
| | | | km | wt% | stdev | wt% | stdev | wt% | stdev | wt% | stdev | wt% | stdev | wt% | stdev | wt% | stdev | wt% | stdev | wt% | stdev | wt% | stdev | wt% | stdev |
| SMA1970-203A | 0.007 | -16.789 | 20.2 | 52.2 | 0.2 | 1.284 | 0.011 | 16.31 | 0.09 | 0.017 | 0.012 | 8.35 | 0.09 | 0.15 | 0.01 | 7.91 | 0.03 | 9.07 | 0.04 | 3.35 | 0.06 | 0.297 | 0.016 | 0.158 | 0.052 |
| SMA1970-203B | 0.007 | -16.789 | 20.2 | 52.6 | 0.2 | 1.302 | 0.019 | 16.45 | 0.10 | 0.016 | 0.009 | 8.53 | 0.06 | 0.14 | 0.01 | 7.71 | 0.10 | 9.11 | 0.09 | 3.35 | 0.05 | 0.283 | 0.008 | 0.111 | 0.030 |
| SMA1970-203C | 0.007 | -16.789 | 20.2 | 51.9 | 0.1 | 1.345 | 0.045 | 16.37 | 0.15 | 0.009 | 0.005 | 8.37 | 0.07 | 0.12 | 0.01 | 7.76 | 0.07 | 9.10 | 0.10 | 3.35 | 0.08 | 0.298 | 0.009 | 0.149 | 0.024 |
| SMA1970-203D | 0.007 | -16.789 | 20.2 | 52.0 | 0.0 | 1.307 | 0.023 | 16.39 | 0.07 | 0.014 | 0.006 | 8.41 | 0.11 | 0.14 | 0.03 | 7.84 | 0.16 | 9.03 | 0.06 | 3.36 | 0.05 | 0.306 | 0.019 | 0.179 | 0.040 |
| SMA1970-204 | 0.007 | -16.789 | 20.2 | 52.4 | 0.2 | 1.318 | 0.053 | 16.34 | 0.07 | 0.017 | 0.009 | 8.44 | 0.13 | 0.15 | 0.01 | 7.29 | 0.19 | 9.37 | 0.08 | 3.42 | 0.04 | 0.275 | 0.013 | 0.165 | 0.025 |
| SMA1970-205 | 0.006 | -16.788 | 20.3 | 52.6 | 0.1 | 1.331 | 0.046 | 16.44 | 0.07 | 0.020 | 0.012 | 8.53 | 0.10 | 0.14 | 0.02 | 7.64 | 0.07 | 9.09 | 0.04 | 3.27 | 0.07 | 0.295 | 0.010 | 0.167 | 0.050 |
| SMA1974-265 | -0.035 | -16.454 | 36.5 | 50.0 | 0.1 | 1.297 | 0.034 | 16.42 | 0.14 | 0.006 | 0.004 | 9.34 | 0.12 | 0.17 | 0.03 | 7.36 | 0.11 | 10.57 | 0.11 | 3.43 | 0.09 | 0.271 | 0.018 | 0.169 | 0.030 |
| SMA1974-268 | -0.035 | -16.454 | 36.5 | 49.3 | 0.4 | 1.230 | 0.025 | 16.81 | 0.05 | 0.009 | 0.007 | 9.31 | 0.03 | 0.16 | 0.01 | 7.45 | 0.09 | 10.68 | 0.08 | 3.27 | 0.07 | 0.262 | 0.013 | 0.150 | 0.018 |
| SMA1975-290 | -0.076 | -16.464 | 40.5 | 51.9 | 0.2 | 1.680 | 0.059 | 15.69 | 0.08 | 0.007 | 0.007 | 8.98 | 0.08 | 0.14 | 0.03 | 7.02 | 0.08 | 10.02 | 0.14 | 3.01 | 0.05 | 0.393 | 0.012 | 0.199 | 0.047 |
| SMA1975-291 | -0.076 | -16.463 | 40.5 | 51.5 | 0.1 | 1.627 | 0.061 | 15.77 | 0.13 | 0.017 | 0.007 | 8.78 | 0.09 | 0.15 | 0.03 | 7.11 | 0.06 | 10.07 | 0.05 | 2.90 | 0.01 | 0.378 | 0.017 | 0.211 | 0.022 |
| SMA1975-292 | -0.076 | -16.463 | 40.5 | 52.5 | 0.1 | 1.588 | 0.060 | 15.97 | 0.07 | 0.013 | 0.009 | 8.86 | 0.08 | 0.15 | 0.01 | 7.04 | 0.09 | 10.04 | 0.11 | 2.81 | 0.08 | 0.375 | 0.013 | 0.185 | 0.007 |
| SMA1975-294 | -0.075 | -16.462 | 40.4 | 51.7 | 0.2 | 1.628 | 0.040 | 15.67 | 0.05 | 0.001 | 0.002 | 8.85 | 0.08 | 0.14 | 0.01 | 7.29 | 0.08 | 10.06 | 0.19 | 2.96 | 0.11 | 0.372 | 0.012 | 0.182 | 0.021 |
| SMA1975-295 | -0.075 | -16.462 | 40.4 | 52.0 | 0.2 | 0.941 | 0.037 | 16.20 | 0.04 | 0.017 | 0.017 | 9.04 | 0.04 | 0.14 | 0.01 | 8.80 | 0.10 | 9.54 | 0.09 | 2.74 | 0.05 | 0.101 | 0.009 | 0.061 | 0.015 |
| SMA1975-297 | -0.074 | -16.460 | 40.4 | 52.7 | 0.1 | 1.555 | 0.034 | 15.63 | 0.06 | 0.013 | 0.004 | 9.12 | 0.03 | 0.14 | 0.01 | 7.58 | 0.08 | 9.82 | 0.07 | 2.87 | 0.10 | 0.299 | 0.007 | 0.154 | 0.007 |
| SMA1975-298 | -0.074 | -16.460 | 40.4 | 52.1 | 0.1 | 1.621 | 0.031 | 15.70 | 0.05 | 0.011 | 0.009 | 8.99 | 0.13 | 0.14 | 0.01 | 7.35 | 0.06 | 9.87 | 0.04 | 2.86 | 0.11 | 0.349 | 0.017 | 0.173 | 0.040 |
| SMA1975-299 | -0.073 | -16.460 | 40.3 | 50.9 | 0.2 | 0.914 | 0.047 | 16.90 | 0.04 | | | 9.24 | 0.05 | 0.17 | 0.00 | 8.06 | 0.08 | 9.78 | 0.06 | 2.90 | 0.05 | 0.124 | 0.018 | 0.084 | 0.014 |
| SMA1975-301 | -0.071 | -16.458 | 40.1 | 51.7 | 0.1 | 0.882 | 0.023 | 16.28 | 0.03 | 0.016 | 0.008 | 8.92 | 0.09 | 0.14 | 0.01 | 8.95 | 0.07 | 9.34 | 0.11 | 2.68 | 0.04 | 0.092 | 0.011 | 0.072 | 0.025 |
| SMA1975-302 | -0.070 | -16.457 | 40.1 | 51.8 | 0.1 | 0.903 | 0.058 | 16.43 | 0.07 | 0.021 | 0.003 | 9.01 | 0.10 | 0.15 | 0.02 | 8.91 | 0.06 | 9.46 | 0.08 | 2.79 | 0.04 | 0.107 | 0.007 | 0.077 | 0.047 |
| SMA1975-304 | -0.068 | -16.455 | 40.0 | 51.9 | 0.1 | 1.624 | 0.044 | 15.70 | 0.06 | 0.013 | 0.009 | 8.88 | 0.09 | 0.14 | 0.01 | 7.50 | 0.05 | 9.86 | 0.09 | 2.93 | 0.08 | 0.327 | 0.010 | 0.166 | 0.047 |
| SMA1975-305 | -0.068 | -16.455 | 39.9 | 51.0 | 0.1 | 0.977 | 0.040 | 17.09 | 0.07 | 0.009 | 0.009 | 9.31 | 0.10 | 0.16 | 0.01 | 8.01 | 0.08 | 9.72 | 0.10 | 2.86 | 0.02 | 0.109 | 0.014 | 0.070 | 0.011 |
| SMA1975-306 | -0.067 | -16.455 | 39.9 | 51.9 | 0.2 | 1.628 | 0.057 | 15.56 | 0.06 | 0.016 | 0.008 | 9.07 | 0.08 | 0.15 | 0.01 | 7.54 | 0.08 | 9.71 | 0.09 | 2.86 | 0.03 | 0.318 | 0.023 | 0.180 | 0.033 |
| SMA1975-307 | -0.065 | -16.455 | 39.7 | 51.4 | 0.2 | 1.050 | 0.018 | 16.62 | 0.11 | 0.001 | 0.001 | 9.22 | 0.11 | 0.16 | 0.02 | 7.71 | 0.04 | 9.67 | 0.05 | 3.09 | 0.06 | 0.204 | 0.025 | 0.123 | 0.017 |
| SMA1975-308 | -0.065 | -16.455 | 39.6 | 50.8 | 0.3 | 0.975 | 0.048 | 17.04 | 0.10 | 0.005 | 0.005 | 9.20 | 0.07 | 0.17 | 0.02 | 7.90 | 0.10 | 9.87 | 0.08 | 2.83 | 0.06 | 0.104 | 0.011 | 0.048 | 0.010 |
| SMA1975-309 | -0.064 | -16.455 | 39.6 | 51.1 | 0.2 | 0.964 | 0.071 | 16.88 | 0.15 | 0.014 | 0.009 | 9.24 | 0.10 | 0.16 | 0.01 | 7.93 | 0.08 | 9.88 | 0.13 | 2.83 | 0.06 | 0.119 | 0.014 | 0.076 | 0.040 |
| SMA1976-310 | -0.004 | -16.657 | 26.0 | 51.0 | 0.0 | 0.916 | 0.070 | 16.75 | 0.08 | 0.010 | 0.007 | 9.13 | 0.09 | 0.14 | 0.01 | 8.02 | 0.08 | 9.76 | 0.17 | 2.93 | 0.03 | 0.157 | 0.006 | 0.058 | 0.036 |
| SMA1976-312 | -0.004 | -16.655 | 26.1 | 53.1 | 0.1 | 1.068 | 0.043 | 15.89 | 0.15 | 0.021 | 0.010 | 8.33 | 0.06 | 0.13 | 0.01 | 8.46 | 0.07 | 9.25 | 0.07 | 3.08 | 0.09 | 0.168 | 0.011 | 0.125 | 0.014 |
| SMA1976-314 | -0.003 | -16.652 | 26.0 | 52.4 | 0.3 | 1.062 | 0.057 | 15.71 | 0.12 | 0.017 | 0.006 | 8.39 | 0.04 | 0.13 | 0.02 | 8.54 | 0.03 | 9.22 | 0.07 | 3.07 | 0.04 | 0.208 | 0.011 | 0.094 | 0.014 |
| SMA1980-378 | 0.007 | -16.757 | 21.3 | 53.1 | 0.3 | 1.033 | 0.046 | 16.30 | 0.08 | 0.017 | 0.006 | 8.49 | 0.06 | 0.15 | 0.01 | 8.08 | 0.07 | 9.12 | 0.04 | 2.97 | 0.03 | 0.251 | 0.013 | 0.129 | 0.045 |
| SMA1980-379 | 0.007 | -16.757 | 21.3 | 52.7 | 0.1 | 1.093 | 0.045 | 16.36 | 0.14 | 0.010 | 0.008 | 8.30 | 0.09 | 0.13 | 0.02 | 7.97 | 0.09 | 9.20 | 0.04 | 3.05 | 0.01 | 0.247 | 0.009 | 0.130 | 0.055 |
| SMA1980-381 | 0.006 | -16.752 | 21.6 | 52.6 | 0.1 | 1.137 | 0.039 | 16.33 | 0.06 | 0.008 | 0.006 | 8.42 | 0.10 | 0.14 | 0.02 | 8.01 | 0.05 | 9.07 | 0.11 | 3.07 | 0.07 | 0.279 | 0.010 | 0.075 | 0.027 |
| SMA1980-382 | 0.004 | -16.751 | 21.8 | 52.6 | 0.0 | 1.064 | 0.021 | 16.32 | 0.05 | 0.008 | 0.005 | 8.45 | 0.08 | 0.14 | 0.03 | 8.05 | 0.05 | 9.10 | 0.08 | 3.01 | 0.06 | 0.232 | 0.008 | 0.123 | 0.040 |
| SMA1980-383 | 0.003 | -16.750 | 22.0 | 52.1 | 0.3 | 1.015 | 0.029 | 16.48 | 0.06 | 0.011 | 0.012 | 8.40 | 0.10 | 0.14 | 0.02 | 7.93 | 0.04 | 9.13 | 0.14 | 2.87 | 0.03 | 0.212 | 0.015 | 0.111 | 0.016 |
| SMA1980-384 | 0.000 | -16.751 | 22.3 | 52.5 | 0.1 | 1.004 | 0.045 | 16.42 | 0.11 | 0.016 | 0.015 | 8.38 | 0.07 | 0.15 | 0.01 | 8.11 | 0.02 | 9.08 | 0.10 | 2.98 | 0.03 | 0.208 | 0.012 | 0.102 | 0.012 |
| SMA1980-385 | -0.001 | -16.750 | 22.4 | 52.6 | 0.1 | 1.059 | 0.023 | 16.34 | 0.04 | 0.008 | 0.012 | 8.58 | 0.02 | 0.13 | 0.01 | 8.05 | 0.07 | 9.23 | 0.01 | 2.94 | 0.03 | 0.213 | 0.015 | 0.109 | 0.018 |
| SMA1980-386 | -0.003 | -16.749 | 22.7 | 51.2 | 0.1 | 0.977 | 0.053 | 16.38 | 0.08 | 0.013 | 0.009 | 8.74 | 0.03 | 0.14 | 0.02 | 7.74 | 0.08 | 9.40 | 0.05 | 3.03 | 0.05 | 0.189 | 0.022 | 0.104 | 0.047 |
| SMA1980-387 | -0.005 | -16.747 | 22.9 | 51.3 | 0.1 | 0.958 | 0.077 | 16.10 | 0.11 | 0.009 | 0.007 | 8.74 | 0.09 | 0.14 | 0.01 | 8.46 | 0.05 | 9.20 | 0.11 | 3.01 | 0.03 | 0.195 | 0.022 | 0.110 | 0.025 |
| SMA1980-388 | -0.006 | -16.747 | 23.0 | 51.6 | 0.3 | 1.034 | 0.045 | 16.48 | 0.14 | 0.011 | 0.012 | 8.67 | 0.04 | 0.14 | 0.02 | 8.33 | 0.10 | 9.25 | 0.07 | 2.96 | 0.04 | 0.202 | 0.011 | 0.074 | 0.023 |
| SMA1980-389 | -0.007 | -16.746 | 23.2 | 51.4 | 0.2 | 0.935 | 0.036 | 16.61 | 0.12 | 0.024 | 0.013 | 8.87 | 0.04 | 0.14 | 0.01 | 8.37 | 0.09 | 9.35 | 0.06 | 2.85 | 0.07 | 0.135 | 0.007 | 0.059 | 0.037 |
| SMA1980-390 | -0.012 | -16.742 | 23.9 | 51.5 | 0.2 | 1.010 | 0.047 | 16.49 | 0.06 | 0.007 | 0.007 | 8.70 | 0.05 | 0.16 | 0.01 | 8.26 | 0.04 | 9.30 | 0.10 | 2.93 | 0.05 | 0.201 | 0.013 | 0.076 | 0.016 |
| SMA1980-391 | -0.013 | -16.741 | 24.0 | 52.0 | 0.1 | 1.034 | 0.031 | 16.50 | 0.04 | 0.017 | 0.010 | 8.81 | 0.06 | 0.14 | 0.01 | 8.35 | 0.04 | 9.18 | 0.02 | 2.92 | 0.05 | 0.199 | 0.011 | 0.100 | 0.030 |
| SMA1981-405 | 0.030 | -16.600 | 24.5 | 54.2 | 0.2 | 1.130 | 0.015 | 16.20 | 0.12 | 0.010 | 0.004 | 7.64 | 0.09 | 0.14 | 0.02 | 7.50 | 0.10 | 9.13 | 0.09 | 3.01 | 0.06 | 0.215 | 0.016 | 0.106 | 0.038 |
| S1644 | 0.090 | -16.709 | 14.3 | 53.9 | | 1.530 | | 16.22 | | | | 8.71 | | 0.13 | | 6.99 | | 9.14 | | 3.50 | | 0.340 | | 0.190 | |
| S1669 | 0.088 | -16.596 | 18.5 | 53.8 | | 1.040 | | 16.50 | | | | 8.53 | | 0.10 | | 8.13 | | 9.12 | | 2.90 | | 0.10 | | 0.060 | |

*Table S6.3 - Trace elements measure with LA-ICP-MS*

| **Sample** | | **Rb** | | **Sr** | | **Y** | | **Zr** | | **Nb** | | **Mo** | | **Cs** | | **Ba** | | **La** | | **Ce** | |
|---|---|---|---|---|---|---|---|---|---|---|---|---|---|---|---|---|---|---|---|---|---|
| | | ppm | stdev | ppm | stdev | ppm | stdev | ppm | stdev | ppm | stdev | ppm | stdev | ppm | stdev | ppm | stdev | ppm | stdev | ppm | stdev |
| SMA1970-203A | B | 5.045 | 0.041 | 226.3 | 1.2 | 16.761 | 0.162 | 76.774 | 0.604 | 8.160 | 0.058 | 0.490 | 0.038 | 0.045 | 0.003 | 57.939 | 0.272 | 6.143 | 0.052 | 15.45 | 0.15 |
| SMA1970-203B | B | 5.054 | 0.084 | 227.2 | 1.2 | 17.161 | 0.120 | 78.085 | 0.553 | 8.175 | 0.024 | 0.476 | 0.045 | 0.044 | 0.004 | 58.197 | 0.280 | 6.211 | 0.048 | 15.54 | 0.14 |
| SMA1970-203C | B | 5.577 | 0.041 | 232.1 | 0.5 | 17.830 | 0.013 | 88.675 | 0.329 | 8.495 | 0.037 | | | | | 58.242 | 0.057 | 6.316 | 0.039 | 15.70 | 0.05 |
| SMA1970-203D | B | 5.581 | 0.096 | 231.0 | 1.4 | 18.623 | 0.380 | 92.106 | 1.642 | 8.347 | 0.055 | | | | | 57.828 | 0.205 | 6.356 | 0.076 | 15.52 | 0.03 |
| SMA1970-204 | B | 4.807 | 0.177 | 230.4 | 2.9 | 16.934 | 0.421 | 76.754 | 1.991 | 7.946 | 0.192 | 0.482 | 0.050 | 0.044 | 0.005 | 55.372 | 1.252 | 6.055 | 0.124 | 15.18 | 0.43 |
| SMA1970-205 | B | 5.555 | 0.021 | 237.7 | 0.5 | 17.740 | 0.065 | 81.735 | 0.286 | 8.808 | 0.040 | 0.545 | 0.011 | 0.054 | 0.002 | 61.493 | 0.031 | 6.548 | 0.019 | 15.86 | 0.01 |
| SMA1974-265 | B | 5.289 | 0.115 | 192.2 | 0.3 | 21.076 | 0.208 | 80.673 | 0.896 | 8.671 | 0.143 | 0.588 | 0.027 | 0.054 | 0.003 | 59.524 | 1.204 | 6.128 | 0.085 | 15.28 | 0.29 |
| SMA1974-268 | B | 4.699 | 0.198 | 200.4 | 4.0 | 18.235 | 0.540 | 63.643 | 2.159 | 7.374 | 0.293 | 0.499 | 0.004 | 0.048 | 0.002 | 56.184 | 1.545 | 5.649 | 0.167 | 14.69 | 0.43 |
| SMA1975-290 | B | 7.141 | 0.035 | 288.0 | 0.8 | 16.815 | 0.058 | 94.750 | 0.108 | 13.028 | 0.009 | 0.799 | 0.008 | 0.073 | 0.001 | 89.984 | 0.192 | 8.803 | 0.020 | 20.15 | 0.03 |
| SMA1975-291 | B | 7.229 | 0.085 | 290.3 | 1.8 | 16.359 | 0.094 | 92.672 | 0.465 | 13.108 | 0.011 | 0.818 | 0.053 | 0.072 | 0.004 | 91.012 | 0.404 | 8.678 | 0.006 | 20.27 | 0.08 |
| SMA1975-292 | B | 7.037 | 0.063 | 291.1 | 1.8 | 17.440 | 0.342 | 96.482 | 1.092 | 12.921 | 0.183 | 0.745 | 0.049 | 0.071 | 0.004 | 89.224 | 1.237 | 8.766 | 0.054 | 19.64 | 0.13 |
| SMA1975-294 | B | 7.214 | 0.080 | 290.1 | 0.4 | 16.502 | 0.151 | 91.494 | 1.005 | 12.968 | 0.036 | 0.785 | 0.028 | 0.067 | 0.004 | 89.378 | 0.576 | 8.505 | 0.040 | 19.73 | 0.11 |
| SMA1975-295 | M | 1.641 | 0.051 | 149.2 | 1.6 | 13.763 | 0.234 | 39.843 | 0.281 | 2.686 | 0.042 | 0.181 | 0.010 | | | 18.743 | 0.257 | 2.432 | 0.033 | 6.13 | 0.06 |
| SMA1975-297 | B | 6.015 | 0.039 | 268.9 | 0.8 | 16.735 | 0.049 | 87.223 | 0.375 | 10.764 | 0.013 | 0.680 | 0.024 | 0.063 | 0.001 | 75.968 | 0.259 | 7.166 | 0.013 | 16.81 | 0.06 |
| SMA1975-298 | B | 6.193 | 0.037 | 269.5 | 0.4 | 16.543 | 0.152 | 86.117 | 0.806 | 10.922 | 0.069 | 0.741 | 0.009 | 0.062 | 0.002 | 78.172 | 0.351 | 7.169 | 0.036 | 17.20 | 0.06 |
| SMA1975-299 | M | 1.901 | 0.073 | 162.0 | 1.1 | 15.970 | 0.185 | 45.810 | 0.420 | 3.068 | 0.031 | 0.204 | 0.043 | | | 21.623 | 0.060 | 2.726 | 0.013 | 6.82 | 0.10 |
| SMA1975-301 | M | 1.629 | 0.143 | 150.3 | 0.5 | 13.467 | 0.041 | 38.567 | 0.057 | 2.645 | 0.027 | 0.178 | 0.011 | | | 18.927 | 0.217 | 2.410 | 0.026 | 6.26 | 0.09 |
| SMA1975-302 | M | 1.681 | 0.154 | 147.7 | 0.6 | 13.680 | 0.115 | 39.140 | 0.516 | 2.591 | 0.010 | 0.172 | 0.016 | | | 18.610 | 0.153 | 2.397 | 0.027 | 6.08 | 0.03 |
| SMA1975-304 | B | 5.990 | 0.055 | 272.1 | 1.6 | 16.939 | 0.064 | 89.167 | 0.456 | 10.712 | 0.023 | 0.655 | 0.025 | 0.057 | 0.004 | 76.715 | 0.321 | 7.253 | 0.034 | 16.81 | 0.09 |
| SMA1975-305 | M | 1.923 | 0.136 | 157.8 | 1.5 | 14.637 | 0.118 | 42.657 | 0.469 | 3.121 | 0.054 | 0.225 | 0.016 | | | 21.607 | 0.117 | 2.702 | 0.021 | 6.97 | 0.07 |
| SMA1975-306 | B | 6.047 | 0.048 | 263.0 | 0.2 | 15.561 | 0.121 | 82.605 | 0.556 | 10.645 | 0.047 | 0.655 | 0.013 | 0.056 | 0.003 | 77.099 | 0.558 | 6.979 | 0.021 | 16.86 | 0.05 |
| SMA1975-307 | B | 4.211 | 0.254 | 164.4 | 1.1 | 19.560 | 0.259 | 71.063 | 0.492 | 6.427 | 0.037 | 0.410 | 0.010 | 0.042 | 0.002 | 39.449 | 0.097 | 4.681 | 0.029 | 11.46 | 0.07 |
| SMA1975-308 | B | 2.003 | 0.050 | 159.7 | 2.0 | 15.025 | 0.227 | 45.814 | 0.699 | 3.164 | 0.036 | 0.242 | 0.013 | 0.006 | 0.008 | 21.943 | 0.249 | 2.648 | 0.050 | 7.20 | 0.05 |
| SMA1975-309 | B | 1.907 | 0.022 | 161.3 | 0.6 | 15.527 | 0.072 | 47.485 | 0.256 | 3.041 | 0.015 | 0.206 | 0.016 | 0.011 | 0.008 | 21.453 | 0.060 | 2.586 | 0.013 | 7.01 | 0.02 |
| SMA1976-310 | M | 2.690 | 0.014 | 184.3 | 4.2 | 12.417 | 0.324 | 41.880 | 1.011 | 3.631 | 0.083 | 0.231 | 0.020 | | | 29.503 | 0.638 | 3.027 | 0.036 | 7.53 | 0.18 |
| SMA1976-312 | M | 2.985 | 0.021 | 185.2 | 1.8 | 14.983 | 0.053 | 59.250 | 0.411 | 4.698 | 0.014 | 0.348 | 0.022 | | | 31.633 | 0.225 | 4.121 | 0.055 | 9.89 | 0.06 |
| SMA1976-314 | M | 3.373 | 0.131 | 180.3 | 0.4 | 14.903 | 0.080 | 59.003 | 0.204 | 5.206 | 0.118 | 0.367 | 0.038 | | | 35.603 | 0.265 | 4.373 | 0.031 | 10.56 | 0.08 |
| SMA1980-378 | M | 4.636 | 0.017 | 194.0 | 2.1 | 15.247 | 0.242 | 59.360 | 0.980 | 6.809 | 0.116 | 0.449 | 0.038 | | | 47.643 | 0.539 | 4.965 | 0.033 | 11.44 | 0.10 |
| SMA1980-379 | B | 5.056 | 0.123 | 194.8 | 1.1 | 14.479 | 0.153 | 60.949 | 0.455 | 7.150 | 0.197 | 0.416 | 0.146 | 0.057 | 0.004 | 49.354 | 0.223 | 4.874 | 0.022 | 11.98 | 0.12 |
| SMA1980-381 | B | 5.642 | 0.097 | 195.4 | 0.1 | 14.722 | 0.069 | 63.901 | 0.552 | 7.969 | 0.112 | 0.439 | 0.028 | 0.063 | 0.009 | 55.388 | 0.684 | 5.266 | 0.017 | 12.78 | 0.15 |
| SMA1980-382 | M | 4.252 | 0.076 | 190.5 | 2.9 | 14.373 | 0.103 | 53.863 | 0.439 | 6.404 | 0.034 | 0.423 | 0.025 | | | 44.953 | 0.373 | 4.640 | 0.028 | 10.78 | 0.07 |

The letters correspond to the place where the analyses have been done: P: PSO Plouzané; M: CIGS Modena; L: previously measured at Lamont Doherty Earth Observatory (Cipriani, A.).

*Table S6.3 (continue)*

| **Sample** | | **Rb** | | **Sr** | | **Y** | | **Zr** | | **Nb** | | **Mo** | | **Cs** | | **Ba** | | **La** | | **Ce** | |
|---|---|---|---|---|---|---|---|---|---|---|---|---|---|---|---|---|---|---|---|---|---|
| | | ppm | stdev | ppm | stdev | ppm | stdev | ppm | stdev | ppm | stdev | ppm | stdev | ppm | stdev | ppm | stdev | ppm | stdev | ppm | stdev |
| SMA1980-383 | B | 4.284 | 0.100 | 189.4 | 1.6 | 13.940 | 0.056 | 56.009 | 0.201 | 6.102 | 0.057 | 0.144 | 0.204 | 0.031 | 0.022 | 42.369 | 0.319 | 4.234 | 0.029 | 10.55 | 0.04 |
| SMA1980-384 | M | 3.666 | 0.098 | 195.4 | 1.6 | 15.363 | 0.025 | 55.280 | 0.366 | 5.640 | 0.067 | 0.366 | 0.016 | | | 40.823 | 0.376 | 4.385 | 0.020 | 10.09 | 0.09 |
| SMA1980-385 | M | 3.785 | 0.058 | 192.6 | 1.6 | 15.420 | 0.265 | 55.403 | 1.014 | 5.614 | 0.047 | 0.374 | 0.020 | | | 41.340 | 0.093 | 4.398 | 0.034 | 10.11 | 0.07 |
| SMA1980-386 | B | 3.781 | 0.043 | 191.5 | 0.4 | 14.744 | 0.155 | 52.782 | 0.559 | 5.290 | 0.004 | | 0.000 | 0.048 | 0.002 | 37.850 | 0.047 | 3.808 | 0.023 | 9.76 | 0.06 |
| SMA1980-387 | M | 3.717 | 0.176 | 184.1 | 2.4 | 14.590 | 0.216 | 49.670 | 0.889 | 5.395 | 0.127 | 0.384 | 0.010 | | | 39.940 | 0.364 | 4.066 | 0.053 | 9.70 | 0.11 |
| SMA1980-388 | M | 3.749 | 0.062 | 186.3 | 2.3 | 14.820 | 0.343 | 51.013 | 1.241 | 5.498 | 0.080 | 0.390 | 0.031 | | | 39.837 | 0.474 | 4.046 | 0.072 | 9.55 | 0.13 |
| SMA1980-389 | M | 2.230 | 0.029 | 181.5 | 0.2 | 13.403 | 0.099 | 39.457 | 0.119 | 3.292 | 0.053 | 0.253 | 0.005 | | | 25.440 | 0.192 | 2.796 | 0.028 | 6.93 | 0.09 |
| SMA1980-390 | M | 3.495 | 0.118 | 189.0 | 0.7 | 14.520 | 0.119 | 48.583 | 0.280 | 5.052 | 0.025 | 0.367 | 0.030 | | | 37.277 | 0.315 | 3.829 | 0.059 | 9.26 | 0.15 |
| SMA1980-391 | M | 3.677 | 0.158 | 190.6 | 2.0 | 15.397 | 0.264 | 51.647 | 0.415 | 5.293 | 0.051 | 0.329 | 0.024 | | | 37.610 | 0.684 | 3.964 | 0.072 | 9.31 | 0.15 |
| SMA1981-405 | B | 4.360 | 0.027 | 200.9 | 0.6 | 13.166 | 0.232 | 62.865 | 0.946 | 6.202 | 0.036 | 0.325 | 0.236 | 0.030 | 0.022 | 41.838 | 0.064 | 4.472 | 0.053 | 11.36 | 0.04 |
| S1644 | | 6.230 | | 232.1 | | 22.400 | | 93.400 | | 8.510 | | | | 0.060 | | 59.400 | | 6.460 | | 15.26 | |
| S1669 | | 2.210 | | 183.6 | | 12.900 | | | | 3.210 | | | | 0.020 | | 21.580 | | 2.920 | | 7.29 | |

*Table S6.3 (continue)*

| **Sample** | **Pr** | | **Nd** | | **Sm** | | **Eu** | | **Gd** | | **Tb** | | **Dy** | | **Ho** | | **Er** | | **Yb** | | **Lu** | |
|---|---|---|---|---|---|---|---|---|---|---|---|---|---|---|---|---|---|---|---|---|---|---|
| | ppm | stdev | ppm | stdev | ppm | stdev | ppm | stdev | ppm | stdev | ppm | stdev | ppm | stdev | ppm | stdev | ppm | stdev | ppm | stdev | ppm | stdev |
| SMA1970-203A | 2.049 | 0.010 | 9.289 | 0.094 | 2.666 | 0.007 | 1.034 | 0.005 | 3.025 | 0.023 | 0.498 | 0.005 | 3.163 | 0.025 | 0.646 | 0.008 | 1.818 | 0.011 | 1.716 | 0.018 | 0.245 | 0.003 |
| SMA1970-203B | 2.051 | 0.009 | 9.441 | 0.094 | 2.687 | 0.030 | 1.049 | 0.007 | 3.101 | 0.027 | 0.512 | 0.006 | 3.230 | 0.034 | 0.665 | 0.004 | 1.855 | 0.006 | 1.767 | 0.031 | 0.252 | 0.001 |
| SMA1970-203C | 2.070 | 0.018 | 9.648 | 0.117 | 2.727 | 0.022 | 1.056 | 0.022 | 3.112 | 0.037 | 0.510 | 0.002 | 3.260 | 0.033 | 0.653 | 0.007 | 1.853 | 0.004 | 1.742 | 0.039 | 0.255 | 0.006 |
| SMA1970-203D | 2.067 | 0.026 | 9.793 | 0.253 | 2.745 | 0.086 | 1.060 | 0.012 | 3.168 | 0.087 | 0.533 | 0.005 | 3.445 | 0.091 | 0.705 | 0.011 | 1.940 | 0.055 | 1.809 | 0.012 | 0.267 | 0.003 |
| SMA1970-204 | 2.043 | 0.058 | 9.347 | 0.199 | 2.714 | 0.061 | 1.058 | 0.018 | 3.065 | 0.095 | 0.511 | 0.015 | 3.226 | 0.073 | 0.654 | 0.020 | 1.830 | 0.048 | 1.758 | 0.030 | 0.251 | 0.008 |
| SMA1970-205 | 2.085 | 0.022 | 9.556 | 0.044 | 2.770 | 0.019 | 1.078 | 0.006 | 3.211 | 0.015 | 0.530 | 0.003 | 3.382 | 0.009 | 0.683 | 0.003 | 1.871 | 0.011 | 1.785 | 0.013 | 0.255 | 0.001 |
| SMA1974-265 | 2.075 | 0.044 | 9.847 | 0.156 | 2.859 | 0.021 | 1.111 | 0.013 | 3.449 | 0.031 | 0.581 | 0.011 | 3.709 | 0.049 | 0.775 | 0.006 | 2.195 | 0.042 | 2.088 | 0.028 | 0.305 | 0.002 |
| SMA1974-268 | 2.016 | 0.071 | 9.343 | 0.304 | 2.697 | 0.081 | 1.103 | 0.025 | 3.194 | 0.103 | 0.542 | 0.018 | 3.449 | 0.114 | 0.712 | 0.019 | 1.991 | 0.072 | 1.905 | 0.070 | 0.275 | 0.009 |
| SMA1975-290 | 2.599 | 0.004 | 11.954 | 0.031 | 3.248 | 0.036 | 1.266 | 0.008 | 3.481 | 0.014 | 0.546 | 0.004 | 3.250 | 0.014 | 0.619 | 0.004 | 1.646 | 0.021 | 1.414 | 0.009 | 0.196 | 0.000 |
| SMA1975-291 | 2.586 | 0.007 | 11.789 | 0.025 | 3.202 | 0.025 | 1.256 | 0.002 | 3.368 | 0.021 | 0.538 | 0.003 | 3.166 | 0.009 | 0.599 | 0.001 | 1.605 | 0.015 | 1.396 | 0.005 | 0.189 | 0.001 |
| SMA1975-292 | 2.565 | 0.019 | 11.991 | 0.124 | 3.313 | 0.018 | 1.250 | 0.010 | 3.628 | 0.079 | 0.563 | 0.013 | 3.351 | 0.052 | 0.642 | 0.014 | 1.703 | 0.032 | 1.470 | 0.005 | 0.205 | 0.005 |
| SMA1975-294 | 2.529 | 0.015 | 11.585 | 0.013 | 3.228 | 0.014 | 1.243 | 0.004 | 3.433 | 0.014 | 0.532 | 0.004 | 3.155 | 0.004 | 0.603 | 0.004 | 1.597 | 0.035 | 1.385 | 0.006 | 0.191 | 0.003 |
| SMA1975-295 | 0.935 | 0.031 | 5.009 | 0.131 | 1.656 | 0.100 | 0.741 | 0.022 | 2.304 | 0.047 | 0.399 | 0.011 | 2.626 | 0.024 | 0.533 | 0.007 | 1.586 | 0.017 | 1.459 | 0.009 | 0.195 | 0.003 |
| SMA1975-297 | 2.235 | 0.004 | 10.601 | 0.038 | 3.078 | 0.012 | 1.194 | 0.006 | 3.443 | 0.010 | 0.542 | 0.003 | 3.226 | 0.016 | 0.623 | 0.006 | 1.639 | 0.006 | 1.405 | 0.012 | 0.196 | 0.001 |
| SMA1975-298 | 2.261 | 0.004 | 10.636 | 0.073 | 3.067 | 0.008 | 1.205 | 0.006 | 3.421 | 0.018 | 0.538 | 0.002 | 3.196 | 0.030 | 0.607 | 0.008 | 1.599 | 0.028 | 1.379 | 0.013 | 0.195 | 0.004 |
| SMA1975-299 | 1.037 | 0.018 | 5.519 | 0.108 | 1.954 | 0.022 | 0.829 | 0.008 | 2.613 | 0.026 | 0.455 | 0.007 | 3.061 | 0.091 | 0.625 | 0.008 | 1.762 | 0.043 | 1.707 | 0.034 | 0.248 | 0.000 |
| SMA1975-301 | 0.939 | 0.012 | 4.882 | 0.075 | 1.675 | 0.030 | 0.741 | 0.012 | 2.251 | 0.064 | 0.396 | 0.014 | 2.510 | 0.013 | 0.525 | 0.012 | 1.464 | 0.022 | 1.388 | 0.032 | 0.198 | 0.004 |
| SMA1975-302 | 0.926 | 0.016 | 4.776 | 0.024 | 1.626 | 0.051 | 0.703 | 0.009 | 2.266 | 0.033 | 0.391 | 0.009 | 2.606 | 0.039 | 0.533 | 0.007 | 1.503 | 0.030 | 1.400 | 0.041 | 0.199 | 0.002 |
| SMA1975-304 | 2.251 | 0.011 | 10.656 | 0.011 | 3.092 | 0.024 | 1.194 | 0.009 | 3.472 | 0.033 | 0.544 | 0.001 | 3.253 | 0.032 | 0.624 | 0.002 | 1.654 | 0.012 | 1.428 | 0.011 | 0.198 | 0.002 |
| SMA1975-305 | 1.017 | 0.006 | 5.495 | 0.094 | 1.887 | 0.048 | 0.820 | 0.006 | 2.421 | 0.051 | 0.427 | 0.012 | 2.820 | 0.121 | 0.580 | 0.009 | 1.661 | 0.015 | 1.637 | 0.028 | 0.224 | 0.006 |
| SMA1975-306 | 2.207 | 0.009 | 10.214 | 0.039 | 2.946 | 0.030 | 1.163 | 0.005 | 3.235 | 0.023 | 0.508 | 0.005 | 3.009 | 0.029 | 0.575 | 0.005 | 1.517 | 0.020 | 1.344 | 0.015 | 0.181 | 0.002 |
| SMA1975-307 | 1.603 | 0.009 | 7.807 | 0.032 | 2.386 | 0.018 | 0.952 | 0.010 | 3.049 | 0.024 | 0.521 | 0.005 | 3.389 | 0.022 | 0.708 | 0.009 | 2.011 | 0.011 | 1.925 | 0.019 | 0.280 | 0.003 |
| SMA1975-308 | 1.042 | 0.011 | 5.348 | 0.055 | 1.790 | 0.021 | 0.795 | 0.007 | 2.340 | 0.022 | 0.404 | 0.003 | 2.650 | 0.007 | 0.555 | 0.005 | 1.551 | 0.025 | 1.466 | 0.010 | 0.210 | 0.003 |
| SMA1975-309 | 1.036 | 0.004 | 5.387 | 0.017 | 1.813 | 0.005 | 0.801 | 0.008 | 2.429 | 0.021 | 0.420 | 0.003 | 2.751 | 0.019 | 0.572 | 0.006 | 1.609 | 0.014 | 1.508 | 0.016 | 0.218 | 0.003 |
| SMA1976-310 | 1.088 | 0.026 | 5.465 | 0.123 | 1.689 | 0.075 | 0.737 | 0.011 | 2.105 | 0.059 | 0.362 | 0.015 | 2.410 | 0.078 | 0.499 | 0.011 | 1.411 | 0.067 | 1.330 | 0.051 | 0.188 | 0.004 |
| SMA1976-312 | 1.439 | 0.026 | 7.071 | 0.139 | 2.250 | 0.012 | 0.906 | 0.016 | 2.672 | 0.047 | 0.455 | 0.006 | 2.903 | 0.066 | 0.599 | 0.007 | 1.677 | 0.016 | 1.615 | 0.015 | 0.223 | 0.005 |
| SMA1976-314 | 1.508 | 0.016 | 7.320 | 0.051 | 2.281 | 0.038 | 0.874 | 0.019 | 2.720 | 0.013 | 0.454 | 0.005 | 2.820 | 0.028 | 0.589 | 0.009 | 1.689 | 0.029 | 1.574 | 0.054 | 0.233 | 0.007 |
| SMA1980-378 | 1.583 | 0.049 | 7.677 | 0.202 | 2.241 | 0.077 | 0.904 | 0.020 | 2.710 | 0.082 | 0.458 | 0.011 | 2.921 | 0.070 | 0.600 | 0.011 | 1.678 | 0.010 | 1.595 | 0.024 | 0.223 | 0.005 |
| SMA1980-379 | 1.607 | 0.016 | 7.596 | 0.012 | 2.171 | 0.033 | 0.891 | 0.019 | 2.477 | 0.042 | 0.413 | 0.006 | 2.603 | 0.020 | 0.542 | 0.007 | 1.521 | 0.029 | 1.389 | 0.027 | 0.209 | 0.005 |
| SMA1980-381 | 1.670 | 0.025 | 7.804 | 0.078 | 2.194 | 0.022 | 0.899 | 0.011 | 2.535 | 0.025 | 0.418 | 0.007 | 2.690 | 0.020 | 0.543 | 0.007 | 1.531 | 0.016 | 1.433 | 0.037 | 0.210 | 0.005 |
| SMA1980-382 | 1.502 | 0.013 | 7.282 | 0.053 | 2.232 | 0.026 | 0.889 | 0.034 | 2.550 | 0.014 | 0.430 | 0.008 | 2.734 | 0.084 | 0.553 | 0.010 | 1.636 | 0.031 | 1.521 | 0.031 | 0.215 | 0.003 |

*Table S6.3 (continue)*

| **Sample** | **Pr** | | **Nd** | | **Sm** | | **Eu** | | **Gd** | | **Tb** | | **Dy** | | **Ho** | | **Er** | | **Yb** | | **Lu** | |
|---|---|---|---|---|---|---|---|---|---|---|---|---|---|---|---|---|---|---|---|---|---|---|
| | ppm | stdev | ppm | stdev | ppm | stdev | ppm | stdev | ppm | stdev | ppm | stdev | ppm | stdev | ppm | stdev | ppm | stdev | ppm | stdev | ppm | stdev |
| SMA1980-383 | 1.438 | 0.013 | 6.853 | 0.048 | 2.011 | 0.023 | 0.834 | 0.012 | 2.321 | 0.028 | 0.392 | 0.003 | 2.527 | 0.021 | 0.518 | 0.007 | 1.474 | 0.023 | 1.392 | 0.024 | 0.201 | 0.003 |
| SMA1980-384 | 1.452 | 0.014 | 7.234 | 0.126 | 2.203 | 0.058 | 0.912 | 0.013 | 2.701 | 0.035 | 0.452 | 0.002 | 2.915 | 0.056 | 0.602 | 0.006 | 1.751 | 0.048 | 1.631 | 0.010 | 0.234 | 0.005 |
| SMA1980-385 | 1.435 | 0.011 | 7.288 | 0.101 | 2.213 | 0.086 | 0.884 | 0.028 | 2.665 | 0.059 | 0.460 | 0.011 | 2.949 | 0.052 | 0.616 | 0.007 | 1.719 | 0.032 | 1.683 | 0.107 | 0.244 | 0.014 |
| SMA1980-386 | 1.338 | 0.005 | 6.504 | 0.059 | 1.963 | 0.022 | 0.848 | 0.009 | 2.375 | 0.034 | 0.398 | 0.011 | 2.595 | 0.020 | 0.534 | 0.020 | 1.572 | 0.031 | 1.498 | 0.031 | 0.213 | 0.003 |
| SMA1980-387 | 1.354 | 0.011 | 6.517 | 0.102 | 2.016 | 0.112 | 0.837 | 0.002 | 2.528 | 0.055 | 0.432 | 0.007 | 2.797 | 0.080 | 0.592 | 0.012 | 1.717 | 0.041 | 1.663 | 0.095 | 0.235 | 0.015 |
| SMA1980-388 | 1.342 | 0.024 | 6.645 | 0.065 | 2.045 | 0.053 | 0.821 | 0.007 | 2.509 | 0.119 | 0.438 | 0.014 | 2.774 | 0.042 | 0.589 | 0.019 | 1.688 | 0.052 | 1.629 | 0.026 | 0.247 | 0.004 |
| SMA1980-389 | 1.057 | 0.004 | 5.363 | 0.148 | 1.740 | 0.047 | 0.769 | 0.010 | 2.158 | 0.023 | 0.377 | 0.006 | 2.493 | 0.030 | 0.517 | 0.004 | 1.575 | 0.037 | 1.510 | 0.027 | 0.215 | 0.002 |
| SMA1980-390 | 1.318 | 0.010 | 6.442 | 0.121 | 1.893 | 0.058 | 0.829 | 0.020 | 2.451 | 0.105 | 0.412 | 0.006 | 2.668 | 0.062 | 0.573 | 0.014 | 1.646 | 0.007 | 1.631 | 0.012 | 0.228 | 0.004 |
| SMA1980-391 | 1.349 | 0.014 | 6.556 | 0.066 | 2.056 | 0.013 | 0.867 | 0.010 | 2.498 | 0.112 | 0.435 | 0.009 | 2.842 | 0.037 | 0.593 | 0.011 | 1.671 | 0.039 | 1.665 | 0.021 | 0.243 | 0.004 |
| SMA1981-405 | 1.572 | 0.009 | 7.483 | 0.084 | 2.205 | 0.015 | 0.912 | 0.016 | 2.458 | 0.076 | 0.405 | 0.005 | 2.478 | 0.016 | 0.492 | 0.010 | 1.338 | 0.025 | 1.203 | 0.044 | 0.174 | 0.003 |
| S1644 | | | 10.420 | | 3.110 | | 1.250 | | 3.990 | | | | 4.190 | | | | 2.340 | | 2.050 | | 0.310 | |
| S1669 | | | 5.570 | | 1.810 | | 0.810 | | 2.350 | | | | 2.470 | | | | 1.340 | | 1.220 | | 0.180 | |

*Table S6.3 (continue)*

| **Sample** | **Hf** | | **Ta** | | **Pb** | | **Th** | | **U** | |
|---|---|---|---|---|---|---|---|---|---|---|
| | ppm | stdev | ppm | stdev | ppm | stdev | ppm | stdev | ppm | stdev |
| SMA1970-203A | 1.846 | 0.025 | 0.421 | 0.004 | 0.598 | 0.008 | 0.503 | 0.007 | 0.174 | 0.002 |
| SMA1970-203B | 1.909 | 0.020 | 0.420 | 0.002 | 0.619 | 0.012 | 0.519 | 0.005 | 0.178 | 0.004 |
| SMA1970-203C | 1.960 | 0.050 | 0.438 | 0.005 | 0.594 | 0.013 | 0.516 | 0.002 | 0.182 | 0.003 |
| SMA1970-203D | 1.970 | 0.038 | 0.442 | 0.008 | 0.624 | 0.003 | 0.525 | 0.012 | 0.186 | 0.007 |
| SMA1970-204 | 1.849 | 0.050 | 0.414 | 0.008 | 0.607 | 0.023 | 0.494 | 0.013 | 0.169 | 0.006 |
| SMA1970-205 | 1.970 | 0.007 | 0.453 | 0.006 | 0.665 | 0.009 | 0.533 | 0.003 | 0.185 | 0.002 |
| SMA1974-265 | 1.857 | 0.022 | 0.449 | 0.008 | 0.752 | 0.012 | 0.584 | 0.009 | 0.198 | 0.005 |
| SMA1974-268 | 1.618 | 0.057 | 0.376 | 0.018 | 0.620 | 0.036 | 0.522 | 0.027 | 0.188 | 0.003 |
| SMA1975-290 | 2.150 | 0.003 | 0.665 | 0.001 | 0.668 | 0.001 | 0.845 | 0.005 | 0.289 | 0.002 |
| SMA1975-291 | 2.073 | 0.010 | 0.654 | 0.002 | 0.681 | 0.007 | 0.827 | 0.004 | 0.291 | 0.003 |
| SMA1975-292 | 2.237 | 0.046 | 0.687 | 0.008 | 0.644 | 0.010 | 0.855 | 0.007 | 0.278 | 0.002 |
| SMA1975-294 | 2.104 | 0.023 | 0.652 | 0.002 | 0.670 | 0.015 | 0.820 | 0.011 | 0.276 | 0.002 |
| SMA1975-295 | 1.169 | 0.029 | 0.155 | 0.003 | 0.309 | 0.008 | 0.191 | 0.011 | 0.061 | 0.006 |
| SMA1975-297 | 2.103 | 0.018 | 0.563 | 0.006 | 0.593 | 0.002 | 0.681 | 0.004 | 0.232 | 0.002 |
| SMA1975-298 | 2.068 | 0.013 | 0.568 | 0.005 | 0.611 | 0.003 | 0.677 | 0.002 | 0.241 | 0.002 |
| SMA1975-299 | 1.331 | 0.030 | 0.183 | 0.007 | 0.705 | 0.062 | 0.235 | 0.003 | 0.066 | 0.002 |
| SMA1975-301 | 1.119 | 0.016 | 0.157 | 0.004 | 0.269 | 0.004 | 0.186 | 0.006 | 0.059 | 0.007 |
| SMA1975-302 | 1.146 | 0.022 | 0.150 | 0.005 | 0.413 | 0.007 | 0.197 | 0.001 | 0.060 | 0.003 |
| SMA1975-304 | 2.095 | 0.009 | 0.565 | 0.005 | 0.559 | 0.004 | 0.676 | 0.006 | 0.228 | 0.001 |
| SMA1975-305 | 1.220 | 0.013 | 0.174 | 0.004 | 0.310 | 0.015 | 0.219 | 0.011 | 0.075 | 0.002 |
| SMA1975-306 | 1.923 | 0.005 | 0.544 | 0.002 | 0.567 | 0.007 | 0.636 | 0.002 | 0.230 | 0.001 |
| SMA1975-307 | 1.628 | 0.013 | 0.335 | 0.005 | 0.455 | 0.006 | 0.440 | 0.004 | 0.154 | 0.001 |
| SMA1975-308 | 1.118 | 0.013 | 0.160 | 0.003 | 0.285 | 0.005 | 0.195 | 0.004 | 0.075 | 0.001 |
| SMA1975-309 | 1.145 | 0.010 | 0.157 | 0.001 | 0.285 | 0.003 | 0.196 | 0.001 | 0.074 | 0.001 |
| SMA1976-310 | 1.119 | 0.042 | 0.209 | 0.013 | 0.445 | 0.025 | 0.243 | 0.009 | 0.081 | 0.002 |
| SMA1976-312 | 1.536 | 0.036 | 0.269 | 0.012 | 0.853 | 0.024 | 0.377 | 0.006 | 0.116 | 0.003 |
| SMA1976-314 | 1.573 | 0.013 | 0.302 | 0.009 | 0.790 | 0.021 | 0.402 | 0.011 | 0.125 | 0.002 |
| SMA1980-378 | 1.559 | 0.036 | 0.376 | 0.005 | 0.595 | 0.008 | 0.501 | 0.014 | 0.149 | 0.005 |
| SMA1980-379 | 1.361 | 0.016 | 0.360 | 0.009 | 0.492 | 0.015 | 0.458 | 0.005 | 0.161 | 0.006 |
| SMA1980-381 | 1.401 | 0.016 | 0.396 | 0.007 | 0.508 | 0.010 | 0.508 | 0.009 | 0.178 | 0.005 |
| SMA1980-382 | 1.418 | 0.010 | 0.348 | 0.005 | 0.526 | 0.009 | 0.459 | 0.001 | 0.142 | 0.004 |
| SMA1980-383 | 1.250 | 0.011 | 0.316 | 0.002 | 0.430 | 0.007 | 0.383 | 0.002 | 0.134 | 0.004 |
| SMA1980-384 | 1.497 | 0.027 | 0.330 | 0.001 | 0.494 | 0.007 | 0.426 | 0.007 | 0.124 | 0.004 |
| SMA1980-385 | 1.537 | 0.065 | 0.335 | 0.006 | 0.537 | 0.012 | 0.438 | 0.015 | 0.131 | 0.006 |
| SMA1980-386 | 1.203 | 0.022 | 0.274 | 0.008 | 0.394 | 0.010 | 0.314 | 0.038 | 0.122 | 0.001 |
| SMA1980-387 | 1.387 | 0.012 | 0.316 | 0.009 | 0.502 | 0.006 | 0.402 | 0.011 | 0.125 | 0.004 |
| SMA1980-388 | 1.310 | 0.053 | 0.304 | 0.002 | 0.476 | 0.008 | 0.398 | 0.017 | 0.124 | 0.004 |
| SMA1980-389 | 1.089 | 0.021 | 0.185 | 0.003 | 0.425 | 0.005 | 0.225 | 0.009 | 0.074 | 0.000 |
| SMA1980-390 | 1.276 | 0.006 | 0.279 | 0.008 | 0.460 | 0.008 | 0.359 | 0.005 | 0.112 | 0.003 |
| SMA1980-391 | 1.348 | 0.018 | 0.294 | 0.002 | 0.607 | 0.021 | 0.381 | 0.009 | 0.112 | 0.005 |
| SMA1981-405 | 1.411 | 0.026 | 0.321 | 0.006 | 0.401 | 0.006 | 0.410 | 0.008 | 0.144 | 0.002 |
| S1644 | 2.500 | | 0.520 | | 0.650 | | 0.600 | | 0.194 | |
| S1669 | 1.300 | | 0.200 | | 0.330 | | 0.240 | | 0.073 | |

# CHAPTER 7 Conclusions and Perspectives

This project took advantage of the anomalous thermal setting of the Eastern Romanche Ridge Transform Intersection (ERRTI), in the Equatorial Mid-Atlantic Ridge (MAR), to identify small scale heterogeneities distributed in the mantle source in a context unaffected by hot-spot thermal and compositional contamination.

The project is based on the assumption that at cold thermal conditions, i.e., close to the ERRTI, melts derived by minor amounts of low solidus lithologies are less diluted by melts generated by the depleted host mantle. The separate extraction of the single contribution of each lithology is expected to be enhanced by heat diffusion from the high- to the low-solidus lithologies (Phipps Morgan, 2001, Brunelli et al., 2018). This thermal setting will only allow recognizing heterogeneities with a solidus lower than the average DM one.

As a general conclusion, we can state that these assumptions proved to be true and have been ground-truthed by the extreme compositional variability recorded in the recovered basalts and discussed in this thesis.

187 samples of MORB glasses recovered by dredge and submersible diving during various oceanographic expeditions: PRIMAR (S13, S16, G96) and SMARTIES in the ERRTI region have been studied for major and trace element compositions and Pb, Sr, Nd and Hf isotope ratios.

On this basis, I show here that basalts generated from a “normal” mantle source, i.e., in a cold thermal regime away from the compositional influence of hot spots, show:

- an extreme compositional variability increasing with the decrease of the mantle potential temperature (chapter 4 and 5).

- the diffuse presence of extremely enriched MORBs encompassing true alkaline basalts, with high $Na_2O$ and $K_2O$ contents and nepheline normative compositions. These rocks strictly resemble those erupted by hotspots. In particular, it appears a strong enrichment in $K_2O$, never reported in Mid-Ocean Ridge setting (chapter 4).

- major element compositions reveal mixing of melts derived from a depleted peridotitic mantle with melts derived from enriched garnet-bearing pyroxenitic material with minor amounts of K-rich phases (phlogopite). The latest are present at very small scale and are more fertile than the surrounding peridotitic mantle (chapter 4).

- melts derived by these low-solidus heterogeneities present distinct radiogenic isotope fingerprints revealing the presence of HIMU- and EMII-type mantle components together with an Ultra-Depleted Mantle (UDM). Small volume of melts derived from these components are mixed in variable amount with a predominant depleted mantle derived melt (chapter 5).

- ultra-depleted components can have variable degrees of fertility and are dispersed at fine scale within the peridotitic mantle (chapter 5).

- a group of MORBs, with coupled Eu and Sr positive anomalies and peculiar major element compositions, allows hypothesizing the presence of transient shallow partial melting event of impregnated Pl-peridotite in an Oceanic Core Complex tectonic setting (chapter 6).

This work reveals the importance of cold spots to un-blend the composition of the local depleted mantle. Hence, what is in general considered as a homogenous mantle source appears to host a minor amount of components closely resembling those largely present in hot spot environments.

Revealing the intimate difference between the large extreme components partially melted at hot spots and the ones present in small filaments dispersed in the depleted MORB mantle is the next challenge. The use of stable isotopes and volatile content (C, O, H, Cl, S, F) in basalts is increasingly described to complement the commonly used tracers of mantle heterogeneities (major and trace elements and radiogenic isotopes). While stable isotopes could help to trace thermal and mineralogical heterogeneities (Schauble, 2004, Young et al., 2015, Soderman et al., 2022), volatile elements are key tools to constrain the influence of source heterogeneity, variations in melting regime, degassing, and shallow contamination (Le Roux et al., 2006, Le Voyer et al., 2015).

Constraining melting in the Pl-stability field is also worth exploring. Only few experimental studies have been made, and most of them focus on extremely high degree of melting (Jaques and Green, 1980; Fujii and Bougault, 1983; Till et al., 2012; Chalot-Prat et al., 2010 and 2013). Experimental partial melting studies of magmatic Pl-bearing peridotites could allow to better constrain shallow, plagioclase stability field, melting processes occasionally occurring at MOR thermal minimum, where the spreading is accommodated by tectonics.

## References

Brunelli, D., Cipriani, A., Bonatti, E., 2018. *Thermal effects of pyroxenites on mantle melting below mid-ocean ridges.* Nature Geosci 11 (7), 520–525. doi:10.1038/s41561-018-0139-z.

Chalot-Prat, F., Falloon, T.J., Green, D.H., Hibberson, W.O., 2010. *An Experimental Study of Liquid Compositions in Equilibrium with Plagioclase + Spinel Lherzolite at Low Pressures (0{middle dot}75 GPa).* J Petrology 51 (11), 2349–2376. doi:10.1093/petrology/egq060.

Chalot-Prat, F., Falloon, T.J., Green, D.H., Hibberson, W.O., 2013. *Melting of plagioclase+spinel lherzolite at low pressures (0.5GPa): An experimental approach to the evolution of basaltic melt during mantle refertilisation at shallow depths.* Lithos 172-173, 61–80. doi:10.1016/j.lithos.2013.03.012.

Fujii, T., Bougault, H., 1983. *Melting relations of a magnesian abyssal tholeiite and the origin of MORBs.* Earth and Planetary Science Letters 62 (2), 283–295. doi:10.1016/0012-821X(83)90091-2.

Jaques, A.L., Green, D.H., 1980. *Anhydrous melting of peridotite at 0.15 Kb pressure and the genesis of tholeiitic basalts.* Contrib Mineral Petrol 73 (3), 287–310. doi:10.1007/BF00381447.

Le Voyer, M., Cottrell, E., Kelley, K.A., Brounce, M., Hauri, E.H., 2015. *The effect of primary versus secondary processes on the volatile content of MORB glasses: An example from the equatorial Mid-Atlantic Ridge (5°N–3°S).* J. Geophys. Res. Solid Earth 120 (1), 125–144. doi:10.1002/2014JB011160.

Leroux, P., Shirey, S., Hauri, E., Perfit, M., Bender, J., 2006. *The effects of variable sources, processes and contaminants on the composition of northern EPR MORB (8–10°N and 12–14°N): Evidence from volatiles (H2O, CO2, S) and halogens (F, Cl).* Earth and Planetary Science Letters 251 (3-4), 209–231. doi:10.1016/j.epsl.2006.09.012.

Phipps Morgan, J., 2001. *Thermodynamics of pressure release melting of a veined plum pudding mantle.* Geochem. Geophys. Geosyst. 2.

Schauble, E.A., 2004. *Applying Stable Isotope Fractionation Theory to New Systems.* Reviews in Mineralogy and Geochemistry 55 (1), 65–111. doi:10.2138/gsrmg.55.1.65.

Soderman, C.R., Shorttle, O., Matthews, S., Williams, H.M., 2022. *Global trends in novel stable isotopes in basalts: Theory and observations.* Geochimica et Cosmochimica Acta 318, 388–414. doi:10.1016/j.gca.2021.12.008.

Till, C.B., Grove, T.L., Krawczynski, M.J., 2012. *A melting model for variably depleted and enriched lherzolite in the plagioclase and spinel stability fields.* J. Geophys. Res. Solid Earth 117 (B6), n/a-n/a. doi:10.1029/2011JB009044.

Young, E.D., Manning, C.E., Schauble, E.A., Shahar, A., Macris, C.A., Lazar, C., Jordan, M., 2015. *High-temperature equilibrium isotope fractionation of non-traditional stable isotopes: Experiments, theory, and applications.* Chemical Geology 395, 176–195. doi:10.1016/j.chemgeo.2014.12.013.